



**THE RELATIONSHIP BETWEEN CHLORIDE RESISTANCE
AND MICROSTRUCTURE OF ALKALI-ACTIVATED FLY ASH-
SLAG CONCRETE**

A Thesis submitted by

Jingxiao Zhang

For the award of

Doctor of Philosophy

2022

ABSTRACT

Due to the threat of global warming, the development of sustainable construction and building materials has attracted extensive attention. Alkali-activated materials (AAMs) are considered as a promising candidate to ordinary Portland cement (OPC). Among all AAMs, the ones based on Class F fly ash (FA), granulated blast furnace slag (GGBFS) and their blends are most intensively investigated due to the huge annual production of these two precursors. For the long-term application of alkali-activated fly ash-slag (AAFS) in chloride-containing environments, it is indispensable to understand its chloride resistance.

Although the chloride resistance of AAFS has been studied for decades, there are still four issues deserving to be further studied: 1. Most previous studies were limited to short-term tests, which may be not suitable for AAFS and cannot show long-term results; 2. The influence mechanism of different parameters on chloride resistance is still not well understood; 3. The existing data is insufficient to establish the long-term prediction model; 4. The measurement of AAFS modified by Mg-based admixtures is not completely accurate. In view of the above four issues, corresponding research has been carried out in this project.

In Chapter 3, AAFS concretes with different parameters (GGBFS content, w/b, Na₂O content, SiO₂ content and s/a) were designed. The chloride resistance of them was investigated by natural chloride diffusion test (NCD) in Chapter 4. The results show that higher GGBFS content, lower w/b, higher Na₂O content and lower SiO₂ content generally improved the chloride resistance of AAFS concretes, while s/a ratio had no obvious effect.

The corresponding microstructure (including phase evolution and pore structure) was analysed in Chapter 5. Compared with the type of reaction products, the quantity of reaction products seemed to be more important for the chloride resistance of AAFS concrete. There was a good correlation between chloride resistance and volume of capillary pores. Besides, the threshold pore diameter also had a certain effect on chloride resistance.

The long-term chloride diffusion in different AAFS concretes and the corresponding time to corrosion initiation were predicted in Chapter 6. According to the prediction results, correctly formulated AAFS concretes (50%-70% GGBFS content, 0.45 w/b, 6% Na₂O content and 6% SiO₂ content) might successfully extend the initiation phase for decades or even more than 100 years.

In Chapter 7, The effects and mechanisms of different Mg-based admixtures were investigated. In AAFS, MgO could fill capillary pores and lead to the formation of more Friedel's salt. Mg-Al-CO₃ LDH and CLDH seemed to result in more air voids, but the enhanced chloride binding had a greater positive impact on chloride resistance.

CERTIFICATION OF THESIS

This Thesis is entirely the work of Jingxiao Zhang except where otherwise acknowledged. The work is original and has not previously been submitted for any other award, except where acknowledged.

Principal Supervisor: Professor Hao Wang

Associate Supervisor: Dr Yuwei Ma

Associate Supervisor: Dr Zuhua Zhang

Student and supervisors signatures of endorsement are held at the University.

ACKNOWLEDGEMENT STATEMENT

I want to thank all the people who have helped me throughout this research. In particular, I would like to acknowledge my supervisor team at Centre for Future Materials (CFM), University of Southern Queensland (USQ). This is an amazing supervisor team with strong academic background on materials science, geopolymer chemistry and engineering experiences. All of their understanding, advice, encouragement and assistance were valuable resources leading to the success of this research. As my principal supervisor, Prof. Hao Wang provided a lot of guidance and support for this research. He was so helpful in examining my research results. The discussions with Hao were always helpful. As my associate supervisor, Dr. Yuwei Ma gave a lot of help in the experimental environment and project discussion. She also spent a lot of time to help me to improve my writing skills, which is very important for the successful publication of my journal papers. As my associate supervisor, Dr. Zuhua Zhang regularly checked my research progress, especially at the beginning of the research. With his help, I successfully applied for USQ International Fees Research Scholarship and USQ International Stipend Research Scholarship, which provided financial support for this research.

I would like to acknowledge USQ for its scholarships and financial support. I would also like to thank my colleagues at CFM, USQ for their support, assistance and encouragement. The support of Research Centre for Wind Engineering and Engineering Vibration, Guangzhou University is also very grateful.

I would take this opportunity to thank my parents, Zhimin and Junru, for their continued financial support and spiritual encouragement over the past four years. Although their income is not high, they tried their best to support me to study for bachelor's, master's and doctor's degrees in Australia over the past nine years.

TABLE OF CONTENTS

ABSTRACT	I
CERTIFICATION OF THESIS.....	III
ACKNOWLEDGEMENT STATEMENT	IV
TABLE OF CONTENTS.....	V
LIST OF FIGURES.....	XI
LIST OF TABLES	XVIII
LIST OF PUBLICATIONS	XIX
ABBREVIATIONS.....	XX
CHAPTER 1: INTRODUCTION	1
1.1 BACKGROUND	1
1.1.1 CURRENT STATUS OF CEMENT INDUSTRY.....	1
1.1.2 ALKALI-ACTIVATED MATERIALS.....	3
1.1.3 CHLORIDE ATTACK IN REINFORCED CONCRETE	10
1.2 OBJECTIVES OF THE RESEARCH.....	14
1.3 OUTLINE OF THE THESIS.....	15
CHAPTER 2: LITERATURE REVIEW	18
2.1 INTRODUCTION	18
2.2 CHLORIDE TRANSPORT MECHANISMS AND INFLUENCING FACTORS	19
2.2.1 CHLORIDE TRANSPORT MECHANISMS	19
2.2.2 INFLUENCING FACTORS	21
2.2.2.1 PORE STRUCTURE.....	22
2.2.2.2 CHLORIDE BINDING CAPACITY	23
2.2.2.3 PORE SOLUTION	25
2.2.2.4 PHASE EVOLUTION.....	27
2.3 ASSESSMENT OF CHLORIDE TRANSPORT IN ALKALI-ACTIVATED MATERIALS.....	27

2.3.1 TESTING METHODS	27
2.3.1.1 RAPID CHLORIDE PERMEABILITY TEST (RCPT)	28
2.3.1.2 NON-STEADY-STATE MIGRATION (NSSM) TEST	30
2.3.1.3 CHLORIDE DIFFUSION TESTS	31
2.3.2 AAM VS. OPC.....	32
2.4 ROLE OF PRECURSORS	40
2.4.1 FA.....	41
2.4.2 GGBFS.....	45
2.4.3 MK	46
2.4.4 FA/GGBFS BINARY SYSTEM	48
2.5 ROLE OF ACTIVATORS	49
2.5.1 WATER/BINDER RATIO	49
2.5.2 ALKALINE COMPONENTS.....	50
2.5.2.1 ALKALI HYDROXIDES	51
2.5.2.2 SODIUM SILICATE	52
2.5.2.3 SODIUM CARBONATE	56
2.6 ROLE OF ADMIXTURES	57
2.6.1 SILICA FUME	58
2.6.2 MG-BASED ADMIXTURES.....	59
2.6.3 NANOPARTICLES	64
2.6.3.1 NANO-SILICA.....	65
2.6.3.2 NANO-TITANIA.....	67
2.7 CONCLUDING REMARKS	69
2.8 RESEARCH GAPS.....	71
 CHAPTER 3: MIXTURE DESIGN AND ENGINEERING PROPERTIES OF ALKALI- ACTIVATED FLY ASH-SLAG SYSTEMS	 73
3.1 INTRODUCTION	73
3.2 MATERIALS.....	74
3.2.1 PRECURSORS	74
3.2.1.1 CHARACTERIZATION OF FA.....	74
3.2.1.2 CHARACTERIZATION OF GGBFS	79

3.2.2 ACTIVATOR.....	84
3.2.3 AGGREGATE	85
3.3 EXPERIMENTAL METHODS.....	85
3.3.1 MIXTURE DESIGN OF AAFS PASTE	85
3.3.2 MIXTURE DESIGN OF AAFS CONCRETE.....	87
3.3.3 COMPRESSIVE STRENGTH OF AAFS PASTE.....	88
3.3.4 WORKABILITY OF AAFS CONCRETE	89
3.3.5 COMPRESSIVE STRENGTH OF AAFS CONCRETE.....	89
3.4 RESULTS AND DISCUSSION.....	89
3.4.1 COMPRESSIVE STRENGTH OF AAFS PASTE.....	90
3.4.2 WORKABILITY OF AAFS CONCRETE	91
3.4.3 COMPRESSIVE STRENGTH OF AAFS CONCRETE.....	93
3.4.3.1 EFFECT OF GGBFS CONTENT	95
3.4.3.2 EFFECT OF WATER/BINDER RATIO (W/B)	97
3.4.3.3 EFFECT OF ALKALI CONTENT.....	98
3.4.3.4 EFFECT OF SILICATE CONTENT	99
3.4.3.5 EFFECT OF SAND/AGGREGATE RATIO (S/A)	101
3.5 CONCLUDING REMARKS	102
CHAPTER 4: CHLORIDE RESISTANCE OF ALKALI-ACTIVATED FLY ASH-SLAG CONCRETES	104
4.1 INTRODUCTION	104
4.2 MATERIALS AND EXPERIMENTAL METHODS	105
4.2.1 MATERIALS AND MIXTURE PROPORTIONS.....	105
4.2.2 SAMPLE PREPARATION	106
4.2.3 NATURAL CHLORIDE DIFFUSION TEST.....	106
4.2.4 WATER ABSORPTION.....	108
4.3 RESULTS AND DISCUSSION.....	108
4.3.1 CHLORIDE PROFILE.....	108
4.3.2 CHLORIDE DIFFUSION COEFFICIENT.....	112
4.3.2.1 EFFECT OF GGBFS CONTENT	114
4.3.2.2 EFFECT OF WATER/BINDER RATIO (W/B)	115

4.3.2.3 EFFECT OF ALKALI CONTENT	116
4.3.2.4 EFFECT OF SILICATE CONTENT	117
4.3.2.5 EFFECT OF SAND/AGGREGATE RATIO (S/A)	117
4.3.3 WATER ABSORPTION	118
4.3.3.1 EFFECT OF GGBFS CONTENT	119
4.3.3.2 EFFECT OF WATER/BINDER RATIO (W/B)	120
4.3.3.3 EFFECT OF ALKALI CONTENT	120
4.3.3.4 EFFECT OF SILICATE CONTENT	120
4.3.3.5 EFFECT OF SAND/AGGREGATE RATIO (S/A)	121
4.3.4 WATER ABSORPTION VS. CHLORIDE DIFFUSION	121
4.4 CONCLUDING REMARKS	122
 CHAPTER 5: MICROSTRUCTURE OF ALKALI-ACTIVATED FLY ASH-SLAG SYSTEMS AND ITS EFFECTS ON CHLORIDE RESISTANCE	
5.1 INTRODUCTION	124
5.2 MATERIALS AND EXPERIMENTAL METHODS	125
5.2.1 MATERIALS AND MIXTURE PROPORTIONS.....	125
5.2.2 SAMPLE PREPARATION	125
5.2.3 X-RAY DIFFRACTION (XRD).....	126
5.2.4 FOURIER TRANSFORM INFRARED SPECTROSCOPY (FTIR).....	126
5.2.5 MERCURY INTRUSION POROSIMETRY (MIP).....	127
5.2.6 NITROGEN ADSORPTION TEST	128
5.3 RESULTS AND DISCUSSION.....	129
5.3.1 PHASE EVOLUTION	129
5.3.1.1 X-RAY DIFFRACTION (XRD)	129
5.3.1.2 FOURIER TRANSFORM INFRARED SPECTROSCOPY (FTIR)	133
5.3.2 PORE STRUCTURE	141
5.3.2.1 MERCURY INTRUSION POROSIMETRY (MIP)	141
5.3.2.2 NITROGEN ADSORPTION	149
5.3.3 RELATIONSHIPS BETWEEN PHASE EVOLUTION, PORE STRUCTURE AND CHLORIDE RESISTANCE	153
5.3.3.1 INFLUENCE MECHANISM OF GGBFS CONTENT.....	154
5.3.3.2 INFLUENCE MECHANISM OF WATER/BINDER RATIO (W/B).....	156

5.3.3.3 INFLUENCE MECHANISM OF ALKALI CONTENT.....	156
5.3.3.4 INFLUENCE MECHANISM OF SILICATE CONTENT	157
5.4 CONCLUDING REMARKS	158
CHAPTER 6: PREDICTION OF CHLORIDE TRANSPORT IN ALKALI-ACTIVATED FLY ASH-SLAG CONCRETES.....	160
6.1 INTRODUCTION	160
6.2 MODELLING OF CHLORIDE DIFFUSION.....	162
6.2.1 CONVENTIONAL CHLORIDE DIFFUSION MODEL	162
6.2.2 MODELLING OF CHLORIDE DIFFUSION COEFFICIENT	164
6.2.3 DETERMINATION OF SURFACE CHLORIDE CONTENT.....	165
6.3 RESULTS AND DISCUSSION.....	166
6.3.1 CHLORIDE DIFFUSION COEFFICIENT.....	166
6.3.1.1 EFFECT OF GGBFS CONTENT	170
6.3.1.2 EFFECT OF WATER/BINDER RATIO (W/B)	171
6.3.1.3 EFFECT OF ALKALI CONTENT.....	171
6.3.1.4 EFFECT OF SILICATE CONTENT	172
6.3.1.5 EFFECT OF SAND/AGGREGATE RATIO (S/A)	172
6.3.2 SURFACE CHLORIDE CONTENT	172
6.3.3 PREDICTION OF CHLORIDE DIFFUSION.....	174
6.3.3.1 EFFECT OF GGBFS CONTENT	177
6.3.3.2 EFFECT OF WATER/BINDER RATIO (W/B)	177
6.3.3.3 EFFECT OF ALKALI CONTENT.....	178
6.3.3.4 EFFECT OF SILICATE CONTENT	178
6.3.3.5 EFFECT OF SAND/AGGREGATE RATIO (S/A)	179
6.3.4 PREDICTION OF CHLORIDE PROFILE.....	179
6.3.5 PREDICTION OF CORROSION INITIATION.....	181
6.4 CONCLUDING REMARKS	183
CHAPTER 7: EFFECTS OF MG-BASED ADMIXTURES ON CHLORIDE RESISTANCE OF ALKALI-ACTIVATED FLY ASH-SLAG SYSTEMS.....	185
7.1 INTRODUCTION	185

7.2 MATERIALS AND EXPERIMENTAL METHODS	186
7.2.1 MATERIALS	186
7.2.2 SAMPLE PREPARATION	188
7.2.3 EXPERIMENTAL METHODS	190
7.2.3.1 COMPRESSIVE STRENGTH.....	190
7.2.3.2 CHLORIDE DIFFUSION TEST.....	190
7.2.3.3 NITROGEN ADSORPTION TEST	191
7.2.3.4 X-RAY DIFFRACTOMETRY (XRD).....	191
7.3 RESULTS AND DISCUSSION.....	192
7.3.1 COMPRESSIVE STRENGTH.....	192
7.3.2 CHLORIDE DIFFUSIVITY	194
7.3.2.1 CHLORIDE PROFILES	194
7.3.2.2 CHLORIDE DIFFUSION COEFFICIENTS (D).....	195
7.3.3 PORE STRUCTURE	198
7.3.4 PHASE COMPOSITION	201
7.3.5 EFFECTS OF MG-BASED ADMIXTURES	205
7.3.5.1 EFFECT OF MAGNESIUM OXIDE.....	205
7.3.5.2 EFFECTS OF LDH AND CLDH	206
7.4 CONCLUDING REMARKS	207
CHAPTER 8: CONCLUSIONS AND RECOMMENDATIONS.....	209
8.1 CONCLUSIONS.....	209
8.2 RECOMMENDATIONS FOR THE FUTURE RESEARCH.....	211
REFERENCE	214

LIST OF FIGURES

Chapter 1

Fig.1-1 Production of Portland cement and concrete (John L Provis & Bernal, 2014).	1
Fig.1-2 Global OPC production at the beginning of the 21st century (Golewski, 2020; <i>Mineral commodity summaries 2021</i> , 2021).	2
Fig.1-3 Atmospheric CO ₂ concentration observed at National Oceanic and Atmospheric Administration's Mauna Loa Observatory in Hawaii (https://gml.noaa.gov/ccgg/trends/).	3
Fig.1-4 Process and reaction products of AAMs (John L Provis & Bernal, 2014). Low-calcium systems react according to the green pathway, whereas high-calcium systems react according to the blue pathway. In high-calcium systems, secondary products are determined by Mg content.	4
Fig.1-5 Schematic representations of (A) N-A-S-H gels in AAFA or AAMK, from (Rowles, Hanna, Pike, Smith, & O'Connor, 2007), and (B) C-A-S-H gels in AAS, adapted from (John L Provis & Bernal, 2014). The blue triangles denote tetrahedral Si sites, the red triangle denotes Al substitution into one bridging site, the green rectangles denote CaO layers, and the circles denote various interlayer species.	6
Fig.1-6 Schematic diagram of the polymerization reaction stage of AAFS: (a) (I) ion dissolution and release stage and (II) ion reconstitution stage; (b) (III) hardening acceleration stage; and (c) (IV) hardening deceleration stage, from (X. Wei et al., 2021).	7
Fig.1-7 Schematic representation of chloride-induced depassivation (B. Zhang et al., 2018).	11
Fig.1-8 Schematic representation of pitting corrosion (Berrocal, 2017).	12
Fig.1-9 Volume of corrosion products relative to that of iron (Poursaee, 2016).	13
Fig.1-10 Service life model of reinforced concrete structures, adapted from (Tuutti, 1982).	14
Fig.1-11 Outline of the thesis.	17

Chapter 2

Fig.2-1 Illustration of factors affecting the chloride transport in AAMs.	21
Fig.2-2 Schematic diagram of the generation of capillary pores in AAMs, from (Y. Ma et al., 2019).	22
Fig.2-3 Porosity and pore size distribution of alkali-activated pastes with different GGBFS contents (Ouyang, Ma, Liu, Liang, & Ye, 2020) and OPC (Guang, 2003) at 7 days.	23
Fig.2-4 Physical binding of chloride ions (Cl ⁻), from (Pargar et al., 2017).	24
Fig.2-5 pH and main element composition in the pore solution of AAMs with different GGBFS contents and OPC at 28 days, reproduced from (Nedeljković et al., 2019).	26

Fig.2-6 Experimental Setup for (A) rapid chloride permeability test (RCPT, ASTM C1202 and AASHTO T277), (B) non-steady-state migration (NSSM) test (NT BUILD 492), (C) bulk diffusion test (ASTM C1556 and NT BUILD 443) and (D) ponding test (ASTM C1543 and AASHTO T259), adapted from (Hasholt & Jensen, 2015; Stanish, Hooton, & Thomas, 2001).....	28
Fig.2-7 Correlation between the results of non-steady-state migration (NSSM) test and bulk diffusion test at 90 days, adapted from (Ramezaniyanpour & Moeini, 2018).....	31
Fig.2-8 Chloride resistance of AAMs compared to OPC (CRTO).....	40
Fig.2-9 SiO ₂ -Al ₂ O ₃ -CaO ternary diagrams of FA (Class F and Class C), GGBFS, MK, SF, Portland cement and fine limestone (A. Wang et al., 2020).....	40
Fig.2-10 Results of (A) bulk diffusion test according to NT BUILD 443 and (B) NSSM test according to NT BUILD 492, adapted from (Gluth et al., 2020).....	41
Fig.2-11 Chloride diffusion coefficients of AAFA and OPC specimens, adapted from (Kupwade-Patil & Allouche, 2013). OH: Class F FA with 1.97% CaO, DH: Class F FA with 5.00% CaO, MO: Class C FA with 12.93% CaO.	43
Fig.2-12 SEM micrographs of AAFA with different D ₁₀ (0.67, 0.40 and 0.39 μm), from (S. Nath & Kumar, 2020).....	44
Fig.2-13 Influence of MgO content on the hydrates present in AAS, adapted from (Haha, Lothenbach, et al., 2011).....	46
Fig.2-14 Chloride penetration in AAFA pastes (A) and mortars (B) with different w/b (0.6, 0.7 and 0.8) after 7 days of immersion, adapted from (Zhu et al., 2014).....	50
Fig.2-15 Effect of NaOH concentration on chloride diffusion coefficient and chloride binding capacity of AAFA concrete, adapted from (P Chindaprasirt & Chalee, 2014).....	52
Fig.2-16 Effect of Na ₂ O content on (A) chloride migration coefficient (D _{NSSM}) and (B) passed charge (6h) of AAFA mortars, adapted from (X. Hu et al., 2019).....	54
Fig.2-17 Effect of silicate modulus (Ms) on (A) chloride migration coefficient (D _{NSSM}) and (B) passed charge (6h) of AAFA mortars, adapted from (X. Hu et al., 2019).	55
Fig.2-18 Chloride migration coefficient (D _{NSSM}) of (A) carbonate-activated and (B) silicate-activated GGBFS mortars at 28, 90, and 180 days, adapted from (Ke, Bernal, Hussein, et al., 2017).....	57
Fig.2-19 Effect of silica fume (SF) content on passing electric charge at 28 days and 90 days, , adapted from (Rostami & Behfarnia, 2017).	59
Fig.2-20 Structure of layered double hydroxides (LDH), from (Bi, Zhang, & Dou, 2014). .	61

Fig.2-21 Chloride penetration depth of AAFS with different MgO addition (0, 5% and 10%) and OPC at 91 days, H-series denote the samples activated by NaOH, and W-series denote the samples activated by $\text{Na}_2\text{O}\cdot n\text{SiO}_2$, adapted from (H. Yoon et al., 2018).....	63
Fig.2-22 Effects of MgO, Mg-Al- NO_3 LDH and CLDH on chloride migration coefficient, adapted from (T. Liu et al., 2020).....	64
Fig.2-23 Enhancing mechanisms of nanoparticles, from (D. Wang, Zhang, Ruan, Yu, & Han, 2018).....	65
Fig.2-24 SEM micrographs of AAFA with different nano- SiO_2 addition (0, 1%, 2% and 3%), from (Phoo-ngernkham et al., 2014).....	67
Fig.2-25 Porosity and pore size distribution of AAFA with different nano- TiO_2 addition (0, 1%, 3% and 5%) at 28 days, adapted from (P. Duan et al., 2016).....	68
Fig.2-26 Rapid chloride permeability test (RCPT) of AAFA containing 5% nano- TiO_2 with different dimension (30, 50 and 100 nm), adapted from (Maiti et al., 2020).....	69

Chapter 3

Fig.3-1 Particle size distribution of FA.	75
Fig.3-2 Morphology of FA.	76
Fig.3-3 X-ray diffraction analysis of FA. M = mullite ($\text{Al}_6\text{Si}_2\text{O}_{13}$, PDF# 15-0776), Q = quartz (SiO_2 , PDF# 46-1045), C = calcite (CaCO_3 , PDF# 05-0586), He = hematite (Fe_2O_3 , PDF# 33-0664).....	77
Fig.3-4 FTIR spectrum of FA.	78
Fig.3-5 Particle size distribution of GGBFS.....	80
Fig.3-6 Morphology of GGBFS.....	81
Fig.3-7 X-ray diffraction analysis of GGBFS.	82
Fig.3-8 FTIR spectrum of GGBFS.	83
Fig.3-9 Compressive strength of AAFS pastes with different GGBFS contents, water/binder ratios (w/b), Na_2O contents and SiO_2 contents at 7 and 28 days.	90
Fig.3-10 Slump of AAFS concretes with different GGBFS contents, water/binder ratios (w/b), Na_2O contents, SiO_2 contents and sand/aggregate ratios (s/a).	92
Fig.3-11 Compressive strength of AAFS concretes with different GGBFS contents, water/binder ratios (w/b), Na_2O contents, SiO_2 contents and sand/aggregate ratios (s/a) at 7, 28, 90 and 180 days.	94
Fig.3-12 Effect of GGBFS content on the development of compressive strength of AAFS concrete (from 7 to 180 days).	95
Fig.3-13 Effect of water/binder ratio (w/b) on the development of compressive strength of AAFS concrete (from 7 to 180 days).	97

Fig.3-14 Effect of Na ₂ O content on the development of compressive strength of AAFS concrete (from 7 to 180 days).	98
Fig.3-15 Effect of SiO ₂ content on the development of compressive strength of AAFS concrete (from 7 to 180 days).	100
Fig.3-16 Effect of sand/aggregate ratio (s/a) on the development of compressive strength of AAFS concrete (from 7 to 180 days).	101

Chapter 4

Fig.4-1 Comparison of total and free chloride profiles of AAFS and OPC mortars after 45 days of immersion in 16.5% NaCl solution (Babae & Castel, 2018).	109
Fig.4-2 Free chloride profiles of AAFS concretes with different (A) GGBFS contents, (B) water/binder ratios (w/b), (C) Na ₂ O contents, (D) SiO ₂ contents and (E) sand/aggregate ratios (s/a) after 90 days of immersion in 3.5% NaCl solution.	110
Fig.4-3 Free chloride profiles of AAFS concretes with different (A) GGBFS contents, (B) water/binder ratios (w/b), (C) Na ₂ O contents, (D) SiO ₂ contents and (E) sand/aggregate ratios (s/a) after 180 days of immersion in 3.5% NaCl solution.	111
Fig.4-4 Fitted curves of SL50 (A) and SL100 (B) after 90 days of immersion in 3.5% NaCl solution.	112
Fig.4-5 Free chloride diffusion coefficient (D_f) of AAFS concretes with different GGBFS contents, water/binder ratios (w/b), Na ₂ O contents, SiO ₂ contents and sand/aggregate ratios (s/a) after 90 and 180 days of immersion in 3.5% NaCl solution.	113
Fig.4-6 Water absorption of AAFS concretes with different (A) GGBFS contents, (B) water/binder ratios (w/b), (C) Na ₂ O contents, (D) SiO ₂ contents and (E) sand/aggregate ratios (s/a).	119
Fig.4-7 Relationship between water absorption and free chloride diffusion coefficient (D_f) at 90 days (A) and 180 days (B).	122

Chapter 5

Fig.5-1 XRD patterns of OPC paste (a) and AAFS pastes with different (a) GGBFS contents, (b) water/binder ratios (w/b), (c) Na ₂ O contents and (c) SiO ₂ contents after 180 days of immersion in 3.5% NaCl solution. M = mullite (Al ₆ Si ₂ O ₁₃ , PDF# 15-0776), Q = quartz (SiO ₂ , PDF# 46-1045), C = calcite (CaCO ₃ , PDF# 05-0586), A = akermanite (Ca ₂ Mg(Si ₂ O ₇), PDF #11-1611), C-S-H = calcium silicate hydrate (PDF# 33-0306), C-(A)-S-H = calcium alumina silicate hydrate (PDF# 33-0306), P: portlandite (Ca(OH) ₂ , PDF# 44-1481), F: Friedel's salt (Ca ₂ Al(OH) ₆ Cl·2H ₂ O, PDF# 42-0558).	131
---	-----

Fig.5-2 FTIR spectra of AAFS pastes with different GGBFS contents before (after 28 days of curing) and after 180 days of immersion in 3.5% NaCl solution.	135
Fig.5-3 FTIR spectra of AAFS pastes with different water/binder ratios (w/b) before (after 28 days of curing) and after 180 days of immersion in 3.5% NaCl solution.	137
Fig.5-4 FTIR spectra of AAFS pastes with different Na ₂ O contents before (after 28 days of curing) and after 180 days of immersion in 3.5% NaCl solution.	138
Fig.5-5 FTIR spectra of AAFS pastes with different SiO ₂ contents before (after 28 days of curing) and after 180 days of immersion in 3.5% NaCl solution.	140
Fig.5-6 Porosity and pore size distribution of AAFS mortars with different GGBFS contents, water/binder ratios (w/b), Na ₂ O contents and SiO ₂ contents after 180 days of immersion in 3.5% NaCl solution, derived from MIP.	142
Fig.5-7 Relationship between total porosity and free chloride diffusion coefficient (D _f) after 180 days of immersion in 3.5% NaCl solution.	143
Fig.5-8 Relationship between volume of capillary pores and free chloride diffusion coefficient (D _f) after 180 days of immersion in 3.5% NaCl solution.	144
Fig.5-9 Effects of GGBFS content, w/b, Na ₂ O content and SiO ₂ content on pore size distribution of AAFS mortar after 180 days of immersion in 3.5% NaCl solution, derived from MIP.	147
Fig.5-10 Pore size distribution of OPC (42.5, w/b=0.4) at 180 days, derived from MIP (Z. Yu, 2015).	148
Fig.5-11 Relationship between diffusion tortuosity and curing time for AAFS, derived from X-ray microtomography (John L Provis et al., 2012).	149
Fig.5-12 Pore size distribution of AAFS pastes with different GGBFS contents after 365 days of immersion in 3.5% NaCl solution, derived from nitrogen adsorption.	150
Fig.5-13 Pore size distribution of AAFS pastes with different water/binder ratios (w/b) after 365 days of immersion in 3.5% NaCl solution, derived from nitrogen adsorption.	151
Fig.5-14 Pore size distribution of AAFS pastes with different Na ₂ O contents after 365 days of immersion in 3.5% NaCl solution, derived from nitrogen adsorption.	152
Fig.5-15 Pore size distribution of AAFS pastes with different SiO ₂ contents after 365 days of immersion in 3.5% NaCl solution, derived from nitrogen adsorption.	153
Fig.5-16 Effects of phase evolution and pore structure on chloride resistance of AAFS. ...	154

Chapter 6

Fig.6-1 Prediction of chloride diffusion and corrosion initiation in concrete.	163
--	-----

Fig.6-2 Fitted curves of apparent chloride diffusion coefficient (D) of AAFS concretes with different (A) GGBFS contents, (B) water/binder ratios (w/b), (C) Na ₂ O contents, (D) SiO ₂ contents and (E) sand/aggregate ratios (s/a).	167
Fig.6-3 Fitted curves of apparent chloride diffusion coefficient (D) of SL50 (quantified by natural chloride diffusion test), SL50' (quantified by RCPT (Tennakoon et al., 2017)) and OPC (quantified by RCPT (Tennakoon et al., 2017)).....	169
Fig.6-4 Time dependent models of apparent chloride diffusion coefficient (D) of AAFS concretes with different (A) GGBFS contents, (B) water/binder ratios (w/b), (C) Na ₂ O contents, (D) SiO ₂ contents and (E) sand/aggregate ratios (s/a).	170
Fig.6-5 Surface chloride content (C _s) of AAFS concretes with different (A) GGBFS contents, (B) water/binder ratios (w/b), (C) Na ₂ O contents, (D) SiO ₂ contents and (E) sand/aggregate ratios (s/a) at 90, 180 ,365 and 730 days.....	174
Fig.6-6 Chloride diffusion in AAFS concretes with different (A) GGBFS contents, (B) water/binder ratios (w/b), (C) Na ₂ O contents, (D) SiO ₂ contents and (E) sand/aggregate ratios (s/a) at 45 mm and 60 mm depths. *W50 adopts a constant D ($0.75 \times 10^{-12} \text{ m}^2/\text{s}$).....	176
Fig.6-7 Chloride profiles of AAFS concretes with different (A) GGBFS contents, (B) water/binder ratios (w/b), (C) Na ₂ O contents, (D) SiO ₂ contents and (E) sand/aggregate ratios (s/a) at 5, 20, 50 and 100 years. *W50 adopts a constant D ($0.75 \times 10^{-12} \text{ m}^2/\text{s}$).	180
Fig.6-8 Time to corrosion initiation of AAFS concretes with different (A) GGBFS contents, (B) water/binder ratios (w/b), (C) Na ₂ O contents, (D) SiO ₂ contents and (E) sand/aggregate ratios (s/a). *W50 adopts a constant D ($0.75 \times 10^{-12} \text{ m}^2/\text{s}$).	182

Chapter 7

Fig.7-1 XRD patterns (a) and FTIR spectra (b) of Mg-Al-CO ₃ LDH and CLDH.....	188
Fig.7-2 Compressive strength of AAFS and OPC mortars at 3, 7, 28 and 63 days.....	193
Fig.7-3 Comparison of chloride profiles of AAFS and OPC mortars after 35 days of immersion in 165 g/L NaCl solution.....	195
Fig.7-4 Fitting curves of AAFS and OPC mortars after 35 days of immersion in 165 g/L NaCl solution.	196
Fig.7-5 Apparent chloride diffusion coefficients (D) of AAFS and OPC mortars after 35 days of immersion in 165 g/L NaCl solution.	197
Fig.7-6 Cumulative pore volume (a) and pore size distribution (b) of AAFS and OPC pastes, derived from nitrogen adsorption test.	200
Fig.7-7 XRD patterns of AAFS and OPC pastes before (a) and after (b) 60 days of immersion in simulated chloride-rich pore solution. L: Mg-Al-CO ₃ LDH (Mg ₆ Al ₂ (OH) ₁₆ CO ₃ ·4H ₂ O, PDF# 00-014-0191); P: portlandite (Ca(OH) ₂ , PDF# 00-044-	

1481); Q: quartz (SiO_2 , PDF# 01-079-1910); Hc: hemicarboaluminate ($\text{C}_4\text{Al}_2\text{O}_5\text{H}_{12}$, PDF# 00-036-0129); C: calcite (CaCO_3 , PDF# 01-071-3699); G: gaylussite ($\text{Na}_2\text{Ca}(\text{CO}_3)_2 \cdot 5\text{H}_2\text{O}$, PDF# 00-021-0343); NS: N-A-S-H (PDF# 00-039-0217); CS: C-S-H (PDF# 00-034-0002)/C-(A)-S-H (PDF# 00-033-0306); F: Friedel's salt ($\text{Ca}_2\text{Al}(\text{OH})_6\text{Cl} \cdot 2\text{H}_2\text{O}$, PDF# 00-042-0558)..... 202

LIST OF TABLES

Chapter 2

Table 2-1 Chloride transport mechanisms.....	19
Table 2-2 Chloride ion penetrability based on charge passed (Whiting, 1981).	29
Table 2-3 Recent studies on chloride resistance of AAMs (pastes, mortars, and concretes) based on different testing methods, as well as comparison of chloride resistance between AAMs and OPC.	33

Chapter 3

Table 3-1 Chemical composition of FA.	75
Table 3-2 FTIR band assignments of FA.	79
Table 3-3 Chemical composition of GGBFS.	80
Table 3-4 FTIR band assignments of GGBFS.	83
Table 3-5 Mixture proportions of AAFS and OPC pastes.	86
Table 3-6 Mixture proportions of AAFS concretes.....	87
Table 3-7 Minimum characteristic compressive strength (f_c) of general concrete structures and bridges under different exposure environments (AS 3600 and AS 5100.5).....	94

Chapter 6

Table 6-1 Design life, minimum characteristic compressive strength (f_c) and required cover for corrosion protection of general concrete structures and bridges under different exposure environments (AS 3600 and AS 5100.5).	164
--	-----

Chapter 7

Table 7-1 Mix proportions of AAFS and OPC mortars (M) and pastes (P).....	189
Table 7-2 Stoichiometric compositions of simulated chloride-rich pore solution.	192

LIST OF PUBLICATIONS

Journal papers

Jingxiao Zhang, Yuwei Ma*, Jiazheng Zheng, Jie Hu, Jiyang Fu, Zuhua Zhang*, Hao Wang*: Chloride diffusion in alkali-activated fly ash/slag concretes: Role of slag content, water/binder ratio, alkali content and sand-aggregate ratio. *Construction and Building Materials* 261 (2020): 119940.

Jingxiao Zhang, Yuwei Ma*, Jie Hu, Hao Wang*, Zuhua Zhang*: Review on chloride transport in alkali-activated materials: Role of precursors, activators and admixtures. *Construction and Building Materials* 328 (2022): 127081.

Refereed conference papers

Jingxiao Zhang, Yuwei Ma, Jiazheng Zheng, Chloride diffusion of alkali-activated fly ash/slag concrete. 4th International RILEM conference on Microstructure Related Durability of Cementitious Composites: Microdurability 2020, Delft University of Technology, the Netherlands - Southeast University, Nanjing, China, from 29 April to 25 May, 2021. Oral presentation.

ABBREVIATIONS

AAFA	alkali-activated fly ash
AAFS	alkali-activated fly ash-slag
AAMK	alkali-activated metakaolin
AAM	alkali activated material
AAS	alkali-activated slag
a/b	activator/binder ratio
ACD	accelerated chloride diffusion test
C-A-S-H gels	calcium aluminosilicate hydrate gels
CLDH	Calcined layered double hydroxides
CRTO	chloride resistance compared to ordinary Portland cement
C_s	surface chloride content
C-S-H	calcium silicate hydrate
C_0	initial chloride content
D	chloride diffusion coefficient
D_f	free chloride diffusion coefficient
D_{NSSM}	non-steady-state migration coefficient
FA	fly ash
f_c	characteristic compressive strength of concrete at 28 days

FTIR	Fourier transform infrared spectroscopy
GGBFS	ground granulated blast furnace slag
ICP-OES	inductively coupled plasma/atomic emission spectroscopy
LDH	layered double hydroxides
LOI	loss on ignition
ITZ	interfacial transition zone
m	age factor
MIP	mercury intrusion porosimetry
MK	metakaolin
Ms	molar ratio of $\text{SiO}_2/\text{Na}_2\text{O}$
N-A-S-H gels	sodium aluminosilicate hydrate gels
NCD	natural chloride diffusion test
NMR	nuclear magnetic resonance
NSSM	non-steady-state migration
OPC	ordinary Portland cement
RCM	rapid chloride migration test
RCPT	rapid chloride permeability test
s/a	sand/aggregate ratio
SCI	steel-concrete interface

SEM	scanning electron microscopy
SF	silica fume
TG/DTG	thermogravimetry/differential thermograms
w/c	water/cement ratio
w/b	water/binder ratio
XRD	X-ray diffraction
XRF	X-ray fluorescence

CHAPTER 1: INTRODUCTION

1.1 BACKGROUND

1.1.1 CURRENT STATUS OF CEMENT INDUSTRY

Ordinary Portland cement (OPC), manufactured by heating a mix of calcium carbonate (e.g. limestone and chalk) and aluminosilicate (e.g. clay and shale) in a rotating kiln (typically 1450 °C) as shown in Fig.1-1, is one of the most useful and versatile materials on the earth (Ajay, Rajeev, & Yadav, 2012; Bye, 1999). OPC can react with water. The hydration products of OPC are mainly calcium silicate hydrate (C-S-H) gels, which make a major contribution to the strength and other properties of hydrated OPC (Allen, Thomas, & Jennings, 2007; L'Hôpital, Lothenbach, Le Saout, Kulik, & Scrivener, 2015; Yan et al., 2022). As can be seen in Fig.1-1, hydrated OPC can bind sand and gravel into a stone-like product – concrete, which is the most consumed material for construction (Richardson, 2008).

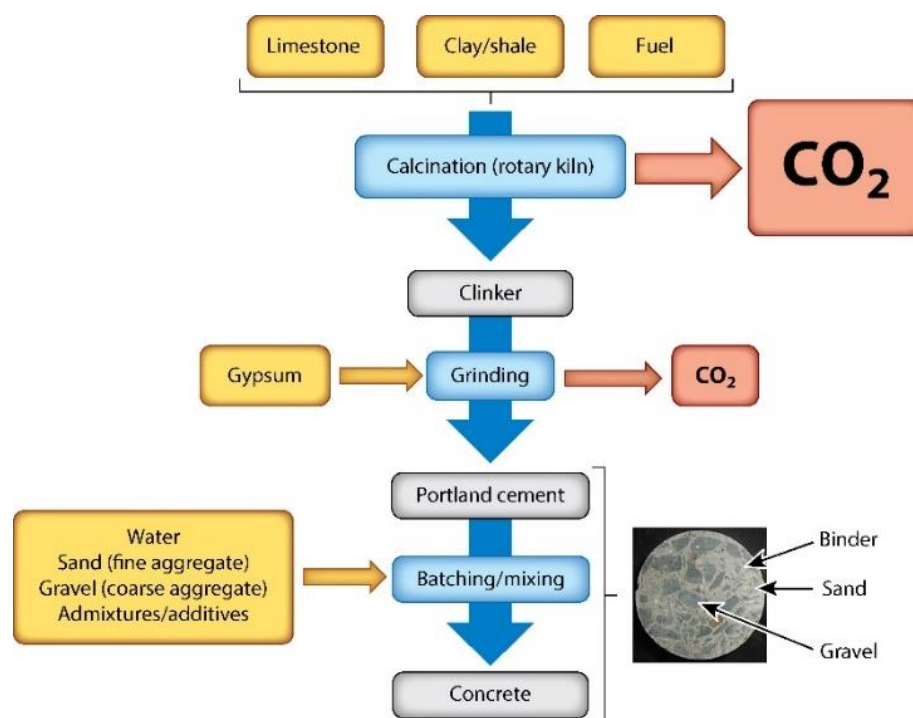


Fig.1-1 Production of Portland cement and concrete (John L Provis & Bernal, 2014).

However, OPC is not without problems. OPC manufacturing is a process that consumes resources and energy, and pollutes the environment. At present, the global OPC production is approximately 4.1 billion tons per year, as shown in Fig.1-2

(Golewski, 2020; *Mineral commodity summaries 2021*, 2021). The vast production of OPC requires a large amount of limestone and clay as raw materials, and consumes a lot of energy to provide heat for calcination, up to 7% of industrial energy consumption (F. Costa & Ribeiro, 2020). Moreover, it emits massive CO₂ into atmosphere due to the burning of fuel and the decomposition of CaCO₃, as shown in Fig.1-1. According to the IEA Greenhouse Gas R&D Programme (Hendriks, Worrell, DeJager, Block, & Riemer, 2000), almost 0.81 tons of CO₂ can be generated for each ton of OPC produced. The decomposition of CaCO₃ accounts for approximately 50% of the CO₂ emitted, while the remaining CO₂ is the result of energy consumption in the production process (Huntzinger & Eatmon, 2009). According to this calculation, the annual CO₂ emissions from OPC production increased from 1.38 billion tons in 2000 to 3.32 billion tons in 2020, up to 8% of global CO₂ emissions (John L Provis & Bernal, 2014).

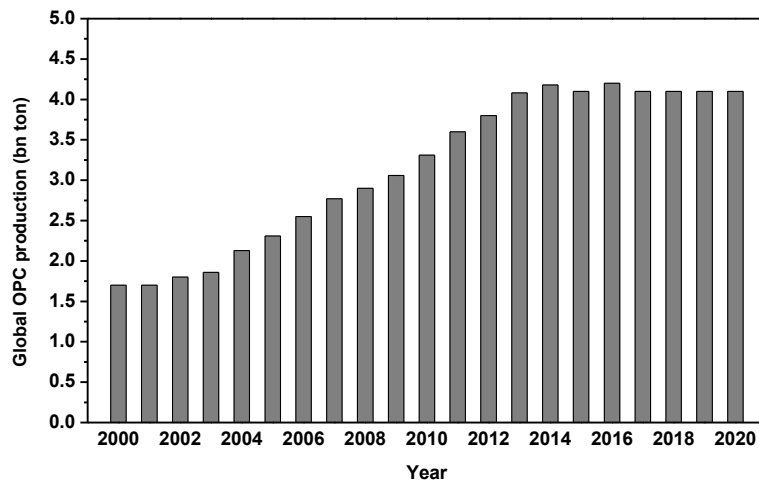


Fig.1-2 Global OPC production at the beginning of the 21st century (Golewski, 2020; *Mineral commodity summaries 2021*, 2021).

CO₂, as one of the major greenhouse gasses, is the main cause of global warming. As shown in Fig.1-3, atmospheric CO₂ concentration is continuously rising and has reached 414.24 parts per million (ppm) in 2020. Increased CO₂ in the atmosphere can trap the IR radiation emitted from the Earth's surface after absorbing sunlight and hence heat the planet, leading to an alarming trend of continuous rise in the temperature of global surface and ocean, which is called global warming (Zandalinas, Fritschi, & Mittler, 2021). Global warming can result in the redistribution of global

precipitation, the melting of glacier ice and permafrost, the rise of sea level, etc (Goudie, 2006). It not only endangers the balance of the ecosystem, but also affects human health and even threatens human survival. Therefore, the cement and concrete industry is under pressure to seek the alternatives of OPC to save resources and energy, reduce greenhouse gas emissions, and create a greener economy.

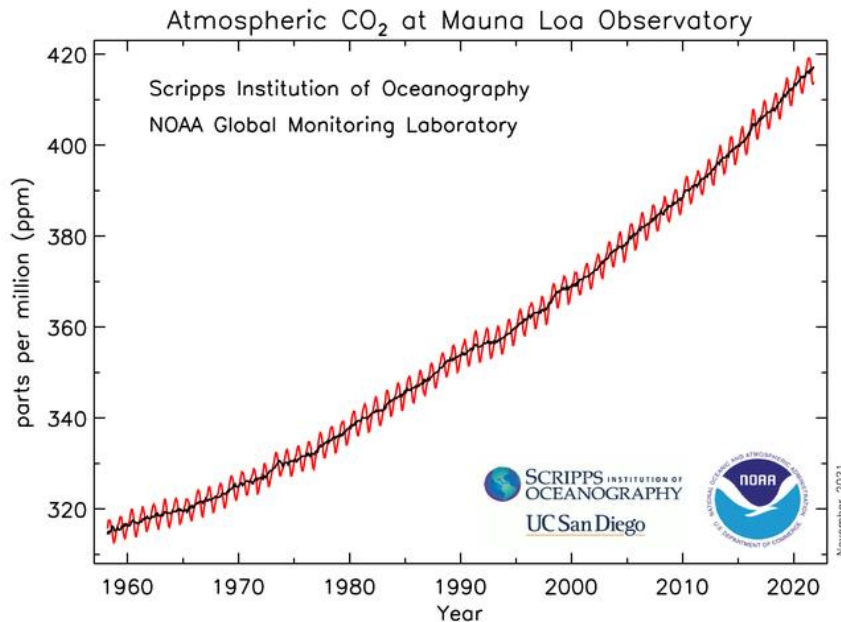


Fig.1-3 Atmospheric CO₂ concentration observed at National Oceanic and Atmospheric Administration's Mauna Loa Observatory in Hawaii (<https://gml.noaa.gov/ccgg/trends/>).

A wide variety of industrial wastes have been used as supplementary cementing materials in OPC, such as fly ash (FA) from coal combustion, ground granulated blast furnace slag (GGBFS) from iron production and silica fume (SF) from elemental silicon or ferrosilicon production (Panesar, 2019; Siddique & Khan, 2011). However, they are only used to replace part of OPC (typically 10 – 50%) in concrete (M. Juenger, Winnefeld, Provis, & Ideker, 2011). There is interest in creating binders made entirely or almost entirely of industrial wastes. Among these alternative cementitious binders, alkali-activated materials (AAMs), especially alkali-activated fly ash-slag (AAFS) system, have attracted much interest in academic and industrial fields over the past decades.

1.1.2 ALKALI-ACTIVATED MATERIALS

Alkali-activated materials (AAMs, also known as geopolymers), prepared through

the reaction of solid aluminosilicates and alkaline activators (Fig.1-4), are considered as a promising candidate to OPC. Industrial wastes or other inexpensive materials termed as ‘precursors’, e.g. fly ash (FA) (Palomo, Grutzeck, & Blanco, 1999; Zhuang et al., 2016), ground granulated blast furnace slag (GGBFS) (Amer, Kohail, El-Feky, Rashad, & Khalaf, 2021; Rodríguez, Bernal, de Gutiérrez, & Puertas, 2008), and metakaolin (MK) (Mobili, Belli, Giosuè, Bellezze, & Tittarelli, 2016; A. M. Rashad, 2013), are commonly used to provide aluminosilicates. The concentrated aqueous solutions of sodium hydroxide (NaOH), sodium silicate ($\text{Na}_2\text{O}\cdot n\text{SiO}_2$) and sodium carbonate (Na_2CO_3) are common alkaline activators to activate precursors (Nodehi & Taghvaei, 2021; Caijun Shi, Roy, & Krivenko, 2003).

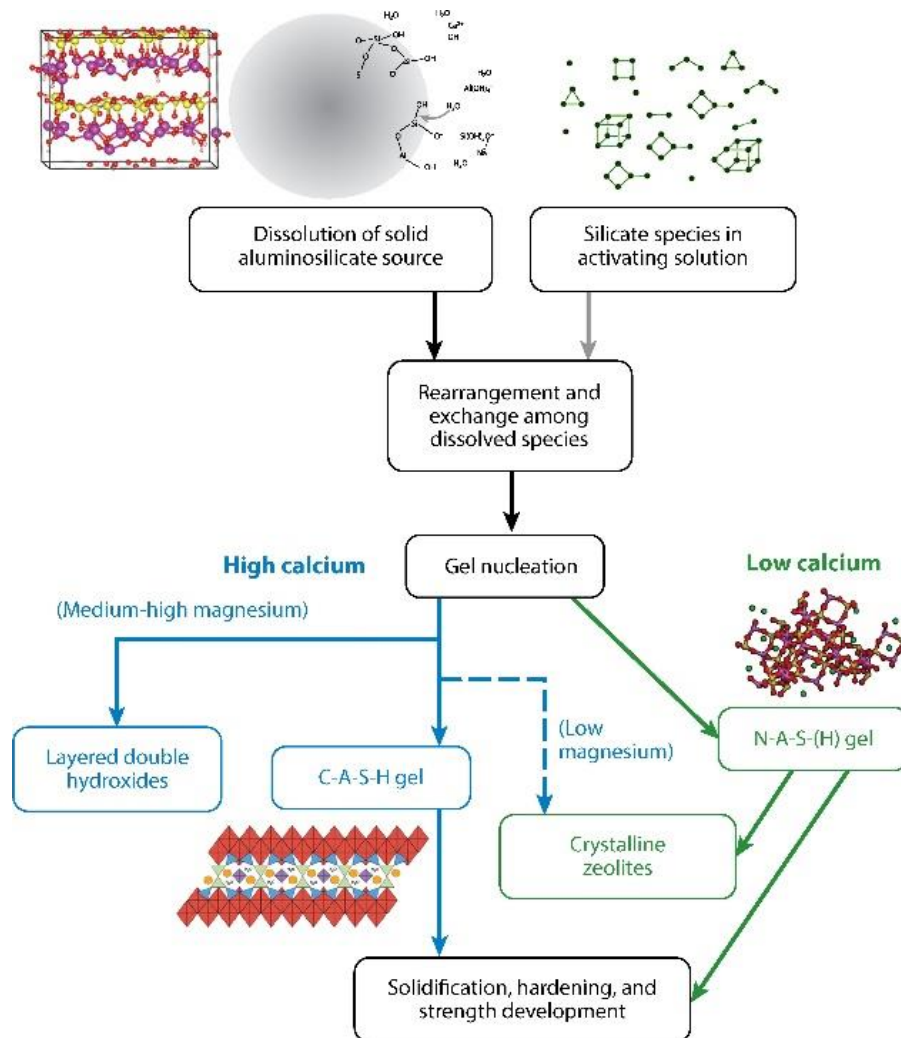


Fig.1-4 Process and reaction products of AAMs (John L Provis & Bernal, 2014). Low-calcium systems react according to the green pathway, whereas high-calcium systems react according to the blue pathway. In high-calcium systems, secondary products are determined by Mg content.

As shown in Fig.1-4, AAMs are divided into two systems according to different reaction products (John L Provis, 2014; John L Provis & Bernal, 2014). The one is low-calcium system, e.g. alkali-activated Class F fly ash (AAFA) and alkali-activated metakaolin (AAMK). In this system, sodium aluminosilicate hydrate (N-A-S-H) gels (Fig.1-5A) are primary reaction products, and crystalline or semi-crystalline zeolites are secondary products. As shown in Fig.1-5A, N-A-S-H gels have a pseudo-zeolitic three-dimensional framework comprising SiO_4 and AlO_4 tetrahedra linked through shared O atoms (Palomo et al., 1999). The negative charge due to the substitution of Si^{4+} by Al^{3+} in tetrahedral coordination is balanced by Na^+ from the activator (Fernández-Jiménez, Palomo, Sobrados, & Sanz, 2006). Besides, Na^+ can also be partially associated in $\text{Na}(\text{H}_2\text{O})_n^+$ and associated with framework oxygen bonds (Longhi, Rodríguez, Walkley, Zhang, & Kirchheim, 2020). The other one is high-calcium system, e.g. alkali-activated slag (AAS). In this system, calcium aluminosilicate hydrate (C-A-S-H) gels (Fig.1-5B) are primary reaction products. When MgO content is moderate to high (> 5 wt.%), layered double hydroxides (LDH) are the secondary products; when MgO content is low, zeolites (e.g. gismondine and garronite) are the secondary products (Bernal et al., 2014; Haha, Lothenbach, Le Saout, & Winnefeld, 2011; Ke, Bernal, & Provis, 2016; John L Provis & Bernal, 2014). As shown in Fig.1-5B, C-A-S-H gels have a tobermorite-like structure similar to that of C-S-H gels in OPC. The principal layer is composed of a calcium oxide sheet with dreierketten silicate chains grafted on the both sides (each chain contains $3n-1$ tetrahedra, n is an integer value). Some aluminium is incorporated into C-S-H gels, leading to the transformation from C-S-H gels to C-A-S-H gels. It is found that the substitution of Si^{4+} by Al^{3+} can significantly increase the degree of polymerization of dreierketten silicate chains (Faucon, Petit, Charpentier, Jacquinet, & Adenot, 1999; Sun, Young, & Kirkpatrick, 2006). Besides, it is confirmed that the aluminium is more favoured in the bridging site rather than in the pairing site of dreierketten silicate chains (Manzano, Dolado, & Ayuela, 2009; Pegado, Labbez, & Churakov, 2014). The interlayer region contains various species (e.g. Ca^{2+} , Na^+ , water, etc). Some alkali cations can balance the negative charge due to the substitution of Si^{4+} by Al^{3+} in tetrahedral chain sites. Besides, N-A-S-H and C-A-S-H gels can coexist in alkali-activated blended systems, e.g. alkali-activated fly ash-slag (AAFS) system (Ismail et al., 2014; Yip, Lukey, & Van Deventer, 2005).

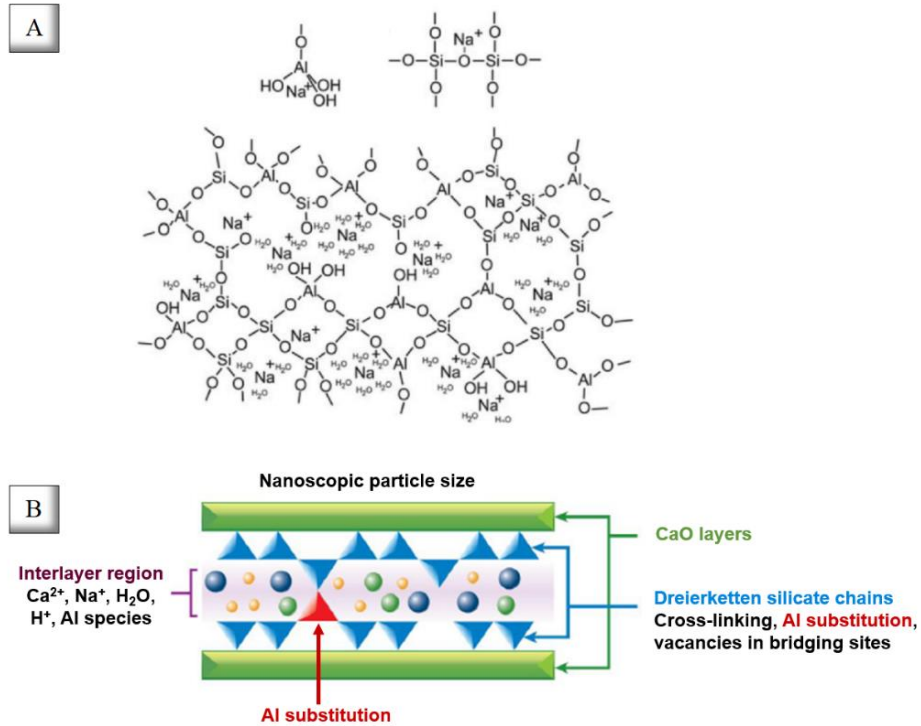
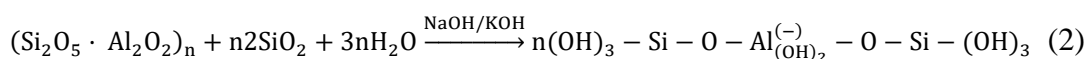
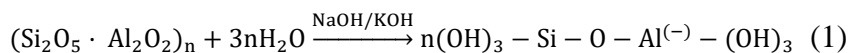


Fig.1-5 Schematic representations of (A) N-A-S-H gels in AAFA or AAMK, from (Rowles, Hanna, Pike, Smith, & O'Connor, 2007), and (B) C-A-S-H gels in AAS, adapted from (John L Provis & Bernal, 2014). The blue triangles denote tetrahedral Si sites, the red triangle denotes Al substitution into one bridging site, the green rectangles denote CaO layers, and the circles denote various interlayer species.

The reaction process of AAMs can be divided into four stages: (I) ion dissolution and release stage, (II) ion reconstitution stage, (III) hardening acceleration stage, and (IV) hardening deceleration stage (X. Wei et al., 2021). For example, Fig.1-6 presents the schematic diagram of each reaction stage in AAFA. The main feature of stage I is the dissolution of precursors (e.g. FA and GGBFS particles in Fig.1-6a). When the particles contact the activator, Na^+ and OH^- enter the system and attack the particle surface. The basic principle of the dissolving chemical reaction is shown in Equation 1 and 2 (Davidovits, 1989, 1991).



Free SiO_4 and AlO_4 tetrahedral units are formed by breaking the Si-O-T bonds, where T is referred to tetrahedral Si or Al. There are also more free moving ions in

the system, e.g. Na^+ , Ca^{2+} , K^+ and OH^- . X. Wei et al. (2021) claimed that the curing temperature could deeply affect this dissolution process. The low curing temperature can reduce the activity of OH^- and hence the dissolution rate of aluminosilicate.

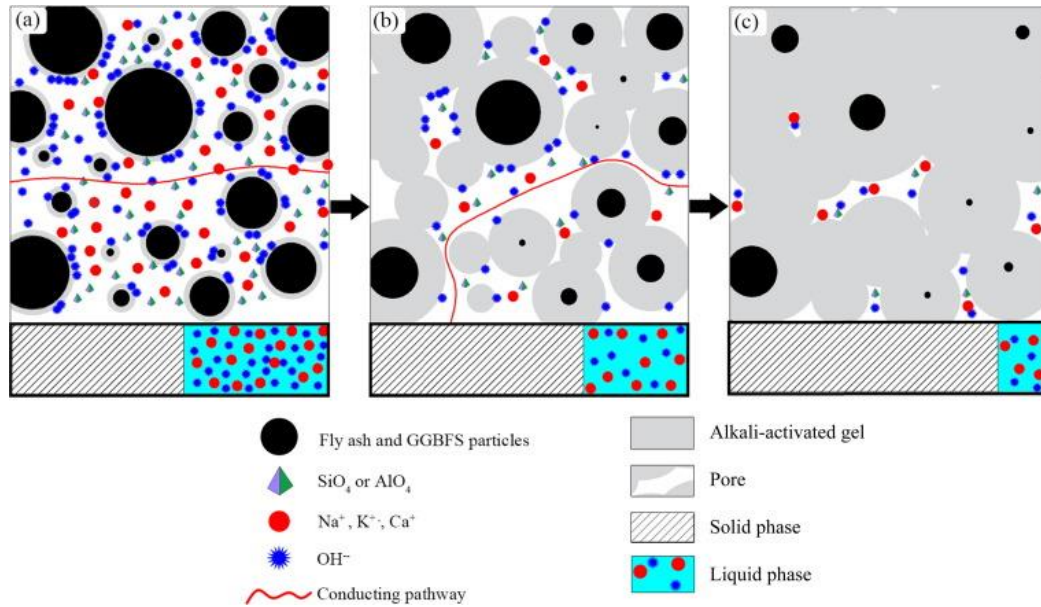
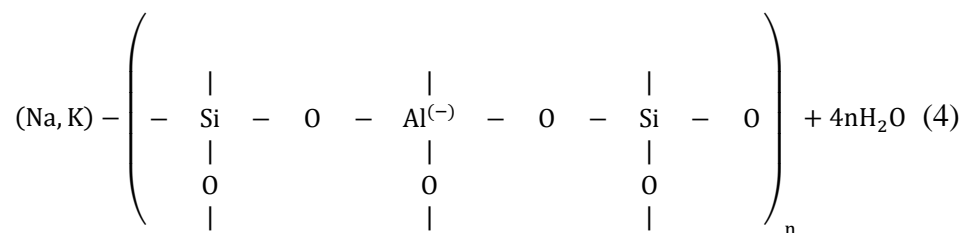
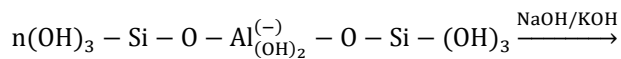
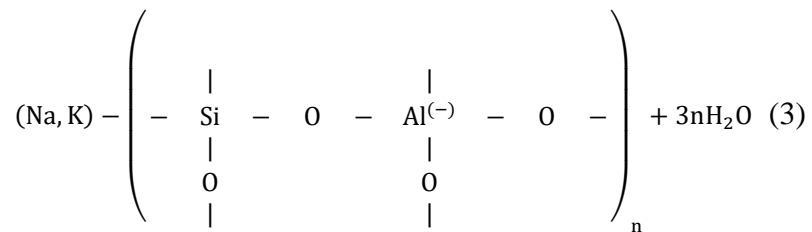
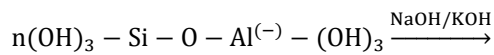


Fig.1-6 Schematic diagram of the polymerization reaction stage of AAFS: (a) (I) ion dissolution and release stage and (II) ion reconstitution stage; (b) (III) hardening acceleration stage; and (c) (IV) hardening deceleration stage, from (X. Wei et al., 2021).

The main feature of stage II is the reconstruction and polycondensation of tetrahedral SiO_4 and AlO_4 , as shown in Equation 3 and 4 (Davidovits, 1989, 1991).



With the increasing concentration of tetrahedral SiO_4 and AlO_4 , collisions are inevitable to form a larger molecular structure. To achieve an effective collision, the energy of reactant molecules needs to reach a critical value, and the active molecules need to collide with each other in a proper direction (Ašperger, 2004). X. Wei et al. (2021) claimed that the curing temperature could affect the molecular energy of reactants and hence change the number of effective collisions per unit time, resulting in different reaction rates.

The main feature of stage III is accelerated hardening. More macromolecules are condensed to form gel networks (N-A-S-H gels, C-A-S-H gels and other hydration products), which greatly increase the solid-phase composition in the system, as shown in Fig.1-6(b). In stage IV, the polymerization continues at a slower rate. Reaction products are mainly filled in the pores, leading to a more compact structure, as shown in Fig.1-6(c). In stage III and stage IV, the curing temperature also has a certain influence.

The hardened N-A-S-H and C-A-S-H gels can provide the similar function as C-S-H gels in hydrated OPC, but the production process of AAMs does not require the high temperature calcination of limestone. As a result, huge amounts of fuel can be saved, and CO_2 emissions due to the burning of fuel and the decomposition of CaCO_3 can be avoided. Properly formulated alkali-activated concrete can provide the same mechanical properties as OPC concrete, but can reduce CO_2 emissions by up to 97% (McLellan, Williams, Lay, Van Riessen, & Corder, 2011). Besides, compared with OPC, AAMs also exhibit higher early age strength, lower hydration heat, faster hardening rate, as well as better performance in harsh environments (John L Provis & Bernal, 2014; John L. Provis, Palomo, & Shi, 2015; John L Provis & Van Deventer, 2009; Caijun Shi, Jiménez, & Palomo, 2011; J. Zhang, Shi, Zhang, & Ou, 2017b). Alkali-activated concrete has been used in several construction projects in Australia, such as the foundations and slabs of VicRoad projects, the long beams of the University of Queensland's Global Change Institute and the foundations of Toowoomba Wellcamp Airport. The success of these projects has put Australia in a leading position in the application of AAMs all over the world. It is encouraging that standardization and regulatory barriers are being gradually removed through the efforts of academia and industry in the past 20 years (Pacheco-Torgal, Labrincha,

Leonelli, Palomo, & Chindaprasit, 2014; John L Provis & Van Deventer, 2013).

As the most common industrial wastes, FA and GGBFS have been increasingly considered as the suitable raw materials for AAMs due to their wide availability and urgent demand for disposal and recycling. However, both pure FA system (AAFA) and pure GGBFS system (AAS) have some limitations in the practical application. Previous investigations found that AAFA exhibited high workability, excellent mechanical properties and excellent durability properties after curing at elevated temperature (Duxson, Provis, Lukey, & Van Deventer, 2007; Fernández-Jiménez, Garcia-Lodeiro, & Palomo, 2007; Y. Ma, 2013b; Rickard, Temuujin, & van Riessen, 2012). But the high temperature curing (normally 60–85°C) is required to activate FA due to the low reactivity of FA at ambient temperature (Fan, Yin, Wen, & Zhong, 1999; Puertas, Martínez-Ramírez, Alonso, & Vazquez, 2000; Somna, Jaturapitakkul, Kajitvichyanukul, & Chindaprasit, 2011). Therefore, AAFA may be suitable for precast concrete manufacturing, instead of cast-in-place concrete (G. Fang, Ho, Tu, & Zhang, 2018). AAS can be cured at ambient temperature and has excellent mechanical and durability properties (Bondar et al., 2018). Despite that, rapid setting and poor workability limit the applicability of AAS on site (R. J. Thomas, Ye, Radlinska, & Peethamparan, 2016). Besides, AAS exhibits significantly higher degree of early age shrinkage than OPC, which will increase the cracking potential of AAS and affect the durability of structure (G. Wang & Ma, 2018). To overcome the shortcomings of AAFA and AAS, alkali-activated fly ash-slag (AAFS) system is proposed as one of the acceptable attempts.

For widespread application, AAFS requires to satisfy a series of performance criteria, e.g. workability, setting time, mechanical properties and durability properties. AAFS normally consists of two parts (i.e. precursor and activator), which means its performance is affected by a range of parameters, e.g. FA/GGBFS ratio, water/binder ratio (w/b) or activator/binder ratio (a/b), alkali content (Na₂O content) and silicate content (SiO₂ content) or silicate modulus (Ms, molar ratio of SiO₂/Na₂O). This is more complicated than that of OPC, of which the performance is mainly determined by w/b. Until now, an increasing number of studies on the workability, setting time, mechanical properties and shrinkage of AAFS have been undertaken. It is found that increasing FA content and a/b can lead to the increased slump flow and prolonged

setting time, but the decreased compressive strength (G. Fang et al., 2018; Gao, Yu, & Brouwers, 2016; P. Nath & Sarker, 2014). Chi and Huang (2013) concluded that AAFS mortars had the higher mechanical strength and lower water absorption compared with OPC mortars. G. Fang et al. (2018) suggested the silicate-activated mixtures with GGBFS content from 20% to 30%, a/b of 0.4, 10 molarity of NaOH solution and $\text{Na}_2\text{SiO}_3/\text{NaOH}$ ratio from 1.5 to 2.5 as the optimal AAFS mixtures to achieve high workability (minimum slump value of 90 mm), suitable setting time (minimum initial setting time of 1 hour) and high compressive strength (minimum 28-d compressive strength of 35 MPa). Abdalqader et al. (2015) claimed that higher Na_2CO_3 content increased the compressive strength of carbonate-activated fly ash-slag systems at all ages, and activating fly ash-slag with Na_2CO_3 and incorporating MgO can achieve high compressive strength (28-d compressive strength > 60 MPa; 90-d compressive strength > 80 MPa). Gao et al. (2016) and Y. Ma, Yang, Hu, Zhang, and Wang (2019) found that decreasing GGBFS content and Ms can reduce the autogenous and drying shrinkage. Except for engineering properties (e.g. workability, setting time, mechanical properties and shrinkage), the chloride resistance of AAFS, which can decide the ability of protecting reinforcement steel in reinforced AAFS concrete under chloride-containing environments, is another technical issue that raises wide concern.

1.1.3 CHLORIDE ATTACK IN REINFORCED CONCRETE

Corrosion of reinforcement steel is the most serious threat to reinforced concrete, which has led to 80% of the degradation of reinforced concrete structures in the world (M Criado, 2015; El-Reedy, 2017). After the 1950s, chloride attack instead of carbonation was considered as the main culprit of steel corrosion in reinforced concrete structures exposed to chloride-containing environments, e.g. deicing salt, salt contaminated aggregates and marine environment (Böhni, 2005). Although chloride ions (Cl^-) usually do not cause the direct damage to the concrete matrix (J. Zhang, Shi, Zhang, & Ou, 2017a), the chloride ingress can result in the accumulation of Cl^- on the surface of reinforcement steel and hence the onset of chloride-induced corrosion, leading to the cracking of cover concrete and hence the failure of reinforced concrete structures.

In general, a thin oxide layer (passive film) can be formed on the surface of

reinforcement steel and maintained in concrete pore solution ($\text{pH} > 12.5$) to prevent corrosion (Montemor, Simoes, & Ferreira, 2003). However, when the critical chloride content (also known as threshold value) is reached due to the transport of Cl^- in cover concrete, this passive film is partly or completely broken down (Tahri, Hu, Shi, & Zhang, 2021). Aberration-corrected transmission electron microscopy (Cs-corrected TEM) was used to unmask the mechanism of chloride-induced depassivation (B. Zhang et al., 2018). As shown in Fig.1-7, the passive film is amorphous with some nanocrystals. When chloride ions (Cl^-) attack the passive film, they penetrate the passive film only through the red tunnels formed by the interfaces between nanocrystals and the amorphous zone (B. Zhang et al., 2018). As a result, an undulating metal/film interface can be formed and impart the pronounced stress, leading to a relatively localized breakdown of the passive film and hence a localized corrosion called “pitting corrosion” (Böhni, 2005; M Criado, 2015; Vu, Gowripalan, De Silva, Kidd, & Sirivivatnanon, 2018; Zhou, Gencturk, Willam, & Attar, 2014).

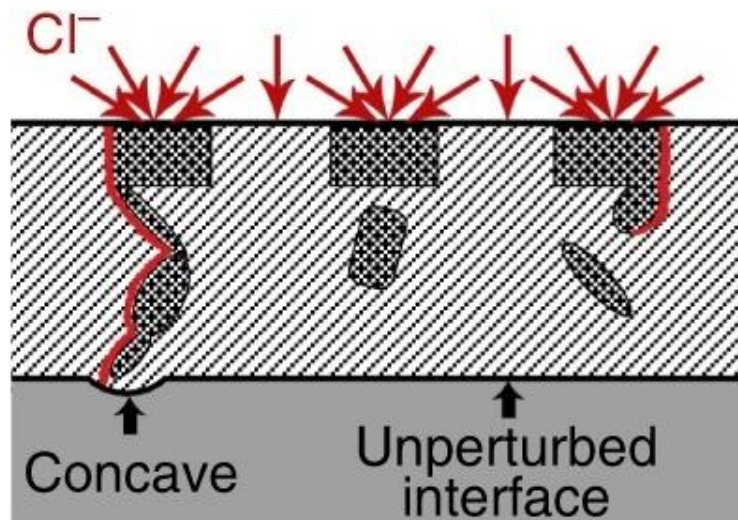


Fig.1-7 Schematic representation of chloride-induced depassivation (B. Zhang et al., 2018).

Once a pit is formed due to chloride-induced depassivation, a local “differential environmental cell” is created as shown in Fig.1-8. The diffusion of oxygen (O_2) into the pit is slower than the consumption of oxygen due to cathodic reaction (Equation 6), leading to the reduction of oxygen. Therefore, the oxidation or dissolution of iron (anodic reaction in Equation 5) is the main reaction in the pit. After that, the environment in the pit becomes particularly aggressive due to the local acidification

caused by the hydrolysis of dissolved Fe^{2+} and increased chloride content caused by the migration of Cl^- to balance the positive charge produced (Berrocal, 2017). Conversely, the nonpitted area can be protected by cathodic reaction. Because the anodic and cathodic reactions are stable, the pitting corrosion process can be sustained. Moreover, chloride ions (Cl^-) can act as catalysts, which are not consumed in the pitting process. Although Cl^- can react with Fe^{2+} to form $\text{FeCl}_2 \cdot 4\text{H}_2\text{O}$ (Equation 7), $\text{FeCl}_2 \cdot 4\text{H}_2\text{O}$ can release Cl^- (Equation 8) and make the growth of the pit become autocatalytic (Poursaee, 2016).

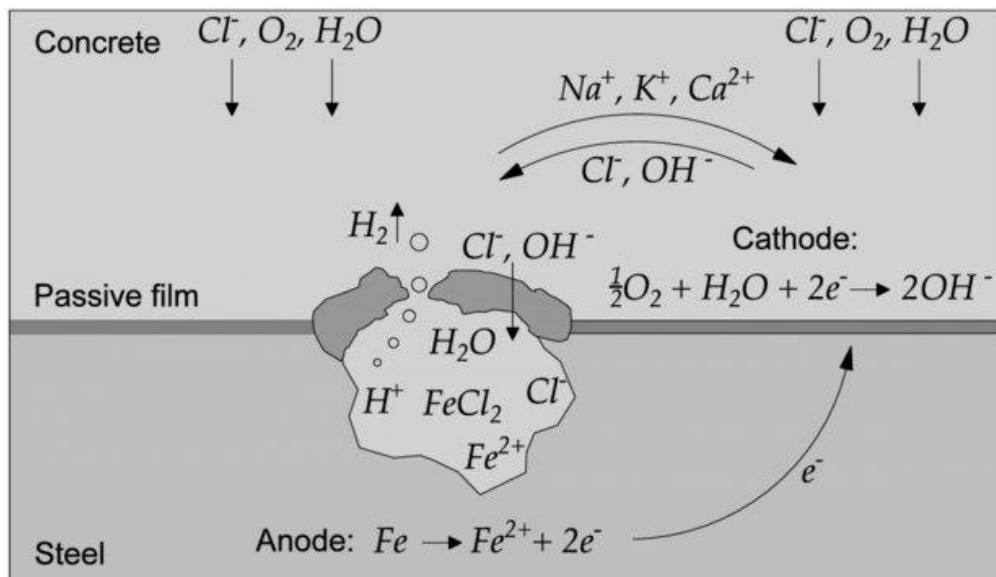
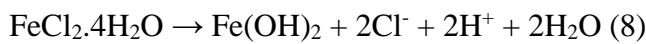
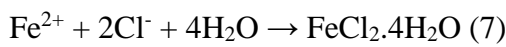
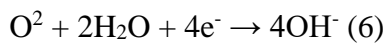
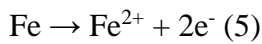


Fig.1-8 Schematic representation of pitting corrosion (Berrocal, 2017).

The anodic and cathodic reactions are only the first step in the process of creating corrosion products (Yuxi Zhao & Jin, 2016). After that, Fe^{2+} react with hydroxyl ions, oxygen and water to produce a variety of corrosion products as shown in Fig.1-9. It can be seen that corrosion products have the larger volumes (up to 6 times the original volume of iron). Therefore, the concrete surrounding the reinforcing steel is subjected to internal expansive pressures. As a result, cracking and further deterioration occur, which further accelerate the corrosion process and ultimately lead to structural destruction (Yuxi Zhao, Dong, Wu, & Jin, 2016; Yuxi Zhao & Jin,

2016).

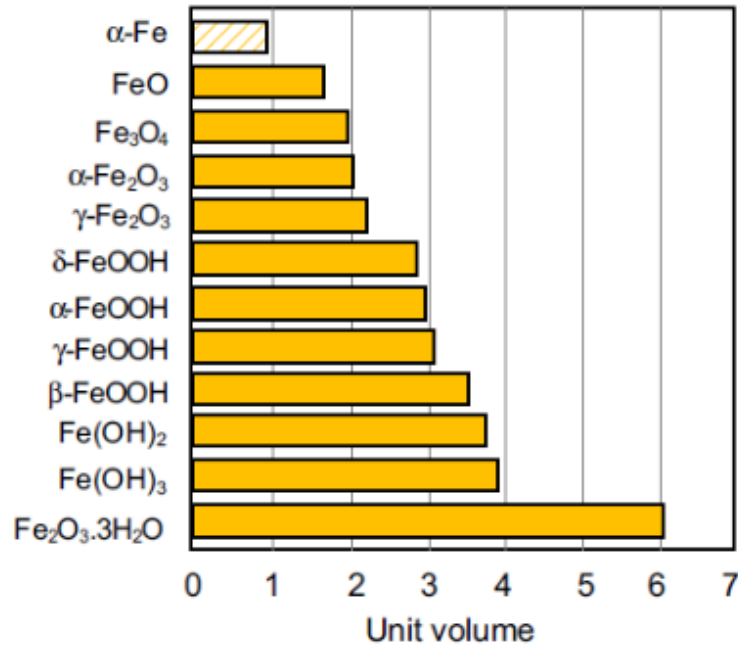


Fig.1-9 Volume of corrosion products relative to that of iron (Poursae, 2016).

The direct and indirect losses caused by the structural destruction due to chloride-induced corrosion are considerable all over the world. Each year almost \$2.5 Trillion USD, taking up 3.4% of the global GDP, is spent on the prevention, mitigation and repair of civil infrastructure damage (Koch et al., 2016). For instance, it is estimated that the United States spends \$50 million to \$200 million USD on repairing bridge decks every year (Berke, Bentur, & Diamond, 2014). Moreover, some buildings in the near coastal zones of the Middle East and North Africa have been fully destroyed due to chloride-induced corrosion (El-Reedy, 2017). Therefore, the service life of reinforced concrete structures under chloride-containing environments should be guaranteed to be long enough. According to Australian standards, the service life of general structures should be around 50 years (AS 3600 Concrete structures). For bridges, it should be more than 100 years (AS 5100 Bridge design).

To estimate the service life of reinforced concrete structures under chloride-containing environments, a corrosion damage model was proposed by Tuutti (Tuutti, 1982) (Fig.1-10). In this model, the service life is roughly divided into the initiation period and propagation period. The initiation period is characterized by chloride

transport. Through the cover concrete, chloride ions gradually move from the concrete surface to the reinforcement steel until depassivation (onset of corrosion). The propagation period corresponds to the corrosion damage of reinforced concrete structures until the acceptable damage level is reached. The initiation period requires to be long enough to postpone the propagation period and prolong the total service life. Therefore, understanding the chloride resistance of AAFS is extremely important for the feasibility of AAFS to replace OPC in the practical construction. AAFS used to replace OPC should have the same or better chloride resistance to ensure the same or longer initiation period. In other words, chloride transport in AAFS should be the same as or slower than that in OPC.

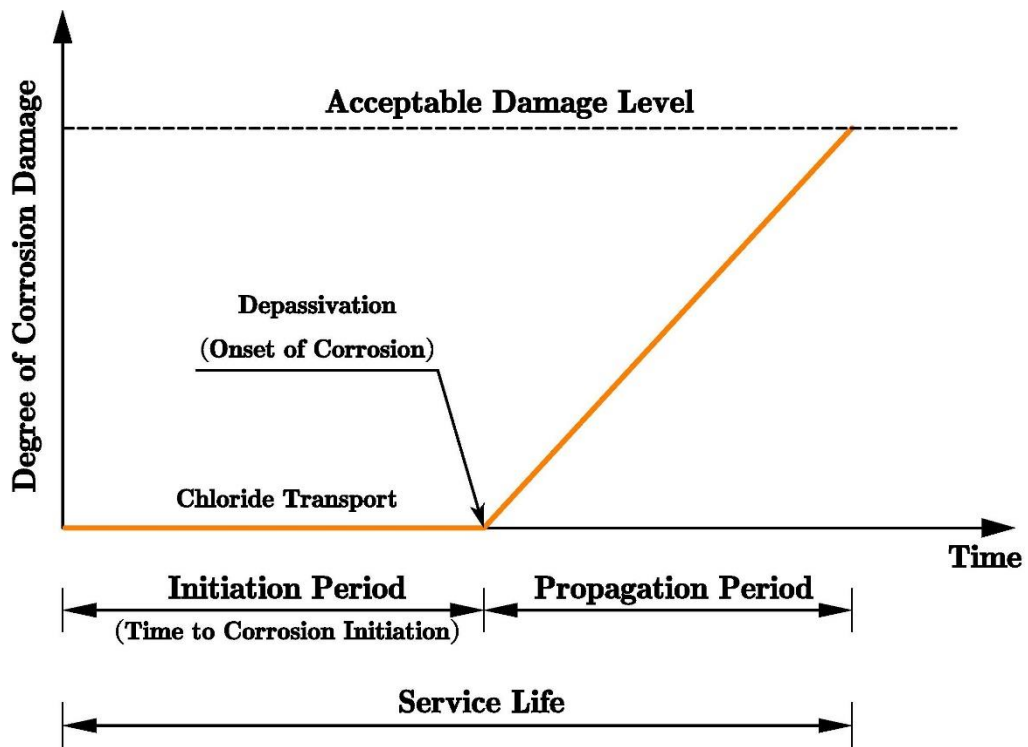


Fig.1-10 Service life model of reinforced concrete structures, adapted from (Tuutti, 1982).

1.2 OBJECTIVES OF THE RESEARCH

The aim of this research is to evaluate the chloride resistance of AAFS concretes by natural chloride diffusion test, and establish the relationship between chloride resistance and microstructure to explore the influence mechanism of different parameters. In addition, the long-term chloride transport in AAFS concretes is predicted and the effects of different Mg-based admixtures are investigated. The main objectives of this project can be summarized as follows:

- 1) To design practical AAFS concretes according to workability and compressive strength, evaluate their chloride resistance by natural chloride diffusion test, and discuss the effects of different parameters.
- 2) To establish the relationship between chloride resistance and microstructure (including phase evolution and pore structure) of different AAFS concretes, and explore the influence mechanism of different parameters.
- 3) To establish the time dependent models of chloride diffusion coefficient (D), and predict the subsequent chloride diffusion, chloride profile and corrosion time in different AAFS concretes.
- 4) To investigate the effects of different Mg-based admixtures on the chloride resistance of AAFS, and identify the correlation between chloride resistance and microstructure.

1.3 OUTLINE OF THE THESIS

The outline of the thesis is given in Fig.1-11.

Chapter 1: Introduction. In Chapter 1, the background and objectives of the research are presented.

Chapter 2: Literature review. In Chapter 2, the literature review establishes an existing knowledge system of chloride transport in AAFS and other AAMs. Finally, research gaps are pointed out as the motivations of this project.

Chapter 3: Mixture Design and engineering properties of alkali-activated fly ash-slag systems. In Chapter 3, the physical and chemical properties of the FA and GGBFS used in the thesis are characterized. AAFS pastes with different FA/GGBFS ratios, water/binder ratios (w/b), Na_2O contents and SiO_2 contents are prepared and verified by compressive strength. AAFA concretes with different FA/GGBFS ratios, water/binder ratios (w/b), Na_2O contents, SiO_2 contents and sand/aggregate ratios (s/a) are prepared. According to the results of workability and compressive strength, a series of practical AAFS concrete mixtures with good engineering properties are selected.

Chapter 4: Chloride resistance of alkali-activated fly ash-slag concretes. In Chapter 4, in order to investigate the chloride resistance of AAFS concretes, long-term natural chloride diffusion tests are conducted. The chloride profiles of different AAFS concretes are obtained. Based on the measured chloride profiles, the free chloride diffusion coefficients (D_f) of different AAFS concretes are determined. The time dependent water absorption of different mixtures (24 hours) is also determined.

Chapter 5: Microstructure of alkali-activated fly ash-slag systems and its effects on chloride resistance. In Chapter 5, the phase evolution of different mixtures is analysed by X-ray diffraction (XRD) and Fourier transform infrared spectroscopy (FTIR). The pore structure of different mixtures is analysed by mercury intrusion porosimetry (MIP) and nitrogen adsorption. The relationship between chloride resistance and microstructure is established to explore the influence mechanism of different parameters.

Chapter 6: Prediction of chloride transport in alkali-activated fly ash-slag concretes. In Chapter 6, the time dependent models of chloride diffusion coefficient (D) in different AAFS concretes are established. The values of surface chloride content (C_s) in different AAFS concretes are compared. Based on Australian standards (AS 3600 and AS 5100.5), the obtained time dependent models of D are used to predict the subsequent chloride diffusion and chloride profile, as well as the time to corrosion initiation.

Chapter 7: Effects of Mg-based admixtures on chloride resistance of alkali-activated fly ash-slag systems. In Chapter 7, AAFS mixes with different Mg-based admixtures are prepared. Compressive strengths at different ages are determined. To investigate the effects of different Mg-based admixtures, the chloride resistance of different mixes is measured by chloride diffusion test. The pore structure analysed by nitrogen adsorption and the phase composition analysed by X-ray diffraction (XRD) are used to explore the influence mechanism.

Chapter 8: Conclusions and recommendations. In Chapter 8, the general conclusions of the research undertaken in this thesis are drawn. Detailed suggestions for the future work are put forward.

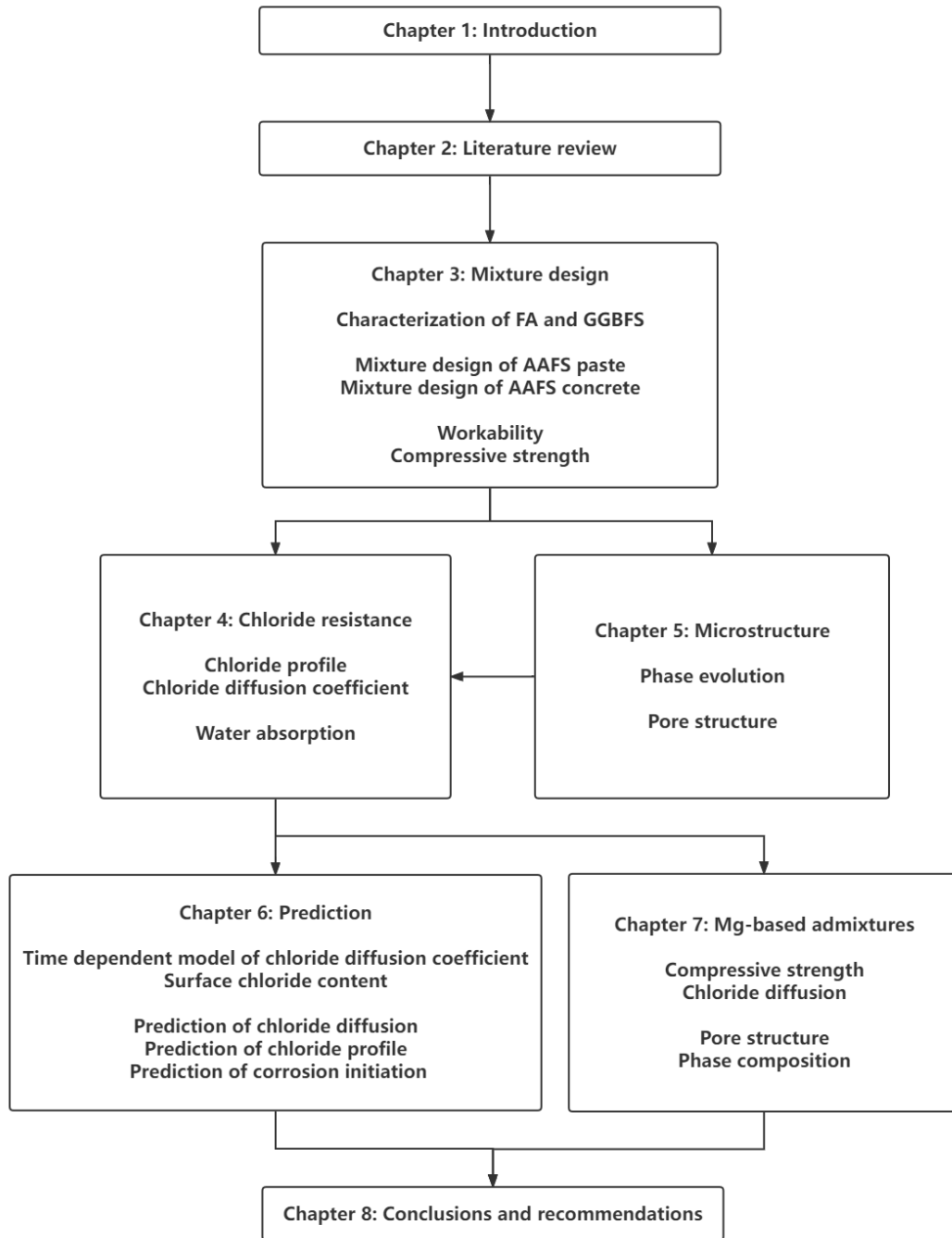


Fig.1-11 Outline of the thesis.

CHAPTER 2: LITERATURE REVIEW

*Note: this chapter is based on the manuscript entitled “Review on chloride transport in alkali-activated materials: Role of precursors, activators and admixtures”, by Jingxiao Zhang, Yuwei Ma, Jie Hu, Hao Wang and Zuhua Zhang, published in journal of **Construction and Building Materials**, 2022.*

2.1 INTRODUCTION

Prior to conducting this research, previous studies should be reviewed to basically understand the current research status of the chloride resistance of AAFS and other AAMs. Numerous studies have been carried out to investigate the chloride resistance of AAMs, but the results among different studies are inconsistent. Most studies reported that AAMs had a higher chloride resistance than OPC (Bernal, de Gutiérrez, & Provis, 2012; Bondar et al., 2018; Kupwade-Patil & Allouche, 2013; Q. Ma, Nanukuttan, Basheer, Bai, & Yang, 2016; C Monticelli et al., 2016; Tennakoon, Shayan, Sanjayan, & Xu, 2017), due to the denser pore structure (X. Hu, Shi, Shi, & Zhang, 2019; Ismail, Bernal, Provis, San Nicolas, et al., 2013). Despite that, some researchers claimed that some AAMs mixtures exhibited a higher chloride penetration rate than OPC (Babaee & Castel, 2018; R. Thomas, Ariyachandra, Lezama, & Peethamparan, 2018; T. Yang, Yao, & Zhang, 2014; Zhu, Zhang, Zhu, & Tian, 2014). The inconsistency of these results may be due to the strong influence of different parameters, such as precursors, activators, and admixtures. Moreover, the mutual interference among different parameters makes the results more confusing. Besides, the testing methods of chloride penetration used in OPC may not always be applicable to AAMs and thus lead to incorrect results. For example, more other ions (e.g. OH⁻) in the pore solution of AAMs may retard the diffusion of Cl⁻, but lead to the opposite result in rapid chloride permeability test (RCPT) and other tests based on electrical resistivity (Arbi, Nedeljković, Zuo, & Ye, 2016). In order to find the correct research direction and appropriate experimental methods for this project, it is necessary to describe, compare and explain different previous results, and integrate them into a knowledge system.

This chapter provides a brief overview of the chloride transport in AAFS and other AAMs. Chloride transport mechanisms are explained. Material characteristics (pore structure, chloride binding capacity, pore solution and phase evolution) are used to

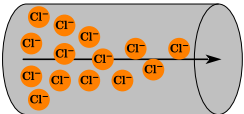
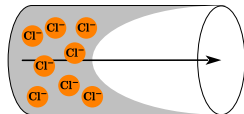
establish the linkages between different parameters and chloride resistance. Advantages and disadvantages of different testing methods are evaluated. The chloride resistance characters of AAMs and OPC are compared. Roles of different parameters including precursors, activators and admixtures are discussed in detail. General recommendations on the types and ratios of precursors, activators and admixtures are put forward. Finally, concluding remarks are made. On the basis of summarizing the previous knowledge system, the motivations of this research are obtained.

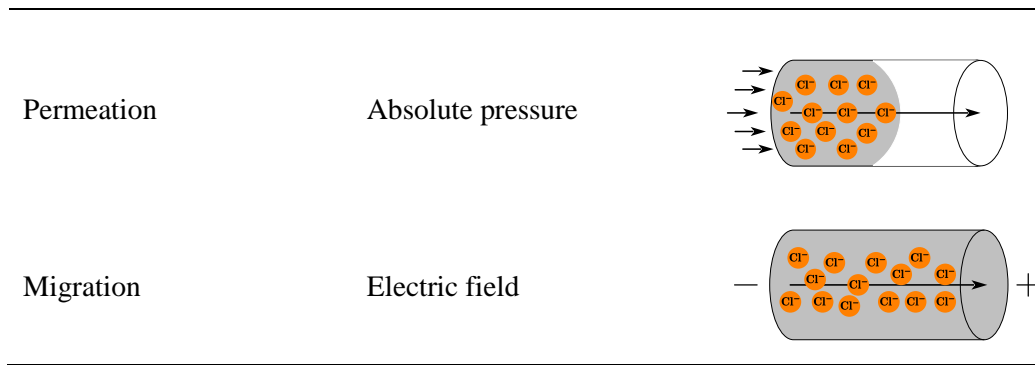
2.2 CHLORIDE TRANSPORT MECHANISMS AND INFLUENCING FACTORS

2.2.1 CHLORIDE TRANSPORT MECHANISMS

As the barriers between external environment and steel reinforcement, both AAMs and OPC are not completely impenetrable and have numerous pores filled with pore solution. The internal connected pore system forms the paths of Cl^- , while the contribution of Cl^- passing through the solid portion is negligible (Yuan, Shi, De Schutter, Audenaert, & Deng, 2009). Chloride transport is a complicated process, involving ionic diffusion, capillary sorption, permeation and migration (Table.2-1) in the pore system, accompanied by the physical adsorption and chemical binding of reaction products (Alexander, 2016; Böhni, 2005; HUKELER, 1994; Paschmann, Grube, & Thielen, 1995).

Table 2-1 Chloride transport mechanisms.

Transport mechanism	Driving force	Schematic representation
Ionic diffusion	Concentration gradient	
Capillary sorption	Surface tension	



Under normal conditions, ionic diffusion, as a process driven by concentration gradient without any flow of water, plays the dominant role in chloride transport. Taking water as the medium, chloride ions move from high concentration to low concentration (J. Li et al., 2020). Capillary sorption is a natural phenomenon caused by surface tension. During this process, ion-containing fluids are absorbed in finer pores. In the climate zone with less rain, the water with Cl^- can be drawn up by “wicking” until it reaches an exposed surface and evaporates, leading to the accumulation of Cl^- (Claisse, 2005). Permeation is determined by absolute pressure. Chloride ions take water as the carrier and move with the flow under different water pressures (J. Li et al., 2020). This phenomenon may occur in some special buildings under an external water pressure (e.g. dams and tunnels). Besides, the water absorption process may also lead to absolute pressure difference and hence permeation. Migration occurs when an electric field is applied, which makes Cl^- move towards the positive electrode.

Though the chloride transport is not a single process, ionic diffusion generally has the dominant effect and can generate a rough figure of the reality to design and assess reinforced concrete structures (Böhni, 2005; Collepardi, Marcialis, & Turriziani, 1970). To describe chloride diffusion in AAMs and OPC, many models are used. Most of them are based on Fick’s second law as shown in Equation 9 or 10 (Babaee & Castel, 2018; P Chindaprasirt & Chalee, 2014; Tennakoon et al., 2017; T. Yang et al., 2014) as follows:

$$c(x, t) = c_s \left[1 - \operatorname{erf} \left(\frac{x}{2\sqrt{D \cdot t}} \right) \right] \quad (9)$$

or

$$c(x, t) = c_0 + (c_s - c_0)[1 - \text{erf}\left(\frac{x}{2\sqrt{D \cdot t}}\right)] \quad (10)$$

where $C(x, t)$ = chloride content (mass %) at depth x (m) and time t (s); C_s = exposure surface chloride content (mass %); C_0 = initial chloride content (mass %); D = chloride diffusion coefficient (m^2/s); and erf denotes error function.

It should be recognized that the D is not constant, but time-varying. The pore-filling effect of continuous reaction can improve the chloride resistance over time. Therefore, the corresponding D also decreases. With the extension of time, the pore-filling effect decreases gradually, and the D tends to be stable.

2.2.2 INFLUENCING FACTORS

Without considering external conditions (e.g. external chloride concentration, temperature, wet-dry cycling action, freeze-thaw and other aggressive substances), the pore structure, chloride binding capacity, pore solution and phase evolution of AAMs can seriously affect chloride transport, which is an integral part of initiation period and total service life (Fig.2-1). These material characteristics are decided by precursors, activators, admixtures and other parameters (e.g. curing conditions, aggregates and initial chloride content). Generally, the contribution of pore structure plays the most decisive role in chloride transport.

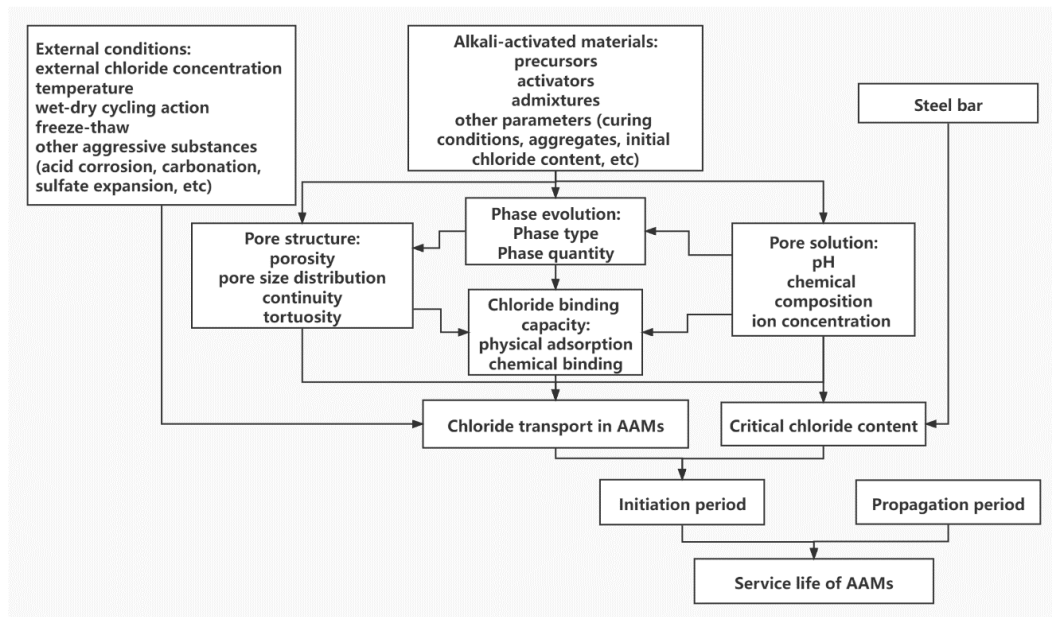


Fig.2-1 Illustration of factors affecting the chloride transport in AAMs.

2.2.2.1 PORE STRUCTURE

Pore structure (including porosity, pore size distribution, continuity, and tortuosity) is the crucial factor determining chloride transport in both OPC and AAMs. In the matrix, the number, diameter, continuity and tortuosity of the paths of Cl^- are decided by pore structure. To characterize pore structure, water absorption, mercury intrusion porosimetry (MIP), N_2 adsorption and scanning electron microscopy (SEM) are frequently used (Y. Ma, Wang, Ye, & Hu, 2018; Zhu et al., 2014). According to the traditional classification (Young, Mindess, & Darwin, 2002), pores in cementitious materials were classified into three classes : gel pores (<10 nm) formed within reaction products, capillary pores (10–10,000 nm) as the remnants of initial water-filled space (Fig.2-2) (H. F. Taylor, 1997), and air voids (>10,000 nm) caused by bubbles trapped.

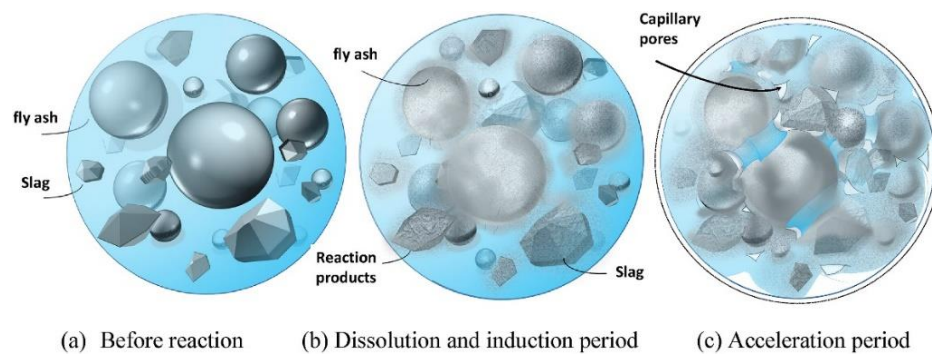


Fig.2-2 Schematic diagram of the generation of capillary pores in AAMs, from (Y. Ma et al., 2019).

Generally, samples with lower total porosity, smaller pore size, poor continuity and higher tortuosity have higher chloride resistance. In OPC, Moukwa (1989) reported that the chloride transport mainly depended on capillary pores larger than 30 nm instead of small pores (3-30 nm). Hornain, Marchand, Duhot, and Moranville-Regourd (1995) confirmed the benefit of higher tortuosity of pores on the improvement of chloride resistance. Moreover, G. Ye (2005) claimed that the pore connectivity was the crucial factor, which was more important than porosity and pore size distribution (Neithalath & Jain, 2010).

Compared with OPC, most of AAMs have finer pore structure dominated by smaller pores, which may lead to better chloride resistance. Fig.2-3 depicts the pore structure of alkali-activated pastes with different GGBFS contents at the age of 7 days. The

total porosity of OPC was 29% and higher than almost all alkali-activated pastes, except for pure FA system (AAFA, 41%). In pure GGBFS system (AAS) and binary system (AAFS), the threshold pore diameter (peak in the curve), as the minimum size of the pores to form a continuous network (G. Ye, 2003), is almost two orders of magnitude lower than AAFA. Gel pores (< 10 nm) instead of capillary pores dominated the pore structure. The increase of GGBFS content from 30% to 100% not only reduced the total porosity from 27% to 3%, but also decreased the threshold pore diameter from 6 nm to 3 nm. Although the chloride transport in AAMs is mainly determined by capillary pores (X. Hu et al., 2019), capillary pores are usually disconnected and connected via small pores (Lloyd, Provis, Smeaton, & van Deventer, 2009). The smaller pores lead to the lower total porosity, smaller pore size, poor continuity and higher tortuosity. As a result, the paths of Cl^- are narrower and have more obstacles. Except for precursors, other parameters (e.g. activators and admixtures) can also change the pore structure and chloride resistance to a great extent in AAMs (discussed in later sections).

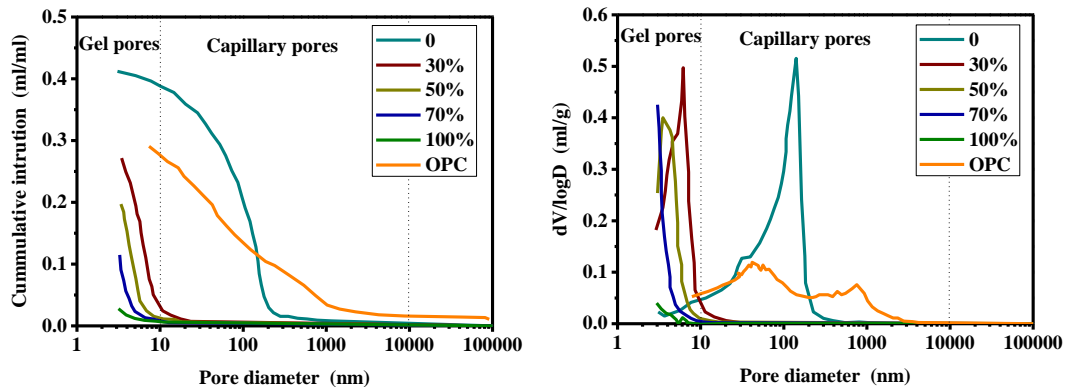


Fig.2-3 Porosity and pore size distribution of alkali-activated pastes with different GGBFS contents (Ouyang, Ma, Liu, Liang, & Ye, 2020) and OPC (Guang, 2003) at 7 days.

2.2.2.2 CHLORIDE BINDING CAPACITY

Chloride binding capacity is also a vital factor influencing the chloride penetration in both OPC and AAMs. The Cl^- passing through the pore system can be captured by the pore wall along the way. Thus, the chloride transport in the matrix is slowed down. Chloride binding capacity is influenced by many factors, e.g. pore structure, phase composition of reaction products, OH^- concentration, chloride concentration, cation type and temperature (Yuan et al., 2009). To investigate the chloride binding

capacity, the leaching method for determining powdered samples is the most conventional technique (e.g. AS 1012.20.1, AS 1012.20.2, ASTM C1152, ASTM C1218, AASHTO T260, BS EN 196-2 and JTJ270-98), in which acid-soluble Cl^- and water-soluble Cl^- are used to ascertain total chloride content and free chloride content, respectively. Therefore, bound chloride content can be obtained according to the difference between total chloride content and free chloride content.

Cl^- can be physically adsorbed on the surface of reaction products due to Van der Waals and electrostatic forces in the electrical double layer (Fig.2-4); or chemically bound into reaction products (Elakneswaran, Nawa, & Kurumisawa, 2009; Pargar, Koleva, & van Breugel, 2017; Yuan et al., 2009). In Fig.2-4, an accumulation of Cl^- and a depletion of cations (e.g. Ca^{2+}) can be found near the charged surface of reaction products. Although this electrical double layer is only a few nanometres, it can adsorb a considerable amount of Cl^- (Elakneswaran et al., 2009). In OPC, chloroaluminates are the main reaction products of chemical chloride binding, such as Friedel's salt ($\text{Ca}_3\text{Al}_2\text{O}_6 \cdot \text{CaCl}_2 \cdot 10\text{H}_2\text{O}$) formed by the reaction between Cl^- and tricalcium aluminate (C_3A) (Pargar et al., 2017; Yuan et al., 2009). In order to distinguish between the physical binding and chemical binding chloride, XRD can be used to obtain Friedel's salt content and hence calculate chemically bound chloride. Generally, the amount of physically bound Cl^- is higher than that of chemically bound Cl^- (Tran, Nawa, & Stitmannathum, 2014).

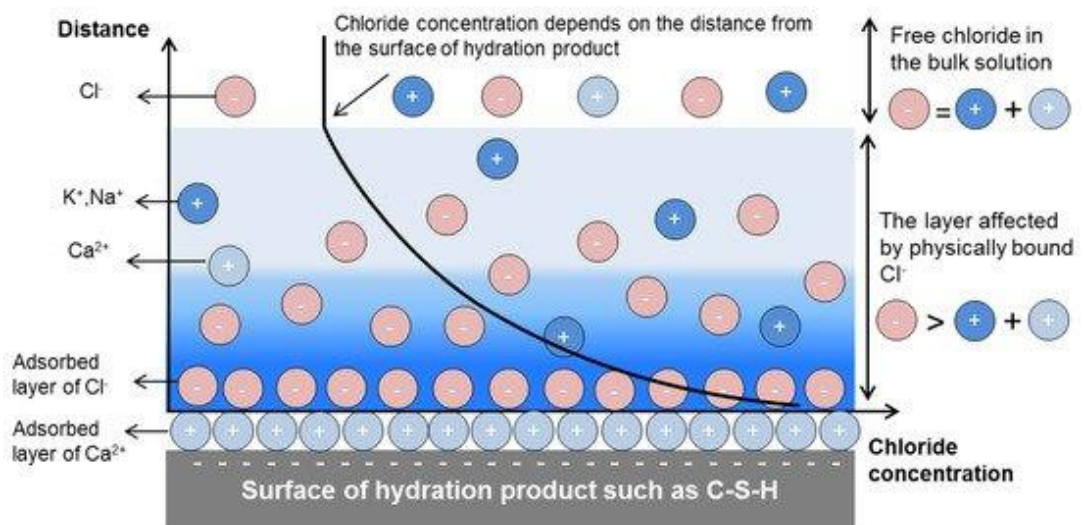


Fig.2-4 Physical binding of chloride ions (Cl^-), from (Pargar et al., 2017).

There are some differences between the mechanisms of chloride binding of AAMs and OPC. Although a few researchers (Ke, Bernal, Hussein, & Provis, 2017; J. Zhang, Shi, & Zhang, 2019b) found Friedel's salt in AAMs, chloroaluminates are normally not formed in AAMs, leading to a low or even insignificant chemical chloride binding capacity. The observations in AAFA (Škvára, Jílek, & Kopecký, 2005), AAS (Brough, Holloway, Sykes, & Atkinson, 2000) and AAFS (Babaee & Castel, 2018) confirmed the above viewpoints. Ismail, Bernal, Provis, San Nicolas, et al. (2013) considered that the Cl^- in AAMs did not involve the formation of phases of new chloroaluminates and thus the chloride binding of AAMs was mainly determined by physical adsorption.

2.2.2.3 PORE SOLUTION

The alkalinity, chemical composition and ion concentration of pore solution have a certain influence on chloride transport in OPC and AAMs. Compared with OPC, the pore solution chemistry of AAMs is more complicated. To extract and analyse the pore solution, the high pressure device and inductively coupled plasma/atomic emission spectroscopy (ICP-OES) can be used (Nedeljkovic, Arbi, Zuo, & Ye, 2016; Nedeljković, Ghiassi, van der Laan, Li, & Ye, 2019; Zuo, Nedeljković, & Ye, 2019). Fig.2-5 presents the alkalinity (pH) and concentration of main ions in the pore solution of AAMs with different GGBFS contents and OPC at 28 days. It is observed that the pH of these mixes had no significant difference. The pH of AAFS slightly increased from 13.02 to 13.60 with increasing GGBFS from 0 to 100%. And the pH of OPC (13.28) was between AAFA (0%) and AAS (100%). Compared with OPC, the pore solution of AAMs contains obviously more Na^+ and sulfur species (mainly HS^- (Gruskovnjak, Lothenbach, Holzer, Figi, & Winnefeld, 2006; Myers, Bernal, & Provis, 2014, 2017)), but has a relatively low K^+ concentration. Besides, higher pH caused by GGBFS addition means higher OH^- concentration in the pore solution of AAMs. Despite the remarkable difference between OPC and AAMs with various mix proportions, the effect of pore solution on chloride resistance has not been fully investigated.

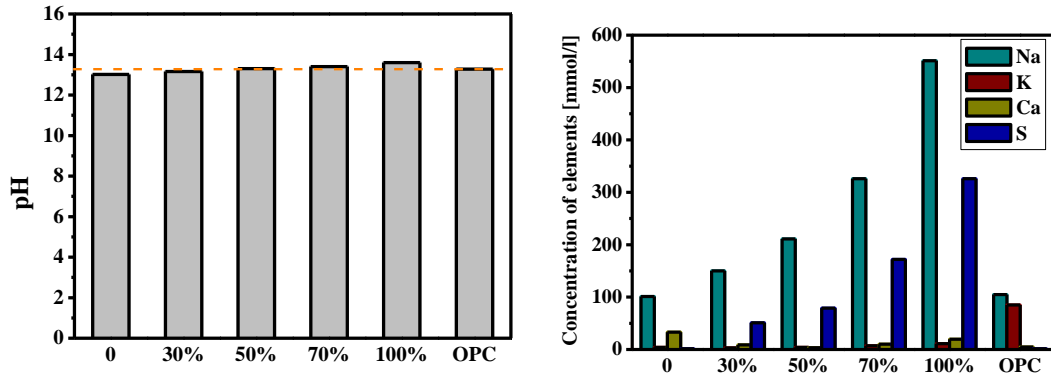


Fig.2-5 pH and main element composition in the pore solution of AAMs with different GGBFS contents and OPC at 28 days, reproduced from (Nedeljković et al., 2019).

As shown in Fig.2-1, pore solution can determine phase structure and chloride binding capacity, and then affect chloride transport. In addition, the type and concentration of other ions can directly affect the diffusion of Cl^- in pore solution. The alkalinity of AAMs is as high as OPC (Nedeljkovic et al., 2016; Nedeljković et al., 2019; Zuo et al., 2019), which can ensure the stability of aluminosilicate gels to retain its structure, and hence maintain the pore structure. But higher OH^- concentration reduces the $[\text{Cl}^-]/[\text{OH}^-]$ ratio and thus the amount of bound chloride (J. Zhang et al., 2019b). Moreover, more ions (e.g. Na^+ , OH^- and HS^-) in the pore solution of AAMs may retard the diffusion of Cl^- . Zhang and Gjörv (T. Zhang & Gjörv, 1996) claimed that the enhanced ionic interaction due to more ions might reduce the chemical potential to drive chloride diffusion, and the lagging motion of more cations (Na^+) might also delay the drift velocity of Cl^- . However, relevant studies are limited and this inference requires further validation. Note that numerous mobile ions may increase the electrical conductivity and reduce the electrical resistivity. As a result, related electrical testing methods (e.g. RCPT) used to measure the chloride transport in AAMs may display the opposite results (Arbi et al., 2016).

Furthermore, pore solution alkalinity (OH^- concentration) and pore solution chemistry (e.g. HS^-) around reinforcing steel greatly influence the critical chloride content for the breakdown of passive film (Fig.2-1) (Mundra, Bernal Lopez, et al., 2017; Mundra, Bernal, & Provis, 2017). The higher critical chloride content means that more Cl^- need to be accumulated on the surface of reinforcement steel to cause corrosion. As a result, the time required for chloride transport is prolonged. Mundra,

Bernal Lopez, et al. (2017) claimed that the steel would remain passive if $[Cl^-]/[OH^-]^3 < 1.25$. Therefore, the critical chloride content increases with higher OH^- concentration. Besides, the role of HS^- in altering passive film and restricting cathodic reduction of oxygen should also be considered (Mundra, Bernal Lopez, et al., 2017; Scott & Alexander, 2016).

2.2.2.4 PHASE EVOLUTION

As shown in Fig.2-1, the phase evolution of AAMs determines pore structure and chloride binding capacity. Phase evolution has a great effect on both gel pores and capillary pores. The type of phase may determine pores in reaction products. For example, N-A-S-H gels have a more porous microstructure compared with C-A-S-H gels (Ismail et al., 2014; Yanru Wang et al., 2022; H. Ye & Radlińska, 2016). More reaction products can further fill capillary pores as the initial gap between particles. Besides, phase evolution can also determine the chloride binding capacity of AAMs. Lee and Lee (2016) reported that N-A-S-H gels had a higher chloride binding capacity compared with C-A-S-H gels because of the larger surface area (Ismail, Bernal, Provis, Hamdan, & van Deventer, 2013a; Lee & Lee, 2016). More reaction products can also lead to a larger total surface area to adsorb Cl^- . Note that the effects of different products in different aspects may conflict each other. For example, N-A-S-H gels have the higher chloride binding capacity due to the larger surface area, but the worse pore structure has a greater negative effect. As the final result, the chloride resistance of N-A-S-H gels is lower than that of C-A-S-H gels (Ismail, Bernal, Provis, San Nicolas, et al., 2013). To analyse the phase evolution, thermogravimetry/differential thermograms (TG/DTG), X-ray diffraction (XRD), Fourier transform infrared spectroscopy (FTIR) and nuclear magnetic resonance (NMR) are commonly used.

2.3 ASSESSMENT OF CHLORIDE TRANSPORT IN ALKALI-ACTIVATED MATERIALS

2.3.1 TESTING METHODS

Common chloride transport tests mainly include rapid chloride permeability test (RCPT, ASTM C1202 and AASHTO T277), non-steady-state migration (NSSM) test (NT BUILD 492), and chloride diffusion tests such as bulk diffusion test (ASTM

C1556 and NT BUILD 443), natural chloride diffusion test (NCD) and ponding test (ASTM C1543 and AASHTO T259), as shown in Fig.2-6. Besides, the electrical resistivity and corrosion behaviour of reinforcement steel investigated by electrochemical tests have been also extensively applied to indirectly estimate chloride transport (Babae & Castel, 2018; Bondar, Basheer, & Nanukuttan, 2019; P Chindaprasirt & Chalee, 2014; Cecilia Monticelli et al., 2016).

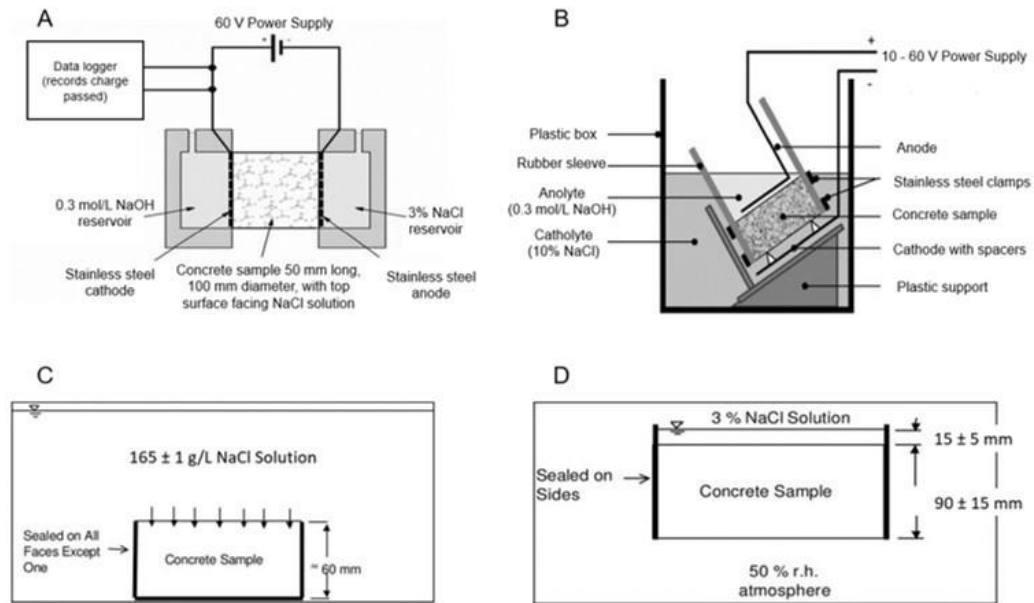


Fig.2-6 Experimental Setup for (A) rapid chloride permeability test (RCPT, ASTM C1202 and AASHTO T277), (B) non-steady-state migration (NSSM) test (NT BUILD 492), (C) bulk diffusion test (ASTM C1556 and NT BUILD 443) and (D) ponding test (ASTM C1543 and AASHTO T259), adapted from (Hasholt & Jensen, 2015; Stanish, Hooton, & Thomas, 2001).

2.3.1.1 RAPID CHLORIDE PERMEABILITY TEST (RCPT)

In order to shorten the test time, RCPT and NSSM test are the preferred methods in OPC materials. During RCPT (Fig.2-6A), one face of the saturated specimen is in contact with 3% NaCl solution, and the other face is in contact with 0.3 mol/L⁻¹ NaOH solution. A 60 V potential is applied between the electrodes placed on both sides of the specimen to obtain the total electrical charge passed in 6 hours. The electrical current is recorded every 30 min and the total electrical charge passed through the specimen in 6 hours is calculated according to Equation 11 (ASTM C1202 (ASTM, 2012)) as follows:

$$Q = 900(I_0 + 2 I_{30} + 2 I_{60} + \dots + 2 I_{300} + 2 I_{330} + I_{360}) \quad (11)$$

where Q = the total electrical charge (C) passed through the specimen; I_0 = the initial electrical current (A); I_t = the electrical current (A) at t min.

After that, the chloride ion penetrability can be obtained based on the measured charge passed according to Table 2-2. RCPT is virtually a measurement of the electrical conductivity and its result is affected by not only pore structure but also chemical composition of pore solution (X. Hu et al., 2019). Because of joule heating and complicated pore solution chemistry, RCPT may be not suitable for AAMs (Bernal et al., 2012; Caijun Shi, 1996). All mobile ions (e.g. Na^+ , OH^- and HS^-), not just Cl^- , in the pore solution of AAMs can affect RCPT results (Arbi et al., 2016). Caijun Shi (1996) found that according to the result of RCPT, the chloride resistance of silicate-activated mixes was lower than hydroxide-activated and carbonate-activated mixes, which was due to higher electrical conductivity of pore solution and might be inconsistent with the fact. Balcikanli and Ozbay (2016) concluded that the high chloride permeability measured by RCPT could not represent the actual chloride permeability of AAS, due to the high Na^+ and OH^- concentration in pore solution. X. Hu et al. (2019) claimed that the higher silicate modulus and alkali dosage resulted in the higher concentration of pore solution in AAFS, leading to the increased electrical conductivity of pore solution and passed charge, but in fact the corresponding chloride resistance was improved due to the improvement of pore structure. Besides, the structural damage of AAMs may be caused by high voltage and associated temperature (Ravikumar & Neithalath, 2013a).

Table 2-2 Chloride ion penetrability based on charge passed (Whiting, 1981).

Charge Passed (coulombs)	Chloride Ion Penetrability
>4,000	High
2,000–4,000	Moderate
1,000–2,000	Low
100–1,000	Very Low
<100	Negligible

2.3.1.2 NON-STEADY-STATE MIGRATION (NSSM) TEST

Compared RCPT, NSSM test, also known as rapid chloride migration test (RCM), has a balance between efficiency and accuracy. During NSSM test, 10% NaCl solution and 0.3 mol/L⁻¹ NaOH solution are used as catholyte solution and anolyte solution, respectively. A 10–60 V potential is applied axially across the saturated specimens which can force the Cl⁻ outside to migrate into them (Fig.2-6B). After a given period (6-96 hours), each specimen is split axially into 2 halves to measure the chloride penetration depth by spraying AgNO₃ solution (0.1 mol/L) on the cross section. Thus, the chloride migration coefficient (D_{NSSM}) can be calculated according to Equation 12 (NT BUILD 492 (Build, 1999)) as follows:

$$D_{NSSM} = \frac{0.0239(273 + T)L}{(U - 2)t} (x_d - 0.0238 \sqrt{\frac{(237 + T)Lx_d}{U - 2}}) \quad (12)$$

where D_{NSSM} = non-steady-state migration coefficient ($\times 10^{-12}$ m²/s); T = the average of measured initial and final temperatures in anolyte solution (°C); L = specimen thickness (mm); U = applied potential (V); t = test duration (h); and x_d = the average of measured chloride penetration depths (mm).

Based on NSSM test, Ismail, Bernal, Provis, San Nicolas, et al. (2013) found that the D_{NSSM} of AAFS was far smaller than OPC and decreased with increasing GGBFS content. X. Hu et al. (2019) reported that the higher silicate modulus and alkali dosage led to the lower D_{NSSM} of AAFS because more reaction products were formed to refine pore structure, which was consistent with the increase of compressive strength. Ramezani pour and Moeini (2018) investigated the effects of nano-silica and silica fume on the chloride resistance of AAS and found a relatively good correlation ($R^2 = 0.9$) between the results of NSSM test and bulk diffusion test at 90 days (Fig.2-7). However, NSSM test still cannot represent the real situation of chloride transport in AAMs, particularly in a longer period, due to the continuous reaction and enhancement of pore structure (Ismail, Bernal, Provis, San Nicolas, et al., 2013). Besides, NSSM test is completed within 9-96 hours and chloride ions migrate rapidly. Therefore, the chloride binding in NSSM test is much weaker and may not reflect the actual situation (Yuanzhan Wang & Fu, 2019). Further validation is required for the applicability of NSSM test in AAMs.

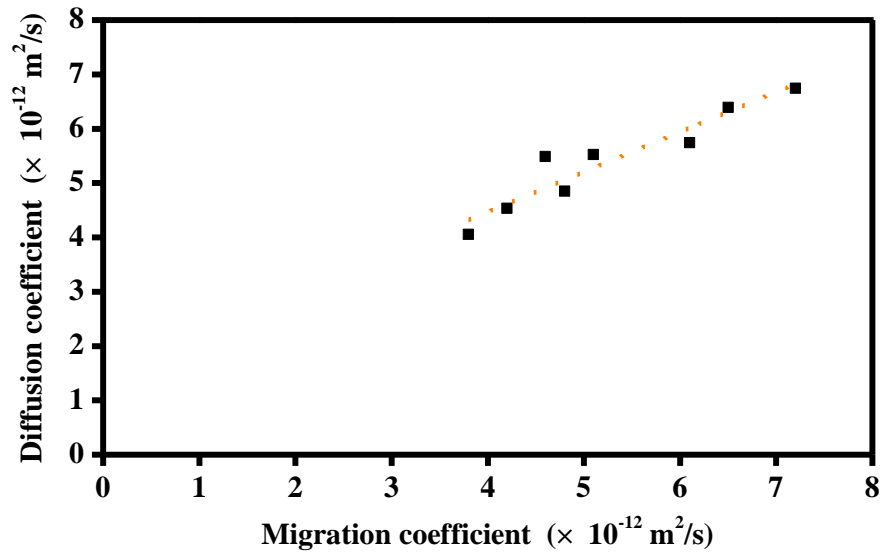


Fig.2-7 Correlation between the results of non-steady-state migration (NSSM) test and bulk diffusion test at 90 days, adapted from (Ramezaniapour & Moeini, 2018).

2.3.1.3 CHLORIDE DIFFUSION TESTS

Compared with RCPT and NSSM test, chloride diffusion tests are the most dependable methods to simulate the real environment. Before the chloride diffusion test, the specimen surfaces other than the exposure surface are sealed to ensure one-dimensional diffusion (Hall, 1977). Subsequently, the sealed specimen is exposed to NaCl solution for a long-term (at least 35 days) one-dimensional diffusion. At the end of testing age, the specimen is taken out and ground into powder layer by layer. After that, the total and/or free chloride content of each layer can be obtained by leaching methods (AS 1012.20.1, AS 1012.20.2, ASTM C1152, ASTM C1218, AASHTO T260, BS EN 196-2 and JTJ270-98) to obtain the chloride profile. Because bound chlorides are fully removed from pore solution and not available for inducing or enhancing corrosion of reinforcement steel, free chloride content is more recommended rather than total chloride content. Despite that, total chloride content is still measured in many experiments and standards to ensure the safety and reliability of design. Based on the chloride profile, the chloride diffusion coefficient (D) can be determined by fitting Fick's second law (Equation 9 and 10).

Bulk diffusion test is known as accelerated chloride diffusion test (ACD), in which the specimen is immersed in concentrated NaCl solution ($165 \pm 1 \text{ g/L}$), as shown in

Fig.2-6C. Although the high NaCl concentration in bulk diffusion test is much higher than the normal concentration of sea water (around 3.5%), the test time can be shortened to 35 days (ASTM C1556 and NT BUILD 443). Based on bulk diffusion test, some studies (Babae & Castel, 2018; Bondar et al., 2019; Bondar et al., 2018; Tennakoon et al., 2017) found that AAS and AAFS with 40% or higher GGBFS content had the lower chloride diffusion coefficient (D) compared with OPC, and the D of AAFS decreased with increasing GGBFS content due to the finer pore structure of C-A-S-H gels. Compared with bulk diffusion test (ACD) using concentrated NaCl solution, natural chloride diffusion test (NCD) is applied in the actual or simulated marine environments to obtain more realistic results. Based on NCD applied in the actual marine environment, P Chindaprasirt and Chalee (2014) found that the D of AAFA decreased with increasing NaOH concentration (8-18 molar).

The experiment setup of ponding test is relatively complex (Fig.2-6D). This test requires the slab with a surface area of greater than 0.030 m² and a thickness of 90 ± 15 mm (ASTM C1543 and AASHTO T259). The sides of slab are sealed and a dike (around 20 mm) is provided on the top surface to retain NaCl solution. During ponding test, 3% NaCl solution is ponded on the top surface (15 ± 5 mm) for 90 days, while the bottom surface is exposed to the drying environment (relative humidity of 50%). After that, the powder is obtained by coring and grinding to obtain the chloride profile. Based on ponding test, Ismail, Bernal, Provis, San Nicolas, et al. (2013) found that the D of AAFS with 50% GGBFS content significantly decreased (from 1.71 × 10⁻¹² m²/s to 0.02 × 10⁻¹² m²/s) with the prolonged curing age (from 28 days to 90 days), indicating that the maturity of reaction products had a significant effect on chloride transport.

2.3.2 AAM VS. OPC

Table 2-3 summarizes the recent studies on the chloride resistance of AAMs (pastes, mortars and concretes) based on different testing methods, as well as the comparison of chloride resistance between AAMs and OPC. Because different precursors, activators and other parameters (e.g. admixtures), the corresponding results were quite different. In the table, “Mixed” means that AAMs with various mix proportions exhibited a range of chloride resistance and the chloride resistance of OPC was within this range. In other words, some but not all mixtures exhibited the better

chloride resistance compared to OPC.

Table 2-3 Recent studies on chloride resistance of AAMs (pastes, mortars, and concretes) based on different testing methods, as well as comparison of chloride resistance between AAMs and OPC.

Testing Methods	Precursor(s)	Activator(s)	Parameter(s)	CRTO	Ref.
Pastes					
Chloride diffusion test (5%, 10%, 15% and 20% NaCl solution)	MK	Na ₂ O·nSiO ₂	Other mineral materials	N/A	(Ren et al., 2017)
Chloride diffusion test (steady-state penetration test)	Binary (FA+GGBFS)	Na ₂ O·nSiO ₂	FA/GGBFS	Mixed	(Lee & Lee, 2016)
Chloride diffusion test (short-term ponding test with XRF)	Binary (FA+GGBFS)	Na ₂ O·nSiO ₂	FA/GGBFS	Mixed	(T. Yang et al., 2014)
Chloride diffusion test (saturated NaCl solution)	Binary (FA+GGBFS)	Na ₂ O·nSiO ₂	FA/GGBFS and w/b	Worse	(Zhu et al., 2014)
Mass loss	Binary (bagasse ash and China clay)	Na ₂ O·nSiO ₂	Bagasse ash/China clay	N/A	(Nawab & Ghani, 2017)
Mortars					
RCPT	FA	Na ₂ O·nSiO ₂	GGBFS, MK, or silica fume as a replacement (<15%), w/b, Ms and curing condition	Mixed	(Alanazi, Hu, & Kim, 2019)
			Ms and nano-SiO ₂	Mixed	(Adak, Sarkar, & Mandal, 2014)
			Nano-TiO ₂	N/A	(Maiti, Sarkar, Maiti, Malik, & Xu, 2020)
	GGBFS	NaOH, Na ₂ O·nSiO ₂ and Na ₂ CO ₃	Types of activators	Better	(Caijun Shi, 1996)
		Na ₂ O·nSiO ₂	Na ₂ O content and Ms	Better	(S. Fang, Lam,

					Li, & Wu, 2020)
	Binary (FA+GGBFS)	NaOH and Na ₂ O·nSiO ₂	FA/GGBFS, types of activators, Na ₂ O content, Ms and curing condition	N/A	(X. Hu et al., 2019)
			Types of activators and MgO	Better	(H. Yoon, Park, & Lee, 2018)
		Na ₂ O·nSiO ₂	Nano-SiO ₂	N/A	(Prakasam, Murthy, & Saffiq Reheman, 2020)
NSSM test	GGBFS	NaOH and KOH	Types of activators, w/b, silica fume and nano-SiO ₂	N/A	(Ramezianpour & Moeini, 2018)
		Na ₂ O·nSiO ₂ and Na ₂ CO ₃	Types of activators and CLDH	N/A	(Ke, Bernal, Hussein, et al., 2017)
		Na ₂ CO ₃ and Na ₂ CO ₃ +NaOH	Activator content, Na ₂ CO ₃ /NaOH and slaked lime	Mixed	(Akturk & Kizilkanat, 2020)
	Binary (FA+GGBFS)	NaOH and Na ₂ O·nSiO ₂	FA/GGBFS, types of activators, Na ₂ O content, Ms and curing condition	N/A	(X. Hu et al., 2019)
		Na ₂ O·nSiO ₂	FA/GGBFS	Better	(Ismail, Bernal, Provis, San Nicolas, et al., 2013)
			MgO, Mg-Al-NO ₃ LDH and CLDH	Better	(T. Liu, Chen, Yu, Fan, & Brouwers, 2020)
Chloride diffusion test (bulk diffusion test)	FA	Na ₂ O·nSiO ₂	Binder content	Worse	(Asprogerakas, Koutelia, Kakali, & Tsivilis, 2014)
	GGBFS	NaOH and KOH	Types of activators, w/b, silica fume and nano-SiO ₂	N/A	(Ramezianpour & Moeini, 2018)
	Binary (FA+GGBFS)	Na(K) ₂ O·nSiO ₂	FA/GGBFS, w/b, Na/(Na + K), Na ₂ O	Mixed	(Babae & Castel, 2018)

			content and Ms		
Chloride diffusion test (ponding test)	Binary (FA+GGBFS)	Na ₂ O·nSiO ₂	FA/GGBFS	Better	(Ismail, Bernal, Provis, San Nicolas, et al., 2013)
Chloride diffusion test (saturated NaCl solution)	Binary (FA+GGBFS)	Na ₂ O·nSiO ₂	FA/GGBFS and w/b	Worse	(Zhu et al., 2014)
Chloride diffusion test (10% NaCl solution)	Binary (FA+GGBFS)	NaOH and Na ₂ O·nSiO ₂	Types of activators and MgO	Better	(H. Yoon et al., 2018)
Corrosion behaviour	FA	Na ₂ O·nSiO ₂	SiO ₂ content	N/A	(María Criado, Bastidas, Fajardo, Fernández-Jiménez, & Bastidas, 2011)
			Ms	Worse	(Cecilia Monticelli et al., 2016)
				Better	(C Monticelli et al., 2016)
	Binary (FA+GGBFS)	Na(K) ₂ O·nSiO ₂	FA/GGBFS, w/b, Na/(Na + K), Na ₂ O content and Ms	Mixed	(Babae & Castel, 2018)
Concretes					
<i>RCPT</i>	FA	Na ₂ O·nSiO ₂	Ms	N/A	(Law, Adam, Molyneaux, Patnaikuni, & Wardhono, 2015)
			Ms and Nano-TiO ₂	N/A	(Sastry, Sahitya, & Ravitheja, 2020)
			Steel fiber	Almost equal	(Ganesan, Abraham, & Raj, 2015)
	FA and GGBFS	Na ₂ O·nSiO ₂	Types of precursors and Ms	Mixed	(R. Thomas et al., 2018)

	FA, GGBFS and MK	$\text{Na}_2\text{O}\cdot n\text{SiO}_2$	Types of precursors	N/A	(Gluth et al., 2020)
	GGBFS	$\text{Na}_2\text{O}\cdot n\text{SiO}_2$	Binder content, Na_2O content and Ms	N/A	(Ravikumar & Neithalath, 2013b)
			Na_2O content and Ms	Mixed	(Al-Otaibi, 2008)
			Na_2O content, Ms, curing temperature and curing time	N/A	(Balcikanli & Ozbay, 2016)
			Na_2O content H_3PO_4 and curing condition	Worse	(M. Chi, 2012)
			Ms	Comparable	(Law, Adam, Molyneaux, & Patnaikuni, 2012)
			Silica fume and nano- SiO_2	N/A	(Behfarnia & Rostami, 2017)
			Silica fume and curing condition	N/A	(Rostami & Behfarnia, 2017)
		Powder sodium silicate and NaOH	Na_2O content and Ms	N/A	(Ravikumar & Neithalath, 2013a)
	MK	$\text{Na}_2\text{O}\cdot n\text{SiO}_2$	Sodium silicate content	Better	(Júnior, Neto, Santana, Cilla, & Ribeiro, 2021)
	Calcined/uncalcined clay	$\text{Na}(\text{K})_2\text{O}\cdot n\text{SiO}_2$	Types of clay and w/b	Better	(Bondar, Lynsdale, Milestone, & Hassani, 2012)
	Binary (FA+GGBFS)	$\text{Na}_2\text{O}\cdot n\text{SiO}_2$	FA/GGBFS	Better	(A. Mehta, Siddique, Ozbakkaloglu, Shaikh, & Belarbi, 2020)
			FA/GGBFS and w/b	Better	(Tennakoon et al., 2017)
			FA/GGBFS, w/b, Na_2O content and Ms	Better	(Adam, 2009)

	Binary (GGBFS+MK)	$\text{Na}_2\text{O}\cdot n\text{SiO}_2$	GGBFS/MK and Na_2O content	N/A	(Bernal et al., 2012)
NSSM test	FA, GGBFS and MK	$\text{Na}_2\text{O}\cdot n\text{SiO}_2$	Types of precursors	N/A	(Gluth et al., 2020)
	GGBFS	$\text{Na}_2\text{O}\cdot n\text{SiO}_2$	Binder content, Na_2O content and Ms	N/A	(Ravikumar & Neithalath, 2013b)
		powder sodium silicate and NaOH	Na_2O content and Ms	N/A	(Ravikumar & Neithalath, 2013a)
	Binary (FA+GGBFS)	$\text{Na}_2\text{O}\cdot n\text{SiO}_2$	FA/GGBFS	Better	(Ismail, Bernal, Provis, San Nicolas, et al., 2013)
Chloride diffusion test (bulk diffusion test)	FA	$\text{Na}_2\text{O}\cdot n\text{SiO}_2$	Curing condition	Worse	(Noushini, Castel, Aldred, & Rawal, 2020)
			Types of FA	Better	(Kupwade-Patil & Allouche, 2013)
			Steel fiber	Almost equal	(Ganesan et al., 2015)
	FA, GGBFS and MK	$\text{Na}_2\text{O}\cdot n\text{SiO}_2$	Types of precursors	N/A	(Gluth et al., 2020)
	GGBFS	$\text{Na}_2\text{O}\cdot n\text{SiO}_2$	Binder content, w/b, Na_2O content and Ms	Better	(Bondar et al., 2018)
			Na_2O content and Ms	Better	(Q. Ma et al., 2016)
			Activator dilution	Better	(Mangat & Ojedokun, 2019)
			Copper slag as fine aggregate	Better	(Mithun & Narasimhan, 2016)
	Calcined/uncalcined clay	$\text{Na}(\text{K})_2\text{O}\cdot n\text{SiO}_2$	Types of clay and w/b	Better	(Bondar et al., 2012)
	Binary (FA+GGBFS)	$\text{Na}_2\text{O}\cdot n\text{SiO}_2$	FA/GGBFS and w/b	Better	(Tennakoon et

					al., 2017)
			FA/GGBFS, w/b, Na ₂ O content and Ms	N/A	(Bondar et al., 2019)
Chloride diffusion test (NCD)	FA	Na ₂ O·nSiO ₂	Na ₂ O content	N/A	(P Chindaprasirt & Chalee, 2014)
Chloride diffusion test (ponding test)	FA	Na ₂ O·nSiO ₂	Types of FA	N/A	(Chamila Gunasekara, Law, & Setunge, 2016)
				N/A	(C Gunasekara, 2016)
			Ms	N/A	(Law et al., 2015)
	FA and GGBFS	Na ₂ O·nSiO ₂	Types of precursors and Ms	Mixed	(R. Thomas et al., 2018)
	GGBFS	Na ₂ O·nSiO ₂	Types of coarse aggregate	Mixed	(Parthiban & Mohan, 2017)
	Binary (FA+GGBFS)	Na ₂ O·nSiO ₂	FA/GGBFS	Better	(Ismail, Bernal, Provis, San Nicolas, et al., 2013)
FA/GGBFS, w/b, Na ₂ O content and Ms			Better	(Adam, 2009)	
Chloride diffusion test (3% NaCl solution)	FA	Na ₂ O·nSiO ₂	Na ₂ O content and types of coarse aggregate	N/A	(Nuaklong, Sata, & Chindaprasirt, 2016)
Chloride diffusion test (5% NaCl solution)	GGBFS	Na ₂ O·nSiO ₂	Activator dilution	Worse	(Mangat & Ojedokun, 2020)
Electrical properties	FA and GGBFS	Na ₂ O·nSiO ₂	Types of precursors and Ms	Mixed	(R. Thomas et al., 2018)
	GGBFS	powder sodium silicate and NaOH	Na ₂ O content and Ms	N/A	(Ravikumar & Neithalath, 2013a)
Corrosion behaviour	FA	Na ₂ O·nSiO ₂	Types of FA	Better	(Kupwade-Patil & Allouche,

					2013)
				Mixed	(Chamila Gunasekara, Bhuiyan, Law, Setunge, & Ward, 2017)
			Na ₂ O content	N/A	(P Chindapasirt & Chalee, 2014)
	GGBFS	Na ₂ O·nSiO ₂	Na ₂ O content and Ms	Better	(Q. Ma et al., 2016)
	Binary (FA+GGBFS)	Na ₂ O·nSiO ₂	N/A	Comparable	(Babae & Castel, 2016)
			FA/GGBFS and w/b	Better	(Tennakoon et al., 2017)
Mass loss	FA	Na ₂ O·nSiO ₂	Silica fume	Better	(Okoye, Prakash, & Singh, 2017)
				N/A	(Jena, Panigrahi, & Sahu, 2019)

CRTO: chloride resistance compared to OPC

Mixed: chloride resistance of OPC is within the range of AAMs

w/b: water/binder ratio

Ms: silicate modulus, molar ratio of SiO₂/Na₂O

Based on the studies in Table 2-3, Fig.2-8 compares the chloride resistance of AAMs and OPC. The results of different testing methods showed that AAMs exhibited comparable or even better chloride resistance than OPC in most studies (84%). Therefore, as long as the mix proportion is suitable, AAMs can completely replace OPC to enhance the resistance of reinforced concrete structures in chloride-containing environments. Some mix proportions (e.g. pure FA system (Noushini et al., 2020) and high FA content (75%) in binary system (Babae & Castel, 2018)) exhibited lower chloride resistance than OPC. Therefore, the effect and optimal range of different parameters require to be further discussed in the following sections. Besides, some of the unsatisfactory results may be caused by inappropriate testing methods, e.g. RCPT (Balcikanli & Ozbay, 2016; X. Hu et al., 2019).

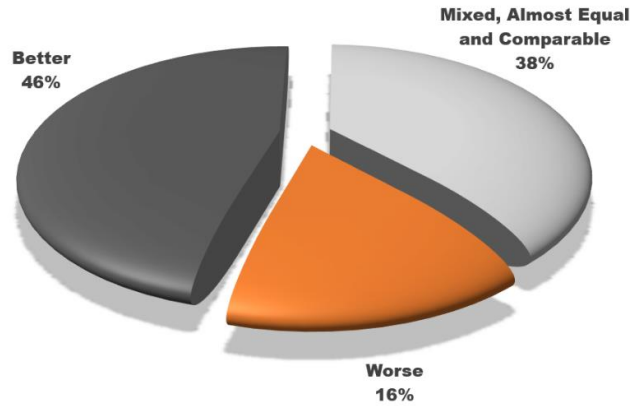


Fig.2-8 Chloride resistance of AAMs compared to OPC (CRTO).

2.4 ROLE OF PRECURSORS

From three aspects of technology, economy and environment, FA, GGBFS and MK are regarded as the most common precursors. In order to better understand the differences between these aluminosilicates, the SiO_2 - Al_2O_3 - CaO ternary diagrams of FA (Class F and Class C), GGBFS and MK, and the comparison of these aluminosilicates with silica fume (SF), Portland cement and fine limestone are shown in Fig.2-9. Besides, many other inexpensive materials and industrial wastes, e.g. heated coal gangue (Cheng et al., 2018), steel slag (Z. Liu et al., 2019), electric arc furnace slag (A. M. Rashad, Khafaga, & Gharieb, 2021), glass cullet (Y. Liu, Shi, Zhang, & Li, 2019), red mud (N. Ye et al., 2016) and rice husk ash (Kim, Lee, Saraswathy, & Kwon, 2014), were also attempted as precursors in AAMs.

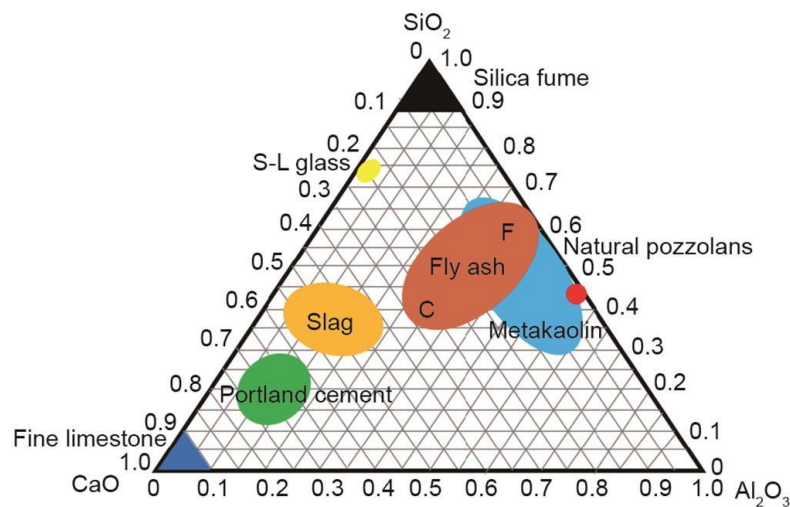


Fig.2-9 SiO_2 - Al_2O_3 - CaO ternary diagrams of FA (Class F and Class C), GGBFS, MK, SF, Portland cement and fine limestone (A. Wang et al., 2020).

The different physicochemical properties (e.g. chemical composition and fineness) and reaction products lead to different pore structure and chloride binding capacity, and hence different chloride resistance of AAMs. When different types of precursors are used, the high Ca content in GGBFS plays a key role to form C-A-H-S gels and improve chloride resistance. Gluth et al. (2020) compared the results of bulk diffusion test and NSSM test for AAFA, AAS and AAMK (Fig.2-10) and confirmed this view. As shown in Fig.2-10, the chloride diffusion/migration coefficient of AAS (around 1×10^{-12} m²/s) was approximately two orders of magnitude lower than that of AAFA and AAMK, which means the chloride resistance was greatly enhanced. Even if the same type of precursor is used, different chemical composition and fineness may still lead to different chloride resistance of AAMs, as described below:

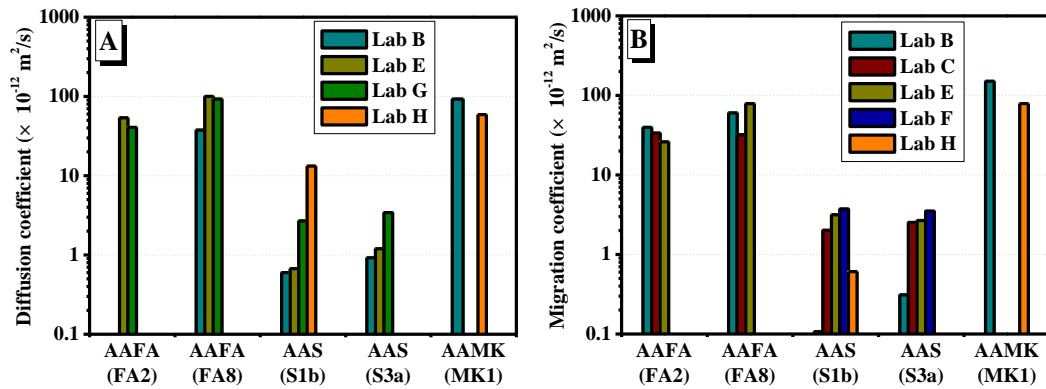


Fig.2-10 Results of (A) bulk diffusion test according to NT BUILD 443 and (B) NSSM test according to NT BUILD 492, adapted from (Gluth et al., 2020).

2.4.1 FA

Fly ash (FA), produced during the coal combustion in power stations, is a fine grey powder recognized as the industrial by-product and environmental pollutant (Ahmaruzzaman, 2010). FA consists mainly of spherical glassy particles and has pozzalonic properties, meaning that it can be applied as a supplementary cementitious material (Thorne & Watt, 1965; Watt & Thorne, 1965). The major chemical compositions of FA are SiO₂, Al₂O₃, CaO and Fe₂O₃. According to ASTM C618, FA can be classified into Class F (SiO₂+Al₂O₃+Fe₂O₃ \geq 70%) and Class C (50% \leq SiO₂+Al₂O₃+Fe₂O₃ < 70%). Besides, according to CaO content, FA can also be classified into low-calcium FA (LCFA, CaO < 10%) and high-calcium FA (HCFA,

CaO \geq 10%) (Papadakis, 1999, 2000). Nowadays, the majority of AAFA studies focus on Class F FA and LCFA. Thus, AAFA represents alkali-activated Class F FA or LCFA in this research if no specific instructions. High temperature curing (40–95°C) is required because the reactivity of FA at ambient temperature is extremely low (G. Fang et al., 2018; Puertas et al., 2000; Somna et al., 2011).

The chemical composition of FA, especially CaO content, has a certain impact on the chloride resistance of AAMs. Although it is commonly considered that the Ca from GGBFS can improve chloride resistance due to the formation of C-A-S-H gels, opposite results may be obtained in pure high-calcium FA system. Kupwade-Patil and Allouche (2013) evaluated the chloride resistance of AAFA manufactured from two types of Class F FA (OH: 1.97% CaO and DH: 5.00% CaO) and one type of Class C FA (MO: 12.93% CaO), as shown in Fig.2-11. At 352 days, the chloride diffusion coefficients of AAFA manufactured by OH, DH and MO were 1.45×10^{-12} , 9.83×10^{-12} and 1.87×10^{-11} m²/s, respectively. AAFA manufactured by high-calcium FA (MO: 12.93% CaO) exhibited a significantly lower chloride resistance than that of low-calcium FA (OH: 1.97% CaO and DH: 5.00% CaO). Previous investigation (Babae & Castel, 2018) indicated that when Ca content was low (e.g. pure or high FA systems), Ca²⁺ might be adsorbed in N-A-S-H gels through charge balance instead of forming C-A-S-H gels. Therefore, the chloride resistance of AAFA manufactured by high-calcium FA was lower due to more opportunities for Cl⁻ to react with Ca²⁺ to form CaCl₂.

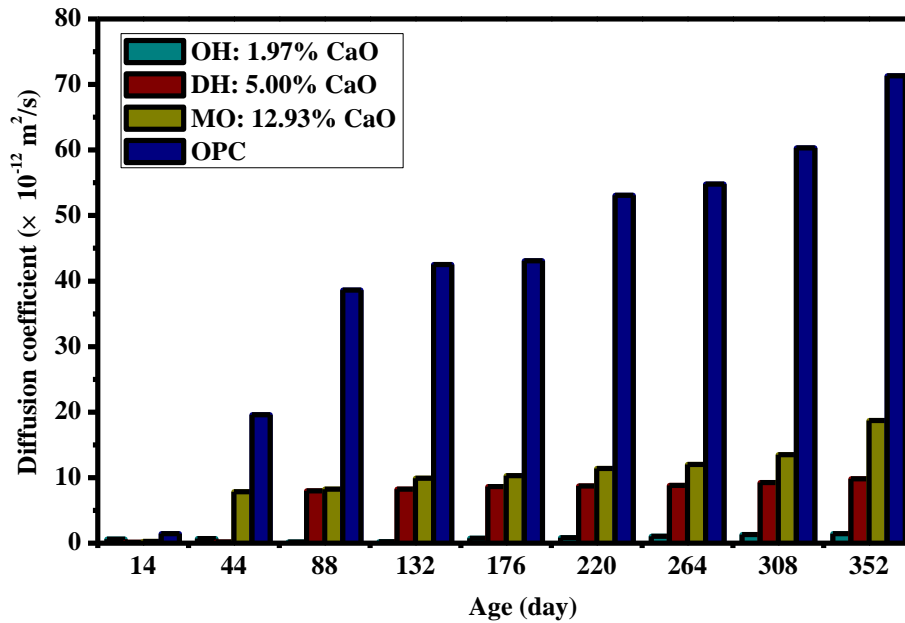


Fig.2-11 Chloride diffusion coefficients of AAFA and OPC specimens, adapted from (Kupwade-Patil & Allouche, 2013). OH: Class F FA with 1.97% CaO, DH: Class F FA with 5.00% CaO, MO: Class C FA with 12.93% CaO.

The fineness or particle size distribution of FA is also the key parameter affecting the chloride resistance of AAMs. Although the effect of the fineness of FA on chloride resistance has not been directly studied, Komljenović, Baščarević, and Bradić (2010) found that the higher content of fine FA particles (<43 μm) improved the compressive strength of AAFA. Therefore, the corresponding chloride resistance may also be improved. One possible reason is the reduction in total porosity and pore size, because of the finer gap between particles and the better solubility of SiO_2 and Al_2O_3 to produce more gels (Mucsi et al., 2015). S. Nath and Kumar (2020) compared the microstructure of AAFA with three size fractions ($D_{10} = 0.67, 0.40$ and $0.39 \mu\text{m}$) and found that non-reacted and non-bridged FA particles decreased with the decrease of particle size due to the formation of more gels to bind particles together (Fig.2-12), which is consistent with other researches (Prinya Chindaprasirt, Jaturapitakkul, Chalee, & Rattanasak, 2009; Mucsi et al., 2015).

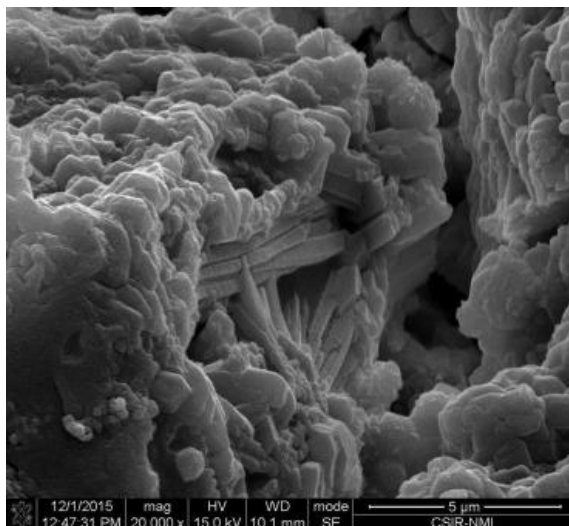
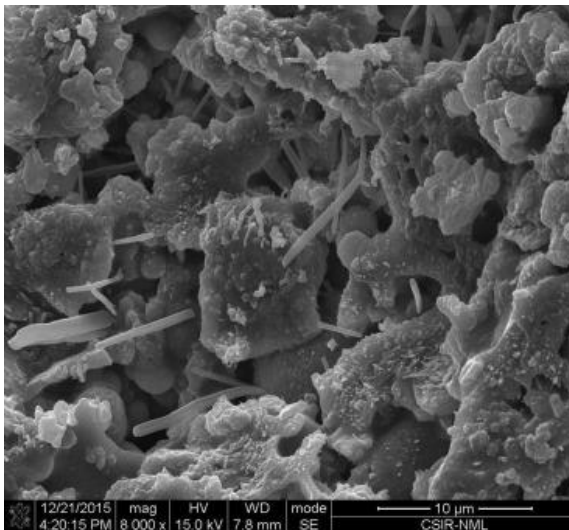
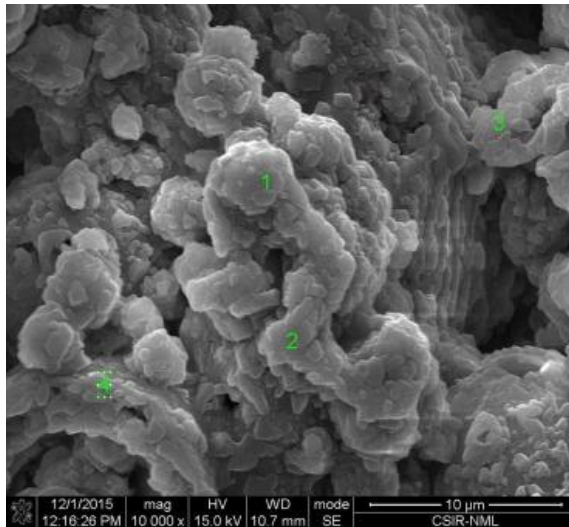


Fig.2-12 SEM micrographs of AAFA with different D_{10} (0.67, 0.40 and 0.39 μm), from (S. Nath & Kumar, 2020).

2.4.2 GGBFS

Ground granulated blast furnace slag (GGBFS), formed by earthy constituents of iron ore and limestone flux, is a by-product obtained in the iron and steel-making industry (Pal, Mukherjee, & Pathak, 2003). GGBFS has an almost fully non-crystalline glassy form with latent hydraulic properties, and thus is often used as an extender in OPC (Potgieter-Vermaak, Potgieter, Belleil, DeWeerd, & Van Grieken, 2006). The major chemical compositions of GGBFS are CaO, SiO₂, Al₂O₃ and MgO, with small amounts of Fe₂O₃ and SO₃. Compared with FA, GGBFS has the higher CaO content and faster reaction rate. Although high temperature curing is not required for AAS, some remaining limitations, e.g. poor workability, rapid setting, and excessive shrinkage, still exist (R. J. Thomas et al., 2016).

Both Ca and Mg content in GGBFS have significant affect to AAMs dominated by GGBFS. Gluth et al. (2020) found that the chloride diffusion/migration coefficients of AAS (pure GGBFS system) were around 1×10^{-12} m²/s, which were approximately two orders of magnitude lower than the results of AAFA and AAMK (Fig.2-10). Because of high Ca content in GGBFS (around 40% (Bondar et al., 2018; X. Hu et al., 2019; Ismail, Bernal, Provis, San Nicolas, et al., 2013)), C-A-S-H gels become dominant in AAS (John L Provis & Bernal, 2014). Thus, the finer pore structure leads to better chloride resistance of AAS compared to that of low-calcium systems. Haha, Lothenbach, et al. (2011) and Bernal et al. (2014) found that the higher MgO content in GGBFS promoted the formation of LDH (Fig.2-13), and hence resulted in larger hydrate volume and less total porosity. Moreover, Ke, Bernal, and Provis (2017b) claimed that LDH had high chloride binding capacity. Although C-A-S-H gels can also bind Cl⁻, they have a much lower binding capacity compared with LDH (Ke, Bernal, Hussein, et al., 2017; Ke, Bernal, & Provis, 2017a). Therefore, selecting GGBFS with high MgO content, which can lead to more LDH formed, may also improve chloride resistance by refining pore structure and enhancing chloride binding capacity.

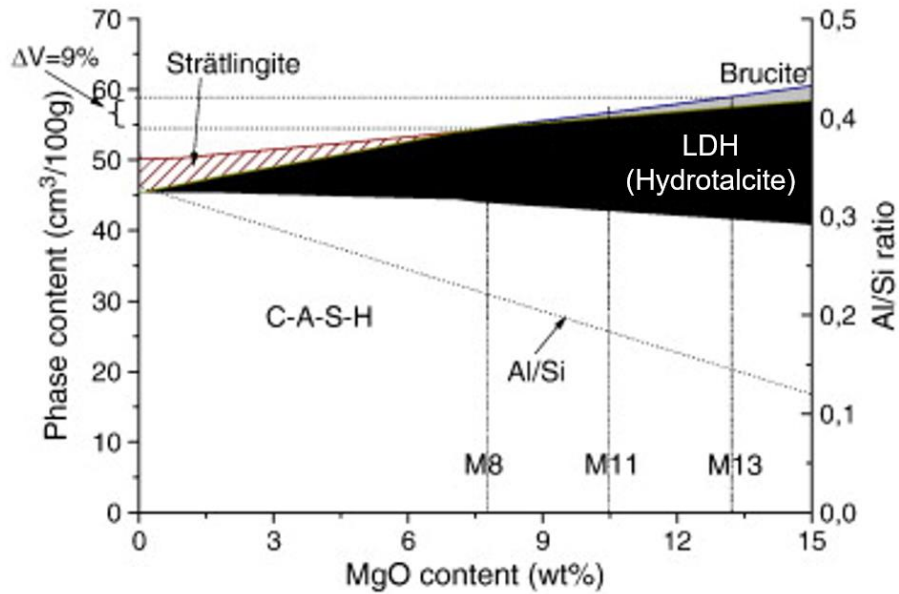


Fig.2-13 Influence of MgO content on the hydrates present in AAS, adapted from (Haha, Lothenbach, et al., 2011).

The optimization of the fineness of GGBFS is also helpful to improve the chloride resistance of AAMs. Although the effect of the fineness of GGBFS on chloride resistance has not been directly studied, Brough and Atkinson (2002) found that increasing GGBFS fineness (from 3320 cm²/g to 5500 cm²/g) led to an increase in mechanical strength (from 65 MPa to 100 MPa), which was linked to the lower total porosity and better chloride resistance (Vu et al., 2018). The reason may be that finer GGBFS particles led to higher packing density and larger reaction area to form more gels. However, Osio-Norgaard, Gevaudan, and Srubar III (2018) claimed that finer GGBFS particles with greater surface area and higher reactivity might lead to higher water demand and hence higher total porosity. Some authors reported that the optimum fineness of GGBFS for mechanical strength was 4000 cm²/g (Talling & Brandstetr, 1989) or 4000-5500 cm²/g (S.-D. Wang, Scrivener, & Pratt, 1994). Further research is required to determine the optimum fineness of GGBFS for chloride resistance.

2.4.3 MK

Metakaolin (MK), an amorphous aluminosilicate obtained by the calcination and dehydroxylation of kaolin (500-900°C), is one type of calcined clay with a distinct pozzolanic activity (Khatib, Baalbaki, & ElKordi, 2018; Panesar, 2019). During the

calcination, the loss of combined water leads to crystalline-to-amorphous structural changes, and hence increases the reactivity (Sabir, Wild, & Bai, 2001). Compared with 1450 °C in OPC, the production of MK has low CO₂ emission (Glavind, 2009). Therefore, MK has been used as the precursor in AAMs or supplementary material in OPC. Although the composition of MK varies with different types of kaolin, the major constituents are SiO₂ and Al₂O₃, and thus MK is considered as a relatively pure aluminosilicate. Compared with AAMs produced by FA and/or GGBFS, there are few researches on the chloride transport in AAMK (Gluth et al., 2020; Júnior et al., 2021; Ren et al., 2017).

The chemical composition of MK has a certain impact on chloride resistance. Although the composition of MK varies with different types of kaolin, MK can be considered as a relatively pure aluminosilicate, in which SiO₂ and Al₂O₃ are the main components. Because both AAMK and AAFA have low Ca content, the chloride diffusion/migration coefficients of them generally exhibited the similar values due to worse pore structure of N-A-S-H gels, which are approximately two orders of magnitude higher than AAS (Fig.2-10). Based on RCPT, Júnior et al. (2021) found that AAMK concrete showed greater total porosity but better chloride resistance compared to that of OPC concrete with the same w/b, possibly owing to high Al content and hence high chloride binding capacity of N-A-S-H gels. Osio-Norgaard et al. (2018) claimed that the higher Si content in MK or FA could lead to the continuing geopolymerization in N-A-S-H gels and lower total porosity, but the detrimental effect of this process on pore solution should also be considered. Davidovits (1999) recommended the optimal range for MK ($3.5 < \text{SiO}_2/\text{Al}_2\text{O}_3 < 4.5$, $0.2 < \text{Na}_2\text{O}/\text{SiO}_2 < 0.48$, $0.8 < \text{Na}_2\text{O}/\text{Al}_2\text{O}_3 < 1.6$) to achieve the excellent mechanical strength and durability. However, Pacheco-Torgal, Castro-Gomes, and Jalali (2008) claimed that what mattered most was the Si/Al in reactive phase, which was also affected by activator, rather than only original materials.

The fineness of MK may be also an important parameter for determining pore structure and thus chloride transport. Weng, Sagoe-Crentsil, Brown, and Song (2005) found that increasing the fineness of MK (from 1567 to 2555 cm²/g) led to the higher strength (from 55 MPa to 74 MPa), which was linked to the lower total porosity and better chloride resistance. Except for the role of packing density, the effect of higher

specific surface area, which results in more $[\text{Al}(\text{OH})_4]^-$ tetrahedral groups to attract negatively charged groups and hence more gels formed to refine pore structure, cannot be disregarded.

2.4.4 FA/GGBFS BINARY SYSTEM

To overcome the shortcomings of AAFA (high temperature curing) and AAS (poor workability, rapid setting and excessive shrinkage), FA/GGBFS binary system (AAFS) is proposed. In this binary system, FA/GGBFS determines the type of primary reaction products and thus chloride resistance. There is no doubt that the chloride resistance of AAFS is greater than that of pure FA system (AAFA). However, researchers still have different opinions on whether the chloride resistance of AAFS is better than that of pure GGBFS system (AAS). Some studies suggested that the coexistence of N-A-S-H and C-A-S-H gels might help to bridge the gaps between different hydrated phases and unreacted particles, and hence led to the finer pore structure and denser matrix (Bernal et al., 2013; Saha & Rajasekaran, 2017; Yip et al., 2005). However, more studies (Babae & Castel, 2018; Bondar et al., 2019; X. Hu et al., 2019; Ismail, Bernal, Provis, San Nicolas, et al., 2013; Lee & Lee, 2016; Tennakoon et al., 2017; T. Yang et al., 2014; Zhu et al., 2014) claimed that AAFS exhibited a lower chloride resistance compared with AAS, and the chloride resistance of AAFS increased with GGBFS content. This trend was obtained in RCPT (X. Hu et al., 2019), NSSM test (X. Hu et al., 2019; Ismail, Bernal, Provis, San Nicolas, et al., 2013), bulk diffusion test (Babae & Castel, 2018) and ponding test (Ismail, Bernal, Provis, San Nicolas, et al., 2013), which may be due to the finer pore structure and higher tortuosity of C-A-S-H gels than N-A-S-H gels (Babae & Castel, 2018; Ismail, Bernal, Provis, San Nicolas, et al., 2013; John L Provis, Myers, White, Rose, & van Deventer, 2012). Babae and Castel (2018) claimed that Ca^{2+} might be adsorbed in N-A-S-H gels through charge balance instead of forming C-A-S-H gels when GGBFS content was lower than 50%. Although the latter view seems more credible, the chloride resistance of AAFS and AAS requires further comparison, and the effect of FA/GGBFS ratio on chloride resistance of AAFS requires further analysis.

Based on the existing research results, the precursors are roughly arranged according to chloride resistance. The best type of precursor is GGBFS, which mainly benefits from the formation of less porous C-A-S-H gels. For the same reason, the chloride

resistance of FA/GGBFS binary system usually increases with the increase of GGBFS content. In AAFS, 40% or higher GGBFS content generally performs better (Babae & Castel, 2018; Bondar et al., 2019; Bondar et al., 2018; Tennakoon et al., 2017)). Because of the formation of porous N-A-S-H gels under low calcium conditions, AAMs produced by FA and MK generally exhibit a lower chloride resistance. Nevertheless, the chloride resistance of low-calcium system is still better than OPC in most cases (e.g. Fig.2-11). Besides, the chemical composition and fineness of different precursors also have significant impact on chloride resistance, which needs to be further studied. In general, GGBFS and FA/GGBFS binary system with high GGBFS content ($\geq 40\%$) are recommended.

2.5 ROLE OF ACTIVATORS

Unlike the hardening of OPC induced by only water, alkaline components are required in the activator of AAMs. Therefore, both w/b and alkaline components in activators have great influence on the chloride transport in AAMs.

2.5.1 WATER/BINDER RATIO

Generally, w/b can affect chloride transport by acting on capillary pores and chemical concentration. In OPC, w/b is widely perceived as the crucial influencing factor of pore structure and hence chloride transport (Goto & Roy, 1981; Page, Short, & El Tarras, 1981). Capillary pores are the remnants of initial water-filled space (Fig.2-2). Higher w/b leads to larger initial water-filled space and hence more capillary pores. Though the composition of activator is more complicated in AAMs, w/b may have the same function. In addition, more and larger pores due to higher w/b may also increase continuity and decrease tortuosity, leading to the acceleration of chloride transport (K. Yang, Yang, Magee, Nanukuttan, & Ye, 2016). Usually, there are more capillary pores around interfacial transition zone (ITZ) (Elsharief, Cohen, & Olek, 2003), as the main path for Cl^- penetration (Jiang, Sun, & Wang, 2013). In OPC, this phenomenon is perhaps due to the deficiency of unhydrated particles around ITZ (Elsharief et al., 2003). In AAMs, it is probably because of the phase evolution with a lower Ca content around ITZ (San Nicolas & Provis, 2015). Besides, higher w/b means lower alkalinity and lower chemical concentration in activator, which may have a negative influence on reaction degree. As a result, fewer

reaction products lead to the worse pore structure and lower chloride resistance of AAMs.

Based on the above mechanisms, w/b may have a certain impact on the chloride resistance of AAMs. However, the results in AAFA and AAS are controversial. Some studies (Škvára, Kopecký, Šmilauer, & Bittnar, 2009; Zhu et al., 2014) claimed that the higher w/b led to the lower chloride resistance of AAFA. Zhu et al. (2014) reported that Cl^- penetrated faster in AAFA pastes and mortars when liquid/solid ratio increased from 0.6 to 0.8, as shown in Fig.2-14. In their study, because the w/b was very high, the chloride resistance was very poor and lower than OPC. Therefore, w/b should not be higher than 0.5. However, Bondar et al. (2018) reported that w/b was ineffective in AAS. The excess water does not directly affect the pore structure and connectivity of AAS as it does for OPC, and therefore AAS can be designed based on the w/b needed for a specified mechanical performance (Bondar et al., 2018). Therefore, the effect of w/b on chloride resistance of AAFS requires further analysis.

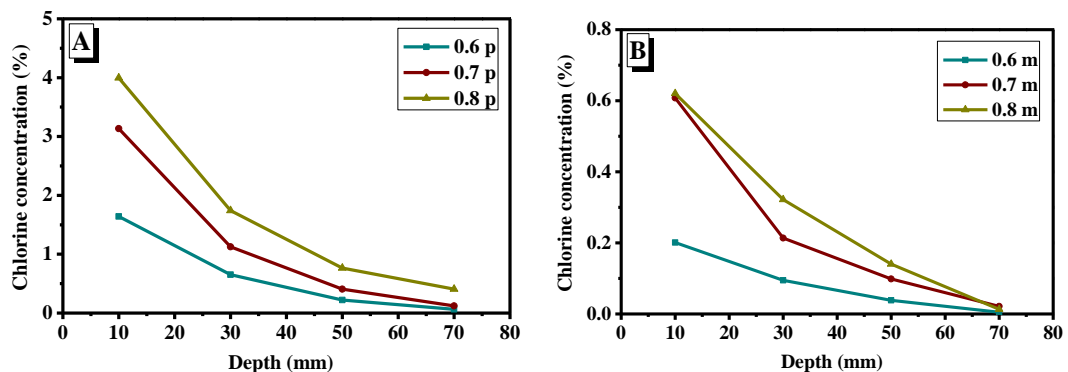


Fig.2-14 Chloride penetration in AAFA pastes (A) and mortars (B) with different w/b (0.6, 0.7 and 0.8) after 7 days of immersion, adapted from (Zhu et al., 2014).

2.5.2 ALKALINE COMPONENTS

The type and concentration of alkaline components determine the formation of gels, which can affect pore structure and chloride binding capacity of AAMs. At present, concentrated aqueous solutions of alkali hydroxides (e.g. NaOH and KOH) and sodium silicate ($\text{Na}_2\text{O} \cdot n\text{SiO}_2$) are conventional alkaline activators (John L Provis & Bernal, 2014). Sodium carbonate (Na_2CO_3) is also usually used, but the studies on chloride resistance of carbonate-activated mixes are limited. Besides, other activators,

e.g. $\text{Ca}(\text{OH})_2$ (Jeon, Jun, Jeong, & Oh, 2015), Na_2SO_4 (A. Rashad, Bai, Basheer, Milestone, & Collier, 2013) and solid silicates (Nematollahi, Sanjayan, & Shaikh, 2015), have been attempted.

2.5.2.1 ALKALI HYDROXIDES

NaOH and KOH are the commonly used hydroxide solutions as alkaline activators, which can be obtained by electrolysis of NaCl and KCl . Due to high cost and scarcity, other alkali hydroxides (e.g. LiOH , RbOH and CsOH) cannot be widely applied (John L Provis, 2009). Because no Si species in alkali hydroxide solution to promote the formation of gels, hydroxide-activated mixes normally have the worse pore structure and hence the lower chloride resistance compared with their silicate-activated counterparts (X. Hu et al., 2019; Caijun Shi, 1996). However, the viscosity of alkali hydroxide solution was considerably lower, leading to a more favourable workability (John L Provis & Bernal, 2014).

Generally, higher alkali concentration (OH^- concentration) can improve the chloride resistance of hydroxide-activated mixes. P Chindaprasirt and Chalee (2014) investigated the effect of NaOH concentration on chloride transport and chloride binding capacity of AAFA under actual marine site (Fig.2-15). With increasing NaOH concentration from 8 to 18 Molar, the D decreased from $6.2 \times 10^{-12} \text{ m}^2/\text{s}$ to $2.9 \times 10^{-12} \text{ m}^2/\text{s}$, while the bound chloride content increased from 14.3% to 30.8%. With higher alkalinity, more Si, Al and Ca components can dissolve from precursors due to the increasing breakage of bonds, e.g. T-O-T bonds (T = Si or Al) in FA and MK, and Si-O and Ca-O bonds in GGBFS. As a result, the reaction becomes more intense and more gels are formed, which can not only refine pore structure but also expand the surface area for Cl^- adsorption. It is noticed that the effect of alkali concentration on chloride binding capacity had a positive correlation with chloride resistance in Fig.2-15, which is different from the correlation of FA/GGBFS. It means that higher NaOH concentration only resulted in more gels, but did not change the phase composition of gels. However, higher alkali concentration may hinder the diffusion of Ca^{2+} from GGBFS and lead to a lower Ca/Si ratio in AAFS and AAS (Babae & Castel, 2018). As a result, more N-A-S-H gels instead of C-A-S-H gels are formed, leading to the lower chloride resistance. Therefore, the effect of NaOH concentration on chloride resistance of AAFS requires further analysis.

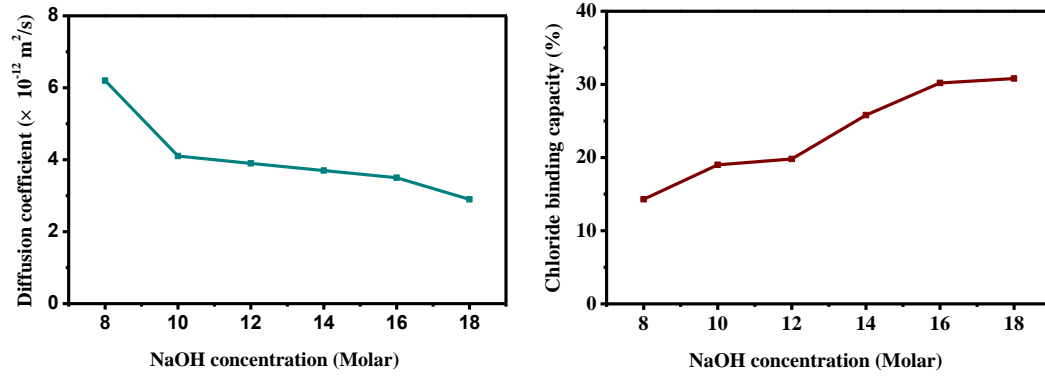


Fig.2-15 Effect of NaOH concentration on chloride diffusion coefficient and chloride binding capacity of AAFA concrete, adapted from (P Chindaprasirt & Chalee, 2014).

2.5.2.2 SODIUM SILICATE

Sodium silicate ($\text{Na}_2\text{O}\cdot n\text{SiO}_2$) solution is the most common alkaline activator of AAMs, which can be modified by dilution in deionised water or adding NaOH to change the silicate modulus (M_s , molar ratio of $\text{SiO}_2/\text{Na}_2\text{O}$) (Garcia-Lodeiro, Palomo, & Fernández-Jiménez, 2015). Due to high concentration, industrial grade waterglass usually cannot be directly used as activator. Therefore, to prepare $\text{Na}_2\text{O}\cdot n\text{SiO}_2$ solution with required Na_2O content and M_s as activator, NaOH, waterglass solution and water should be mixed in proportion. Besides, some researchers (Bondar et al., 2019) believed that SiO_2 content (Na_2O content $\times M_s$) rather than M_s should be considered as a parameter. For $\text{Na}_2\text{O}\cdot n\text{SiO}_2$ solution, Na_2O content can be regarded as alkali content (Babaee & Castel, 2018) or alkali dosage (X. Hu et al., 2019). Compared with alkali hydroxides (e.g. NaOH), $\text{Na}_2\text{O}\cdot n\text{SiO}_2$ can provide Si species to produce more reaction products.

Among different studies, the effects of Na_2O content and M_s (or SiO_2 content) were clear inconsistency. Normally, moderately increasing Na_2O content and M_s are considered beneficial in improving chloride resistance. Despite that, some studies obtained the opposite results. The most probable causes may be different chemical compositions in various precursors (especially Ca/Si ratio) and different w/b. Therefore, the effects of Na_2O content and M_s require to be combined with other parameters. Moreover, incorrect results caused by inappropriate testing methods (e.g. RCPT) should be valued. For example, X. Hu et al. (2019) found that higher Na_2O content and M_s led to the worse results of RCPT due to higher ion concentration of

pore solution, which were contrary to the actual situation.

2.5.2.2.1 ALKALI CONTENT

Usually, higher Na₂O content, which means higher alkali concentration, can lead to the better chloride resistance of AAMs. Most studies (Bondar et al., 2018; X. Hu et al., 2019; Q. Ma et al., 2016) agreed with the above viewpoint. X. Hu et al. (2019) investigated the effect of Na₂O content on D_{NSSM} and passed charge (6h) of AAFS mortars at 28 and 91 days (Fig.2-16). As shown in Fig.2-16A, with increasing Na₂O content from 2% to 8%, the 28-d D_{NSSM} gradually decreased from 2.95×10^{-12} m²/s to 1.26×10^{-12} m²/s, and the 91-d D_{NSSM} gradually decreased from 2.17×10^{-12} m²/s to 1.03×10^{-12} m²/s. Generally, the increase of Na₂O content can accelerate the activation of precursors. Because of higher alkalinity, more Si, Al and Ca components dissolve from precursors, and thus more gels are formed to refine pore structure and improve chloride resistance. However, Babae and Castel (2018) claimed that higher alkalinity hindered the diffusion of Ca²⁺ from GGBFS and thus limited the formation of C-A-S-H gels, leading to a low chloride resistance. It should be noted that higher Na₂O content may lead to the misleading result of RCPT due to more OH⁻ (Al-Otaibi, 2008; X. Hu et al., 2019). In contrast to other testing methods, the result obtained from RCPT is strongly affected by pore solution chemistry. Z. Shi, Shi, Wan, and Zhang (2018) found that the OH⁻ concentration of the extracted pore solution from AAS increased with the increase of Na₂O content. Furthermore, X. Hu et al. (2019) reported that the conductivity of the extracted pore solution from AAS increased from 16.84 S/m to 32.71 S/m with increasing Na₂O content from 2% to 8%. Therefore, higher Na₂O content may lead to higher OH⁻ concentration of pore solution and hence higher passed charge in RCPT. For example, as shown in Fig.2-16B, the total electrical charge at 28 and 91 days increased with the increase of Na₂O content from 4% to 8%, which is obviously inconsistent with the result of NSSM test (Fig.2-16A).

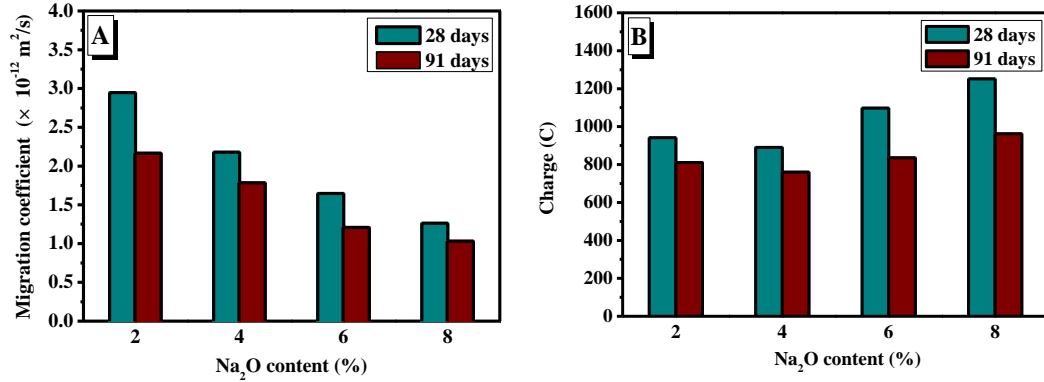


Fig.2-16 Effect of Na₂O content on (A) chloride migration coefficient (D_{NSSM}) and (B) passed charge (6h) of AAFS mortars, adapted from (X. Hu et al., 2019).

Although higher Na₂O content is generally beneficial, the maximum Na₂O content should be limited to 8% to avoid the undesirable efflorescence due to excessive free alkali ions in pore solution (Babae & Castel, 2018; Z. Zhang, Provis, Reid, & Wang, 2014). According to the existing research results (Babae & Castel, 2018; Bondar et al., 2018; X. Hu et al., 2019), the chloride resistance of AAMs with 4%-8% Na₂O content was generally good.

2.5.2.2.2 SILICATE MODULUS

The effects of Ms (or SiO₂ content) among different studies are controversial. The interference of different w/b should be considered. For example, Bondar et al. (2018) reported that when w/b = 0.47, AAS concrete with higher Ms showed a lower D in bulk diffusion test and the optimum Ms was around 1.5. When w/b = 0.55, although the D still decreased with the increase of Ms in AAS with low Na₂O content (< 5%), the opposite result was observed in AAS with high Na₂O content (> 5%) (Bondar et al., 2018). Besides, different Ca/Si ratios in various precursors may also lead to different effects of Ms. Some researchers (Babae & Castel, 2018; Law et al., 2015) considered that increasing Ms (or SiO₂ content) accelerated the chloride transport in AAMs. Babae and Castel (2018) investigated the effect of Ms on the chloride resistance of AAFS mortars by bulk diffusion test, and found that increasing Ms from 1.0 to 1.5 increased the D of all mixtures (containing 25%, 50% and 75% GGBFS). One possible explanation is that more Si species from activator led to a lower Ca/Si ratio. As a result, the alkali reaction slowed down and more porous aluminosilicate gels were formed. However, more researches (Adam, 2009; Al-

Otaibi, 2008; X. Hu et al., 2019; Q. Ma et al., 2016; Ravikumar & Neithalath, 2013b) concluded that AAMs exhibited the better chloride resistance with the increase of Ms. For example, X. Hu et al. (2019) found that the D_{NSSM} of AAFS mortars at 28 and 91 days gradually decreased with the increase of Ms (Fig.2-17A). With increasing Ms from 0 to 1.5, the 28-d D_{NSSM} decreased from $3.22 \times 10^{-12} \text{ m}^2/\text{s}$ to $1.61 \times 10^{-12} \text{ m}^2/\text{s}$, and the 91-d D_{NSSM} decreased from $2.50 \times 10^{-12} \text{ m}^2/\text{s}$ to $1.24 \times 10^{-12} \text{ m}^2/\text{s}$. The reason may be that the precursors used in these studies had a relatively high Ca/Si ratio. Appropriately increasing Ms did not lead to too low Ca/Si ratio in mixtures, as well as significant changes in the type and microstructure of reaction products. Therefore, more Si species led to the formation of more reaction products, resulting in the finer pore structure and hence better chloride resistance of AAMs. Also note that higher Ms may lead to higher conductivity of pore solution, resulting in the misleading result of RCPT. Z. Shi, Shi, Wan, and Zhang (2018) reported that increasing Ms led to higher OH^- concentration of pore solution, which further led to higher passed charge. As shown in Fig.2-17B, the total electrical charge at 28 and 91 days increased with the increase of Ms from 0.5 to 1.5, which is inconsistent with the decrease of D_{NSSM} (Fig.2-17A). Besides, some researchers (Bondar et al., 2019) believed that considering SiO_2 content (Na_2O content \times Ms) was more reasonable than considering Ms alone. Bondar et al. (2019) considered that Ms should be adjusted with Na_2O content to reach 6% SiO_2 content, so as to achieve the best chloride resistance.

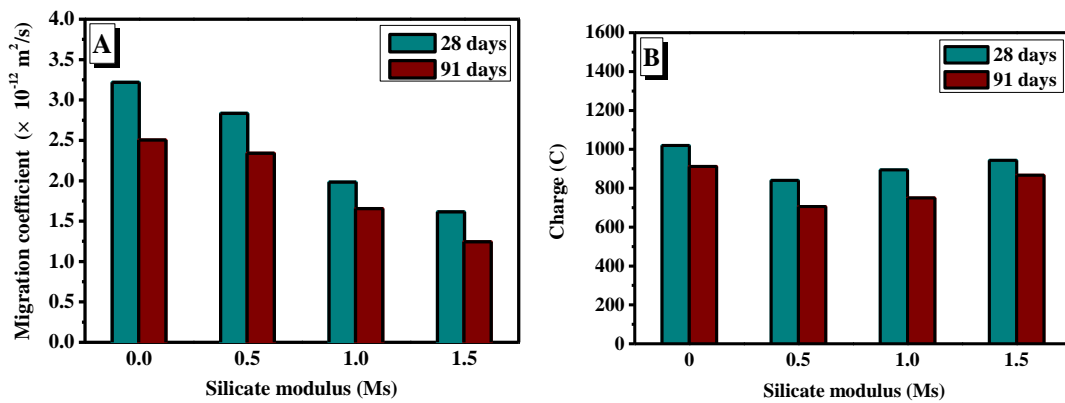


Fig.2-17 Effect of silicate modulus (Ms) on (A) chloride migration coefficient (D_{NSSM}) and (B) passed charge (6h) of AAFS mortars, adapted from (X. Hu et al., 2019).

Although the optimal Ms (or SiO_2 content) is not constant due to differences in w/b,

Na₂O content and chemical composition in precursor, a medium Ms in the range of 1 to 1.5 ensured a relatively good chloride resistance in most studies (Babae & Castel, 2018; Bondar et al., 2018; X. Hu et al., 2019). In this range, the chloride resistance of AAMs was generally good, and the influence of the change of Ms was relatively small (e.g. Fig.2-17A) to avoid large deviations. However, the optimal Ms (or SiO₂ content) in each mixture still needs to be found in future studies to improve the chloride resistance of AAFS and other AAMs as much as possible.

2.5.2.3 SODIUM CARBONATE

Although alkali hydroxides and sodium silicate are conventional activators, the production process of them leads to energy consumption and enlarges carbon footprint (Caijun Shi et al., 2003; Turner & Collins, 2013). Sodium carbonate (Na₂CO₃), as another activator, can provide many benefits in lower consumption and carbon footprint, as well as better workability (A. Abdalqader, Jin, & Al-Tabbaa, 2019). Despite that, Na₂CO₃ was mainly used for blending with other activators instead of being used individually (Cheah, Tan, & Ramli, 2019; Ishwarya, Singh, Deshwal, & Bhattacharyya, 2019). Compared with the studies focusing on the durability performance of hydroxide-activated mixes and silicate-activated mixes, the studies on the chloride resistance of carbonate-activated mixes are limited. In a few related studies, only GGBFS was activated in most cases (Akturk & Kizilkanat, 2020; Ke, Bernal, Hussein, et al., 2017; Caijun Shi, 1996).

Although relevant studies are limited, it is generally believed that carbonate-activated mixes have the lower chloride resistance compared with counterparts activated by NaOH and Na₂O·nSiO₂. Based on NSSM test, Ke, Bernal, Hussein, et al. (2017) found that carbonate-activated GGBFS mortars had a significantly higher D_{NSSM} than silicate-activated counterparts (Fig.2-18). At 180 days, the range of D_{NSSM} in carbonate-activated mixes was between $0.45 \times 10^{-12} \text{ m}^2/\text{s}$ and $1.00 \times 10^{-12} \text{ m}^2/\text{s}$, while the range of D_{NSSM} in silicate-activated mixes was between $0.35 \times 10^{-12} \text{ m}^2/\text{s}$ and $0.75 \times 10^{-12} \text{ m}^2/\text{s}$. At 28 and 90 days, the gaps were more obvious. The primary cause may be higher total porosity and larger pore size due to lower alkali content and hence the slow dissolution of precursors (Akturk & Kizilkanat, 2020; Akturk, Nayak, Das, & Kizilkanat, 2019; Ke, Bernal, Hussein, et al., 2017). To overcome this problem, Akturk and Kizilkanat (2020) reported that the incorporation of Ca(OH)₂ had a

remarkable effect on the microstructure and chloride migration resistance of carbonate-activated mixes. More efforts are still needed. Besides, low OH⁻ concentration in the pore solution of carbonate-activated mixes may lead to misleading results in RCPT. RCPT results showed that the chloride resistance of carbonate-activated mixes was excellent, even better than silicate-activated counterparts, which was seriously inconsistent with the fact (Caijun Shi, 1996).

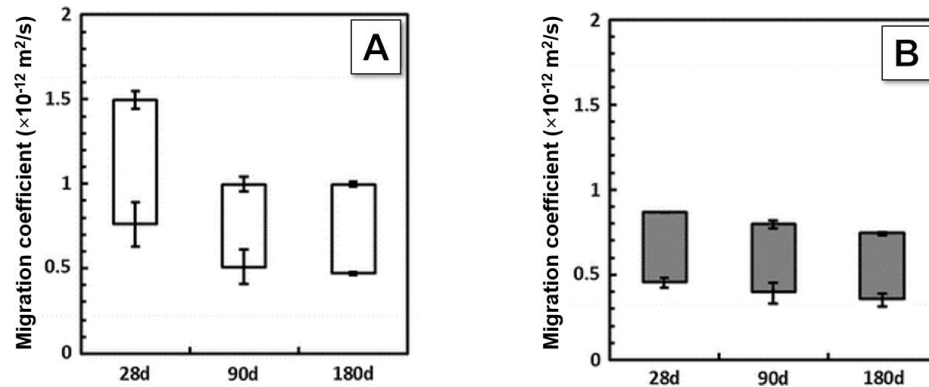


Fig.2-18 Chloride migration coefficient (D_{NSSM}) of (A) carbonate-activated and (B) silicate-activated GGBFS mortars at 28, 90, and 180 days, adapted from (Ke, Bernal, Hussein, et al., 2017).

Based on the existing research results, the activators are roughly arranged. Sodium silicate solution is the best alkaline activator that can resist chloride diffusion due to more Si species. The chloride resistance of hydroxide-activated mixes is usually lower than that of silicate-activated mixes (e.g. Fig.2-17A). The chloride resistance of carbonate-activated mixes is the worst and needs to be improved. The effect of different activators on pore solution chemistry may lead to misleading results of RCPT, which requires special attention. Generally, sodium silicate solution with 4%-8% Na₂O content and 1.0-1.5 Ms is the most recommended (Babae & Castel, 2018; Bondar et al., 2018; X. Hu et al., 2019). Besides, w/b should also be strictly controlled (≤ 0.5).

2.6 ROLE OF ADMIXTURES

Different admixtures with various physicochemical properties and reaction products can change the pore structure and chloride binding capacity, thus affecting the chloride resistance of AAMs. At present, silica fume, Mg-based admixtures (e.g. MgO and LDH), and nanoparticles (e.g. nano-SiO₂ and nano-TiO₂) are regarded as

the most common admixtures in AAMs and OPC. The main enhancing mechanism of these admixtures is the improvement of pore structure due to their pore-filling effect. Besides, more LDH formed by adding Mg-based admixtures can also improve the chloride binding capacity.

2.6.1 SILICA FUME

Silica fume (SF), also known as micro-SiO₂, is a by-product of producing elemental silicon or ferrosilicon, and has been utilized in OPC for decades (M. I. Khan & Siddique, 2011; Panesar, 2019). The major chemical composition of SF is SiO₂, with small amounts of Fe₂O₃, MgO and alkali oxides (Siddique, 2011). Although not as fine as nano-SiO₂ (<100 nm), the average particle size of SF (micro-SiO₂) is still pretty small (e.g. 229 nm in (Behfarnia & Rostami, 2017)). SF is highly effective in both OPC and AAMs. In OPC, it is found that moderate SF (<20%) could significantly improve chloride resistance, and the optimum addition was around 10% (M. I. Khan & Siddique, 2011; Perraton, Aiticin, & Vezina, 1988).

In AAMs, the effects of SF addition among different studies are inconsistency. The most probable causes may be different SiO₂, Al₂O₃, and CaO contents in mixtures, as well as different physicochemical properties of SF. Normally, it is considered that a relatively small quantity of SF addition can increase the chloride resistance of AAMs. Jena et al. (2019) found that AAFA concrete with 5% SF exhibited the excellent resistance to chloride attack. Based on NSSM test and bulk diffusion test, Ramezaniapour and Moeini (2018) investigated the effect of SF on the chloride resistance of AAFA and found that the 90-d D_{NSSM} decreased from 6.1×10^{-12} m²/s to 4.6×10^{-12} m²/s after adding 5% SF, while the 90-d D decreased from 5.7×10^{-12} m²/s to 5.5×10^{-12} m²/s. The small unreacted spherical SF can fill capillary pores and refine the pore structure. In addition, SF also provides more active SiO₂ to form siloxo bridges during the geopolymerization processing, which can firmly bind particles to form a denser matrix (Jithendra & Elavenil, 2020; Memon, Nuruddin, & Shafiq, 2013; ZX Yang, Ha, Jang, & Hwang, 2009). Adding excessive SF may be non-essential or even harmful. Alanazi et al. (2019) claimed that increasing SF from 5% to 10% reduced the alkalinity of activator and thus reduced the dissolution of FA with low activity, resulting in the more porous structure of AAFA. Besides, more Si species from SF may increase Si content, resulting in a lower Ca/Si ratio and hence

the formation of more porous aluminosilicate gels. However, it is found that AAS containing 10% SF (Behfarnia & Rostami, 2017) and 15% SF (Rostami & Behfarnia, 2017) still had excellent chloride resistance. Based on RCPT, Rostami and Behfarnia (2017) investigated the effect of SF addition on the chloride ion penetrability of AAS (Fig.2-17), and found that the total electrical charge at 28 days decreased from 2897C (moderate) to 1499C (low) with increasing SF from 0 to 15%, while the total electrical charge at 90 days decreased from 1923C (low) to 969C (very low). The most likely reasons are the high activity and high Ca content of GGBFS. Therefore, the adverse effects of reducing alkalinity and increasing Si content are relatively limited in AAS. The effect of SF on the chloride resistance of different AAMs and the corresponding optimum addition still require further analysis.

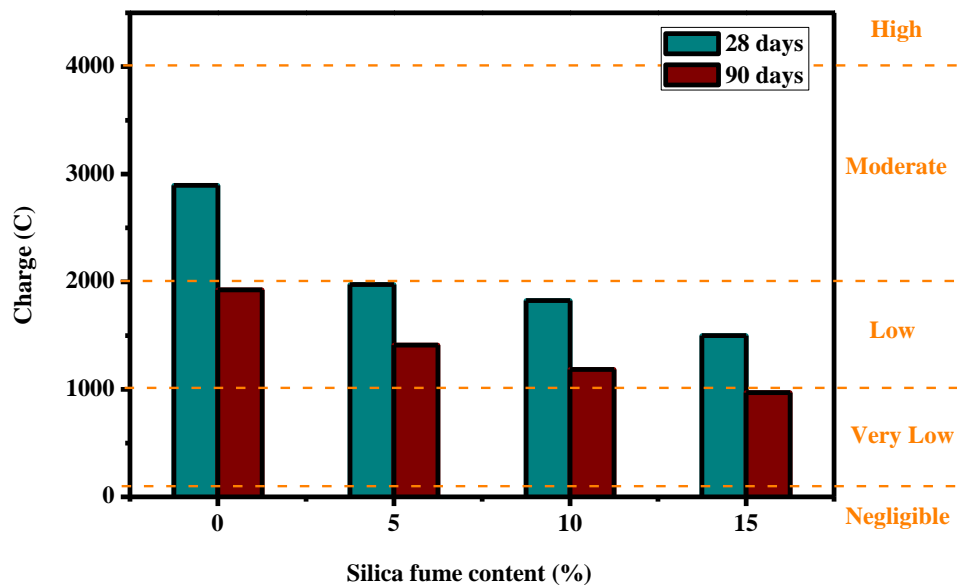


Fig.2-19 Effect of silica fume (SF) content on passing electric charge at 28 days and 90 days, , adapted from (Rostami & Behfarnia, 2017).

2.6.2 MG-BASED ADMIXTURES

Layered double hydroxides (LDH), also known as anionic clays, are a class of ionic lamellar compounds. The general formula of LDH is $[M^{2+}_{1-x}M^{3+}_x(OH)_2]^{x+}[A^{n-}_{x/n}]^{x-} \cdot mH_2O$, which consists of octahedral brucite-like layers (M^{2+} represents divalent metal cations, e.g. Mg^{2+} ; M^{3+} represents trivalent metal cations, e.g. Al^{3+} ; $x = 0.2-0.33$), non-framework charge compensating anions (A^{n-} represents n-valent anions, e.g. CO_3^{2-} , NO_3^- , Cl^- , and OH^-), and interlayer water molecules (X. Duan & Evans,

2006; R. Ma, Liu, Li, Iyi, & Sasaki, 2006; Q. Wang & O'Hare, 2012; M. Q. Zhao, Zhang, Huang, & Wei, 2012). The structure of LDH is schematically shown in Fig.2-20, which originates from a rhombohedral structure of the naturally occurring hydrotalcite, $Mg_6Al_2(OH)_{16}CO_3 \cdot 4H_2O$ (Hochstetter, 1842; Miyata, 1975; Miyata & Kumura, 1973; H. Taylor, 1973). As shown in Fig.2-20, the skeleton of LDH composed of octahedral brucite-like layers is positively charged with a charge density determined by the molar ratio of $M^{3+}/(M^{2+}+M^{3+})$, x . In the interlayer, anions (A^{n-}) are weakly bonded to the skeleton by hydrogen bonding, and thus can be exchanged by other anions (Z. Shui et al., 2018). The most common LDH is Mg-Al LDH, such as the naturally occurring hydrotalcite, Mg-Al- CO_3 LDH. LDH has been applied in a wide range of important areas, i.e. catalysis, photochemistry, electrochemistry, pharmaceuticals and ion-exchange/adsorption (X. Duan & Evans, 2006; Goh, Lim, & Dong, 2008). Tsyganok et al. (2003) claimed that LDH could be used as catalysis in the production of basic chemicals, as well as redox processes (Nishimura, Kakiuchi, Inoue, & Uemura, 2000) and acid-base processes (Roelofs, Lensveld, Van Dillen, & De Jong, 2001). Shimizu, Okubo, Nakamoto, Enomoto, and Kojima (2006) found that LDH could be useful photoresponsive materials due to the photodimerization and photoisomerization of interlayer anions. H. Chen et al. (2003) underlined the use of LDH as electrode for alkaline secondary cells. Gardner (1985) reported that LDH could be used in pharmaceutical formulations. Furthermore, because of relatively large surface area and high anion exchange capacity, LDH has been extensively studied for their potential to adsorb anionic contaminants, e.g. fluorine species (H. Wang et al., 2007), chlorine species (Lv et al., 2009), bromine species (Lv, Wang, Wei, & Cheng, 2008), iodine species (Fetter et al., 1997), 2,4-dichlorophenoxyacetate (Chao, Chen, & Wang, 2008), benzoate (Cardoso, Tronto, Crepaldi, & Barros Valim, 2003), phosphate (S.-L. Wang et al., 2007), chromate (S. Wang et al., 2006) and arsenate (L. Yang et al., 2006), from aqueous solutions.

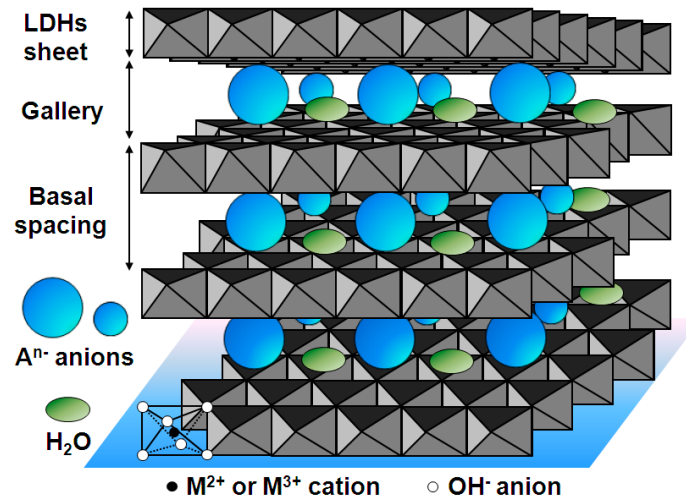


Fig.2-20 Structure of layered double hydroxides (LDH), from (Bi, Zhang, & Dou, 2014).

In AAS, Mg-Al LDH is often formed when $MgO > 5$ wt.% (Bernal et al., 2014; Haha, Lothenbach, et al., 2011; Ke et al., 2016). Besides, OH^- often acts as interlayer anions in hydroxide-activated and silicate-activated mixes due to the absence of CO_3^{2-} (Haha, Lothenbach, et al., 2011; Ke, Bernal, & Provis, 2018). The formation of Mg-Al LDH can refine pore structure of AAMs. Moreover, although the replacement order of anions in LDH is $CO_3^{2-} > OH^- > Cl^- > NO_3^-$ (D. G. Costa, Rocha, Souza, Chiaro, & Leitão, 2012), Ke, Bernal, et al. (2017b) claimed that surface adsorption was the main chloride binding mechanism (90%) of Mg-Al LDH rather than ion exchange. Therefore, Mg-Al-OH LDH and Mg-Al- CO_3 LDH formed in AAMs can still adsorb Cl^- . In this article, LDH represents Mg-Al LDH if no specific instructions. However, Ca-Al LDH (known as AFm phase or strätlingite) are also commonly observed secondary products in AAS, which can act as the same role in hindering Cl^- (Y. Chen, Shui, Chen, & Chen, 2015; L. Chi, Wang, Zhou, Lu, & Yao, 2018; Ke, Bernal, et al., 2017b; Qu, Yu, & Brouwers, 2018).

Inspired by the benefits of higher MgO content in GGBFS, the addition of Mg-based admixtures (e.g. MgO or synthetic LDH) is regarded as an effective method to increase LDH content in reaction products, and hence prevent the chloride transport in AAMs and OPC. Similar to MgO within GGBFS, additional MgO can also play a role of promoting the formation of LDH and improving chloride resistance. However, the formation of LDH is difficult to be controlled by adding MgO because the reaction can be affected by various parameters, e.g. the ratio of two metal ions (Y.

Chen et al., 2015). By comparison, the addition of synthetic LDH is a more direct approach. In OPC, the addition of MgO and synthetic LDH has been attempted. Choi, Jang, Kim, and Lee (2014) reported that the addition of 5% MgO decreased the capillary pores between 30 and 300 nm, and hence improved the chloride resistance of OPC. Z. H. Shui, Ma, Chen, and Gao (2012) found that Mg-Al-NO₃ LDH could not only refine pore structure of OPC but also adsorb Cl⁻ in pore solution. Besides, S. Yoon et al. (2014) claimed that calcined LDH (CLDH) added in OPC can rebuild layered double structure and hence improve chloride resistance.

In AAMs, MgO and synthetic LDH are also conducive to improve chloride resistance. Based on chloride diffusion test (10% NaCl solution for 91 days), H. Yoon et al. (2018) reported that a small quantity of MgO addition (<5%) can increase the chloride resistance of AAFS. As shown in Fig.2-21, with 5% MgO addition, the chloride penetration depth of hydroxide-activated mixes decreased from 4.4 mm to 3.6 mm, while the chloride penetration depth of silicate-activated mixes decreased from 3.9 mm to 3.5 mm. One possible reason is that MgO addition promoted the formation of LDH, which can refine pore structure, adsorb Cl⁻ and hence hinder chloride transport. However, H. Yoon et al. (2018) claimed that adding excessive MgO led to a higher extent of Cl⁻ penetration. With increasing MgO addition from 5 to 10%, the chloride penetration depth of hydroxide-activated mixes increased from 3.6 mm to 13.5 mm, while the chloride penetration depth of silicate-activated mixes increased from 3.5 mm to 4.0 mm (Fig.2-21). It may be due to larger threshold pore diameter, higher continuity and different pore solution composition (H. Yoon et al., 2018). Besides, it is noticed that the effect of MgO in hydroxide-activated mixes was more obvious than that in silicate-activated mixes, as shown in Fig.2-21. One explanation may be that less dissolved Si in hydroxide-activated mixes hindered the formation of gels. Therefore, more dissolved Al could be provided to form LDH.

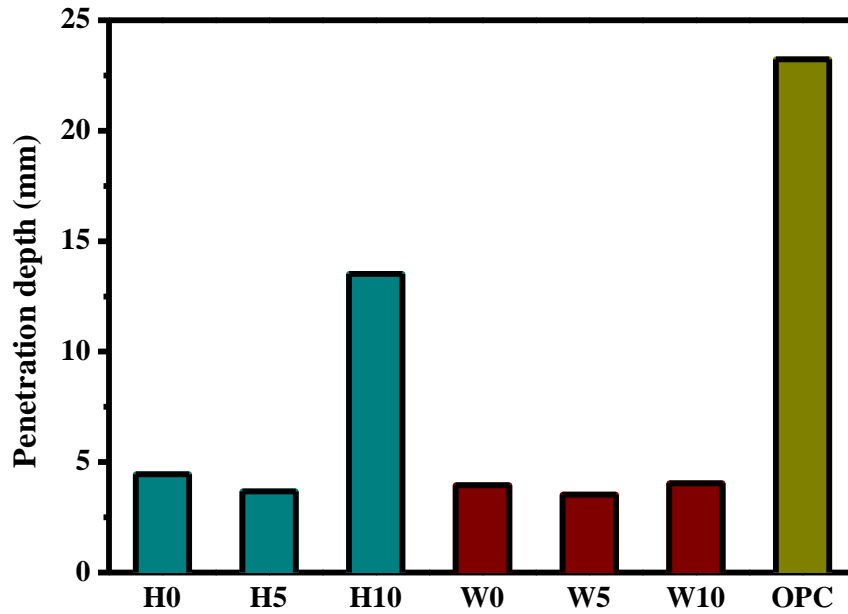


Fig.2-21 Chloride penetration depth of AAFS with different MgO addition (0, 5% and 10%) and OPC at 91 days, H-series denote the samples activated by NaOH, and W-series denote the samples activated by $\text{Na}_2\text{O} \cdot n\text{SiO}_2$, adapted from (H. Yoon et al., 2018).

Some researchers (Ke, Bernal, Hussein, et al., 2017; T. Liu et al., 2020) concluded that directly adding synthetic LDH also improved the chloride resistance of AAMs. T. Liu et al. (2020) found that AAFS with 4% CLDH had the lower D_{NSSM} ($2.88 \times 10^{-12} \text{ m}^2/\text{s}$) compared with MgO ($4.55 \times 10^{-12} \text{ m}^2/\text{s}$) and Mg-Al- NO_3 LDH ($4.49 \times 10^{-12} \text{ m}^2/\text{s}$), as shown in Fig.2-22. It may be related to the filler effect due to the restructure of LDH from CLDH. Besides, Ke, Bernal, Hussein, et al. (2017) claimed that 5% CLDH not only refined the pore structure but also enhanced the chloride binding capacity of carbonate-activated GGBFS, which even led to the higher chloride resistance than silicate-activated counterparts. However, according to the result of excessive MgO addition, it can be inferred that the addition of synthetic LDH should not be excessive.

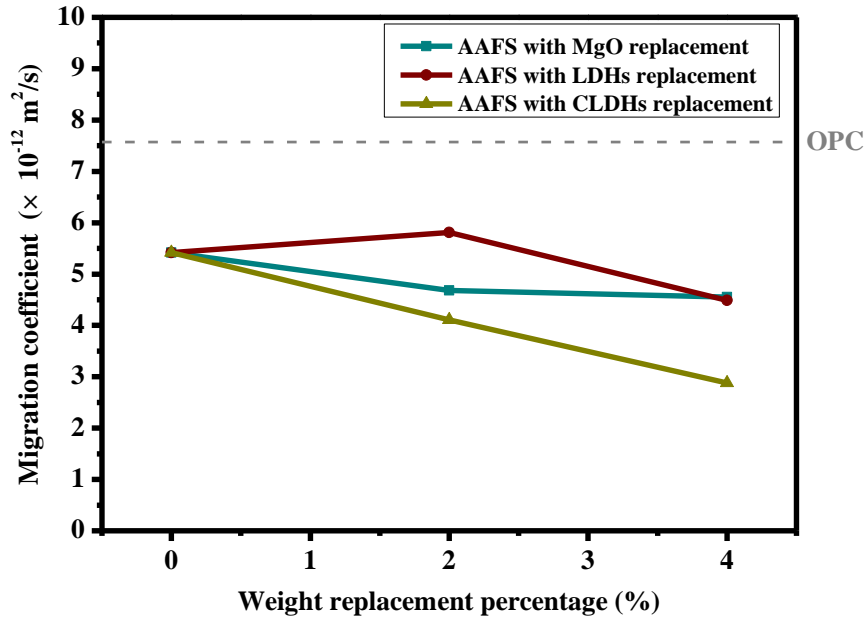


Fig.2-22 Effects of MgO, Mg-Al-NO₃ LDH and CLDH on chloride migration coefficient, adapted from (T. Liu et al., 2020).

The effect of Mg-based admixtures on chloride resistance of AAFS still requires further analysis. On the one hand, in addition to the benefit of Mg-based admixtures on pore structure, the possible benefit of Mg-based admixtures on the chloride binding capacity of AAFS also needs to be confirmed. On the other hand, Mg-Al-NO₃ LDH is usually used according to the replacement order of anions in LDH (CO₃²⁻ > OH⁻ > Cl⁻ > NO₃⁻). However, Mg-Al-NO₃ LDH needs to be prepared by a co-precipitation method (T. Liu et al., 2020), which is not suitable for the large-scale application in reality. Ke, Bernal, et al. (2017b) found that surface adsorption rather than ion exchange was the main chloride binding mechanism (90%) of Mg-Al LDH. Therefore, Mg-Al-CO₃ LDH, as the naturally occurring hydrotalcite, may also be able to adsorb Cl⁻, refine pore structure, and thus improve chloride resistance of AAFS. If this inference is confirmed, the large-scale application of LDH in reality can be realized.

2.6.3 NANOPARTICLES

Nanoparticles are small particles with diameters < 100 nm (Whitesides, 2005). Because of their extraordinary properties to improve pore structure, various nanoparticles (e.g. nano-SiO₂, nano-TiO₂, nano-Al₂O₃, nano-clay, and carbon nano-

tubes) are common admixtures applied in OPC to improve chloride resistance (Sanchez & Sobolev, 2010). In AAMs, the addition of nanoparticles (e.g. nano-SiO₂ and nano-TiO₂) is also tried to prevent Cl⁻ penetration. The enhancement of nanoparticles mainly depends on their nucleation and pore-filling effect (Fig.2-23). Besides, some nanoparticles (e.g. nano-SiO₂) may provide more active substances and larger active surface area to promote the alkali reaction of AAMs. However, excessive nanoparticles may lead to agglomerates, and the effective dispersion is also a difficult problem for the addition of nanoparticles.

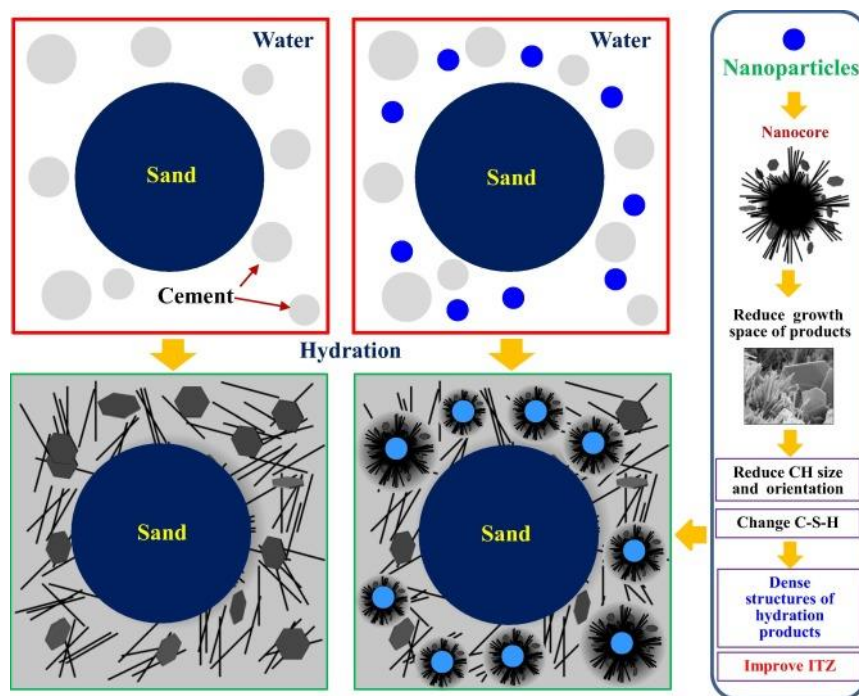


Fig.2-23 Enhancing mechanisms of nanoparticles, from (D. Wang, Zhang, Ruan, Yu, & Han, 2018).

2.6.3.1 NANO-SILICA

Nano-silica (nano-SiO₂) is the most common nanomaterial applied in AAMs and OPC. Normally, it is considered that a very small quantity of nano-SiO₂ addition can increase the chloride resistance of AAMs. Based on RCPT, Prakasam et al. (2020) investigated the effect of nano-SiO₂ addition on the chloride ion penetrability of AAFS, and found that the total electrical charge decreased from 4228C (high) to 1002C (low) with increasing nano-SiO₂ from 0 to 2%. Based on NSSM test and bulk diffusion test, Ramezaniapour and Moeini (2018) investigated the effect of nano-SiO₂ addition on the chloride resistance of AAS mortars, and found that the 90-d

D_{NSSM} decreased from $6.1 \times 10^{-12} \text{ m}^2/\text{s}$ to $4.8 \times 10^{-12} \text{ m}^2/\text{s}$ after adding 2% nano-SiO₂, while the 90-d D decreased from $5.7 \times 10^{-12} \text{ m}^2/\text{s}$ to $4.8 \times 10^{-12} \text{ m}^2/\text{s}$. The main reason may be the pozzolanic activity and pore-filling effect of nano-SiO₂ (Jindal & Sharma, 2020). The particle packing of nano-SiO₂ can lead to the wider distribution of binder particle size and hence the finer pore structure due to the higher packing density (Deb, Sarker, & Barbhuiya, 2016). Moreover, nano-SiO₂ can increase the soluble Si and promote the geopolymerization process (Deb, Sarker, & Barbhuiya, 2015). As a result, more gels are formed to refine pore structure and hence improve chloride resistance. Besides, nano-SiO₂ has the larger surface area with high reactivity, which can also accelerate the geopolymerization process (Deb et al., 2016). However, excessive nano-SiO₂ addition may be non-essential or even harmful. Phoo-ngernkham, Chindaprasirt, Sata, Hanjitsuwan, and Hatanaka (2014) found that the microstructures of AAFA pastes with 1–2% nano-SiO₂ addition had the denser matrix, but 3% nano-SiO₂ led to the less dense structure, which might accelerate the transport of Cl⁻ (Fig.2-24). It may be caused by the agglomeration of nano-SiO₂. Besides, porous aluminosilicate gels may be formed due to a lower Ca/Si ratio.

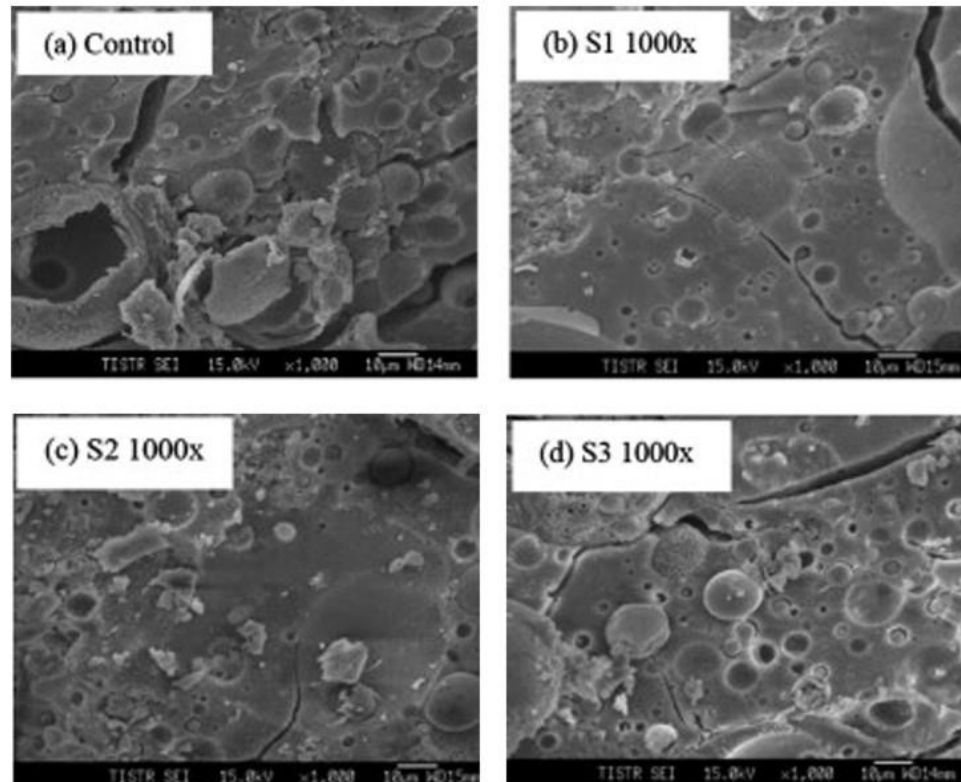


Fig.2-24 SEM micrographs of AAFA with different nano-SiO₂ addition (0, 1%, 2% and 3%), from (Phoo-ngernkham et al., 2014).

Despite that, different views on the quantity of nano-SiO₂ addition in AAMs were expressed. Adak et al. (2014) found that AAFA with a relatively high nano-SiO₂ content (6%) had the better chloride resistance. The possible reason is that AAFA had been dominated by N-A-S-H gels, so more Si species only led to the formation of more reaction products, but did not lead to more porous reaction products. On the contrary, Behfarnia and Rostami (2017) claimed that adding a very small quantity of nano-SiO₂ (0.5%) still decreased the chloride resistance of AAS. It may be due to the formation of a new phase named calcium silicate carbonate (Tilleyite) with a layered or laminate structure (Grice, 2005). Therefore, the effect of nano-SiO₂ on the chloride resistance of different AAMs and the corresponding optimum addition still require further analysis.

2.6.3.2 NANO-TITANIA

Nano-titania (nano-TiO₂) is also considered as a common nanomaterial to improve chloride resistance of AAMs and OPC. Normally, a very small quantity of nano-TiO₂ addition can achieve a good enhancement result. Based on RCPT in OPC, it is found

that the chloride resistance significantly increased with increasing nano-TiO₂ from 0 to 5% (Mohseni, Miyandehi, Yang, & Yazdi, 2015; Praveenkumar, Vijayalakshmi, & Meddah, 2019). Based on RCPT in AAFA, Sastry et al. (2020) found that the total electrical charge decreased from 2984C to 2016C with increasing nano-TiO₂ from 0 to 3%. P. Duan, Yan, Luo, and Zhou (2016) claimed that the conglomerations containing nano-TiO₂ as nucleus can expand and fill up the pore space around them, leading to the improvement of pore structure in AAFA. As shown in Fig.2-25, increasing nano-TiO₂ from 0 to 3% reduced the total porosity from 12.54% to 7.28%, and 1% nano-TiO₂ addition decreased the threshold pore diameter from 94 to 41 nm. However, Sastry et al. (2020) reported that AAFA with 4-5% nano-TiO₂ exhibited the higher chloride ion penetrability than the reference sample in RCPT, although they had the higher compressive strength and finer pore structure. It may be due to the higher concentration of pore solution, which leads to the increase of electrical conductivity of pore solution and passed charge, resulting in the worse RCPT result than the actual situation. Further study is required to establish the facts.

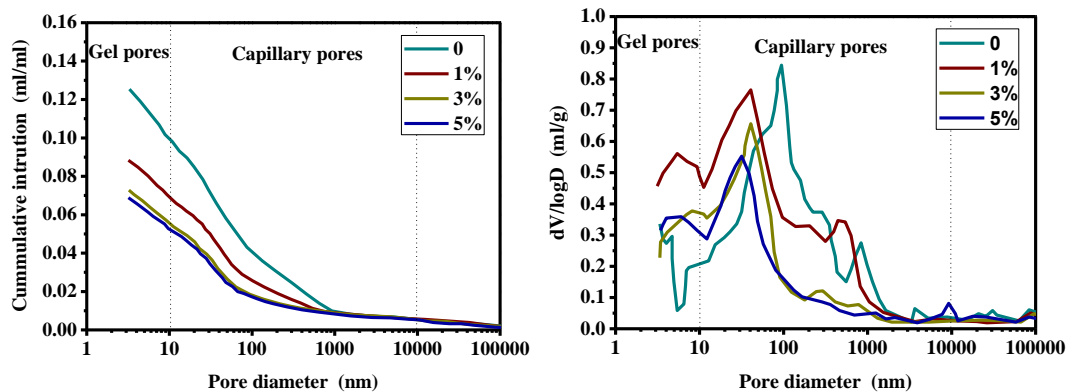


Fig.2-25 Porosity and pore size distribution of AAFA with different nano-TiO₂ addition (0, 1%, 3% and 5%) at 28 days, adapted from (P. Duan et al., 2016).

Based on RCPT, Maiti et al. (2020) investigated the effect of the size of nano-TiO₂ on the chloride ion penetrability of AAFA and found that decreasing the size of nano-TiO₂ from 100 nm to 30 nm reduced total electrical charge from 1515C to 555C (Fig.2-26). As shown in Fig.2-26, 5% nano-TiO₂ with the size of 100 nm changed the chloride ion penetrability from moderate to low, while 5% nano-TiO₂ with the size of 50 nm and 30 nm changed the chloride ion penetrability from moderate to very low. One possible reason is that nano-TiO₂ with the smaller size can fill voids

easier and hence result in higher chloride resistance.

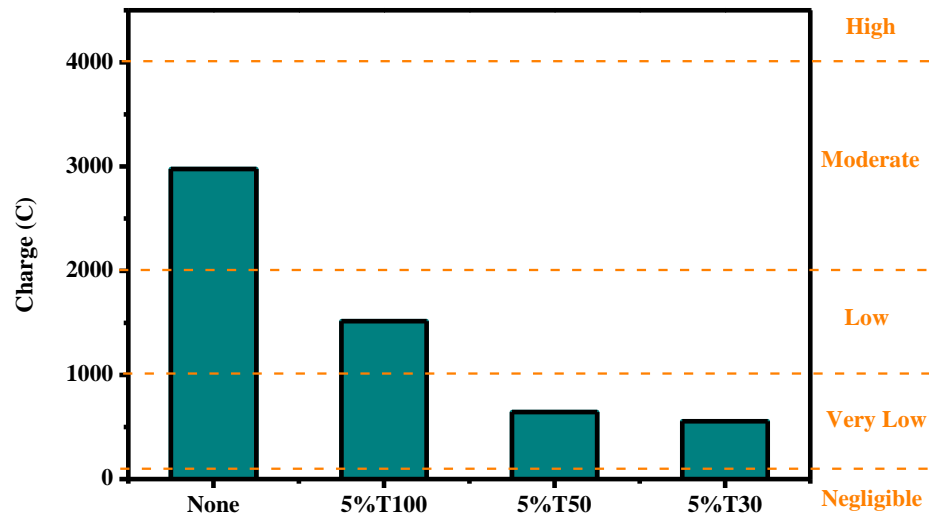


Fig.2-26 Rapid chloride permeability test (RCPT) of AAFA containing 5% nano-TiO₂ with different dimension (30, 50 and 100 nm), adapted from (Maiti et al., 2020).

Existing studies have shown that moderate admixtures can improve the chloride resistance of AAMs. Normally, the optimum addition amounts of SF, Mg-based admixtures (MgO, LDH and CLDH) and nanoparticles (nano-SiO₂ and nano-TiO₂) are in the range of 5%-15% (Behfarnia & Rostami, 2017; Jena et al., 2019; Ramezani-pour & Moeini, 2018; Rostami & Behfarnia, 2017), 4%-5% (Ke, Bernal, Hussein, et al., 2017; T. Liu et al., 2020; H. Yoon et al., 2018) and 2%-3% (Prakasam et al., 2020; Ramezani-pour & Moeini, 2018; Sastry et al., 2020), respectively. The exact value is not absolute and needs to be combined with the chemical composition in the mixture, which needs to be further studied.

2.7 CONCLUDING REMARKS

In this chapter, an existing knowledge system of chloride transport in AAFS and other AAMs is constructed. The roles of precursors, activators and admixtures on the chloride resistance of AAMs are summarized, and their influence mechanisms are explained from the aspects of phase evolution, pore structure, chloride binding capacity and pore solution. The advantages and limitations of current testing methods are addressed to explore the reliability of different previous results. By comparing the chloride resistance of OPC and AAMs with different parameters, the feasibility

of using AAFS and other AAMs with suitable mix proportions to replace OPC is confirmed. The optimum types and ratios of precursors, activators and admixtures are suggested for the future research and practical application of AAFS and other AAMs. The concluding remarks are as follows:

- 1) The ingress of Cl^- is mainly through the pore system of matrix. In a variety of transport mechanisms, ionic diffusion has the most dominant effect. The chloride transport in AAFS and other AAMs depends on pore structure, phase evolution, chloride binding capacity and pore solution. Among these influencing factors, pore structure acts as a decisive role in the paths of Cl^- . Chloride binding capacity can decrease free Cl^- in pore solution. Phase evolution determines pore structure and chloride binding capacity to some extent. Properties of pore solution also have a certain role on chloride transport, which require to be further investigated.
- 2) Most chloride transport tests in AAFS and other AAMs are based on the testing methods for OPC. When adopting the existing standards for chloride transport measurements, AAMs may present inaccurate results due to different pore solution and microstructure, especially when RCPT method is applied. Due to the neglect of continuous reaction and chloride binding, the applicability of NSSM test in AAMs needs to be further verified. Compared with rapid testing methods, chloride diffusion tests can better reflect the real chloride resistance of AAMs.
- 3) Most published results demonstrated that AAFS and other AAMs generally have better chloride resistance than OPC. The physical and chemical properties of precursors, as well as the type and concentration of alkaline components in activators are important parameters for the chloride resistance of AAMs. AAMs with low calcium content in precursor and high w/b may exhibit lower chloride resistance.
- 4) The physicochemical properties and reaction products of precursors affect the chloride resistance of AAFS and other AAMs. The finer pore structure of C-A-S-H gels enables the high-calcium system to present stronger chloride resistance than the low-calcium system. High MgO content in GGBFS leads to the formation of more LDH, which may hinder the transport of Cl^- . To ensure high chloride resistance, AAS and AAFS with high GGBFS content ($\geq 40\%$) are

recommended. Increasing the fineness of precursors can also improve the chloride resistance of AAMs.

- 5) As in OPC, w/b can affect the chloride transport in AAFS and other AAMs by capillary pores and should be controlled below 0.5. Chemical composition and concentration determine the formation of gels, thus further affect the chloride resistance of AAMs. Properly increasing alkali content usually promotes the dissolution of precursors and results in the better chloride resistance of AAMs. Compared with hydroxide solutions, sodium silicate solution with 4%-8% Na₂O content and 1.0-1.5 Ms has better effect. The optimal Ms (or SiO₂ content) is not absolute and needs to be combined with other parameters, which is necessary in future research. The chloride resistance of AAMs activated by Na₂CO₃ is relatively low.
- 6) Normally, the use of silica fume, Mg-based admixtures and nanoparticles can refine the pore structure and thus improve the chloride resistance of AAMs and OPC. Besides, the addition of MgO, LDH and CLDH can also enhance the adsorption of Cl⁻ in AAMs. Generally, 5%-15% SF, 4%-5% Mg-based admixtures (MgO, LDH and CLDH) and 2%-3% nanoparticles (nano-SiO₂ and nano-TiO₂) are recommended. The exact amount of admixture depends on the chemical composition in the mixture, which is the focus of future research.

2.8 RESEARCH GAPS

Although significant progresses have been made in previous studies, there are still many research gaps in the chloride resistance of AAFS and other AAMs, which are desired to be filled in order to apply them in actual reinforced concrete structures under chloride-containing environments.

- 1) Most previous studies were limited to short-term tests (e.g. RCPT, NSSM test and ACD). Due to joule heating and complicated pore solution chemistry, RCPT is not suitable for AAFS. NSSM test cannot reflect the actual effect of chloride binding. Moreover, the chloride resistance of AAFS may change greatly in the later stage, which cannot be measured by short-term tests. As the most reliable method to obtain more realistic results, natural chloride diffusion test (NCD) is

too time-consuming, so it has not been applied in AAFS concretes.

- 2) Although the effects of different parameters on the chloride resistance of AAFS have been roughly understood, an in-depth understanding of the influence mechanism of different parameters is still lacking. The microstructure of AAFS (e.g. phase evolution and pore structure) has not been well used to establish the relationship between different parameters and chloride resistance.
- 3) Studies concerning the chloride transport in AAFS mainly focused on early measurement results. Because the pore-filling effect of continuous reaction can improve the chloride resistance over time, these measurement results cannot establish the long-term prediction model to ensure the service life, which is an indispensable step before attempting to apply AAFS in practical engineering.
- 4) The chloride resistance of AAFS mixes modified by Mg-based admixtures were mainly evaluated by short-term tests (RCPT and NSSM test), which only focused on pore structure and could not consider chloride binding. Because Mg-based admixtures can greatly enhance the chloride binding capacity of AAFS, previous studies may not reflect the real situation. Chloride diffusion test is still needed to explore the real effect and influence mechanism of each Mg-based admixture in AAFS.

In view of the above four research gaps, studies in this project aim to provide new breakthroughs on the basis of previous progresses. which will be described in detail in Chapter 3-7.

CHAPTER 3: MIXTURE DESIGN AND ENGINEERING PROPERTIES OF ALKALI-ACTIVATED FLY ASH-SLAG SYSTEMS

*Note: the experimental results of AAFS concrete in this chapter are based on the manuscript entitled “Chloride diffusion in alkali-activated fly ash/slag concretes: Role of slag content, water/binder ratio, alkali content and sand-aggregate ratio”, by Jingxiao Zhang, Yuwei Ma, Jiazheng Zheng, Jie Hu, Jiyang Fu, Zuhua Zhang and Hao Wang, published in journal of **Construction and Building Materials**, 2020.*

3.1 INTRODUCTION

As described in Section 1.1.2, alkali-activated fly ash-slag (AAFS) system can overcome the shortcomings of alkali-activated fly ash (AAFA) and alkali-activated slag (AAS). However, the widespread application of AAFS concrete still requires the satisfaction of a series of performance criteria both from its engineering properties (e.g. workability and strength) and long-term stability. Compared with OPC, AAFA and AAS, the composition of AAFS is more complex. It means that the performance of AAFS can be affected by a series of parameters, e.g. FA/GGBFS, w/b, Na₂O content and SiO₂ content. As described in Section 1.1.2, significant efforts were made to explore the effect of different parameters on the engineering properties of AAFS.

As stated in Chapter 2 (Section 2.4.1 and Section 2.4.2), FA and GGBFS are highly variable materials. The expected performance of AAFS is largely dependent on the chemical composition, particle size distribution and phase composition of FA and GGBFS sources, as well as on the mix proportion of activator (e.g. w/b, Na₂O content and SiO₂ content) and other parameters (e.g. s/a in concrete and curing conditions). Despite all this, Fig.2-9 shows that although the chemical compositions of Class F FA and GGBFS fluctuate within a certain range, this is not very important compared with the difference in chemical compositions between them, especially Ca content. In AAFS, the total Ca content plays a key role in the type of reaction products and thus chloride resistance. Therefore, FA/GGBFS ratio is preferred, rather than their respective chemical components. Besides, the fineness of untreated FA and GGBFS does not fluctuate greatly. To change the fineness, FA and GGBFS need to be ground and sieved. This is not applicable to the large-scale production and application of AAFS in practical engineering. The optimal range of different

parameters (GGBFS content $\geq 40\%$, w/b ≤ 0.5 , 4%-8% Na₂O content and 1.0-1.5 Ms) has been recommended in Chapter 2. However, no “universal” mixture design exists for all types of FA and GGBFS. Before evaluating the chloride resistance, it is still necessary to characterize the raw materials and determine the practical AAFS concrete mixtures according to engineering properties (e.g. workability and strength).

This chapter presents a preliminary study on the mixture design of different AAFS pastes and concretes in the laboratory. As the most important parameters, FA/GGBFS ratio, water/binder ratio (w/b), Na₂O content, SiO₂ content and sand/aggregate ratio (s/a) are the main variables for the mixture design. Other parameters (e.g. binder/aggregate ratio, curing condition and curing temperature) are kept constant. First, the chemical composition, particle size distribution, morphology and phase composition of the FA and GGBFS used in this thesis are characterized. After that, different AAFS pastes are prepared and verified by compressive strength at early 28 days. Further, the current production process and test methods of OPC concrete are applied to different AAFA concretes. The workability of fresh concrete and compressive strength at different ages (up to 180 days) are determined to evaluate engineering properties and select a series of practical AAFS concrete mixtures.

3.2 MATERIALS

3.2.1 PRECURSORS

3.2.1.1 CHARACTERIZATION OF FA

Fly ash (FA) used in this study to manufacture AAFS paste and concrete is Class F FA (according to ASTM C618, SiO₂+Al₂O₃+Fe₂O₃ $\geq 70\%$) obtained from Zhongshan Power Station, Guangdong, China. Table 3-1 presents the chemical composition of FA determined by X-ray fluorescence (XRF). The loss on ignition (LOI) of FA was determined according to ASTM D7348. As shown in Table 3-1, the CaO content is 9.84%. Therefore, it also belongs to low-calcium FA (LCFA, CaO < 10%) (Papadakis, 1999, 2000). The Fe₂O₃ content is 6.92% and the LOI is 2.22%. These values meet the recommended values of FA for alkali activation (Fe₂O₃ content $\leq 10\%$ and LOI $\leq 5\%$) proposed by Fernández-Jiménez and Palomo (2003).

Table 3-1 Chemical composition of FA.

Oxide	SiO ₂	Al ₂ O ₃	CaO	Fe ₂ O ₃	MgO	SO ₂	Na ₂ O	K ₂ O	LOI ^a
Weight (%)	50.59	25.55	9.84	6.92	1.12	1.12	1.45	1.19	2.22

^a LOI is Loss on Ignition

The particle size distribution of FA measured by laser diffraction technique is shown in Fig.3-1. The D₁₀, D₅₀ (mean particle size) and D₉₀ of FA are 3.48 μm, 14.09 μm, and 46.55 μm, respectively.

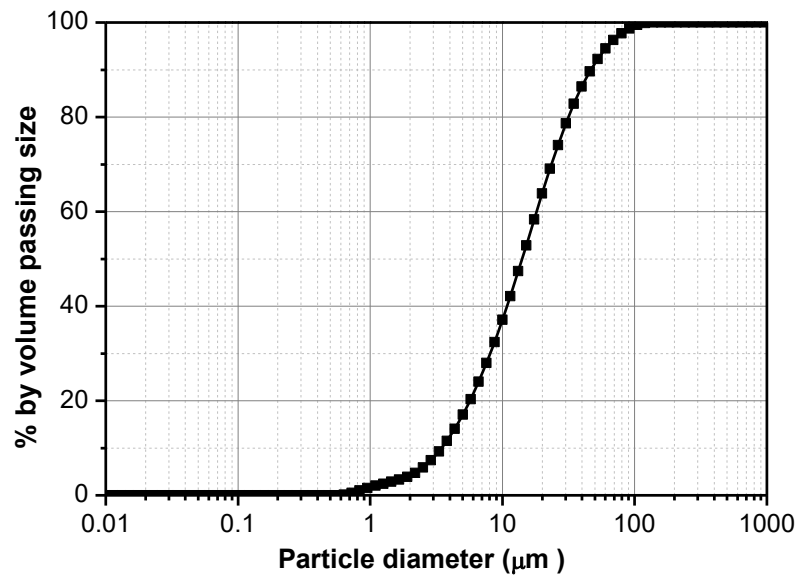


Fig.3-1 Particle size distribution of FA.

The morphology of FA investigated by scanning electron microscopy (SEM) is shown in Fig.3-2. As can be seen, most FA particles are spherical, but some irregular particles still exist, which may be the unburned carbon (Booher, Martello, Tamilia, & Irdi, 1994; T. Yang et al., 2018). Because of the microsphere capture occurred in the combustion zone, the coarse grains consist of a cluster of microspheres (Booher et al., 1994; T. Yang et al., 2018).

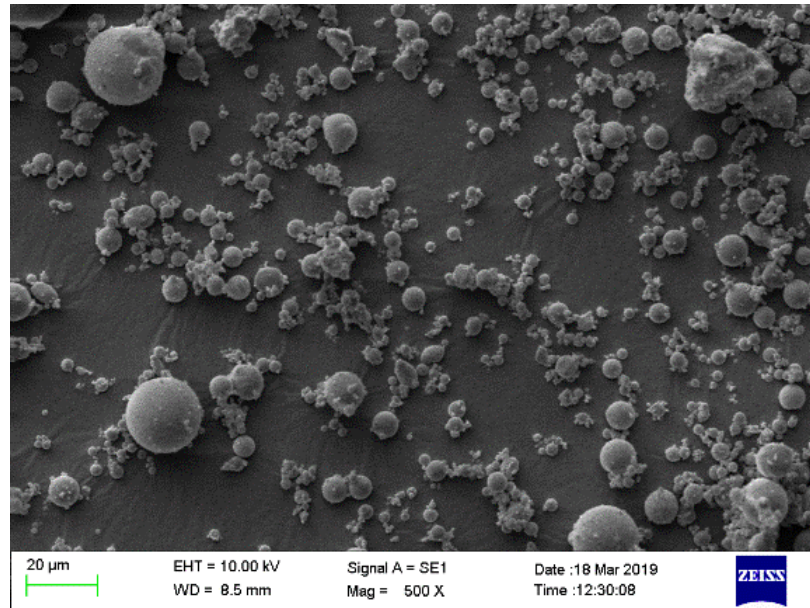


Fig.3-2 Morphology of FA.

FA is an amorphous material, which contains some minority crystalline phases such as quartz, mullite and hematite (Darmayanti, Notodarmojo, Damanhuri, Kadja, & Mukti, 2019). The X-ray diffraction (XRD) pattern of FA is shown in Fig.3-3. As can be seen, the major crystalline phases in FA are quartz (Q, SiO_2 , PDF# 46-1045) and mullite (M, $3\text{Al}_2\text{O}_3\cdot 2\text{SiO}_2$, PDF# 15-0776). The amorphous part in FA exhibits a bump between 17° and 38° 2θ .

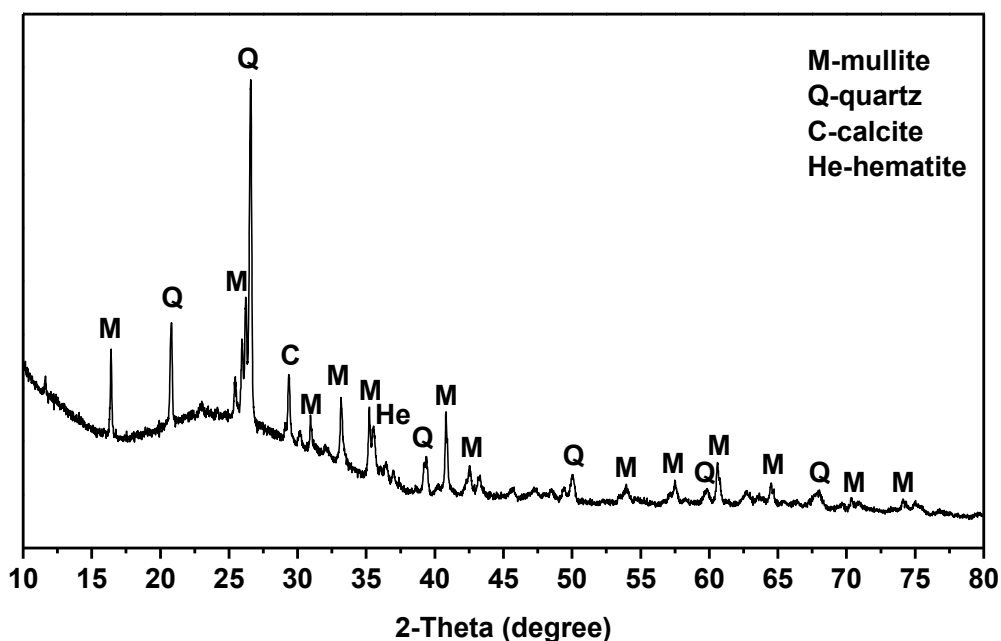


Fig.3-3 X-ray diffraction analysis of FA. M = mullite ($\text{Al}_6\text{Si}_2\text{O}_{13}$, PDF# 15-0776), Q = quartz (SiO_2 , PDF# 46-1045), C = calcite (CaCO_3 , PDF# 05-0586), He = hematite (Fe_2O_3 , PDF# 33-0664).

The FTIR spectrum of FA in the range of $2000\text{--}450\text{ cm}^{-1}$ is shown in Fig.3-4. It contains two main bands in the ranges of $1300\text{--}800\text{ cm}^{-1}$ (c) and $520\text{--}450\text{ cm}^{-1}$ (g), which are the indication of anti-symmetric stretching and bending vibrations of tetrahedral SiO_4 and AlO_4 groups, respectively (Pan, Tao, Cao, Wuhrer, & Murphy, 2018). The main absorption band between 1300 cm^{-1} and 800 cm^{-1} (c) is associated with the anti-symmetric stretching vibrations of Si-O-T bonds of SiQ_n units ($n = 4 - 0$), where T is referred to tetrahedral Si or Al (Lecomte et al., 2006; Lodeiro, Macphee, Palomo, & Fernández-Jiménez, 2009). SiQ_n units are the structural units in aluminosilicates, where n represents the degree of condensation of SiO_4 tetrahedra (Z. S. Wei & Zongjin, 2009). If $n = 0, 1, 2, 3$ and 4 , silicon is in the isolated mono-group (SiQ_0), disilicates and chain end groups (SiQ_1), middle groups in chains (SiQ_2), sheet sites (SiQ_3), and three-dimensional cross-linked sites (SiQ_4), respectively (Z. S. Wei & Zongjin, 2009; Y. Zhang, Sun, & Li, 2008). If there is no Al, the absorption bands corresponding to the Si-O-Si stretching vibrations of $\text{SiQ}_0, \text{SiQ}_1, \text{SiQ}_2, \text{SiQ}_3$ and SiQ_4 are located at $850, 900, 950, 1100$ and 1200 cm^{-1} , respectively (Clayden, Esposito, Aronne, & Pernice, 1999). Because of the extension of bond length and decrease in bonding force, replacing Si by Al can result in a lower wavenumber

(Fernández-Jiménez & Palomo, 2005). The band between 520 cm^{-1} and 450 cm^{-1} (g) is due to the bending vibration of in-plane Si–O in SiO_4 tetrahedra (García-Lodeiro, Fernández-Jiménez, Blanco, & Palomo, 2008; Ismail et al., 2014; Lecomte et al., 2006; Lodeiro et al., 2009; Pan et al., 2018; P. Yu, Kirkpatrick, Poe, McMillan, & Cong, 1999).

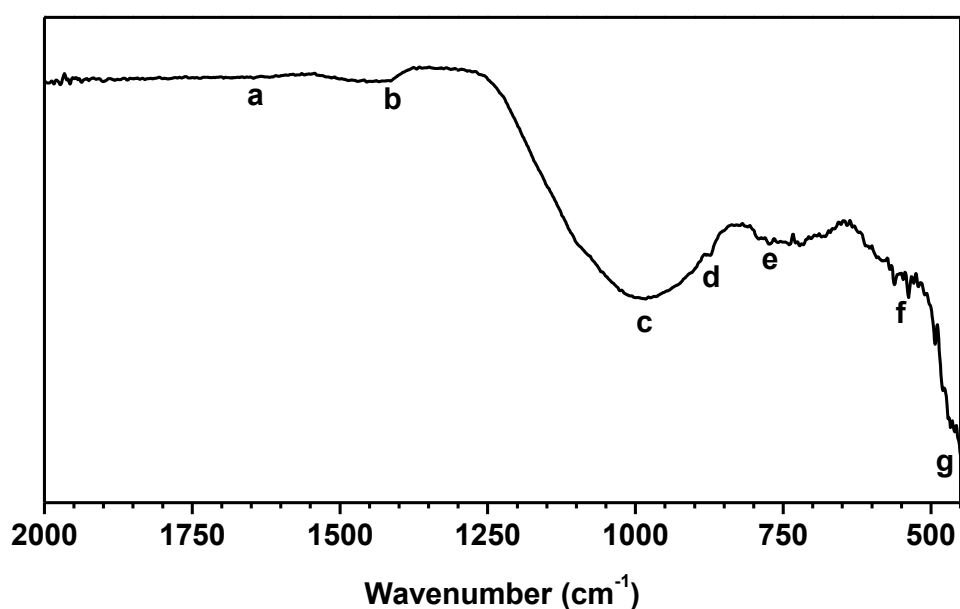


Fig.3-4 FTIR spectrum of FA.

In addition to the main bands, other bands can also provide important information. The FTIR band assignments of FA are summarized in Table.3-2. The very small absorption band at 1647 cm^{-1} (a) is observed, which is attributed to the bending vibration of H–OH bonds in bound water (Ismail, Bernal, Provis, Hamdan, & van Deventer, 2013b; Ismail et al., 2014; Lee & Lee, 2015; Z. Shi, Shi, Wan, Li, & Zhang, 2018). The asymmetric stretching vibration of O–C–O bonds in CO_3^{2-} groups at 1414 cm^{-1} (b) is also observed (García-Lodeiro et al., 2008; P. Yu et al., 1999), which is consistent with the calcite observed in the XRD pattern (Fig.3-3). The shoulder at 874 cm^{-1} (d) is related to the asymmetric stretching vibration of AlO_4^{4-} groups in the glass phases or out-of-plane bending vibration of CO_3^{2-} groups (García-Lodeiro et al., 2008; Ismail et al., 2014; P. Yu et al., 1999). The broad band at 983 cm^{-1} (c) and weak band at 791 cm^{-1} (e) correspond to the asymmetric stretching vibration and symmetric stretching vibration of Si–O–Si in quartz, respectively (Ismail et al., 2014; Pan et al., 2018). The band at 550 cm^{-1} (f) is

assigned to the octahedrally coordinated aluminium in mullite (Beran, Voll, & Schneider, 2001; Ismail et al., 2014; Pan et al., 2018). These results are consistent with the presence of quartz and mullite, as identified by XRD (Fig.3-3).

Table 3-2 FTIR band assignments of FA.

Band	Wavenumber (cm ⁻¹)	Assignment	Reference
a	1647	Bending vibration of H–O–H bonds in bound water	(García-Lodeiro et al., 2008; Lecomte et al., 2006; P. Yu et al., 1999)
b	1414	Asymmetric stretching vibration of O–C–O bonds in CO ₃ ²⁻ groups	(García-Lodeiro et al., 2008; P. Yu et al., 1999)
c	983	Anti-symmetric stretching vibration of Si–O–T bonds of SiQn units (n = 4 - 0), where T is referred to tetrahedral Si or Al	(Ismail et al., 2014; Lecomte et al., 2006; Z. Shi, Shi, Wan, Li, et al., 2018)
d	874	Asymmetric stretching vibration of AlO ₄ ⁻ groups or out-of-plane bending vibration of CO ₃ ²⁻ groups	(García-Lodeiro et al., 2008; Ismail et al., 2014; P. Yu et al., 1999)
e	791	Symmetric stretching vibration of Si–O–Si in quartz	(Ismail et al., 2014; Pan et al., 2018)
f	550	Octahedrally coordinated aluminium in mullite	(Beran et al., 2001; Ismail et al., 2014; Pan et al., 2018)
g	450	Bending vibration of in-plane Si–O in SiO ₄ tetrahedra	(García-Lodeiro et al., 2008; Ismail et al., 2014; Lecomte et al., 2006; Lodeiro et al., 2009; Pan et al., 2018; P. Yu et al., 1999)

3.2.1.2 CHARACTERIZATION OF GGBFS

Ground granulated blast furnace slag (GGBFS) used in this study to manufacture AAFS paste and concrete is obtained from Shaoguan Steel Group Company Limited, Guangdong, China. Table 3-3 presents the chemical composition of GGBFS determined by X-ray fluorescence (XRF). The major chemical compositions of GGBFS are CaO, SiO₂, Al₂O₃ and MgO. Compared with FA, GGBFS has the higher CaO content (38.13%) and hence the higher reactivity to achieve the activation at ambient temperature. Therefore, high temperature curing is not required for the AAS

and AAFS (GGBFS content $\geq 30\%$) in this study. The MgO content of GGBFS is 6.23%. Because of the high MgO content ($> 5\%$), Mg-Al LDH may be formed as the secondary products (Bernal et al., 2014; Haha, Lothenbach, et al., 2011; Ke et al., 2016).

Table 3-3 Chemical composition of GGBFS.

Oxide	SiO ₂	Al ₂ O ₃	CaO	Fe ₂ O ₃	MgO	SO ₂	Na ₂ O	K ₂ O	LOI ^a
Weight (%)	34.36	16.89	38.13	0.36	6.23	2.3	0.24	0.41	1.08

^a LOI is Loss on Ignition

The particle size distribution of GGBFS measured by laser diffraction technique is shown in Fig.3-5. The D₁₀, D₅₀ (mean particle size) and D₉₀ of GGBFS are 1.44 μm , 11.67 μm , and 32.11 μm , respectively. As can be seen, GGBFS (D₅₀ of 11.67 μm) is finer than FA (D₅₀ of 14.09 μm) in this study, which may lead to the higher packing density and larger reaction area to refine pore structure and improve chloride resistance of AAS and AAFS.

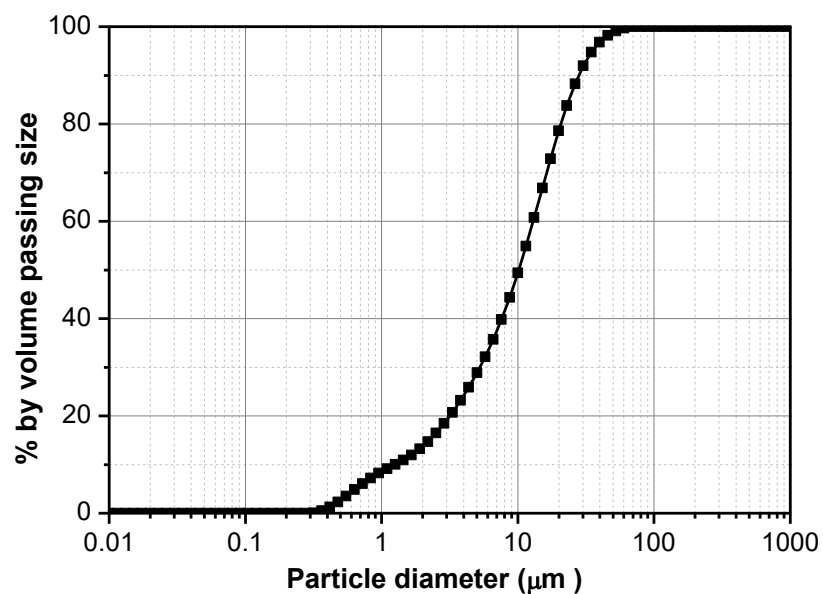


Fig.3-5 Particle size distribution of GGBFS.

The morphology of GGBFS investigated by scanning electron microscopy (SEM) is shown in Fig.3-6. As can be seen, the GGBFS particles exhibit a typical angular

shape. The angular shape of GGBFS particles can increase the tortuosity of pore structure in AAS and AAFS, leading to the higher chloride resistance (Zhu et al., 2014). However, it may increase the friction between particles, and thus lead to the lower workability (Deb, Nath, & Sarker, 2014).

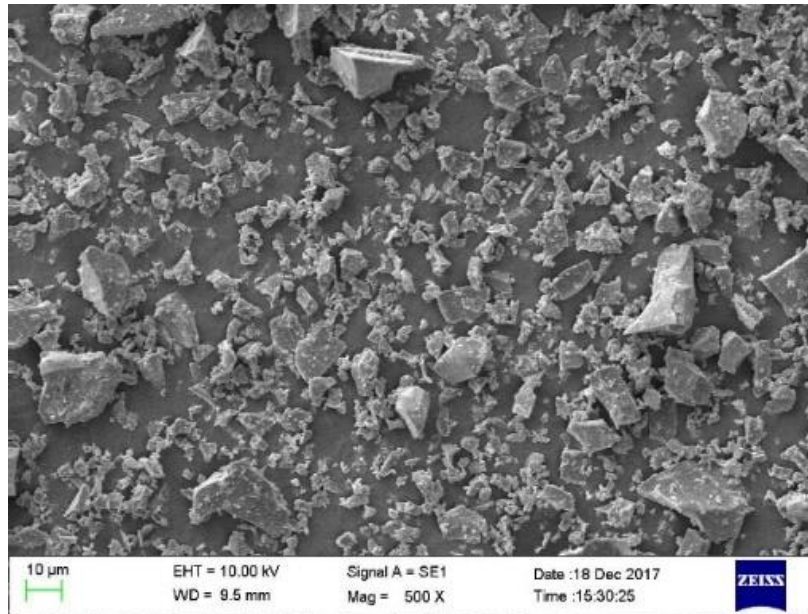


Fig.3-6 Morphology of GGBFS.

The X-ray diffraction (XRD) pattern of GGBFS is shown in Fig.3-7. As can be seen, the GGBFS used in this study is mainly amorphous and has almost no obvious crystalline peak. The amorphous component exhibits a bump between 25° and $38^{\circ} 2\theta$. Although both FA and GGBFS show the broad ‘hump’ feature due to amorphous component, the difference of the location of amorphous hump in FA (17° to $38^{\circ} 2\theta$) and GGBFS (25° to $38^{\circ} 2\theta$) is associated with the structural difference of the amorphous glasses in FA and GGBFS (Ismail et al., 2014).

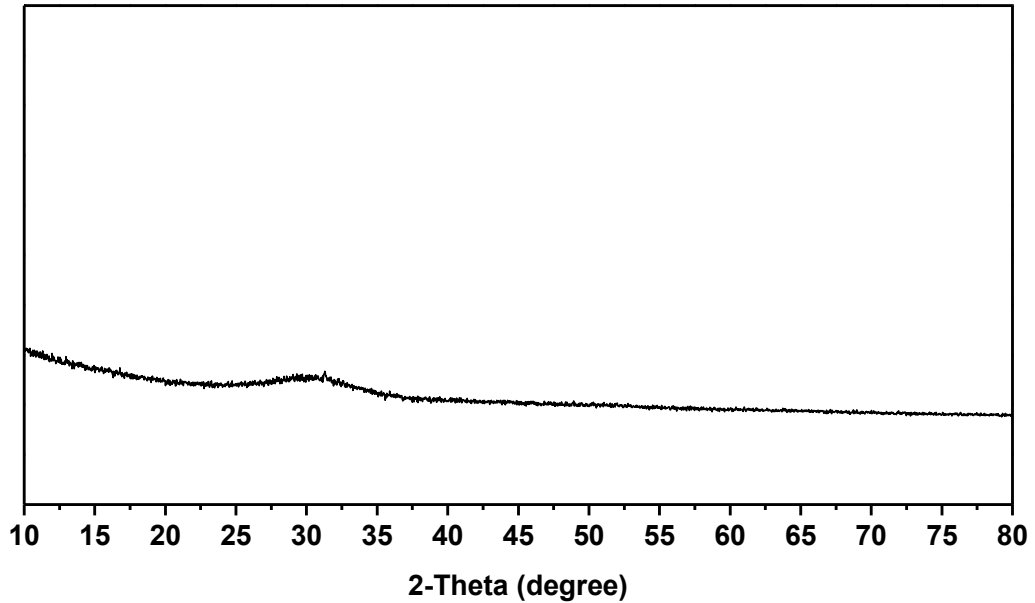


Fig.3-7 X-ray diffraction analysis of GGBFS.

The FTIR spectrum of GGBFS in the range of $2000\text{--}450\text{ cm}^{-1}$ is shown in Fig.3-8. Like the FTIR spectrum of FA, it also contains two main bands in the ranges of $1150\text{--}740\text{ cm}^{-1}$ (c) and $610\text{--}450\text{ cm}^{-1}$ (f), as the indication of anti-symmetric stretching and bending vibrations of tetrahedral SiO_4 and AlO_4 groups, respectively (Pan et al., 2018). The main absorption band associated with the anti-symmetric stretching vibrations of Si–O–T bonds of SiQ_n units (c) is centered at 900 cm^{-1} in GGBFS but 983 cm^{-1} in FA, which is consistent with the differences in chemical composition (Table 3-3 and Table 3-1) and glass structure between GGBFS and FA (Ismail et al., 2014). The shift of this band to the lower wavenumber is associated with the lower degree of crosslinking of the amorphous phase in GGBFS compared to that in FA, which is induced by the high calcium content in GGBFS (Ismail et al., 2014). The band between 610 cm^{-1} and 450 cm^{-1} (f) is assigned to the bending vibration of in-plane Si–O in SiO_4 tetrahedra (García-Lodeiro et al., 2008; Ismail et al., 2014; Lecomte et al., 2006; Lodeiro et al., 2009; Pan et al., 2018; P. Yu et al., 1999)

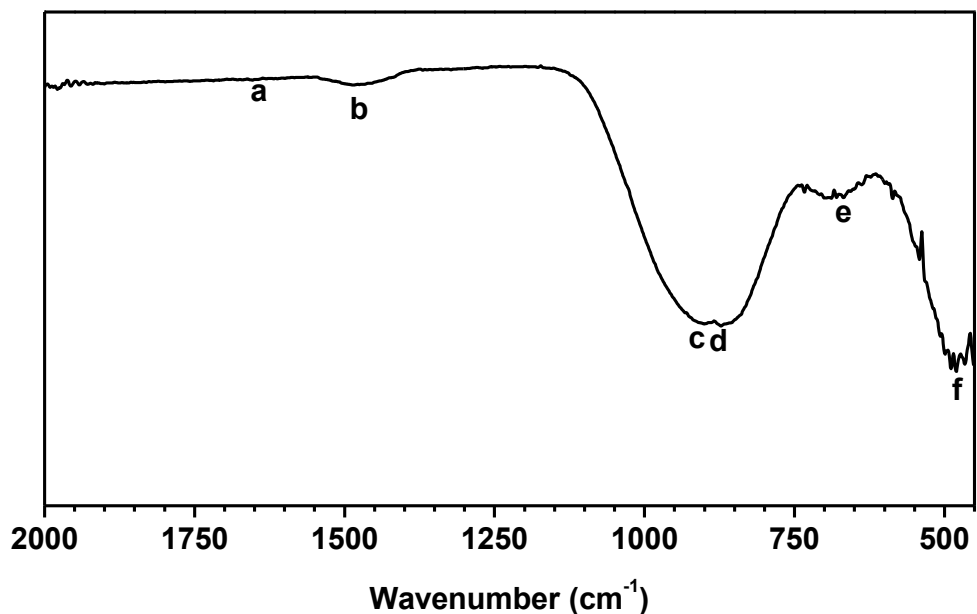


Fig.3-8 FTIR spectrum of GGBFS.

The FTIR band assignments of GGBFS are summarized in Table.3-4. The very small absorption band at 1647 cm^{-1} (a) corresponds to the bending vibration of H–OH bonds in bound water (Ismail, Bernal, et al., 2013b; Ismail et al., 2014; Lee & Lee, 2015; Z. Shi, Shi, Wan, Li, et al., 2018). The asymmetric stretching vibration of O–C–O bonds in carbonates (b) is also observed at 1480 cm^{-1} (García-Lodeiro et al., 2008; P. Yu et al., 1999). The shoulder at 874 cm^{-1} (d) is due to the asymmetric stretching vibration of AlO^{4-} groups in the glass phases or out-of-plane bending vibration of CO_3^{2-} groups (García-Lodeiro et al., 2008; Ismail et al., 2014; P. Yu et al., 1999). The absorption at 670 cm^{-1} (e) is linked with the bending vibration of S–O in gypsum (Ismail et al., 2014; Pan et al., 2018; Yingliang Zhao et al., 2020).

Table 3-4 FTIR band assignments of GGBFS.

Band	Wavenumber (cm^{-1})	Assignment	Reference
a	1647	Bending vibration of H–O–H bonds in bound water	(García-Lodeiro et al., 2008; Lecomte et al., 2006; P. Yu et al., 1999)
b	1480	Asymmetric stretching vibration of O–C–O bonds in CO_3^{2-} groups	(García-Lodeiro et al., 2008; P. Yu et al., 1999)
c	900	Anti-symmetric stretching vibration of	(Ismail et al., 2014; Lecomte et

		Si-O-T bonds of SiQn units (n = 4 - 0), where T is referred to tetrahedral Si or Al	al., 2006; Z. Shi, Shi, Wan, Li, et al., 2018)
d	874	Asymmetric stretching vibration of AlO_4^- groups or out-of-plane bending vibration of CO_3^{2-} groups	(García-Lodeiro et al., 2008; Ismail et al., 2014; P. Yu et al., 1999)
e	670	Bending vibration of S-O in gypsum	(Ismail et al., 2014; Pan et al., 2018; Yingliang Zhao et al., 2020)
f	480	Bending vibration of in-plane Si-O in SiO_4 tetrahedra	(García-Lodeiro et al., 2008; Ismail et al., 2014; Lecomte et al., 2006; Lodeiro et al., 2009; Pan et al., 2018; P. Yu et al., 1999)

3.2.2 ACTIVATOR

Activator is a key ingredient in AAFS manufacturing. It not only provides a strong alkaline reaction medium for precursors (FA and GGBFS), but also is the main cost of AAFS. On the one hand, different activators generate the AAFS with different microstructure (e.g. phase evolution and pore structure), thus further affect the mechanical properties and durability properties of AAFS. On the other hand, the economic and environmental costs of AAFS are heavily dependent on the activator used in manufacture. According to the literature review in Chapter 2 (Section 2.5), and considering from three aspects of technology, economy and environment, sodium silicate ($Na_2O \cdot nSiO_2$) solution was selected to activate precursors in this research.

In this chapter, a series of sodium silicate solutions with different Na_2O contents (mass ratios of Na_2O to precursor) and SiO_2 contents (mass ratios of SiO_2 to precursor) were prepared by mixing analytic grade NaOH powder (purity > 98%), industrial grade waterglass ($Na_2O = 12.19$ wt.%, $SiO_2 = 28.18$ wt.%, $H_2O = 58.92$ wt.%) and water. Because of the large consumption of water to manufacture AAFS concretes, tap water was used in this chapter to reduce cost. First, NaOH powder was dissolved in distilled water to prepare NaOH solution. After that, NaOH solution, industrial grade waterglass and tap water were mixed in proportions to prepare sodium silicate solutions with different Na_2O contents (from 4% to 6%) and SiO_2

contents (from 4% to 6%). The w/b (mass ratio of water to precursor) was between 0.40 to 0.50 in this chapter. In most mixtures, the w/b was kept constant at 0.45. Before sample preparation, the activators were cooled down and stored at room temperature (20 °C) for 24 hours.

3.2.3 AGGREGATE

In this chapter, the aggregates used to manufacture AAFS concrete were river sand and crushed granite from local sources in Guangdong, China. Natural river sand was used as the fine aggregate. The grain size of sand was in the range of 0.25-0.5 mm. The fineness modulus of sand was 2.57. The apparent density and bulk density of sand were 2650 kg/m³ and 1510 kg/m³, respectively. One week before AAFS concrete preparation, the sand was placed in the open air to dry naturally.

Local crushed granite was used as the coarse aggregate. The apparent density and bulk density of crushed granite were 2700 kg/m³ and 1240 kg/m³, respectively. First, small size crushed granite (10–20 mm) and medium size crushed granite (5–10 mm) were sieved by a ZBSX-92A standard electric sieve shaker. One week before AAFS concrete preparation, small size crushed granite and medium size crushed granite were washed several times and dried in the open air. Finally, small size crushed granite and medium size crushed granite were mixed together with a mass ratio of 2:3.

3.3 EXPERIMENTAL METHODS

3.3.1 MIXTURE DESIGN OF AAFS PASTE

Based on the previous studies (Y. Ma et al., 2019; G. Wang & Ma, 2018), a total of 9 AAFS paste mixtures with different GGBFS contents, water/binder ratios (w/b), Na₂O contents and SiO₂ contents were selected in this project. The mixture proportion for each mixture is shown in Table 3-5 and denoted as: GGBFS content (SL), w/b (W), Na₂O content (N) and SiO₂ content (Si). It is noted that SL50, W45 and Si6 are the same mixture, while N4 and Si4 are the same mixture. Na₂O content was designed as low as possible with the consideration of concrete cost. OPC (PO 42.5 cement manufactured at Yangchun Cement Pty Ltd, Shandong Province, China) pastes with the water/cement ratio (w/c) similar to the water/binder ratio (w/b) of

AAFS pastes (0.45) were also prepared as reference samples.

Table 3-5 Mixture proportions of AAFS and OPC pastes.

Sample	FA	GGBFS	Cement	Na ₂ O ^c	SiO ₂ ^d	w/b ^e
SL30	70%	30%				
SL50 ^a	50%	50%				
SL70	30%	70%	0	4%	6%	0.45
SL100	0	100%				
W40						0.40
W45 ^a	50%	50%	0	4%	6%	0.45
W50						0.50
N4 ^b				4%		
N5	50%	50%	0	5%	4%	0.45
N6				6%		
Si4 ^b	50%	50%			4%	
Si6 ^a	50%	50%	0	4%	6%	0.45
OPC	0	0	100%			0.45

^aSL50, W45 and Si6 are the same mix proportion

^bN4 and Si4 are the same mix proportion

^cNa₂O% = Na₂O/(FA + GGBFS) (%)

^dSiO₂% = SiO₂/(FA + GGBFS) (%)

^ew/b= water/binder ratio (water/cement ratio in OPC)

AAFS pastes were prepared by a JJ-5 rotary mixer. To achieve a uniform dispersion, precursors (FA and GGBFS) were first dry mixed for 2 mins at medium speed. Subsequently, the alkaline activator was slowly added. The paste was immediately mixed for 2 mins at low speed. After scraping down the blade and bowl, mixing continued for another 2 mins at medium speed. Then the paste was transferred into 40 mm × 40 mm × 40 mm cubic moulds. After curing at room temperature (20 °C)

for 24 hours, the paste samples were demolded and placed in a curing chamber (relative humidity of 95% and temperature of $20 \pm 2^\circ\text{C}$) until the testing day. OPC pastes ($w/c = 0.45$) were also prepared according to the same steps.

3.3.2 MIXTURE DESIGN OF AAFS CONCRETE

Based on the mixture proportions of AAFS pastes, a total of 13 AAFS concrete mixtures with different GGBFS contents, water/binder ratios (w/b), Na_2O contents, SiO_2 contents and sand/aggregate ratios (s/a) were selected in this project. The mixture proportion for each mixture is shown in Table 3-6 and denoted as: GGBFS content (SL), w/b (W), Na_2O content (N), SiO_2 content (Si) and s/a (S). It is noted that SL50, W45, Si6 and S40 are the same mixture, while N4 and Si4 are the same mixture. The total binder content (defined as the sum of FA and GGBFS) was kept constant at 400 kg/m^3 and the unit weight of AAFS concrete was in the range of $2350\text{-}2450 \text{ kg/m}^3$.

Table 3-6 Mixture proportions of AAFS concretes.

Sample	FA/ GGBFS ^c	$\text{Na}_2\text{O}\%$ ^d	$\text{SiO}_2\%$ ^e	Sand (kg/m^3)	CA ^f (kg/m^3)	w/b ^g	s/a ^h
SL30	70/30						
SL50 ^a	50/50						
		4%	6%	720.3	1080.4	0.45	0.40
SL70	30/70						
SL100	0/100						
W40	50/50					0.40	
W45 ^a	50/50	4%	6%	720.3	1080.4	0.45	0.40
W50	50/50					0.50	
N4 ^b	50/50	4%					
N5	50/50	5%	4%	720.3	1080.4	0.45	0.40
N6	50/50	6%					

Si4 ^b	50/50		4%				
		4%		720.3	1080.4	0.45	0.40
Si6 ^a	50/50		6%				
S36	50/50			648.3	1152.5		0.36
S38	50/50			684.3	1116.5		0.38
S40 ^a	50/50	4%	6%	720.3	1080.4	0.45	0.40
S42	50/50			756.3	1044.5		0.42
S44	50/50			792.3	1008.5		0.44

^aSL50, W45, Si6 and S40 are the same mix proportion

^bN4 and Si4 are the same mix proportion

^c(FA + GGBFS) = 400 kg/m³

^dNa₂O% = Na₂O/(FA + GGBFS) (%)

^eSiO₂% = SiO₂/(FA + GGBFS) (%)

^fCA = Coarse Aggregate (kg/m³)

^gw/b= water/binder ratio

^hs/a= sand/aggregate ratio

AAFS concretes were prepared in a single horizontal shaft concrete mixer. First, precursors (FA and GGBFS), sand and crushed granite were dry-mixed for 2 mins. Subsequently, the activator was added into the mixture, followed by another 2 mins of mixing. After the mixing, the fresh concrete was cast into cube moulds (100 mm × 100 mm × 100 mm). Then the AAFS concrete specimens together with moulds were cured at room temperature for 24 hours. After demolding, the AAFS concrete specimens were placed in a curing chamber (20 ± 2°C and 95% relative humidity) until the testing day.

3.3.3 COMPRESSIVE STRENGTH OF AAFS PASTE

To verify the practicality of different AAFS paste mixtures, the compressive strength of different AAFS paste specimens was measured and compared with that of OPC paste specimens. After 7 and 28 days of curing, the cubic paste specimens (40 mm × 40 mm × 40 mm) were tested according to the previous work (Yanru Wang et al., 2021). The compression load was applied using a universal testing machine (Instron, UK) at a rate of 2.4 kN/s. For statistical reliability, the average result of three

specimens was calculated for each mix proportion at each testing age.

3.3.4 WORKABILITY OF AAFS CONCRETE

Workability is defined as the ease of working with freshly mixed concrete in handling, placing, compacting and finishing (Deb et al., 2014). In this chapter, the workability of AAFS concrete was determined by the slump test in accordance with GB/T 50080-2002 (Chinese Standard, 2003). After the mixing, the fresh AAFS concrete was immediately poured into a slump cone (height of 300 mm, top diameter of 100 mm and bottom diameter of 200 mm) in three layers. For each layer, the AAFS concrete was tamped with a rod (around 25 times) to ensure that the height of the layer after tamping was 1/3 of the slump cone. It is noted that the AAFS concrete should be higher than the slump cone verge when placing the top layer, and the excessive AAFS concrete should be removed with a float to smooth the AAFS concrete surface. Subsequently, the slump cone was lifted vertically and steadily, and the vertical distance between the top of the slumped concrete and the top of the slump cone was measured to indicate the slump of AAFS concrete.

3.3.5 COMPRESSIVE STRENGTH OF AAFS CONCRETE

Compressive strength is the most common characteristic of concrete. In practical engineering, concrete is often used to withstand compressive forces, so compressive strength is the most direct standard for evaluating the mechanical properties of concrete. Besides, compressive strength can also be used as the indicator of other mechanical properties, which are usually closely related to compressive strength (Deb et al., 2014). In this chapter, the compressive strength of AAFS concrete at 7, 28, 90 and 180 days was measured according to GB/T 50081-2002 (China Standard, 2002). The compression test was carried out by using a C086-02N concrete compression machine with a maximum load capacity of 5000 kN (Matest, Italy). Cubic AAFS concrete specimens (100 mm × 100 mm × 100 mm) were used to determine the compressive strength of different mix proportions at different ages. For statistical reliability, three replicates were used for each mix proportion at each testing age.

3.4 RESULTS AND DISCUSSION

3.4.1 COMPRESSIVE STRENGTH OF AAFS PASTE

Fig.3-9 shows the compressive strength of AAFS pastes with different GGBFS contents, water/binder ratios (w/b), Na₂O contents and SiO₂ contents at 7 and 28 days. As shown in Fig.3-9, except SL30, all AAFS pastes exhibited higher compressive strength than that of OPC paste at the same age. Therefore, these AAFS paste mixtures can be considered as the feasible mixtures used in real construction. On this basis, the corresponding AAFS concretes can be prepared.

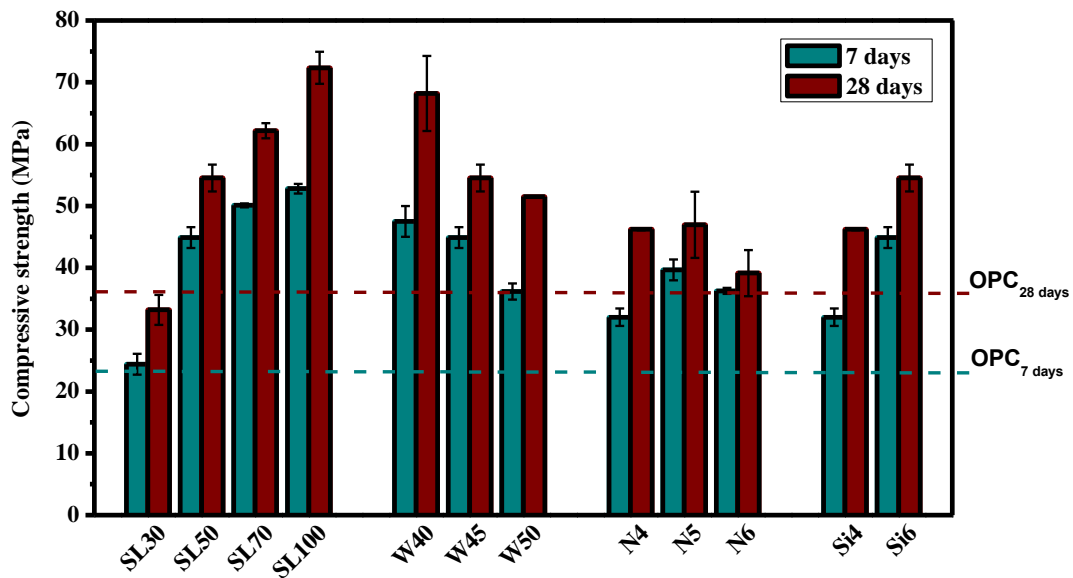


Fig.3-9 Compressive strength of AAFS pastes with different GGBFS contents, water/binder ratios (w/b), Na₂O contents and SiO₂ contents at 7 and 28 days.

GGBFS content is an important factor affecting the compressive strength of AAFS paste. At 28 days, the compressive strength of AAFS paste increased from 33.20 MPa to 72.35 MPa with the increase of GGBFS content from 30% to 100%, which is consistent with the result of previous studies (Deb et al., 2014; G. Fang et al., 2018; X. Hu et al., 2019; P. Nath & Sarker, 2014). One possible explanation is that the main reaction products were transformed from N-A-S-H gels to C-A-S-H gels, which had a finer pore structure (Babae & Castel, 2018; G. Fang et al., 2018; X. Hu et al., 2019). Besides, the reactivity of GGBFS in alkali condition is higher than that of FA. As a result, more gels may be formed to fill capillary pores (remnants of initial water-filled space as shown in Fig.2-2). S. Zhang, Li, Ghiassi, Yin, and Ye (2021) reported that the compressive strength of AAFS was primarily determined by

capillary pores (>10 nm) rather than gel pores (<10 nm). Therefore, the better filling of capillary pores led to the improvement of compressive strength.

The compressive strength of AAFS paste also showed a high sensitivity to w/b. With increasing w/b from 0.40 to 0.50, the 28-d compressive strength of AAFS paste decreased from 68.19 MPa to 51.49 MPa. It is consistent with the tendency of OPC (Singh, Munjal, & Thammishetti, 2015). The reason may be that the higher w/b led to the larger initial water-filled space and hence more capillary pores (Fig.2-2), which needs to be confirmed by microstructure analysis, e.g. mercury intrusion porosimetry (MIP) and scanning electron microscopy (SEM).

With increasing Na₂O content from 4% to 5%, the 7-d compressive strength of AAFS paste increased from 32.00 MPa to 36.26 MPa. It means that the higher alkalinity accelerated the activation of FA and GGBFS. At 28 days, the effect of increasing Na₂O content from 4% to 5% was relatively limited. G. Fang et al. (2018) claimed that the reaction rate of AAFS slowed down after 14 days because most of raw materials had been reacted. When Na₂O content increased from 5% to 6%, the compressive strength of AAFS paste decreased at 7 and 28 days. One possible reason is that the higher alkalinity hindered the diffusion of Ca²⁺ from GGBFS to form less porous C-A-S-H gels (Babae & Castel, 2018).

With the increasing SiO₂ content from 4% to 6%, the 7-d compressive strength of AAFS paste increased from 32.00 MPa to 44.88 MPa, and the 28-d compressive strength of AAFS paste increased from 46.25 MPa to 54.52 MPa. It may be due to more Si components to form gels. As a result, capillary pores (Fig.2-2) can be better filled, leading to the denser matrix of AAFS. However, this effect is limited to the SiO₂ content below an optimum value (De Vargas et al., 2011; Z. Shi, Shi, Wan, & Zhang, 2018). Another possibility is that the volume or diameter of gel pores in Si4 is larger, resulting in lower compressive strength. In order to find out the real reasons, both capillary pores and gel pores need to be analysed. This can be achieved by the combination of mercury intrusion porosimetry (MIP) and nitrogen adsorption.

3.4.2 WORKABILITY OF AAFS CONCRETE

Fig.3-10 presents the slump of AAFS concretes prepared with different GGBFS

contents, water/binder ratios (w/b), Na₂O contents, SiO₂ contents and sand/aggregate ratios (s/a). According to Chinese standard GB50164-92, concrete can be classified as low fluidity concrete (10-40 mm), plastic concrete (50-90 mm), flow concrete (100-150 mm) and high flow concrete (>160 mm) based on its slump value. It can be observed from Fig.3-10 that the slump values of all AAFS concrete mixtures were greater than 50 mm; and most of them were greater than 100 mm. It means that these AAFS concretes can be regarded as flow/high flow concretes according to the standard. This result also shows that AAFS concrete with different workability can be designed by adjusting the mix proportion of each mix component.

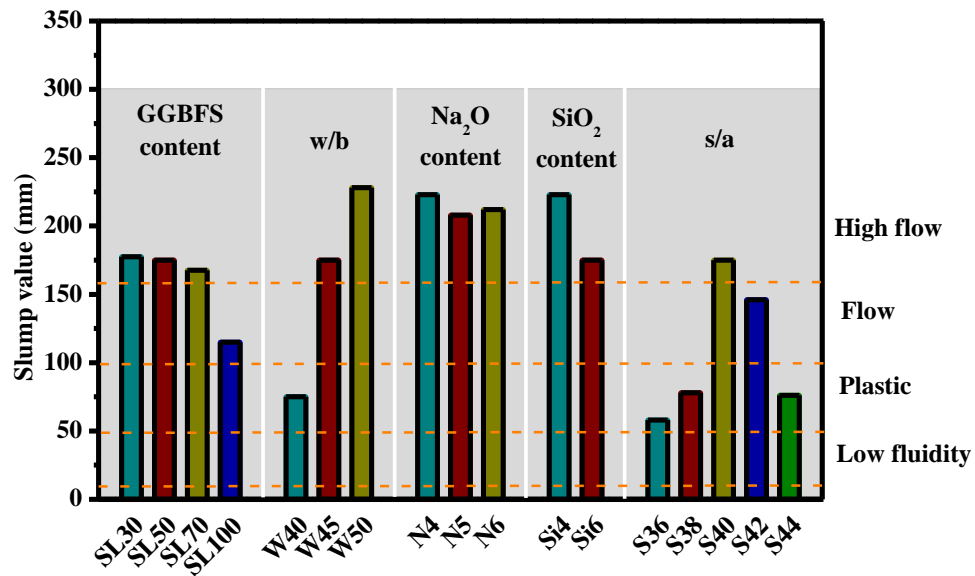


Fig.3-10 Slump of AAFS concretes with different GGBFS contents, water/binder ratios (w/b), Na₂O contents, SiO₂ contents and sand/aggregate ratios (s/a).

The w/b and s/a exhibited a more prominent effect on workability than the other three parameters (GGBFS content, Na₂O content and SiO₂ content). When w/b increased from 0.4 to 0.5, the slump of AAFS concrete increased from 75 mm to 228 mm, changing from plastic concrete to high flow concrete. The dominant role of w/b in the workability of AAFS concrete is consistent with other studies (G. Fang et al., 2018; P. Nath & Sarker, 2014). The slump of AAFS concrete first increased and then decreased with increasing s/a from 0.36 to 0.44, changing from plastic concrete to high flow concrete. S40, with a s/a of 0.40, exhibited the highest slump value (175 mm) among all mixtures. When the s/a increased from 0.36 to 0.40, the added sand

increased the mortar content in concrete and filled the gaps between coarse aggregates, which was beneficial to the workability of concrete. As the sand amount was excessive ($s/a > 0.40$), the entire surface of sand and coarse aggregate was too large to be covered up by the AAFS binder, leading to a reduced workability.

The effects of GGBFS content, Na_2O content and SiO_2 content on the slump of AAFS concrete was relatively small in this study. SL100, which contained 100% GGBFS content, had a comparably low slump value than the other mixtures. It is maybe related to the accelerated reaction of Ca. Besides, the angular shape of GGBFS (Fig.3-6) may increase the friction between particles, resulting in a lower slump value (Deb et al., 2014). The slump of mixture N4, N5 and N6, with different Na_2O content (4%-6%), was similar. Such results are different with the findings in previous research, which may be related to the relatively small variation of Na_2O content among N4, N5 and N6. Fang et al. (2018) claimed that the workability of AAFS concrete significantly decreased when Na_2O content increased. However, in their investigation, SiO_2 content increased with the increase of Na_2O content to keep a constant sodium silicate/sodium hydroxide ratio. It is likely that the decrease of the slump was related to the higher SiO_2 content rather than the higher Na_2O content. Compare Si4 and Si6, when the SiO_2 content increased from 4% to 6%, the workability decreased from 223 mm to 175 mm. This is consistent with the above viewpoint. Sodium silicate ($\text{Na}_2\text{O}\cdot n\text{SiO}_2$) is the most viscous solution among various activators, higher SiO_2 content can increase the viscosity of AAFS mixture, leading to a lower workability (Deb et al., 2014; Deb, Nath, & Sarker, 2015; G. Fang et al., 2018; P. Nath & Sarker, 2014).

3.4.3 COMPRESSIVE STRENGTH OF AAFS CONCRETE

Fig.3-11 presents the compressive strength of AAFS concretes with different GGBFS contents, water/binder ratios (w/b), Na_2O contents, SiO_2 contents and sand/aggregate ratios (s/a) at 7, 28, 90 and 180 days. Overall, the compressive strength of most AAFS concrete mixtures increased gradually with the increase of curing age. Most of them exhibited the relatively high compressive strength at early 28 days. Except for SL30 and N4 (also named as Si4), the compressive strength of all AAFS concrete mixtures was higher than 50 MPa at 28 days. According to Australian standards (AS 3600 and AS 5100.5) shown in Table 3-7, these AAFS concrete mixtures meet the

minimum requirements of general concrete structures and bridges under marine environments (submerged zone, spray zone and tidal/splash zone). However, the development of compressive strength of AAFS concrete in different mixtures is different, which needs further study.

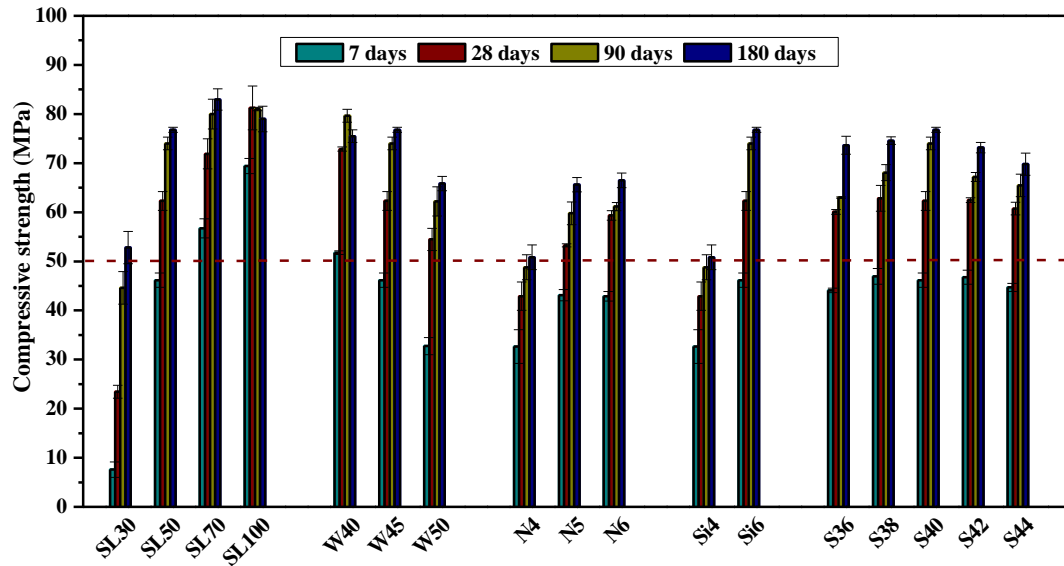


Fig.3-11 Compressive strength of AAFS concretes with different GGBFS contents, water/binder ratios (w/b), Na₂O contents, SiO₂ contents and sand/aggregate ratios (s/a) at 7, 28, 90 and 180 days.

Table 3-7 Minimum characteristic compressive strength (f_c) of general concrete structures and bridges under different exposure environments (AS 3600 and AS 5100.5)

Structure	Standard	Exposure environment	Minimum f_c^a (Mpa)
General Concrete Structures	AS 3600 Concrete Structures	Permanently submerged (B2)	40
		In spray zone (C1)	50
		In tidal/splash zone (C2)	50
Bridges	AS 5100.5 Bridge design Part 5: Concrete	Permanently submerged (B2)	40
		In spray zone (C1)	50
		In tidal/splash zone (C2)	50

^a f_c = characteristic compressive strength of concrete at 28 days

Fig.3-12, Fig.3-13, Fig.3-14, Fig.3-15 and Fig.3-16 show the effects of GGBFS content, water/binder ratio (w/b), Na₂O content, SiO₂ content and sand/aggregate ratio (s/a) on the development of compressive strength of AAFS concrete (from 7 to 180 days), respectively. It can be seen that the development of compressive strength of AAFS concrete follows the similar trend but different magnitudes in different mixtures (except SL100 and W40). The compressive strength of all AAFS concrete mixtures increased significantly at the early age. After 28 days, the increasing rate became slower and slower, and the compressive strength of AAFS concrete tended to be stable. This tendency is consistent with the tendency of AAFS concrete in previous studies (G. Fang et al., 2018; X. Hu et al., 2019) and the tendency of OPC concrete (Gonen & Yazicioglu, 2007), which is mainly attributed to the continuous reaction and enhancement of pore structure (Ismail, Bernal, Provis, San Nicolas, et al., 2013). Although the overall trend is similar, the impact of each parameter on the compressive strength of AAFS concrete is different and needs to be discussed separately.

3.4.3.1 EFFECT OF GGBFS CONTENT

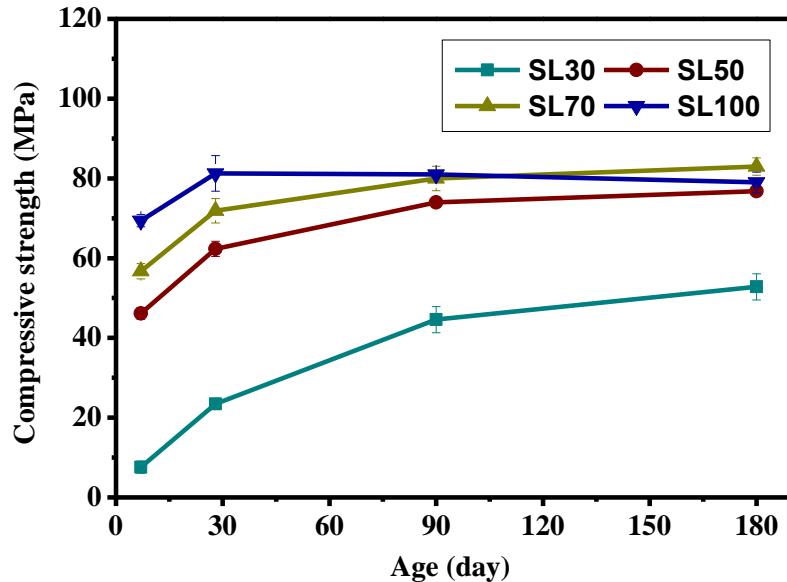


Fig.3-12 Effect of GGBFS content on the development of compressive strength of AAFS concrete (from 7 to 180 days).

As shown in Fig.3-12, FA/GGBFS ratio is an important factor that influencing the development of compressive strength of AAFS concrete. At early 28 days, the

compressive strength of AAFS concrete increased from 23.43 MPa to 81.25 MPa with the increase of GGBFS content from 30% to 100%, which is consistent with the change trend of AAFS paste (Fig.3-9). A possible reason for the upward trend is that the main reaction products are transformed from N-A-S-H gels to C-A-S-H gels due to higher Ca content, which have a finer pore structure (Babae & Castel, 2018; G. Fang et al., 2018; X. Hu et al., 2019). Moreover, the reactivity of GGBFS in alkali condition is higher than that of FA, which may fill capillary pores faster and help to improve the compressive strength of AAFS concrete (X. Hu et al., 2019; Ismail et al., 2014). Besides, GGBFS is finer than FA in this study (Fig.3-1 and Fig.3-5), which may lead to the higher packing density and larger reaction area to refine pore structure and improve compressive strength. The upward trend of 28-d compressive strength was more notable (from 23.43 MPa to 62.32 MPa) when the GGBFS content increased from 30% to 50%. When the GGBFS content increased from 50% to 100%, the increase of 28-d compressive strength became less obvious (from 62.32 MPa to 81.25 MPa). Therefore, the reaction products of SL30 and SL50 may have significant changes. Babae and Castel (2018) claimed that Ca^{2+} tended to adhere to N-A-S-H gels through charge balance instead of forming C-A-S-H gels when the GGBFS content was low (<50%). As a result, reducing the GGBFS content from 50% to 30% may lead to significant changes in the type of reaction products (from C-A-S-H gels to N-A-S-H gels). This seems to explain the huge difference in compressive strength between SL30 and other mixtures.

As can be seen in Fig.3-12, the compressive strength of SL50 and SL70 reached a relatively stable value at 90 days (74.00 MPa and 79.98 MPa, respectively), and then increased slowly until 180 days. However, the increase of compressive strength from 90 days to 180 days was more evident in SL30 compared with SL50 and SL70, which means that the compressive strength of SL30 reached a relatively stable value later (52.81 MPa at 180 days). It is likely related to the slower reaction rate of FA to form N-A-S-H gels. Moreover, the compressive strength of SL100 (AAS) slightly decreased after 28 days, which is consistent with the previous study (Wardhono, Gunasekara, Law, & Setunge, 2017). It may be related to the microcracking caused by the high shrinkage of AAS system (Collins & Sanjayan, 2001; Kutti, Berntsson, & Chandra, 1992). At 180 days, the compressive strength of SL70 (82.96 MPa) was

higher than that of SL100 (79.00 MPa). Therefore, the optimum AAFS concrete (e.g. 70% GGBFS content) can achieve the better long-term mechanical properties compared with AAS concrete.

3.4.3.2 EFFECT OF WATER/BINDER RATIO (W/B)

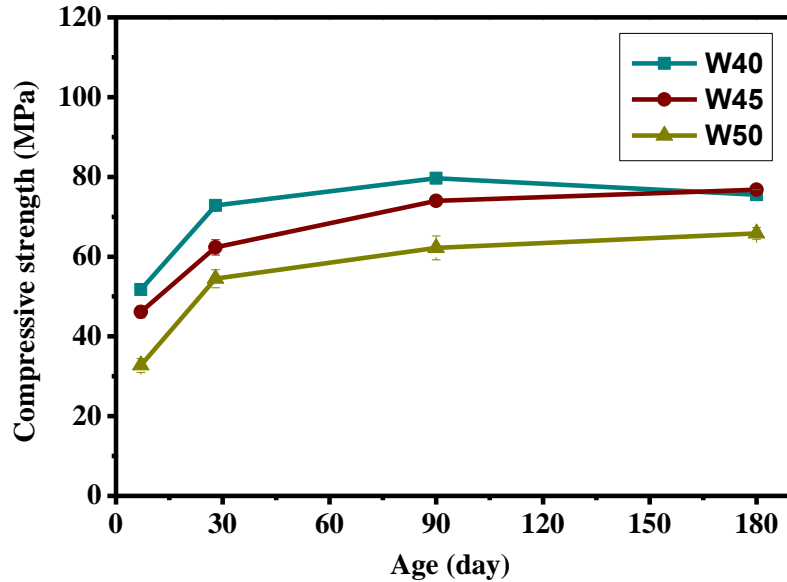


Fig.3-13 Effect of water/binder ratio (w/b) on the development of compressive strength of AAFS concrete (from 7 to 180 days).

Fig.3-13 shows the effect of water/binder ratio (w/b) on the development of compressive strength of AAFS concrete (from 7 to 180 days). It was found that the compressive strength of AAFS concrete showed a high sensitivity to w/b at the early age. With the increasing w/b from 0.40 (W40) to 0.50 (W50), the compressive strength of AAFS concrete gradually decreased at early 90 days. The 28-d compressive strengths of W40, W45 and W50 are 72.87 MPa, 62.32 MPa and 54.46 MPa, respectively. The 90-d compressive strengths of W40, W45 and W50 are 79.63 MPa, 74.00 MPa and 62.22 MPa, respectively. This tendency is consistent with the tendency of of AAFS paste (Fig.3-9) and OPC (Singh et al., 2015). The higher w/b can lead to the larger initial water-filled space and hence more capillary pores (Fig.2-2). Though the composition of activator is more complicated in AAFS compared with the water in OPC, the w/b may have the same function. Besides, increasing w/b can result in the decrease of alkali dosage in activator, and hence a lower degree of reaction.

After 90 days, the compressive strength of W45 and W50 increased slowly until 180 days, which may be due to the continuous reaction and enhancement of pore structure. The difference of compressive strength between W45 and W50 did not change significantly (11.78-10.95 MPa). The compressive strength of W40 decreased significantly from 90 days to 180 days, which may be related to the microcracking caused by the drying shrinkage, as the contracting of concrete due to the loss of capillary water (G. Wang & Ma, 2018). At 180 days, the compressive strength of W45 (76.79 MPa) was higher than those of W40 (75.50 MPa) and W50 (65.84 MPa). Therefore, the w/b should be moderate (around 0.45) to obtain the optimum AAFS concrete with good long-term mechanical properties.

3.4.3.3 EFFECT OF ALKALI CONTENT

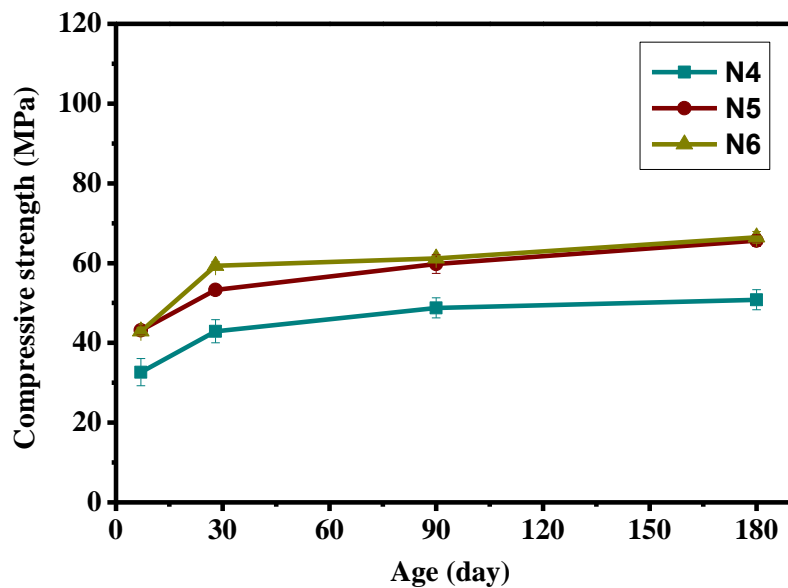


Fig.3-14 Effect of Na₂O content on the development of compressive strength of AAFS concrete (from 7 to 180 days).

Fig.3-14 shows the effect of Na₂O content on the development of compressive strength of AAFS concrete (from 7 to 180 days). At early 28 days, increasing Na₂O content from 4% (N4) to 6% (N6) gradually increased the compressive strength of AAFS concrete from 42.90 MPa to 59.36 MPa, which is consistent with the previous studies (G. Fang et al., 2018; X. Hu et al., 2019). It can be explained by the formation of more reaction products to fill capillary pores. Generally, the increasing Na₂O content can accelerate the activation of FA and GGBFS. The high alkalinity

can lead to the increased breakage of Si–O–T bonds (T is referred to tetrahedral Si or Al) in FA, and Ca-O and Si-O bonds in GGBFS). As a result, there are more Si, Al and Ca components to form N-A-S-H and C-A-S-H gels, leading to the finer pore structure and denser matrix of AAFS concrete.

Overall, the compressive strength of N4, N5 and N6 continued to increase after 28 days until 180 days. However, the increase of compressive strength of N6 was relatively small compared with N4 and N5. At 90 and 180 days, there was only a slight difference in the compressive strength of N5 and N6 (1.37 MPa and 0.87 MPa, respectively). This phenomenon may be caused by many reasons. The higher alkalinity may hinder the diffusion of Ca^{2+} from GGBFS (Babae & Castel, 2018) but promote the diffusion of Si components from FA and GGBFS, which can lead to a lower Ca/Si ratio and limit the formation of less porous C-A-S-H gels when most of Ca^{2+} are consumed. As a result, the pore-filling effect due to the continuous reaction is relatively slow at the late age. Besides, the higher alkalinity may promote the efflorescence (Z. Zhang et al., 2014) and drying shrinkage (Y. Ma & Ye, 2015) of AAFS, which are harmful to the compressive strength of N6. Therefore, the Na_2O content is not as high as possible, and should be moderate (around 5%-6%) to obtain the optimum AAFS concrete with good long-term mechanical properties.

3.4.3.4 EFFECT OF SILICATE CONTENT

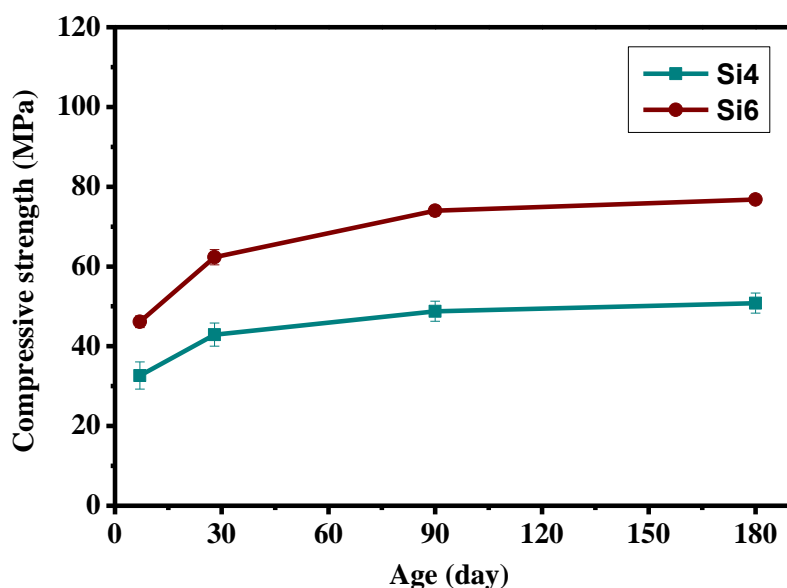


Fig.3-15 Effect of SiO₂ content on the development of compressive strength of AAFC concrete (from 7 to 180 days).

Fig.3-15 compares the development of compressive strength of AAFC concretes with 4% SiO₂ content (Si4) and 6% SiO₂ content (Si6). With the increasing SiO₂ content from 4% to 6%, the 28-d compressive strength of AAFC concrete increased from 42.90 MPa to 62.32 MPa, which is consistent with the change trend of AAFC paste (Fig.3-9) and previous studies (G. Fang et al., 2018; X. Hu et al., 2019). A possible reason is that the activator with higher SiO₂ content provided more Si components to form N-A-S-H and C-A-S-H gels. Therefore, capillary pores were better filled, leading to the denser matrix of AAFC concrete. However, this effect seems to be limited to the SiO₂ content (or Ms) below an optimum value (De Vargas et al., 2011; Z. Shi, Shi, Wan, & Zhang, 2018). With excessive SiO₂ content, the compressive strength remained unchanged or decreased. Excessive Si components led to a lower Ca/Si ratio, which may result in the formation of C-A-S-H gels with a lower Ca/Si ratio (X. Hu et al., 2019) or even the formation of N-A-S-H gels (Babae & Castel, 2018). Besides, the higher SiO₂ content may reduce the alkalinity and hence the compressive strength of specimens (S.-D. Wang et al., 1994).

As can be seen in Fig.3-15, the compressive strength of Si4 and Si6 continued to increase after 28 days until 180 days. From 28 days to 90 days, the increase of compressive strength was more evident in Si6 compared to that in Si4, which means that the compressive strength of Si6 (SL50) reached a relatively stable value later

(74.00 MPa at 90 days). This result is similar to that of SL30, which is likely related to the slower reaction rate due to a lower Ca/Si ratio. However, the effect of higher SiO₂ content was positive from beginning to end, which was opposite to the effect of lower GGBFS content. A possible reason is the relatively sufficient Ca²⁺ in Si6 (SL50) compared to that in SL30. Therefore, the optimum value of SiO₂ content (or Ms) is different in different AAFS concrete mixtures, especially affected by the total Ca content in precursors.

3.4.3.5 EFFECT OF SAND/AGGREGATE RATIO (S/A)

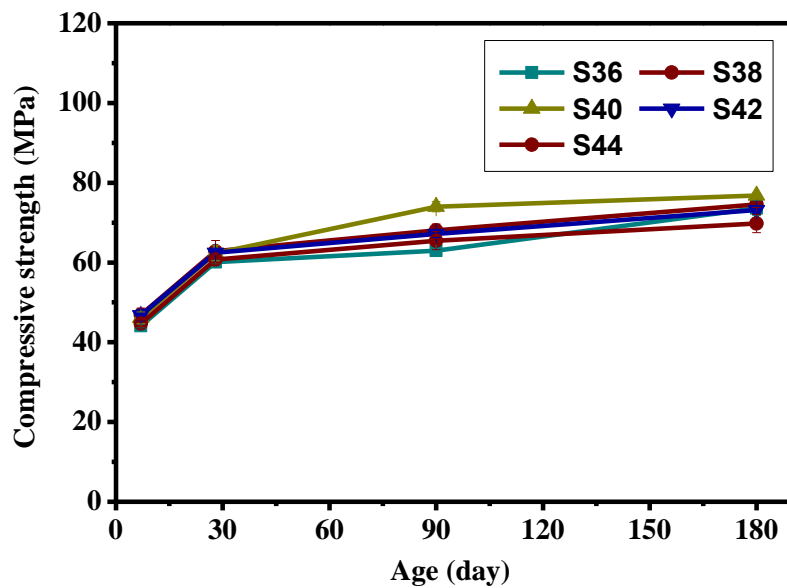


Fig.3-16 Effect of sand/aggregate ratio (s/a) on the development of compressive strength of AAFS concrete (from 7 to 180 days).

Fig.3-16 shows the effect of sand/aggregate ratio (s/a) on the development of compressive strength of AAFS concrete (from 7 to 180 days). Compared to other parameters, the s/a showed relatively smaller effect on the compressive strength of AAFS concrete. The compressive strength of all mixtures exceeded 60 MPa at 28 days, and continued to increase in the following time. The compressive strength of AAFS concrete first increased with increasing s/a from 0.36 to 0.40 and then decreased with increasing s/a from 0.40 to 0.44, which is consistent with the change of workability. S40, which contained 40% sand in the total aggregate, presented the highest compressive strength among all mixtures at almost all curing ages (e.g. 74.00 MPa at 90 day). Therefore, the s/a of AAFS concrete should be moderate (around

0.40) to achieve the best mechanical properties.

When the s/a was too low (e.g. S36), the mortar content decreased and the coarse aggregate content increased. Therefore, the gaps between coarse aggregates cannot be well filled. Besides, the segregation of AAFS concrete may occur due to the excessive coarse aggregate content. The adverse effect of low s/a was particularly evident at the early age. For example, the 90-d compressive strength of S36 (62.98 MPa) was significantly lower than other mixtures. With the increase of curing age, this adverse effect can be gradually compensated, which may be due to the faster enhancement of pore structure. When the sand was excessive (e.g. S44), the entire surface of sand and coarse aggregate was too large to be covered up by the AAFS binder, leading to the decrease of the compactness of AAFS concrete. Although the compressive strength of S44 also gradually increased over time due to the continuous reaction and enhancement of pore structure, the initial gap was not filled because the compressive strength of other mixtures also increased at a similar or even faster rate.

3.5 CONCLUDING REMARKS

This chapter focused on the mixture design and engineering properties of AAFS systems prepared with different parameters, including GGBFS content, w/b, Na₂O content, SiO₂ content and s/a. The main outcomes from the experimental work can be summarized as follows:

- 1) There were obvious differences in the chemical composition, particle size distribution, morphology and phase composition between FA and GGBFS. Compared with FA, GGBFS had higher Ca content, finer particle size, more angular shape, less crystalline phase and lower degree of crosslinking of amorphous phase.
- 2) Except SL30 (30% GGBFS content), all AAFS pastes (50%-100% GGBFS content, 0.40-0.50 w/b, 4%-6% Na₂O content and 4%-6% SiO₂ content) exhibited higher compressive strength than OPC at 7 and 28 days. Therefore, the corresponding AAFS concretes can be prepared. Higher GGBFS content, lower w/b and higher SiO₂ content led to higher compressive strength of AAFS paste at early 28 days. Proper increase of Na₂O content (up to 5%) was also helpful to

improve the compressive strength of AAFS paste at early 28 days.

- 3) Most AAFS concretes manufactured using the parameters in this chapter exhibited high workability with slump > 100 mm. Compared with other parameters, the w/b and s/a had a more prominent effect on the workability. The workability of AAFS concrete decreased with decreasing w/b as well as increasing GGBFS content and SiO₂ content. With increasing s/a, slump increased at first and then decreased. Mixture with 40% sand exhibited the highest slump value. The variation of Na₂O content from 4% to 6% had no significant effect on the workability.
- 4) To ensure a good mechanical strength of AAFS concrete (28-day compressive strength ≥ 50 MPa), AAFS mixtures with GGBFS content $\geq 50\%$, w/b ≤ 0.5 , Na₂O content $\geq 5\%$, and SiO₂ content between 4% and 6% were recommended. At the early age, higher GGBFS content, lower w/b, higher Na₂O content and higher SiO₂ content led to higher compressive strength of AAFS concrete, which is consistent with the result of AAFS paste. The s/a had no significant effect on the compressive strength of AAFS concrete.
- 5) Overall, the compressive strength of AAFS concrete continued to increase in the later stage. With the passage of time, the increasing rate became slower and slower, and the compressive strength of AAFS concrete tended to be stable. However, the compressive strength of AAFS concrete with 100% GGBFS and w/b of 0.4 declined in the later stage. The most likely explanation is the shrinkage and efflorescence of AAFS.

CHAPTER 4: CHLORIDE RESISTANCE OF ALKALI-ACTIVATED FLY ASH-SLAG CONCRETES

Note: this chapter is based on the manuscript entitled “Chloride diffusion in alkali-activated fly ash/slag concretes: Role of slag content, water/binder ratio, alkali content and sand-aggregate ratio”, by Jingxiao Zhang, Yuwei Ma, Jiazheng Zheng, Jie Hu, Jiyang Fu, Zuhua Zhang and Hao Wang, published in journal of Construction and Building Materials, 2020.

4.1 INTRODUCTION

As described in Section 1.1.3, in addition to engineering properties, understanding the chloride resistance of AAFS is also extremely important for the feasibility of AAFS replacing OPC in reinforced concrete structures under chloride-containing environments. Chloride-induced corrosion has been regarded as the most concerned issue for reinforced concrete durability. As long as chloride ions penetrate into concrete and come into contact with reinforced steel bars, they can destroy the passivated layer and initiate corrosion of steel bars, leading to the loss of strength. According to the literature review in Chapter 2, most chloride transport tests in AAFS and other AAMs are based on the testing methods for OPC, such as rapid chloride permeability test (RCPT) documented in ASTM C1202, non-steady-state migration (NSSM) test documented in Nordtest NT BUILD 492 (also known as rapid chloride migration test, RCM), bulk diffusion test documented in ASTM C1556 and Nordtest NT BUILD 443, and ponding test documented in ASTM C1543. The advantages and disadvantages of these testing methods are discussed in Section 2.3.1.

Among them, RCPT (Fig.2-6A) and NSSM test (Fig.2-6B) are the mostly applied methods mainly due to their time-efficiency benefit. However, RCPT is inadaptable in the measurement of AAFS and other AAMs due to joule heating and complicated pore solution chemistry (Arbi et al., 2016; Bernal et al., 2012; Caijun Shi, 1996). The conductivity of pore solution is decided by all mobile ions rather than chloride ions (Arbi et al., 2016). Besides, high voltage (typically 60 V) and associated temperature may lead to structural damage in AAFS and other AAMs (Ravikumar & Neithalath, 2013a). Compared to RCPT, NSSM test provides a more reliable assessment of the chloride resistance of AAFS and other AAMs. Ramezani pour and Moeini (2018) found a relatively good correlation ($R^2 = 0.9$) between the chloride migration coefficient (D_{NSSM}) measured by NSSM test and the chloride diffusion coefficient (D)

measured by bulk diffusion test (Fig.2-7). Despite that, Ismail et al (2013) claimed that the use of accelerating tests (e.g. NSSM test) could not reflect the real chloride resistance of AAFS, particularly at long period. Besides, Yuanzhan Wang and Fu (2019) reported that NSSM test could not reflect the actual effect of chloride binding.

Compared with RCPT and NSSM test, chloride diffusion tests are time-consuming, but they can obtain more realistic results. Bulk diffusion test (also known as accelerated chloride diffusion test, ACD) can shorten the test time to 35 days (ASTM C1556 and Nordtest NT BUILD 443). However, in order to achieve this goal, concentrated NaCl solution (165 ± 1 g/L) is applied as immersion solution (Fig.2-6C), which is much higher than the normal concentration of seawater (around 3.5%). Although ponding test uses 3% NaCl solution, its experiment setup is relatively complex (Fig.2-6D). Therefore, natural chloride diffusion test (NCD) applied in the actual marine environment or simulated marine environment (e.g. 3.5% NaCl solution) is the most dependable method to obtain more realistic results. Based on natural chloride diffusion test applied in the actual marine environment (3 years), P Chindaprasirt and Chalee (2014) reported that the D of AAFA decreased from 6.2×10^{-12} m²/s to 2.9×10^{-12} m²/s with the increase of NaOH concentration from 8 to 18 Molar (Fig.2-15). However, because natural chloride diffusion test is too time-consuming, it has not been applied to the determination of the chloride resistance of AAFS concrete.

In this chapter, natural chloride diffusion tests (NCD) are conducted to evaluate the chloride resistance of different AAFS concretes (designed in Chapter 3) at 90 and 180 days. The free chloride profiles of different AAFS concretes at 90 and 180 days are compared. Based on Fick's second law (Equation 10), the free chloride diffusion coefficients (D_f) of different AAFS concretes at 90 and 180 days are determined. The effects of different parameters, including GGBFS content, w/b, Na₂O content, SiO₂ content and s/a, on chloride diffusion are discussed. The time dependent water absorption of different AAFS concretes is determined to preliminarily explore the influence mechanism of different parameters.

4.2 MATERIALS AND EXPERIMENTAL METHODS

4.2.1 MATERIALS AND MIXTURE PROPORTIONS

The materials (including precursors, activators and aggregates) and mixture proportions used in this chapter to manufacture AAFS concretes are the same as those in Chapter 3. The chemical and physical properties of FA and GGBFS (including chemical composition, particle size distribution, morphology and phase composition) are given in Section 3.2.1. As described in Section 3.2.2, a series of sodium silicate solutions with different Na₂O contents and SiO₂ contents were prepared by mixing analytic grade NaOH powder (purity > 98%), industrial grade waterglass (Na₂O = 12.19 wt.%, SiO₂ = 28.18 wt.%, H₂O = 58.92 wt.%) and water. As described in Section 3.2.3, natural river sand and crushed granite were used as fine aggregate and coarse aggregate, respectively. PO 42.5 cement manufactured at Yangchun Cement Pty Ltd (Shandong Province, China) was utilized to prepare OPC concretes.

The mixture proportions of different AAFS concrete mixtures are shown in Table 3-6 and denoted as: GGBFS content (SL), w/b (W), Na₂O content (N), SiO₂ content (Si) and s/a (S). In addition, the mixture proportion of OPC concrete (cement content = 400 kg/m³, w/c = 0.45, s/a = 0.40) was also designed.

4.2.2 SAMPLE PREPARATION

The mixing and curing procedures of AAFS concretes were the same as those in Chapter 3 (Section 3.3.2). Cubic AAFS concrete specimens (100 mm × 100 mm × 100 mm) after 28 days of curing were used for natural chloride diffusion tests and water absorption tests. According to the same steps, cubic OPC concrete specimens (100 mm × 100 mm × 100 mm) were also prepared as the reference samples for natural chloride diffusion test. Therefore, the chloride resistance of different AAFS concretes could be compared with that of OPC concrete.

4.2.3 NATURAL CHLORIDE DIFFUSION TEST

According to a slightly modified form of ASTM C1543, natural chloride diffusion tests were carried out on AAFS and OPC concrete specimens. First, the surfaces of each 28 day-cured concrete specimen were sealed with water-resistant paraffin wax, and only the bottom surface was not sealed to achieve one-dimensional diffusion (Hall, 1977). Subsequently, sealed concrete specimens were immersed in 3.5% NaCl solution for another 90 and 180 days. To maintain the concentration of NaCl, the

solution was renewed every 30 days. To avoid water evaporation, the container was sealed from beginning to end. At the end of each testing age, concrete specimens were taken out from NaCl solution and ground into powder layer by layer. A DRB-H1 concrete grinding machine was used to grind concrete specimens. After removing water-resistant paraffin wax, 10 layers were ground from the exposed surface of each concrete specimen and each layer was kept in 2 mm. The grinded powder was then sieved with a 0.6 mm sieve-mesh, dried in an oven ($55\text{ }^{\circ}\text{C} \pm 5^{\circ}$) for 2 hours, and put in a desiccator to cool to $20\text{ }^{\circ}\text{C}$ (Yanru Wang et al., 2019). For statistical reliability, three parallel concrete specimens were ground to powder for each concrete mixture at each testing age.

After that, the free chloride content of grinded powder was measured in accordance with JTJ270-98. 2 g concrete powder (G) was put in 50 ml distilled water (V_1). After shaking for 20 min and standing for 24 hours, suspension liquid was filtered. Subsequently, 20 ml filtered solution (V_2) was pipetted into an Erlenmeyer flask with 2 drops of phenolphthalein. Diluted H_2SO_4 solution was then used to neutralize until the solution became colorless. Afterwards, 10 drops of K_2CrO_4 solution were added and 0.02 mol/L AgNO_3 solution was used to titrate until the solution become red. The volume of consumed AgNO_3 solution (V_3) was recorded. The free chloride content was calculated based on Equation 13 (Yanru Wang et al., 2019):

$$C = \frac{C_{AgNO_3} V_3 \times 0.03545}{G \times \frac{V_2}{V_1}} \times 100\% \quad (13)$$

Where:

C is free chloride content in concrete powder (mass %); C_{AgNO_3} is content of AgNO_3 solution, 0.02 mol/L; G is weight of concrete powder, 2 g; V_1 is volume of water used to dissolve concrete powder, 50 ml; V_2 is volume of filtrate, 20 ml; and V_3 is volume of AgNO_3 solution for titration (ml).

For statistical reliability, each grinded powder was assessed three times; and the average result was calculated. Note that the total chloride content of AAFS concrete has also been tried to be measured in accordance with JTJ270-98. However, the match between the measured total and free chloride profiles in AAFS concretes was

remarkably good, which is consistent with the previous study (Babae & Castel, 2018). This may be because the chemical chloride binding capacity of AAFS is insignificant, as described in Section 2.2.2.2. Therefore, only the free chloride content was selected and analysed in this study.

By fitting Fick's second law as expressed in Equation 10, the free chloride diffusion coefficient (D_f) was determined according to the measured free chloride profile (using MATLAB):

$$c(x, t) = c_0 + (c_s - c_0) \left[1 - \operatorname{erf} \left(\frac{x}{2\sqrt{D_f t}} \right) \right] \quad (10)$$

Where:

$C(x, t)$ is free chloride content (mass %) at depth x (m) and time t (s); C_0 is initial chloride content (mass %); C_s is exposure surface chloride content (mass %); D_f is free chloride diffusion coefficient (m^2/s); and erf is error function.

4.2.4 WATER ABSORPTION

The time dependent water absorption of AAFS concrete was determined according to ASTM C642. After curing for 28 days, cubic concrete specimens were dried in an oven (105-110 °C) for more than 48 hours to achieve a constant mass. Dried concrete specimens were left at 20 °C to measure the initial weight (w_i), and then immersed in water and recorded the weight (w) at different time, i.e. 0.5, 1, 3, 6, 12 and 24 hours. Water absorption was considered as the change in weight as a percentage of w_i , as expressed in Equation 14:

$$\text{Water absorption} = \frac{w - w_i}{w_i} \times 100\% \quad (14)$$

Where:

w is weight at different time; and w_i is initial weight.

4.3 RESULTS AND DISCUSSION

4.3.1 CHLORIDE PROFILE

It was reported that the formation of Friedel's salt ($\text{Ca}_2\text{Al}(\text{OH})_6\text{Cl} \cdot 2\text{H}_2\text{O}$) was not

observed in AAFS (Babae & Castel, 2018; Ismail, Bernal, Provis, San Nicolas, et al., 2013). As a result, the chemical chloride binding capacity of AAFS was insignificant, leading to a remarkably good match between the measured total and free chloride profiles in AAFS (e.g. Fig.4-1). In this study, the same result was observed in all AAFS concrete mixtures. Therefore, only the free chloride profiles of AAFS concretes were analysed and discussed.

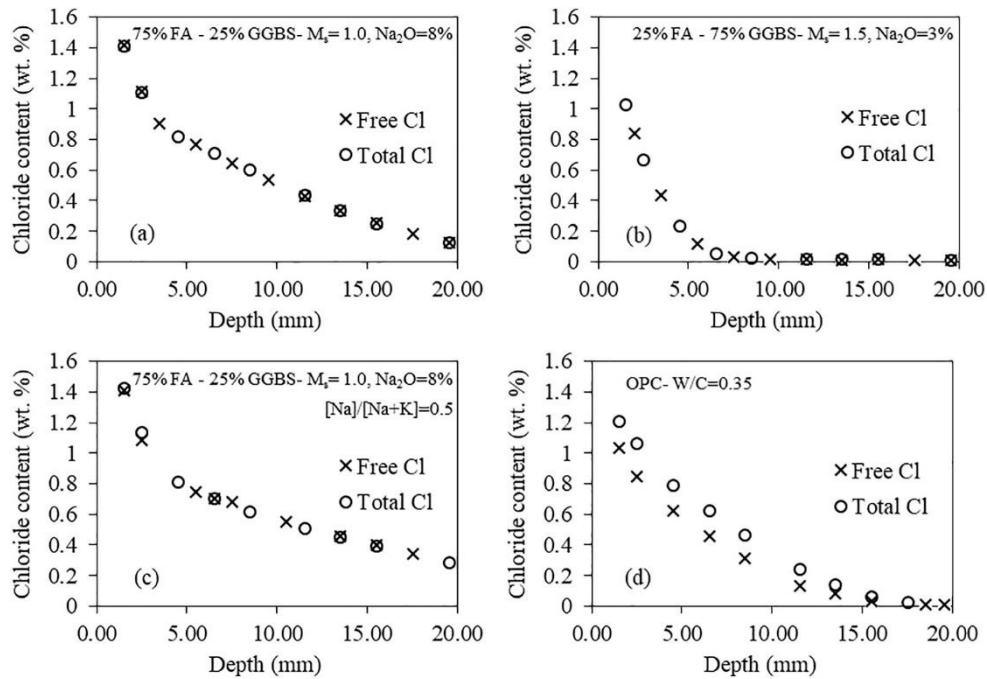


Fig.4-1 Comparison of total and free chloride profiles of AAFS and OPC mortars after 45 days of immersion in 16.5% NaCl solution (Babae & Castel, 2018).

Fig.4-2 and Fig.4-3 present the free chloride profiles of AAFS concretes with different GGBFS contents, water/binder ratios (w/b), Na_2O contents, SiO_2 contents and sand/aggregate ratios (s/a) after 90 and 180 days of immersion in 3.5% NaCl solution. The similar tendency was found in different mixtures. Near the exposure surface, the free chloride content decreased sharply along the depth, as the distance to the exposure surface. For example, after 90 days of immersion, when the depth increased from 2 mm to 4 mm, the free chloride content in SL30 decreased from 0.62% to 0.35% (Fig.4-2A). With the increasing depth, the downward trend slowed down until reached a stable value (around 0.071%), which can be regarded as the initial free chloride content in AAFS concrete (C_0). With the extension of immersion time, the free chloride content near the exposure surface further increased. For example, with the extension of immersion time from 90 days to 180 days, the free chloride

content at 2 mm in SL30 increased from 0.62% (Fig.4-2A) to 0.71% (Fig.4-3A). Moreover, with the extension of immersion time, the free chloride content in the deeper layer began to increase slowly, which means the increase of chloride diffusion depth. For example, with the extension of immersion time from 90 days to 180 days, the chloride diffusion depth in SL50 increased from 14 mm (Fig.4-2A) to 16 mm (Fig.4-3A).

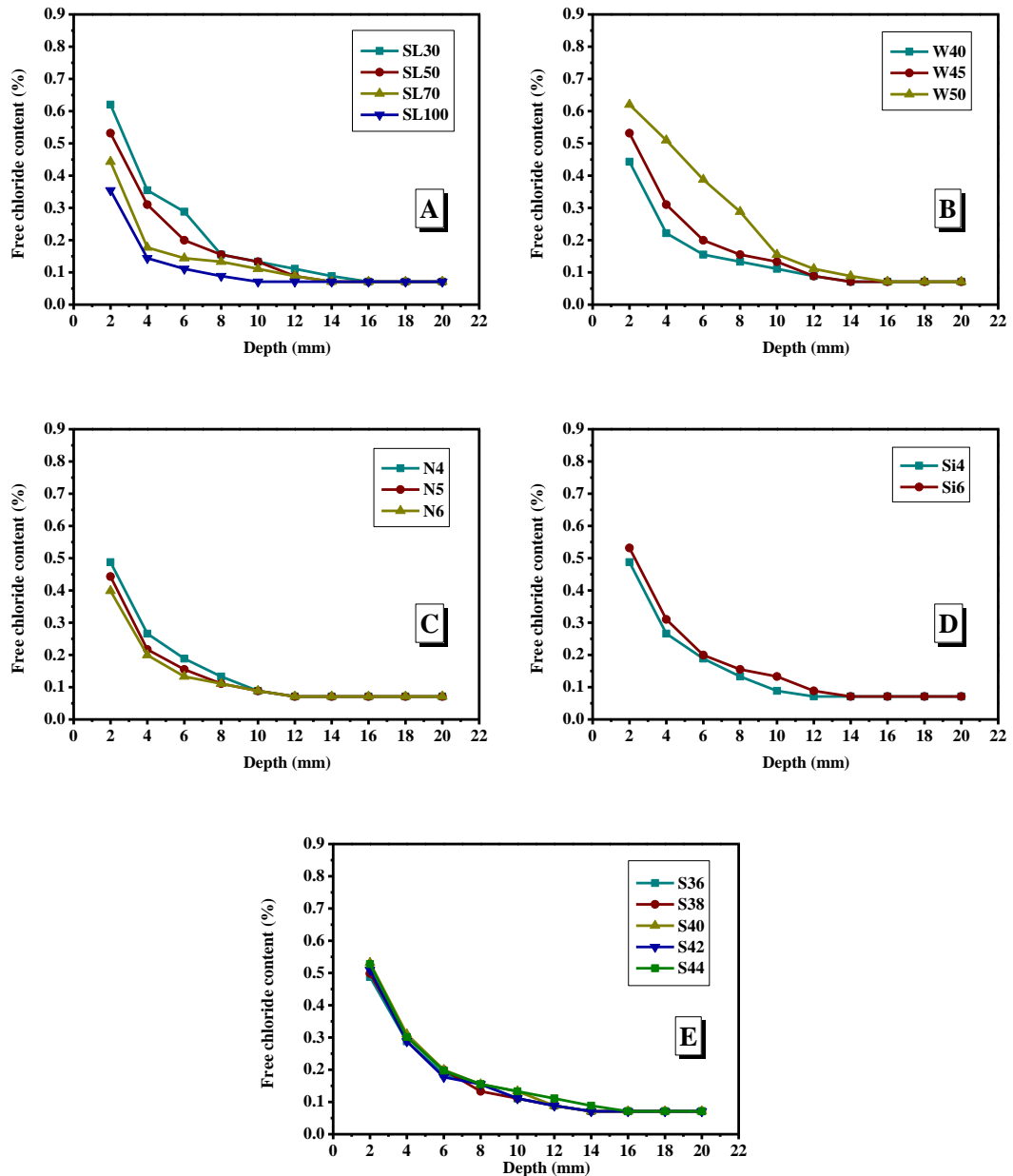


Fig.4-2 Free chloride profiles of AAFS concretes with different (A) GGBFS contents, (B) water/binder ratios (w/b), (C) Na_2O contents, (D) SiO_2 contents and (E) sand/aggregate ratios (s/a) after 90 days of immersion in 3.5% NaCl solution.

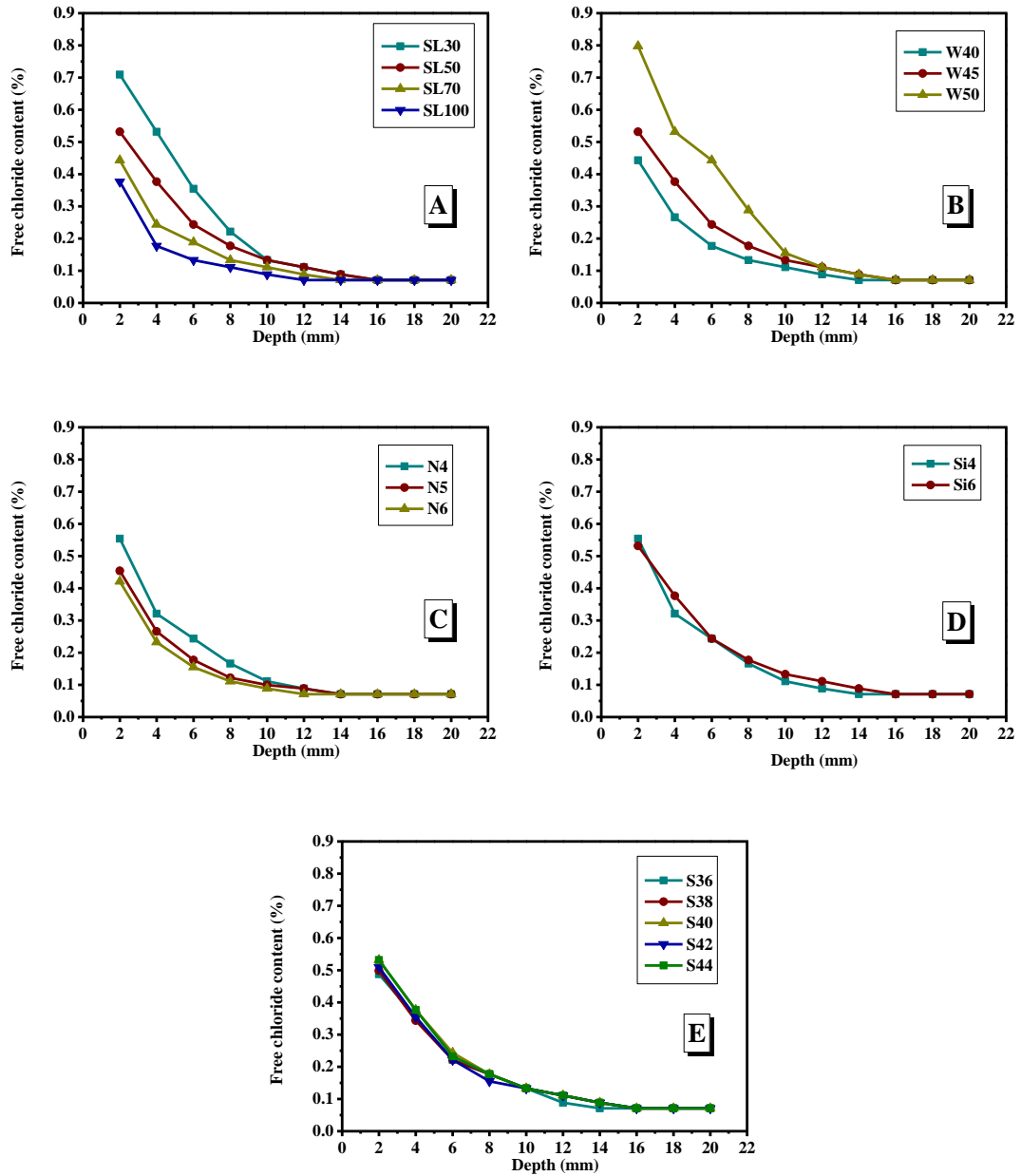


Fig.4-3 Free chloride profiles of AAFS concretes with different (A) GGBFS contents, (B) water/binder ratios (w/b), (C) Na_2O contents, (D) SiO_2 contents and (E) sand/aggregate ratios (s/a) after 180 days of immersion in 3.5% NaCl solution.

In general, increasing GGBFS content from 30% to 100% (Fig.4-2A and Fig.4-3A), decreasing w/b from 0.50 to 0.40 (Fig.4-2B and Fig.4-3B), increasing Na_2O content from 4% to 6% (Fig.4-2C and Fig.4-3C) and decreasing SiO_2 content from 6% to 4% (Fig.4-2D and Fig.4-3D) were beneficial to hinder the chloride transport in AAFS concrete. By comparison, the free chloride profiles of AAFS concretes with different sand/aggregate ratios (s/a) had no obvious difference (Fig.4-2E and Fig.4-3E). Among these parameters, GGBFS content and w/b presented the significant effect on

the chloride diffusion in AAFS concrete. In SL30 and W50, the free chloride content in the first 8 mm depth was significantly higher, which means that the chloride intrusion in these mixtures was more severe. Therefore, it can be considered that the pore structure of SL30 and W50 is coarser than that of other mixtures. Compared with GGBFS content and w/b, the effects of other parameters (including Na₂O content, SiO₂ content and s/a) on chloride diffusion in AAFS concrete were relatively small, or even negligible.

4.3.2 CHLORIDE DIFFUSION COEFFICIENT

Based on Fick's second law (Equation 10), the free chloride diffusion coefficients (D_f) of different AAFS concretes can be determined by a nonlinear regression analysis (using MATLAB). For example, the free chloride profiles and associated fitted curves of SL50 (AAFS) and SL100 (AAS) after 90 days of immersion are shown in Fig.4-4. Compared with the D_f of pure GGBFS system (SL100), the D_f of AAFS with 50% GGBFS content was more than three times after 90 days of immersion, which means the relatively lower chloride resistance.

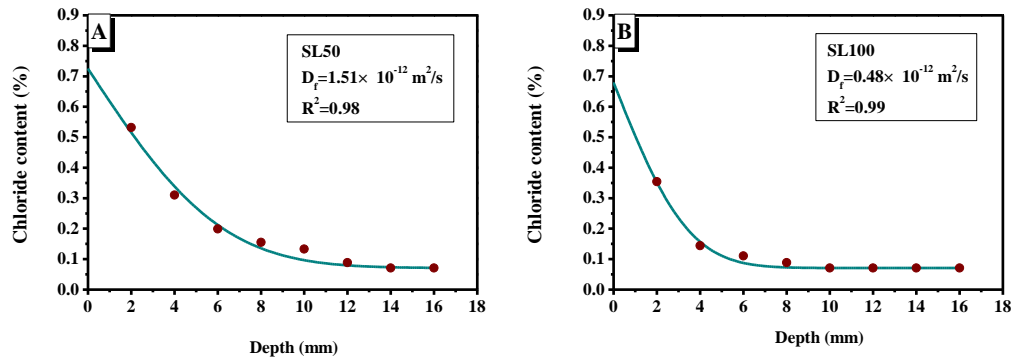


Fig.4-4 Fitted curves of SL50 (A) and SL100 (B) after 90 days of immersion in 3.5% NaCl solution.

Fig.4-5 shows the free chloride diffusion coefficients (D_f) of AAFS concretes with different GGBFS contents, water/binder ratios (w/b), Na₂O contents, SiO₂ contents and sand/aggregate ratios (s/a) after 90 and 180 days of immersion in 3.5% NaCl solution. Overall, the D_f of most AAFS concrete mixtures decreased gradually with the prolonged immersion time, which means that the diffusion rate of Cl⁻ became slower gradually. This tendency is consistent with the tendency of the compressive

strength of AAFS concrete (Fig.3-11), which is caused by the improvement of pore structure due to the continuing of alkali activation (Ismail, Bernal, Provis, San Nicolas, et al., 2013). The formation of more gels can further fill capillary pores, as the remnants of initial water-filled space (Fig.2-2). Although capillary pores may be disconnected and need to be connected via gel pores (Lloyd et al., 2009), they still have a decisive effect on chloride transport (X. Hu et al., 2019). Similar results were also found in the rapid chloride migration test (RCM) of AAFS mortar (X. Hu et al., 2019), as well as in the natural chloride diffusion test and RCM of OPC (Yuanzhan Wang & Fu, 2019). However, although the overall trend remained unchanged, the immersion time exhibited the different effects on the D_f in different mixtures. For example, the difference between 90-d D_f and 180-d D_f was significant in W50 compared with other mixtures. Moreover, the decrease of D_f with the prolonged exposure time was not pronounced in SL70 and SL100 from 90 days to 180 days. As a result, the effects of different parameters showed different degrees at 90 and 180 days. The reason may be that the microstructure (e.g. phase evolution and pore structure) of AAFS changed over time.

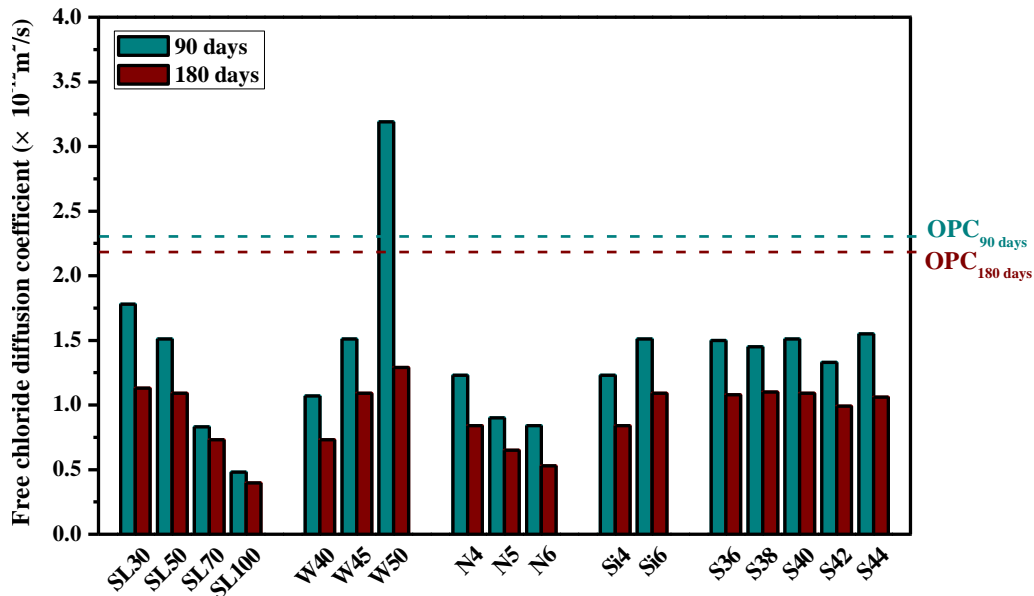


Fig.4-5 Free chloride diffusion coefficient (D_f) of AAFS concretes with different GGBFS contents, water/binder ratios (w/b), Na_2O contents, SiO_2 contents and sand/aggregate ratios (s/a) after 90 and 180 days of immersion in 3.5% NaCl solution.

The D_f of OPC concretes after 90 and 180 days of immersion in 3.5% NaCl solution

is also shown in Fig.4-5. Except the 90-d D_f of W50, the D_f of all AAFS concretes at all times was lower than that of OPC concretes. Therefore, all mixtures investigated in this study can be considered as the optimal mixtures to achieve excellent chloride resistance.

4.3.2.1 EFFECT OF GGBFS CONTENT

As shown in Fig.4-5, FA/GGBFS ratio is an important factor that influencing the D_f of AAFS concrete. After 90 days of immersion, the D_f of AAFS concrete decreased from $1.78 \times 10^{-12} \text{ m}^2/\text{s}$ to $0.48 \times 10^{-12} \text{ m}^2/\text{s}$ with increasing GGBFS content from 30% to 100%. It means the improvement of chloride resistance, which is consistent with the upward trend of compressive strength (Fig.3-9 and Fig.3-12). The same trend was also obtained in RCPT (X. Hu et al., 2019), NSSM test (X. Hu et al., 2019; Ismail, Bernal, Provis, San Nicolas, et al., 2013), bulk diffusion test (Babae & Castel, 2018) and ponding test (Ismail, Bernal, Provis, San Nicolas, et al., 2013). With the increase of Ca content, the main reaction products are transformed from N-A-S-H gels to C-A-S-H gels, which have a more compact structure (Babae & Castel, 2018; G. Fang et al., 2018; X. Hu et al., 2019). Moreover, the reactivity of GGBFS is higher than that of FA, so the reaction rate of AAFS concrete with higher GGBFS content is faster (X. Hu et al., 2019; Ismail et al., 2014). As a result, capillary pores can be rapidly filled and the microstructure can be rapidly improved. In addition, GGBFS is finer than FA, which may lead to higher packing density and larger reaction area to refine pore structure and improve chloride resistance. Besides, FA is comprised of spherical particles, whereas GGBFS is comprised of irregular jagged particles. Therefore, high GGBFS content can increase the tortuosity and thus hinder the chloride transport in AAFS (Zhu et al., 2014).

As can be seen in Fig.4-5, with the extension of exposure time, the decrease of D_f was more pronounced in SL30 and SL50. With the immersion time extending from 90 to 180 days, the D_f of SL30 decreased from $1.78 \times 10^{-12} \text{ m}^2/\text{s}$ to $1.13 \times 10^{-12} \text{ m}^2/\text{s}$ and the D_f of SL50 decreased from $1.51 \times 10^{-12} \text{ m}^2/\text{s}$ to $1.09 \times 10^{-12} \text{ m}^2/\text{s}$. This may be due to the continuous reaction dominated by FA. Because of the low reactivity, the reaction rate of FA is slower than that of GGBFS. When GGBFS content is low, the reaction products at the early age, which are dominated by C-A-S-H gels, cannot fill capillary pores well. As a result, a longer time is needed to fill capillary pores. Thus,

the D_f takes longer to reach a relatively stable value. By comparison, the decrease of D_f from 90 to 180 days is relatively small in SL70 and SL100. It means that the D_f reached a relatively stable value at early 90 days, which is likely related to the faster reaction rate of GGBFS to form C-A-S-H gels.

4.3.2.2 EFFECT OF WATER/BINDER RATIO (W/B)

It was found in Fig.4-5 that the D_f of AAFS concrete showed a high sensitivity to w/b at 90 days. With increasing w/b from 0.40 to 0.50, the 90-d D_f of AAFS concrete increased from $1.07 \times 10^{-12} \text{ m}^2/\text{s}$ to $3.19 \times 10^{-12} \text{ m}^2/\text{s}$. This trend is consistent with the decrease of compressive strength shown in Fig.3-9 and Fig.3-13, as well as the result of the chloride penetration in AAFA shown in Fig.2-14 (Zhu et al., 2014). One possible reason is that the higher w/b can lead to the larger initial water-filled space and hence more capillary pores (Fig.2-2). Though the composition of activator is more complicated in AAFS, the w/b may have the same function. The extra water in the alkaline activator may act as capillary pores in the concrete matrix, particularly around the ITZ (Elsharief et al., 2003; Zhu et al., 2014). Therefore, more fast paths for Cl^- penetration are provided. Besides, increasing w/b means the decrease of Na_2O concentration in activator, which may lead to a lower degree of reaction and thus more porous microstructure. Such results were different from the findings in AAS concrete (Bondar et al., 2018), in which the excess water did not affect the pore structure and chloride transport. One possible explanation is the faster reaction rate of GGBFS to form C-A-S-H gels. Therefore, capillary pores in AAS with high w/b can still be well filled at the early age. It is also important to note that the effect of w/b on chloride resistance is not gradual. The gap between W45 and W50 ($1.68 \times 10^{-12} \text{ m}^2/\text{s}$) at 90 days is much larger than the gap between W40 and W45 ($0.44 \times 10^{-12} \text{ m}^2/\text{s}$). Therefore, when w/b exceeds a certain value, even a small increase will greatly reduce the chloride resistance of AAFS at the early age.

At 180 days, the D_f of mixtures with different w/b decreased significantly, indicating a significantly pore refinement between 90 and 180 days. Among them, the change of D_f in W50 (from $3.19 \times 10^{-12} \text{ m}^2/\text{s}$ to $1.29 \times 10^{-12} \text{ m}^2/\text{s}$) was the most obvious. It means that due to the continuous reaction and the formation of more reaction products, most of the remaining capillary pores in the early stage were filled. Therefore, the adverse impact caused by high w/b may not have much impact on the

total service life of AAMs in the chloride-containing environment (more than 50 years).

4.3.2.3 EFFECT OF ALKALI CONTENT

As shown in Fig.4-5, the effect of Na₂O content was relatively small compared with that of GGBFS content and w/b. At 90 days, increasing Na₂O content from 4% to 6% slightly reduced the D_f of AAFS concrete from $1.23 \times 10^{-12} \text{ m}^2/\text{s}$ to $0.71 \times 10^{-12} \text{ m}^2/\text{s}$. This trend is consistent with the upward trend of compressive strength (Fig.3-9 and Fig.3-14) and the results of previous studies (Bondar et al., 2018; P Chindaprasirt & Chalee, 2014; X. Hu et al., 2019). The increasing Na₂O content can accelerate the activation of FA and GGBFS. As a result, more Si, Al and Ca components dissolve from precursors to form more reaction products, which can fill capillary pores and improve chloride resistance. However, such findings were different from the result by Babae and Castel (2018), in which they noted that increasing Na₂O content increased the D_f of AAFS. They ascribed it to the high alkaline environment that hindered the diffusion of calcium from GGBFS. It should be noted that in their experiments, to keep a constant modulus (SiO₂/Na₂O), the SiO₂ content increased as the Na₂O content increased. The excessive SiO₂ content is known to decrease the overall pH of activator, leading to a lower degree of reaction (Babae & Castel, 2018). Moreover, more Si species from activator may lead to a lower Ca/Si ratio and hence the formation of more porous aluminosilicate gels. Therefore, SiO₂ content (Na₂O content × Ms) instead of Ms should be kept constant. From 90 to 180 days, the D_f of all mixtures decreased and the influencing tendency of Na₂O content remained unchanged.

Besides, the effect of Na₂O content on chloride resistance is not gradual. When the Na₂O content was higher than 5%, the improvement of chloride resistance was not significant with the increase of Na₂O content. As shown in Fig.4-5, the gap between N5 and N6 ($0.06 \times 10^{-12} \text{ m}^2/\text{s}$) at 90 days is much smaller than the gap between N4 and N5 ($0.33 \times 10^{-12} \text{ m}^2/\text{s}$). The reasons may be multifaceted. The higher alkalinity may hinder the diffusion of Ca²⁺ from GGBFS (Babae & Castel, 2018) but promote the diffusion of Si components from FA and GGBFS. As a result, the formation of less porous C-A-S-H gels is limited when most of Ca²⁺ are consumed. Thus, the pore-filling effect of continuous reaction is relatively slow. Besides, the higher

alkalinity may also promote the efflorescence (Z. Zhang et al., 2014) and drying shrinkage (Y. Ma & Ye, 2015). Therefore, the Na₂O content is not as high as possible, and should be moderate (around 5%-6%).

4.3.2.4 EFFECT OF SILICATE CONTENT

Fig.4-5 also compares the D_f of AAFS concretes with 4% SiO₂ content (Si4) and 6% SiO₂ content (Si6). With the increasing SiO₂ content from 4% to 6%, the 90-d D_f of AAFS concrete increased from 1.23×10^{-12} m²/s to 1.51×10^{-12} m²/s, and the 180-d D_f of AAFS concrete increased from 0.84×10^{-12} m²/s to 1.09×10^{-12} m²/s, which is consistent with the previous studies (Babae & Castel, 2018; Law et al., 2015). Babae and Castel (2018) claimed that more Si species from activator led to a lower Ca/Si ratio. Therefore, more porous N-A-S-H gels were formed, leading to a higher porosity of AAFS. However, this view is inconsistent with the increase of compressive strength (Fig.3-9 and Fig.3-15). One possible explanation for the opposite change trend between compressive strength and chloride resistance is that not only pore structure but also chloride binding capacity can affect the chloride transport in AAFS concrete. Although the microstructure of N4 was more porous due to lower SiO₂ content (X. Hu et al., 2019), the chloride binding capacity of N4 might be higher due to more LDH formed (J. Zhang, Shi, & Zhang, 2019a; J. Zhang et al., 2019b). As a result, N4 had higher chloride resistance. The opposite trend obtained in NSSM test (X. Hu et al., 2019) can confirm this view. It is found that lower SiO₂ content led to a higher D_{NSSM} , which may be because the influence of chloride binding in NSSM test was too weak (Yuanzhan Wang & Fu, 2019). Another explanation is that the pore size that affects the compressive strength and chloride resistance is different. In order to explore the real reason, the corresponding phase evolution and pore structure of AAFS need to be analysed.

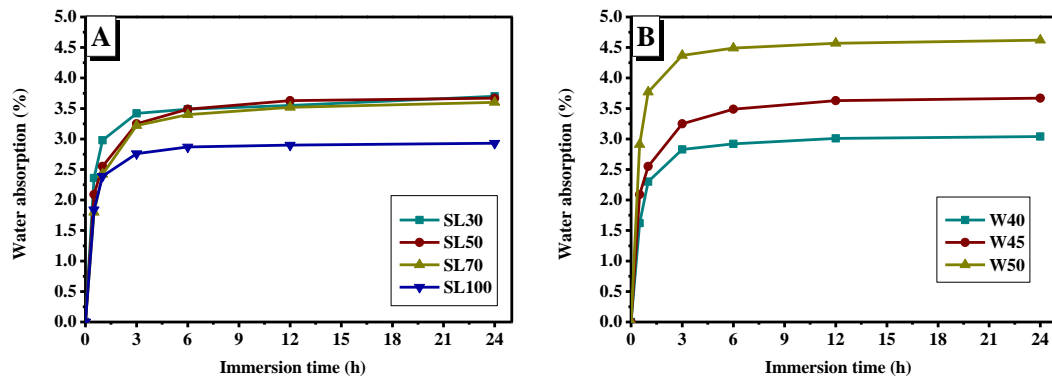
4.3.2.5 EFFECT OF SAND/AGGREGATE RATIO (S/A)

As shown in Fig.4-5, compared to other parameters, the s/a showed relatively smaller effect on the D_f of AAFS concrete. Among the mixtures with different s/a, S42 presented the lowest D_f (1.33×10^{-12} m²/s at 90 days and 0.99×10^{-12} m²/s at 180 days). Therefore, the s/a of AAFS concrete should be moderate, which is consistent with the result of compressive strength (Fig.3-16). However, the gap between

different mixtures was very small ($< 0.22 \times 10^{-12} \text{ m}^2/\text{s}$). With the prolonged immersion time, the D_f of these mixtures tended to be consistent (around $1.06 \times 10^{-12} \text{ m}^2/\text{s}$ at 180 days).

4.3.3 WATER ABSORPTION

To understand the influence mechanism of different parameters on the chloride diffusion in AAFS, the water absorption of AAFS concretes with different GGBFS contents, water/binder ratios (w/b), Na_2O contents, SiO_2 contents and sand/aggregate ratios (s/a) was measured (Fig.4-6). Within 24 hours, water absorption sharply increased and got equilibrium quickly. As shown in Fig.4-6, AAFS concretes with lower GGBFS content, higher w/b and lower Na_2O content exhibited higher water absorption, which is roughly consistent with the change trends of compressive strength (Fig.3-9 and Fig.3-11) and chloride resistance (Fig.4-5). Higher SiO_2 content resulted in higher water absorption, which is consistent with the reduction of chloride resistance (Fig.4-5), but not consistent with the increase of compressive strength (Fig.3-9 and Fig.3-11). Besides, higher s/a also led to higher water absorption. Similar to the results of compressive strength (Fig.3-9 and Fig.3-11) and D_f (Fig.4-5), the effects of GGBFS content and w/b on water absorption were more pronounced than other parameters (Fig. 4-6A and Fig. 4-6B).



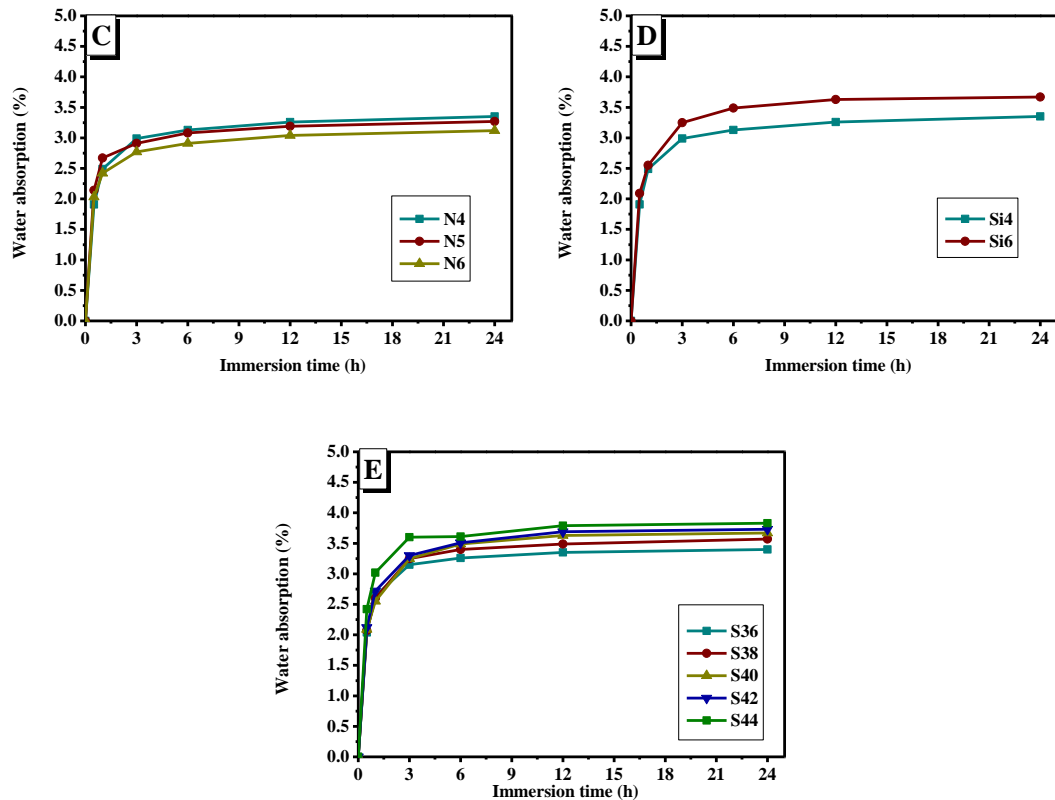


Fig.4-6 Water absorption of AAFS concretes with different (A) GGBFS contents, (B) water/binder ratios (w/b), (C) Na_2O contents, (D) SiO_2 contents and (E) sand/aggregate ratios (s/a).

4.3.3.1 EFFECT OF GGBFS CONTENT

As shown in Fig.4-6A, the gap between SL30, SL50 and SL70 was relatively smaller (from 3.70% to 3.60%). This slight difference is in good agreement with the previous research (Zhu et al., 2014). With increasing GGBFS content from 70% to 100%, the water absorption of AAFS concrete decreased significantly (from 3.76% to 2.93%), which means the reduction of total porosity. The overall change trend of water absorption is consistent with the change trend of compressive strength (Fig.3-12) and chloride resistance (Fig.4-5), because they all depend on the pore structure of AAFS concrete. Although the overall change trend was the same, there were some differences in the change degree of water absorption and Cl^- precipitation rate. For example, as shown in Fig.4-5, the 90-d D_f of AAFS concrete decreased significantly with increasing GGBFS content from 30% to 70%, which is inconsistent with the slight difference of water absorption. Zhu et al. (2014) claimed that the chloride transport in AAFS was not simply related to the porosity but also other pore features (e.g. pore size distribution, continuity and tortuosity) and chloride binding capacity.

This may be the reason for the inconsistency between water absorption and Cl^- precipitation rate.

4.3.3.2 EFFECT OF WATER/BINDER RATIO (W/B)

As shown in Fig.4-6B, with increasing w/b from 0.40 to 0.50, the water absorption of AAFS concrete gradually increased from 3.04% to 4.62%, with is consistent with the reduction of compressive strength (Fig.3-13) and chloride resistance (Fig.4-5). This observation is also in good agreement with the previous study (Zhu et al., 2014). Higher w/b leads to larger initial water-filled space and hence more capillary pores (Fig.2-2). Besides, the increase of w/b means the decrease of alkali dosage in activator, which may also lead to lower degree of reaction and hence higher porosity.

4.3.3.3 EFFECT OF ALKALI CONTENT

The increasing Na_2O content from 4% to 6% led to slightly lower water absorption of AAFS concrete (from 3.35% to 3.12%, as shown in Fig.4-6C), which was not as significant as the effects of GGBFS content and w/b. This observation is consistent with the slight increase of compressive strength (Fig.3-14) and chloride resistance (Fig.4-5). Higher Na_2O content accelerated the activation of FA and GGBFS. Therefore, more Si, Al and Ca components dissolved from precursors to form more reaction products to fill capillary pores. There were also some differences in the change degree of water absorption and Cl^- precipitation rate. When the Na_2O content increased from 4% to 5%, the 90-d D_f of AAFS concrete decreased significantly (Fig.4-5), but the water absorption did not change significantly (Fig.4-6C). When the Na_2O content increased from 5% to 6%, the water absorption of AAFS concrete decreased significantly (Fig.4-6C), but the difference of 90-d D_f was small (Fig.4-5).

4.3.3.4 EFFECT OF SILICATE CONTENT

As shown in Fig.4-6D, with the increase of SiO_2 content from 4% to 6%, the water absorption of AAFS concrete slightly increased from 3.35% to 3.67%, with is consistent with the reduction of chloride resistance (Fig.4-5). Babae and Castel (2018) claimed that more Si species from activator led to a lower Ca/Si ratio, resulting in slower formation of reaction products to fill capillary pores. However, this view is inconsistent with the increase of compressive strength (Fig.3-15). One

possible reason is that Si4 has more large gel pores, which have a certain effect on compressive strength. To confirm the above speculation, the capillary pores and gel pores of AAFS should be analysed by the combination of mercury intrusion porosimetry (MIP) and nitrogen adsorption.

4.3.3.5 EFFECT OF SAND/AGGREGATE RATIO (S/A)

AAFS concrete with higher s/a exhibited slightly higher amount of water absorption, as shown in Fig.4-6E. With the increase of s/a, the mortar content increased and the coarse aggregate content decreased, leading to a higher porosity. However, the excessive sand (e.g. 0.44 in S44) may lead to the larger entire surface of sand and coarse aggregate, which cannot be well covered up by the AAFS binder. It may lead to more pores at local locations, which explains the decline of compressive strength (Fig.3-16) and chloride resistance (Fig.4-5).

4.3.4 WATER ABSORPTION VS. CHLORIDE DIFFUSION

As well known, both water absorption and chloride transport are closely related to the pore structure of AAFS. Fig.4-7 correlates the water absorption and D_f of different AAFS concretes at 90 and 180 days. At 90 days (Fig.4-7A), there was a positive correlation between water absorption and D_f . However, the error was relatively high ($R^2 = 0.8178$). One possible explanation is that not only porosity, but also pore size distribution, connectivity, tortuosity and chloride binding capacity are important parameters influencing the chloride transportation properties (X. Hu et al., 2019; Zhu et al., 2014). At 180 days (Fig.4-7B), the water absorption cannot fit well with the D_f of AAFS concrete. One reason is that the continuous reaction of AAFS changed the pore volume to varying degrees. Therefore, the early pore structure analysis may not correspond well to the long-term chloride resistance, because the changes of microstructure (phase evolution and pore structure) in AAFS concretes with different parameters are different.

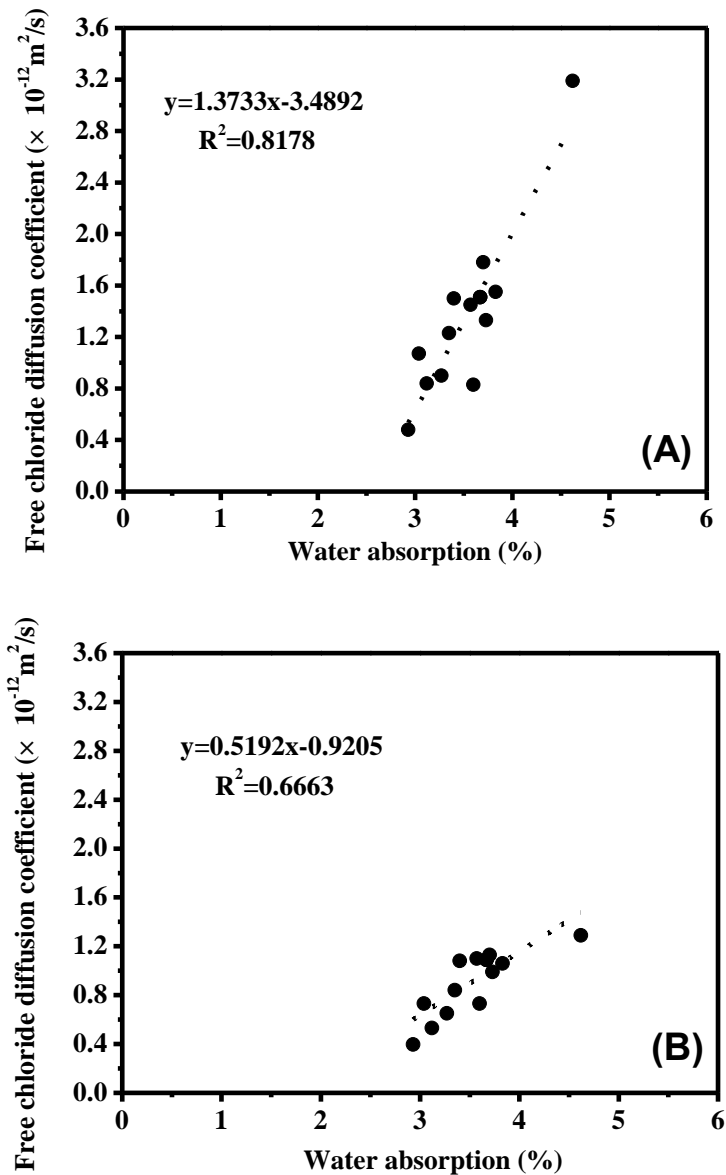


Fig.4-7 Relationship between water absorption and free chloride diffusion coefficient (D_f) at 90 days (A) and 180 days (B).

4.4 CONCLUDING REMARKS

This chapter investigated the free chloride profile, free chloride diffusion coefficient (D_f) and water absorption of AAFS concretes with different parameters, including GGBFS content, w/b, Na_2O content, SiO_2 content and s/a. The main outcomes of this chapter can be summarized as follows:

- 1) Compared with other parameters (including Na_2O content, SiO_2 content and s/a), GGBFS content and w/b presented the significant effect on the free chloride

profile of AAFS concrete. In SL30 and W50, the chloride intrusion was more severe. The measurement results showed that increasing GGBFS content from 30% to 100%, decreasing w/b from 0.50 to 0.40, increasing Na₂O content from 4% to 6%, and decreasing SiO₂ content from 6% to 4% were beneficial to the improvement of chloride resistance of AAFS concrete.

- 2) The D_f of AAFS concrete was generally lower than that of OPC concrete. FA/GGBFS and w/b had a more prominent effect on the D_f of AAFS concrete than Na₂O content, SiO₂ content and s/a. More C-A-S-H gels (by increasing GGBFS content) and lower w/b (≤ 0.45) were obviously beneficial. The D_f also gradually decreased with increasing Na₂O content and decreasing SiO₂ content, while s/a ratio had no obvious effect. In some cases (such as when SiO₂ content changed), the changes of chloride resistance and compressive strength of AAFS concrete were inconsistent. In order to explore influence mechanism of different parameters, the corresponding phase evolution and pore structure need to be analysed.
- 3) AAFS concretes with lower GGBFS content, higher w/b, lower Na₂O content and higher SiO₂ content exhibited higher water absorption, which is roughly consistent with the change trends of compressive strength and chloride resistance. However, the water absorption cannot fit well with the D_f of AAFS concrete, especially in the later stage. Not only porosity, but also pore size distribution, connectivity, tortuosity and chloride binding capacity affect the chloride transport. Moreover, the early pore structure analysis cannot correspond well to the long-term chloride resistance, because the changes of microstructure (phase evolution and pore structure) in different AAFS mixtures are different.

CHAPTER 5: MICROSTRUCTURE OF ALKALI-ACTIVATED FLY ASH-SLAG SYSTEMS AND ITS EFFECTS ON CHLORIDE RESISTANCE

*Note: the MIP results in this chapter are based on the manuscript entitled “Chloride diffusion in alkali-activated fly ash/slag concretes: Role of slag content, water/binder ratio, alkali content and sand-aggregate ratio”, by Jingxiao Zhang, Yuwei Ma, Jiazheng Zheng, Jie Hu, Jiyang Fu, Zuhua Zhang and Hao Wang, published in journal of **Construction and Building Materials**, 2020.*

5.1 INTRODUCTION

The previous chapters described the engineering properties and chloride resistance of AAFS concrete. Most of AAFS mixtures exhibited higher compressive strength and chloride resistance than OPC. However, an in-depth understanding of the influence mechanism of different parameters is still lacking. The reason why different mixtures have different chloride resistance needs to be explained in the aspect of microstructure (e.g. phase evolution and pore structure). The solid phases in hardened AAFS mainly consist of N-A-S-H and C-A-S-H gels, as well as un-reacted FA and GGBFS. As shown in Fig.2-1, the type, quantity and distribution of reaction products determine the pore structure and other properties (e.g. chloride binding capacity) of AAFS, which further determine the compressive strength and chloride resistance of AAFS. In order to better understand and assess the chloride resistance of AAFS, an extensive characterization of the reaction products is necessary. Therefore, in this chapter, the reaction products of AAFS are characterized with respect to the phase composition and chemical bond environment. Besides, the pore structure, which is mainly determined by gel pores (<10 nm) within reaction products and capillary pores (10–10,000 nm) as the remnants of initial water-filled space (Fig.2-2), is another vital factor influencing the chloride transport in AAFS. In the previous chapter, the water absorption cannot fit well with the D_f of AAFS concrete. It means that the influence of pore structure on chloride transport is from many aspects (e.g. porosity, pore size distribution, continuity, and tortuosity). Thus, in this chapter, the pore structure of AAFS is further characterized.

The main objective of this chapter is to study the microstructure (phase evolution and pore structure) of AAFS and its effects on chloride resistance. First, AAFS pastes with different GGBFS contents, water/binder ratios (w/b), Na_2O contents and SiO_2

contents (designed in Chapter 3) are prepared. To study the phase composition and chemical bond environment of the reaction products in different AAFS mixtures, X-ray diffraction (XRD) and Fourier transform infrared spectroscopy (FTIR) are applied. Mercury intrusion porosimetry (MIP) and nitrogen adsorption, which are commonly used experimental techniques in OPC, are also applied to study the pore structure of AAFS mixtures.

5.2 MATERIALS AND EXPERIMENTAL METHODS

5.2.1 MATERIALS AND MIXTURE PROPORTIONS

The materials (including precursors and activators) and mixture proportions used in this chapter to manufacture AAFS pastes are the same as those in Chapter 3. The chemical and physical properties (including chemical composition, particle size distribution, morphology and phase composition) of FA and GGBFS are given in Section 3.2.1. According to Section 3.2.2, a series of sodium silicate solutions with different Na₂O contents and SiO₂ contents were prepared by mixing analytic grade NaOH powder (purity > 98%), industrial grade waterglass (Na₂O = 12.19 wt.%, SiO₂ = 28.18 wt.%, H₂O = 58.92 wt.%) and water. PO 42.5 cement manufactured at Yangchun Cement Pty Ltd (Shandong Province, China) was utilized to prepare OPC pastes as reference samples.

The mixture proportions of different AAFS pastes are shown in Table 3-5 and denoted as: GGBFS content (SL), w/b (W), Na₂O content (N) and SiO₂ content (Si). In addition, OPC pastes with w/c = 0.45 (Table 3-5) were also prepared as reference samples.

5.2.2 SAMPLE PREPARATION

The mixing procedure of AAFS and OPC pastes was the same as that in Chapter 3 (Section 3.3.1). After mixing, the fresh pastes were poured into plastic bottles (Ø 36 mm × 68 mm) (Y. Ma, 2013a; Z. Yu, 2015). The bottles were then put on a vibrating table for 2 mins to remove air bubbles and sealed with a lid to prevent moisture loss (Y. Ma, 2013a; Z. Yu, 2015). After that, the sealed bottles were put in a curing chamber (20 ± 2°C). After 28 days of curing, the paste specimens were demoulded from plastic bottles and immersed in 3.5 wt.% NaCl solution until the testing day.

Besides, AAFS mortar specimens (2 mm × 2 mm × 2 mm) were obtained from the AAFS concrete specimens after 180 days of immersion in Chapter 4.

5.2.3 X-RAY DIFFRACTION (XRD)

In this chapter, X-ray diffraction (XRD) analysis was performed to identify crystalline and semi-crystalline phases of AAFS. Besides, OPC (w/c = 0.45) was used as a control group. XRD is a non-destructive analytical technique, which is based on observing the scattering intensity of the X-ray beam hitting the sample. The spacing of the crystal layers (path difference) of each kind of inclusion can be calculated according to Bragg's Law (Equation 15) (Bragg & Bragg, 1913).

$$2d \sin \theta = n\lambda \quad (15)$$

where d = the spacing of the crystal layers (path difference); θ = the incident/scattering angle; λ = the wavelength of the X-ray; and n = an integer, the "order" of reflection.

When a crystal is bombarded by the X-ray at an incidence angle (θ), the intense reflected X-ray is produced at the same scattering angle (θ) when a constructive interference occurs. In order for the waves to interfere constructively, the path difference (d) should be equal to an integer (n) multiple of the wavelength (λ). In XRD, the wavelength (λ) is known and the incidence angle (θ) at which the constructive interference occurs is measured. According to Bragg's Law (Equation 15), the path difference (d) for identification can be obtained.

In this chapter, the paste specimens after 180 days of immersion were crushed into pieces. Afterward, the fragments in the centre were chosen and ground into powder. The powder was then sieved through a 45 μm sieve to make the fineness as uniform as possible. After 2 days of drying in a vacuumed chamber (60 °C), the powder was analysed using a PW 3040/60 X'Pert Pro powder diffractometer (PANalytical, Netherland) with Cu-K α radiation ($\lambda = 1.5418 \text{ \AA}$). During the test, a 2θ scan range from 5 to 80° and a scanning step size of 0.012° were applied.

5.2.4 FOURIER TRANSFORM INFRARED SPECTROSCOPY (FTIR)

In this chapter, Fourier transform infrared spectroscopy (FTIR) analysis was

performed to determine the chemical bond environment of AAFS. According to the absorption of infrared radiation at various wavelengths, FTIR analysis can identify different chemical bonds (Y. Ma, 2013b). This technique is powerful to determine the structure of functional groups, which build up the molecules (J. Zhang, Shi, & Zhang, 2020). It can enable the characterization of Si–O–T (T is referred to tetrahedral Si or Al) symmetric and asymmetric bonds, which helps to track the changes of gel structures in AAFS as a function of various parameters. Therefore, it was considered that FTIR can provide reliable indicators of the changes in reaction sequence and product formation, as well as the chemical arrangement in AAFS and other AAMs (Dakhane, Madavarapu, Marzke, & Neithalath, 2017; J. Zhang et al., 2020).

The same powders used in XRD (from the specimens after 180 days of immersion) were analysed by a Tensor II FTIR spectrometer coupled with a Hyperion 2000 FTIR microscope (Bruker, Germany). Besides, the powder from the specimen before immersion (after 28 days of curing) was also analysed. The FTIR spectra were recorded over the wavenumber range from 2000 to 450 cm^{-1} . Each sample was tested at a resolution of 2 cm^{-1} with 16 scans.

5.2.5 MERCURY INTRUSION POROSIMETRY (MIP)

In this chapter, mercury intrusion porosimetry (MIP) was used to determine the total porosity and pore size distribution of AAFS mortar specimens (Xue et al., 2020). MIP is a useful technique to characterize the pore structure of various porous materials. Besides, it is the only available technique which can cover a broad range of pore sizes (from several nanometres to hundreds of micrometres) by applying different pressures (Aligizaki, 2005). The principle of MIP is to progressively record the volume of mercury intruding into porous samples under controlled pressure. The Washburn equation (Equation 16) (Washburn, 1921) can be used to calculate the average diameter of the pores intruded by mercury at each pressure step. As a result, the pore size distribution curve and differential pore size distribution curve can be plotted.

$$D = \frac{-4\gamma\cos\theta}{P} \quad (16)$$

where D = the average diameter of the pores; γ = the surface tension of mercury; θ = the contact angle between mercury and pore surface of the sample; and P = the applied pressure.

Mortar specimens with a size of 2 mm × 2 mm × 2 mm were obtained from the AAFS concrete specimens after 180 days of immersion in Chapter 4. Coarse aggregates were eliminated and the mortars were then immersed in ethanol for 2 weeks to stop further reaction. Afterwards, mortar samples were put in freeze-dryer for another 2 weeks of drying process. An Autopore IV 9500 Mercury Porosimeter (Micromeritics, USA) was used for the MIP measurement. The pressure ranged from 0.51 psia to 60000 psia was applied with a contact angle (θ) of 130° and a surface tension (γ) of 0.485 N/m. According to the Washburn equation (Equation 16), the pore size ranging from 353123.2 nm to 3.0 nm was detected.

5.2.6 NITROGEN ADSORPTION TEST

In this chapter, nitrogen adsorption was used to analyse the pores in the nanoscale. This technique can measure the specific surface area and distinguish the pore sizes from 0.3 to 300 nm (Gerhardt, 1988). When the clean solid surface is exposed to the gas, gas molecules impinge upon the solid and stay on the solid surface for a finite time, which is called adsorption (Aligizaki, 2005). The adsorption process is accompanied by the increase of sample mass and the decrease of gas pressure. According to the gas adsorption amount and the corresponding relative gas pressure, an isothermal adsorption curve can be obtained. The Barrett-Joyner-Halenda (BJH) model (Barrett, Joyner, & Halenda, 1951) can be used to derive the pore size distribution curve from the nitrogen adsorption result, which introduces the Kelvin equation (Equation 17) (Bahafid, Ghabezloo, Faure, Duc, & Sulem, 2018). The Kelvin equation can be used to relate the pore size to the relative pressure of nitrogen, at which capillary condensation occurs.

$$\ln \frac{p}{p_0} = -\frac{2\gamma V_L \cos \theta}{rRT} \quad (17)$$

where p = the equilibrium vapor pressure (N/m²) of the liquid in the pore with radius r (m), p_0 = the equilibrium reference pressure of the liquid on the plane surface (N/m²). γ = the surface tension of the liquid (N/m), V_L = the volume of the liquid

(m^3/mol), θ = the contact angle between the liquid and the pore wall (usually assumed to be 0), R = the gas constant (8.314 J/(K mol)), T = the temperature (K).

In this chapter, the paste specimens after 365 days of immersion were crushed into pieces. Afterward, the fragments in the centre were chosen and further crushed into small pieces (about 1-2 mm^3). Small pieces were then immersed in ethanol for 2 weeks to stop further reaction. Afterwards, small pieces were put in freeze-dryer for another 2 weeks of drying process. The equipment used for the nitrogen adsorption test was an ASAP 2460 Surface Area and Porosimetry Analyzer (Micromeritics, USA). Prior to the nitrogen adsorption test, the samples were degassed at 60 °C.

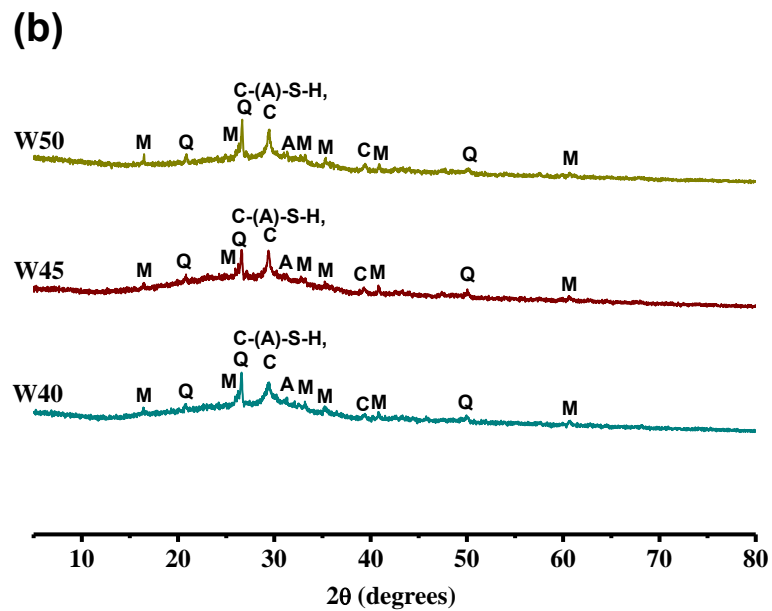
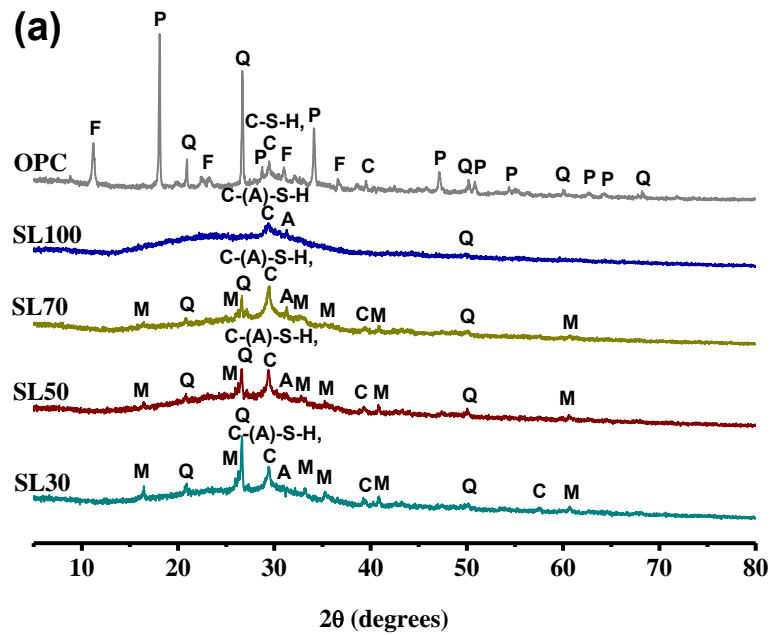
5.3 RESULTS AND DISCUSSION

5.3.1 PHASE EVOLUTION

5.3.1.1 X-RAY DIFFRACTION (XRD)

The XRD analysis of the OPC paste and AAFS pastes with different GGBFS contents, water/binder ratios (w/b), Na_2O contents and SiO_2 contents after 180 days of immersion in 3.5% NaCl solution is shown in Fig.5-1. In Fig.5-1(a), a low intensity peak centered at around $29^\circ 2\theta$ is identified in all AAFS mixtures, which indicates that the poorly crystalline C-(A)-S-H phases with tobermorite-like structure (PDF# 33-0306) always exist as one of the main reaction products, even in the mixture with low GGBFS content (SL30) (Ismail, Bernal, et al., 2013b; Ismail et al., 2014; Z. Shi, Shi, Wan, Li, et al., 2018). With the incorporation of FA, a low intensity hump around $26^\circ 2\theta$ indicates the high content of amorphous phases with the diffraction characteristics of N-A-S-H phases (Lee, Jang, & Lee, 2014; N. Li, Shi, Wang, Zhang, & Ou, 2017). Therefore, there should be a range of C-(A)-S-H and N-A-S-H gels co-existing within AAFS mixtures. Various crystalline phases can be observed in AAFS, and the FA content plays a decisive role in the appearance of these crystalline phases. The presence of quartz (Q, PDF# 46-1045) is identified in all AAFS mixtures as the remnant crystalline phase of FA and GGBFS, and the former plays a more important role. SL30, SL50 and SL70 show the peaks related to mullite (M, PDF# 15-0776), indicating the remnant crystalline phase of FA. With the increase of FA content from 30% to 70%, the intensities of the peaks related to quartz (Q, PDF# 46-1045) and mullite (M, PDF# 15-0776) increase. This fully shows

that quartz and mullite are not products, but remnant crystalline phases of FA, which is consistent with the X-ray diffraction analysis of FA (Fig.3-3). In addition, a small amount of akermanite (A, PDF #11-1611) is observed as the remnant crystalline phase of incompletely reacted GGBFS (Z. Shi, Shi, Wan, Li, et al., 2018). Calcite (C, PDF# 05-0586) is also observed as the product of carbonization.



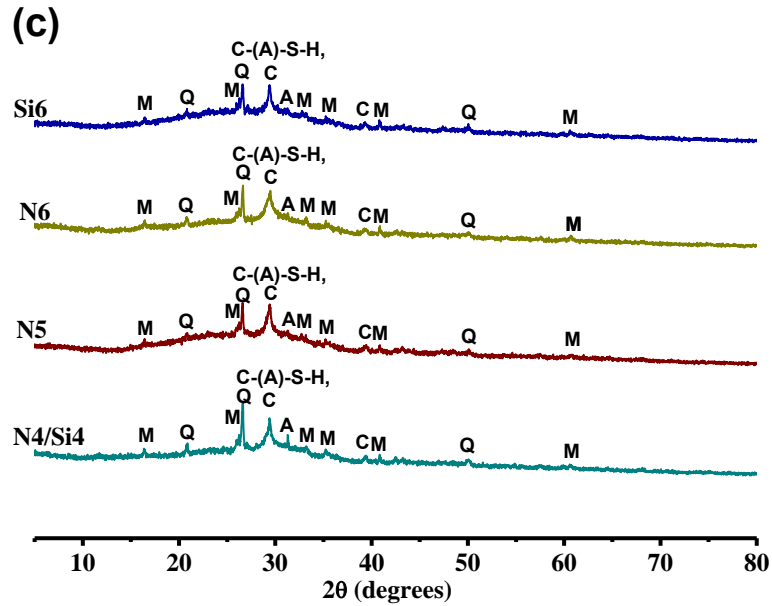


Fig.5-1 XRD patterns of OPC paste (a) and AAFS pastes with different (a) GGBFS contents, (b) water/binder ratios (w/b), (c) Na₂O contents and (c) SiO₂ contents after 180 days of immersion in 3.5% NaCl solution. M = mullite (Al₆Si₂O₁₃, PDF# 15-0776), Q = quartz (SiO₂, PDF# 46-1045), C = calcite (CaCO₃, PDF# 05-0586), A = akermanite (Ca₂Mg(Si₂O₇), PDF #11-1611), C-S-H = calcium silicate hydrate (PDF# 33-0306), C-(A)-S-H = calcium alumina silicate hydrate (PDF# 33-0306), P: portlandite (Ca(OH)₂, PDF# 44-1481), F: Friedel's salt (Ca₂Al(OH)₆Cl·2H₂O, PDF# 42-0558).

Fig.5-1(b) and Fig.5-1(c) show that the positions and intensities of the peaks in AAFS pastes with different water/binder ratios, Na₂O contents and SiO₂ contents are not significantly different, indicating no significant change in phase evolution. It means that the effects of w/b, Na₂O content and SiO₂ content on peak positions are relatively limited. This observation seems to be inconsistent with some previous studies. The possible explanation is that these parameters selected in this study according to the literature review in Chapter 2 are moderate, and their variation ranges are very small. J. Zhang et al. (2020) reported that when the w/b increased from 0.30 to 0.50, the peak assigned to C-(A)-S-H phases became more intense and narrower, due to a higher degree of structural ordering. Ismail, Bernal, et al. (2013b) claimed that the intensity of the peak assigned to C-(A)-S-H phases decreased with increasing w/b from 0.40 to 0.60, because the addition of water reduced the alkalinity and thus influenced the binder development of AAFS. In Fig.5-1(b), no change is found in either direction with increasing w/b from 0.40 to 0.50. It was investigated that higher Na₂O content could accelerate the reaction kinetics (Gebregziabihier,

Thomas, & Peethamparan, 2016) and lead to the formation of more reaction products (Y. Ma, Hu, & Ye, 2012). However, Zuo, Nedeljković, and Ye (2018) and J. Zhang et al. (2020) reported that the effect of Na₂O content on the type of reaction products was limited. As shown in Fig.5-1(c), no obvious change is found in the positions of the peaks with increasing Na₂O content from 4% to 6%, which is consistent with previous studies (Z. Shi, Shi, Wan, Li, et al., 2018; J. Zhang et al., 2020). Note that in hydroxide-activated mixes, the change of peak intensity caused by the change of Na₂O content may be more pronounced. Z. Shi, Shi, Wan, Li, et al. (2018) found that in hydroxide-activated GGBFS, the increase of Na₂O content from 6% to 8% led to a significant increase in the intensity of the peak assigned to C-(A)-S-H phases. Earlier studies (Haha, Le Saout, Winnefeld, & Lothenbach, 2011; Haha, Lothenbach, et al., 2011; S.-D. Wang & Scrivener, 1995) reported that C-(A)-S-H phases were more crystalline in hydroxide-activated mixes than in silicate-activated mixes. As a result, the reflections associated with C-(A)-S-H phases were much clearer in hydroxide-activated mixes (Z. Shi, Shi, Wan, Li, et al., 2018). As shown in Fig.5-1(c), no obvious change is found in the positions of the peaks with increasing SiO₂ content from 4% to 6%. As described in Section 2.5.2.2, the SiO₂ content (4%-6%) used in this study is moderate, so its change in this range has relatively little effect on Ca/Si ratio and hence the type of reaction products. According to the above results, it can be inferred that although the optimal values of w/b, Na₂O content and SiO₂ content change with the chemical compositions of raw materials, almost the same type of products can be obtained by controlling these parameters within a reasonable range.

Unlike the OPC paste in Fig.5-1(a), the formation of Friedel's salt (Ca₂Al(OH)₆Cl·2H₂O, PDF# 42-0558), also known as hydrocalumite belonging to layered double hydroxides (LDH), is not observed in all AAFS pastes, indicating a lack of chemical binding capacity. This result is consistent with the previous studies (Babaee & Castel, 2018; Ismail, Bernal, Provis, San Nicolas, et al., 2013), in which the chloride binding of AAFS was mainly determined by physical adsorption. However, there are indications that the pure GGBFS-based geopolymers are capable of binding Cl⁻ through not only surface adsorption but also inter-layer ion-exchange in Mg-Al LDH and Ca-Al LDH (also known as AFm phase), with the former having a more important role (Ke, Bernal, et al., 2017b; M. Khan, Kayali, & Troitzsch,

2016). In the present study, the lack of chemical binding in AAFS is attributed to the absence of Mg-Al LDH and Ca-Al LDH, which is consistent with the viewpoint in the previous study (Babae & Castel, 2018). The GGBFS in this study has a lower Mg content compared to that in the previous study (M. Khan et al., 2016). In addition, J. Zhang et al. (2019a) claimed that the amount of LDH was lower in the silicate-activated slag. The availability of free Si in sodium silicate solution may enhance the incorporation of Al in C-A-S-H gels during the initial reaction stage (Morandea & White, 2015), resulting in less Al being available to form LDH. Moreover, more Si species in sodium silicate solution leads to a lower Ca/Si ratio. Therefore, Mg^{2+} may be involved in the formation of C-(A)-S-H gels rather than the formation of Mg-Al LDH (M. Khan & Castel, 2018). Furthermore, the incorporation of FA, which leads to lower Mg content and lower Ca/Si ratio in the mixture, may also hinder the formation of LDH. Due to the lack of chemical binding, the surface area of gels to physically adsorb Cl^- is particularly important for the chloride binding capacity of AAFS in this study.

The XRD analysis provides important information regarding the different phases of AAFS. However, because the main reaction products of AAFS are disordered, the results are relatively limited. The techniques which are sensitive to the bonding environments in non-crystalline phases should be also applied (Ismail et al., 2014), e.g. FTIR discussed in the following section.

5.3.1.2 FOURIER TRANSFORM INFRARED SPECTROSCOPY (FTIR)

Fig.5-2, Fig.5-3, Fig.5-4 and Fig.5-5 show the FTIR spectra of AAFS pastes with different GGBFS contents, water/binder ratios (w/b), Na_2O contents and SiO_2 contents before (after 28 days of curing) and after 180 days of immersion in 3.5% NaCl solution. Compared with the FTIR spectra of FA (Fig.3-4) and GGBFS (Fig.3-8), the intensity of the absorption band at 1647 cm^{-1} , which is assigned to the bending vibration of H-OH bonds in bound water (Ismail, Bernal, et al., 2013b; Ismail et al., 2014; Lee & Lee, 2015; Z. Shi, Shi, Wan, Li, et al., 2018), appears to increase in all mixtures. It means the formation of hydrated reaction products, such as N-A-S-H gels and C-A-S-H gels. The asymmetric stretching vibration of O-C-O bonds in CO_3^{2-} groups at 1417 cm^{-1} and the out-of-plane bending vibration of CO_3^{2-} groups at 876 cm^{-1} (although some researchers claim that it may be the asymmetric stretching

vibration of AlO^{4-} groups in the glass phases) are also observed (García-Lodeiro et al., 2008; Ismail et al., 2014; Z. Shi, Shi, Wan, Li, et al., 2018; P. Yu et al., 1999; J. Zhang et al., 2019a, 2020), which is consistent with the calcite observed in the XRD pattern (Fig.5-1).

The spectra of AAFS pastes show particular differences in the main absorption band in the range of $1300\text{-}800\text{ cm}^{-1}$, which is assigned to the anti-symmetric stretching vibrations of Si–O–T bonds (T: tetrahedral Si or Al) within reaction products (Lecomte et al., 2006; Lodeiro, Macphee, Palomo, & Fernández-Jiménez, 2009). As described in Section 3.2.1.1, the lower wavenumber means depolymerized and/or highly substituted silicate gels (e.g. C-A-S-H gels), while the higher wavenumber is due to more crosslinked and/or highly siliceous gels (e.g. N-A-S-H gels) (Ismail, Bernal, et al., 2013b). After 180 days of immersion, the peak of the main absorption band shifts slightly toward a higher wavenumber in all mixtures, which may be due to the increase of the overall degree of crosslinking of the gels (Ismail et al., 2014) and/or lower Al substitution (Fernández-Jiménez & Palomo, 2005).

5.3.1.2.1 EFFECT OF GGBFS CONTENT

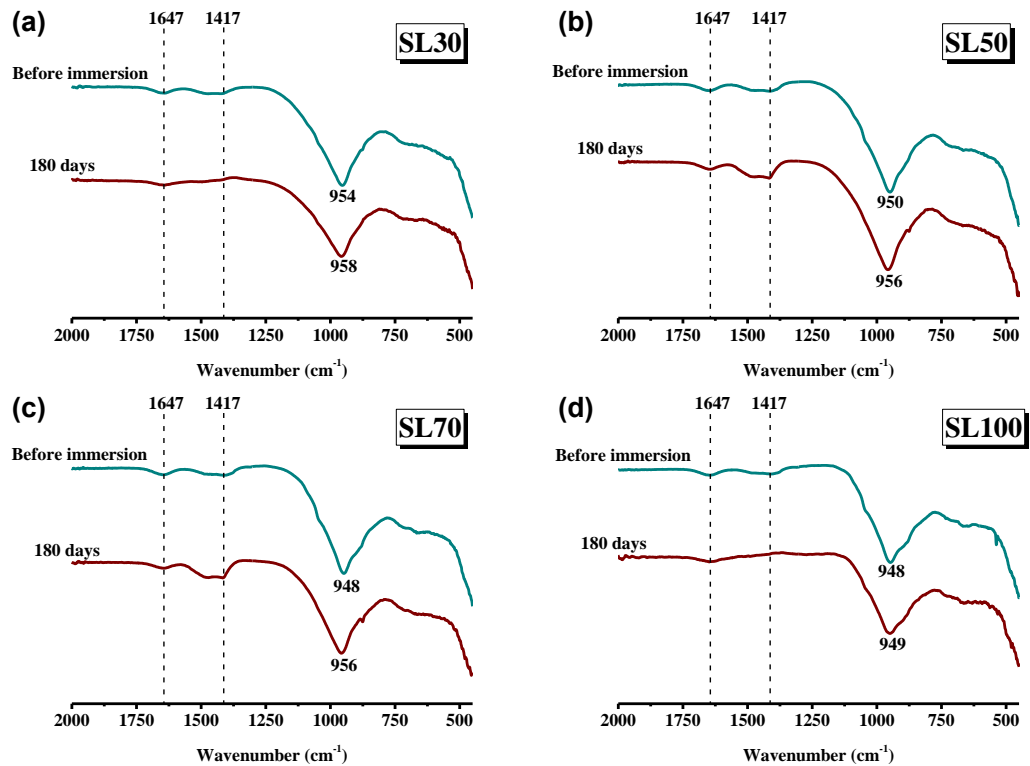


Fig.5-2 FTIR spectra of AAFS pastes with different GGBFS contents before (after 28 days of curing) and after 180 days of immersion in 3.5% NaCl solution.

As shown in Fig.5-2, with the decrease of GGBFS content, the peak of the main absorption band shifts toward a higher wavenumber. This may indicate that the Al content in C–A–S–H gels derived from the activation of GGBFS decreases in the presence of FA (Fernández-Jiménez & Palomo, 2005), or that the activation of FA promotes the formation of N–A–S–H gels with a higher polymerization degree of Si (Maria Criado, Aperador, & Sobrados, 2016; J. Zhang et al., 2020). Compared with GGBFS (16.89% Al₂O₃ in Table 3-3), FA is rich in Al (25.55% Al₂O₃ in Table 3-1). Therefore, the latter explanation seems more likely (Ismail et al., 2014). This explanation is consistent with the observation obtained by deconvolution of ²⁹Si magic angle spinning nuclear magnetic resonance (MAS NMR) spectra for AAFS (Bernal et al., 2013), in which the coexistence of N–A–S–H gels and C–A–S–H gels in AAFS was confirmed by the different effects of carbonation on each gel structure. Besides, with the increase of FA, there may be more unreacted FA with numerous SiQ₃ and SiQ₄ units, resulting in a higher wavenumber (Ismail et al., 2014).

In AAFS, the formation of C–A–S–H gels may be earlier than that of N–A–S–H gels. At the early age, there are a large number of Ca^{2+} due to the high dissolution rate of GGBFS. Therefore, Si and Al components tend to react with Ca^{2+} to form C-A-S-H gels, in which the polymerization degree is limited by their short chain structure (Gao, Yu, & Brouwers, 2015). The existence of the poorly crystalline C-(A)-S-H phases with tobermorite-like structure (PDF# 33-0306) in all AAFS mixtures, even in SL30, confirms the above view (Fig.5-1). In the mixture with high GGBFS content, when most Ca^{2+} are consumed, there may be no extra Si and Al to form N-A-S-H gels (e.g. in SL100), or the remaining Si, Al and alkalis may not be enough for the polymerization of long chain structure (SiQ_3 and SiQ_4 units) in the short term (e.g. in SL50 and SL70) (Gao et al., 2015). This well explains the small gap between the FTIR spectra of SL50, SL70 and SL100 before immersion (after 28 days of curing). In the mixture with low GGBFS content (e.g. SL30), Ca^{2+} are quickly consumed, thus the formation of N-A-S-H gels plays a dominant role, resulting in a higher wavenumber. Besides, Babae and Castel (2018) believed that when GGBFS content was low (<50%), Ca^{2+} tended to adhere to N-A-S-H gels through charge balance instead of forming C-A-S-H gels. Compared with the formation of C-A-S-H gels, the formation of N-A-S-H gels is much slower, leading to less reaction products at the early age. As a result, the compressive strength (Fig.3-9 and Fig.3-12) and chloride resistance (Fig.4-5) of SL30 are significantly lower, especially at the early stage.

In the later stage, the continuous dissolution of FA leads to more Si and Al components. Therefore, in addition to SL30, the formation of N-A-S-H gels may also play a dominant role in SL50 and SL70 in the later stage. This explains why the wavenumber of the main absorption increases in SL50 and SL70 after 180 days of immersion (Fig.5-2b and Fig.5-2c), just as in SL30 (Fig.5-2a) and AAFA (pure FA system) reported in the previous study (Ismail et al., 2014). Due to the increase of the overall degree of crosslinking, the peak of the main absorption band shifts toward a higher wavenumber in AAFS mixtures. In SL100 (AAS, pure GGBFS system), the wavenumber of the main absorption remains almost unchanged before and after 180 days of immersion (Fig.5-2d), indicating that the overall degree of crosslinking is almost unchanged. It can be inferred that N-A-S-H gels are not formed in this system.

Besides, the dissolution rate of Si is lower than that of active Al (Fernández-Jiménez & Palomo, 2005). Most Al components may dissolve and participate in the reaction at the early stage. In the later stage, more Si components may be dissolved from FA, which can increase the Si/Al ratio. As a result, gels with lower Al substitution are formed, which can also lead to the increase of the wavenumber of the main absorption band.

5.3.1.2.2 EFFECT OF WATER/BINDER RATIO (W/B)

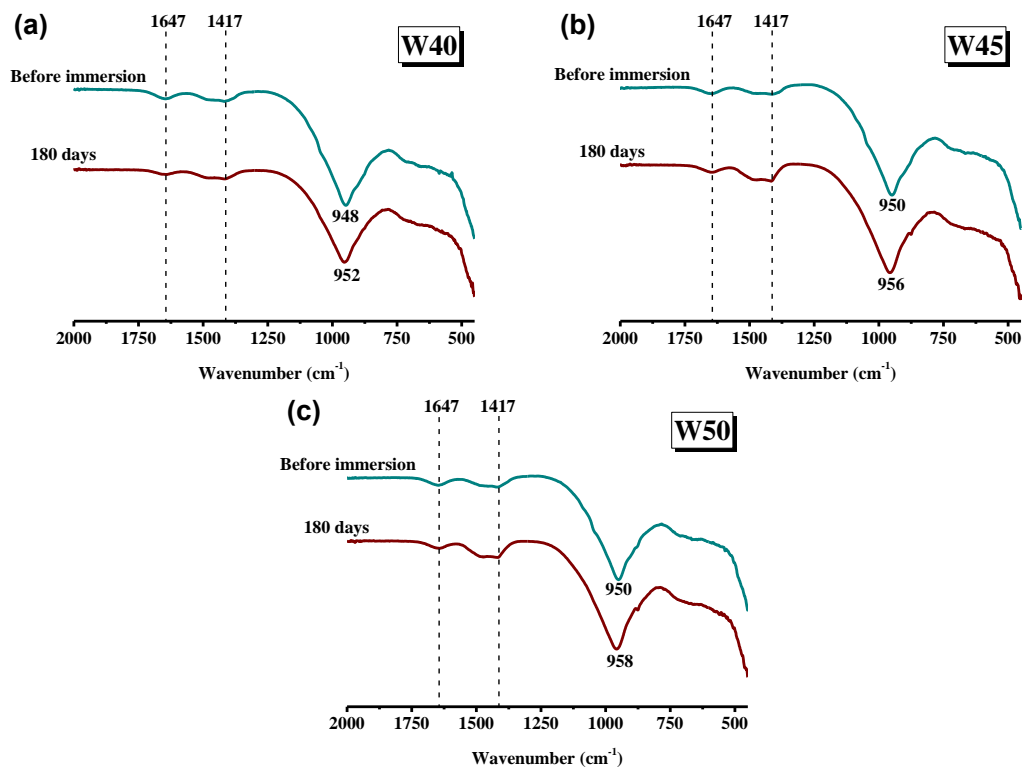


Fig.5-3 FTIR spectra of AAFS pastes with different water/binder ratios (w/b) before (after 28 days of curing) and after 180 days of immersion in 3.5% NaCl solution.

As shown in Fig.5-3, before immersion (after 28 days of curing), the effect of w/b on the peak of the main absorption band is relatively limited, indicating no significant changes in phase evolution. However, after 180 days of immersion, the peak of the main absorption band shifts toward a higher wavenumber in W45 and W50. It may be due to the continuous reaction of FA and the formation of more N-A-S-H gels to fill capillary pores in the later stage, which have higher polymerization degree of Si (Maria Criado et al., 2016; J. Zhang et al., 2020) and lower Al substitution (Fernández-Jiménez & Palomo, 2005). Compared with W45 and W50, the capillary

pores of W40 can be well filled in the initial stage. As a result, the continuous reaction of FA has relatively little effect on the later phase evolution and main absorption band (Fig.5-3a). The above explanation is consistent with the change trend of the compressive strength (Fig.3-9 and Fig.3-13) and chloride resistance (Fig.4-5) of W40, W45 and W50.

Besides, with the increase of w/b, the intensity of the peak at 1417 cm^{-1} , which is related to the asymmetric stretching vibration of O–C–O bonds in CO_3^{2-} groups, is much higher. It indicates the formation of more calcium carbonate (Z. Shi, Shi, Wan, Li, et al., 2018). Higher w/b may lead to larger initial water-filled space and hence more capillary pores. As a result, in addition to the rate of chloride transport, the rate of carbonation of gels also increases.

5.3.1.2.3 EFFECT OF ALKALI CONTENT

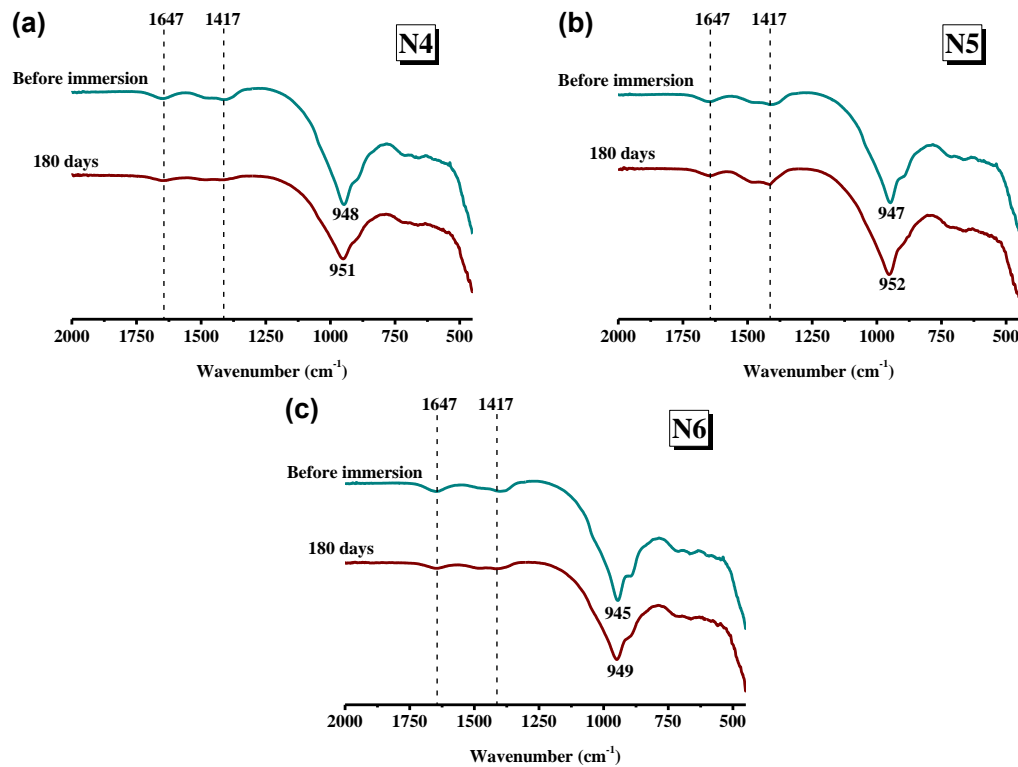


Fig.5-4 FTIR spectra of AAFS pastes with different Na_2O contents before (after 28 days of curing) and after 180 days of immersion in 3.5% NaCl solution.

As shown in Fig.5-4, with the increase of Na_2O content from 4% to 6%, the wavenumber of the main band decreases slightly, which is inconsistent with previous research results (Z. Shi, Shi, Wan, Li, et al., 2018; J. Zhang et al., 2020). Z. Shi, Shi,

Wan, Li, et al. (2018) reported that no shift of the wavenumber of the main band was observed in AAS when Na₂O content increased from 6% to 8%, indicating that the phase evolution did not change. J. Zhang et al. (2020) found that the peak of the main absorption band in AAFS moved slightly toward a higher wavenumber with the increase of Na₂O content from 6% to 8%, which might be related to the higher reaction degree of FA. In this study, the change trend of the peak of the main absorption band is consistent with the results of AAFA (Y. Ma, 2013a). Y. Ma (2013a) claimed that specimens with higher Na₂O content exhibited a lower wavenumber of the main absorption band, indicating that the resulting gels had a lower Si/Al ratio. It is known that the dissolution of FA can be accelerated by higher alkalinity, and the dissolution rate of active Al is faster than that of Si (Fernández-Jiménez & Palomo, 2005). Higher Na₂O content may lead to higher Al content in the early stage, resulting in higher Al substitution in gels. As a result, the wavenumber of the main absorption band decreases (Fernández-Jiménez & Palomo, 2005). This view is consistent with the change trend of compressive strength (Fig.3-9 and Fig.3-14) and chloride resistance (Fig.4-5) at the early age.

As the reaction proceeds, the dissolution of Si in FA continues. More Si components are gradually incorporated into gels, which increases the Si/Al ratio and decreases the Ca/Si ratio in reaction products. Therefore, after 180 days of immersion, the peak of the main absorption band in each mixture shifts toward a higher wavenumber due to lower Al substitution (Fernández-Jiménez & Palomo, 2005) and higher polymerization degree of Si (Maria Criado et al., 2016; J. Zhang et al., 2020). Despite all this, due to the initial gap, mixtures with higher Na₂O content still exhibit a lower wavenumber of the main absorption band after 180 days of immersion.

5.3.1.2.4 EFFECT OF SILICATE CONTENT

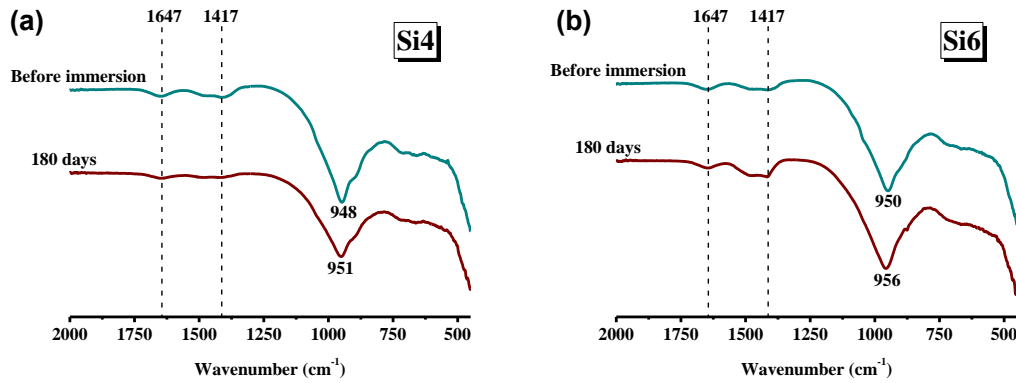


Fig.5-5 FTIR spectra of AAFS pastes with different SiO₂ contents before (after 28 days of curing) and after 180 days of immersion in 3.5% NaCl solution.

As shown in Fig.5-5, with the increase of SiO₂ content from 4% to 6%, the peak of the main absorption band shifts toward a higher wavenumber, which is consistent with previous studies (Z. Shi, Shi, Wan, Li, et al., 2018; J. Zhang et al., 2019a; S. Zhang et al., 2021). The activator with higher SiO₂ content can provide more Si components at the early stage of alkaline activation, which decreases the Ca/Si ratio and increases the Si/Al ratio in reaction products. Lower Ca/Si ratio may promote the formation of gels with a higher polymerization degree of Si (Maria Criado et al., 2016; J. Zhang et al., 2020). Higher Si/Al ratio may lead to lower Al substitution in gels (Fernández-Jiménez & Palomo, 2005). Both higher polymerization degree and lower Al substitution can lead to a higher wavenumber of the main absorption band. However, it should be noted that when SiO₂ content is too high, the alkalinity may be reduced (Babae & Castel, 2018; X. Hu et al., 2019; S.-D. Wang et al., 1994).

Compared with SL30, Si4 and Si6 (also named as SL50) have relatively sufficient Ca²⁺. Therefore, the formation of C-A-S-H gels may still play a dominant role in the early stage. X. Hu et al. (2019) considered that in AAFS with high GGBFS content (80%), higher SiO₂ content resulted in the formation of C-A-S-H gels with lower Ca/Si ratio instead of N-A-S-H gels. This well explains why higher SiO₂ content and higher FA content have the same effect on the peak of the main absorption band, but have the opposite effect on the compressive strength of AAFS paste (Fig.3-9). With the increase of SiO₂ content, more Si components are provided. The formation of more C-A-S-H gels with lower Ca/Si ratio can better fill capillary pores, thereby

increasing the compressive strength. Besides, the higher surface area of C-A-S-H gels with lower Ca/Si ratio was also considered to contribute to the improvement of compressive strength (Kunther, Ferreiro, & Skibsted, 2017). By comparison, the increase of FA content leads to the lack of Ca^{2+} , which hinders the formation of the less porous and pore-filling C-A-S-H gels. As a result, with the increase of FA content in AAFS, although the peak of the main absorption band shifts toward a higher wavenumber, the compressive strength decreases. However, the assumption of the previous study (X. Hu et al., 2019) may not be applicable to this study. Compared with the 80% GGBFS content used in the previous study (X. Hu et al., 2019), the 50% GGBFS content used in Si4 and Si6 is still insufficient. Therefore, the Ca content may not be particularly sufficient. As a result, in addition to higher FA content, higher SiO_2 content may also lead to the conversion of main reaction products from C-A-S-H gels to N-A-S-H gels, leading to the movement of the main band to a higher wavenumber. The lower reaction rate may result in more capillary pores, which is consistent with the increase of D_f (Fig.4-5). This view seems to be inconsistent with the increase of compressive strength (Fig.3-9 and Fig.3-15). One possible explanation is that the volume or diameter of gel pores in Si4 is larger, resulting in lower compressive strength.

5.3.2 PORE STRUCTURE

5.3.2.1 MERCURY INTRUSION POROSIMETRY (MIP)

5.3.2.1.1 TOTAL POROSITY

MIP can determine the required range of pore sizes (Y. Ma et al., 2018). Although there are some arguments that MIP cannot reflect the real pore size distribution of material due to the different pore shape and “ink-bottle” effect, MIP can reflect different pore structure for equally prepared samples. The porosity and pore size distribution of AAFS mortars with different GGBFS contents, water/binder ratios (w/b), Na_2O contents and SiO_2 contents after 180 days of immersion in 3.5% NaCl solution are shown in Fig.5-6. The results show that both porosity and pore size distribution of AAFS are strongly affected by GGBFS content, w/b, Na_2O content and SiO_2 content. Overall, with the increase of GGBFS content, Na_2O content and SiO_2 content, the total porosity of AAFS decreases, which is consistent with the

previous study (X. Hu et al., 2019). The total porosity of AAFS decreases from 10.18% to 8.32% with the increase of GGBFS content from 30% to 100%. Increasing Na₂O content from 4% to 6% reduces the total porosity of AAFS from 8.99% to 7.18%. The mixture with 6% SiO₂ content (Si6) also exhibits a lower total porosity (8.55%) compared with the mixture with 4% SiO₂ content (Si4, 8.99%). By comparison, higher total porosity (12.72%) is observed in AAFS with higher w/b (W50).

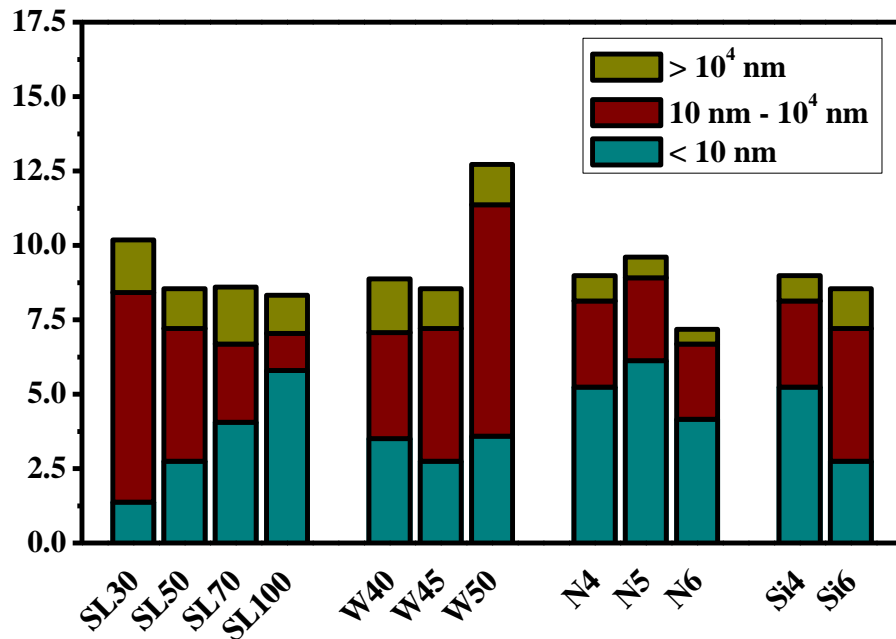


Fig.5-6 Porosity and pore size distribution of AAFS mortars with different GGBFS contents, water/binder ratios (w/b), Na₂O contents and SiO₂ contents after 180 days of immersion in 3.5% NaCl solution, derived from MIP.

According to common sense, lower total porosity means that the matrix is denser, resulting in higher chloride resistance. The effects of GGBFS content, w/b and Na₂O content on the change trend of the total porosity seem to be consistent with the change trend of the free chloride diffusion coefficient (D_f) of AAFS concrete after 180 days of immersion in Chapter 4 (Fig.4-5). However, the increase of SiO₂ content from 4% to 6% increases the D_f of AAFS concrete from $0.84 \times 10^{-12} \text{ m}^2/\text{s}$ to $1.09 \times 10^{-12} \text{ m}^2/\text{s}$ (Fig.4-5), which is inconsistent with the reduction of total porosity. This result is different from previous studies (Babae & Castel, 2018; X. Hu et al., 2019), although the results of previous studies are also different. X. Hu et al. (2019) found both the total porosity and chloride migration coefficient (D_{NSSM}) of AAFS (80% GGBFS content) decreased with the increase of Ms from 0 to 1.5. However, Babae

and Castel (2018) claimed that increasing SiO₂ content generally increased the chloride diffusion coefficient (D) of AAFS due to a more porous and permeable matrix, especially for samples dominated by FA (25% GGBFS content). Fig.5-7 correlates the total porosity and D_f after 180 days of immersion. It is observed that the total porosity cannot fit well with the D_f (R² = 0.4437). One possible explanation is that not only total porosity, but also pore size distribution can affect the chloride transport in AAFS (X. Hu et al., 2019). This view is consistent with the research result of water absorption in Section 4.3.4.

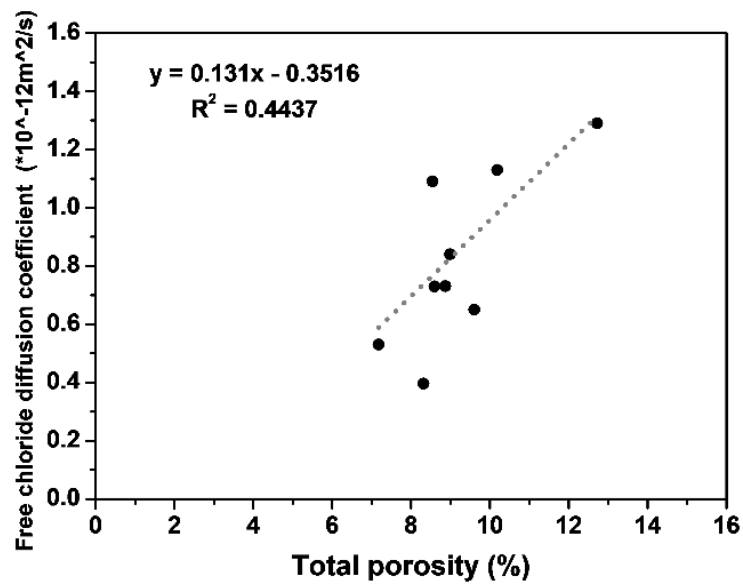


Fig.5-7 Relationship between total porosity and free chloride diffusion coefficient (D_f) after 180 days of immersion in 3.5% NaCl solution.

5.3.2.1.2 CAPILLARY PORES

From the pore size distribution shown in Fig.5-6, the change of the total porosity is mainly attributed to the volume change of gel pores (<10 nm) formed in reaction products and capillary pores (10–10,000 nm) as the remnants of initial water-filled space (Fig.2-2) (H. F. Taylor, 1997), whereas the volume change of air voids (>10,000 nm) caused by bubbles trapped is not significant. C Shi, Tang, and Li (1989) investigated the effect of pore size distribution on the properties of AAMs and found that shrinkage and creep were mainly controlled by gel pores, while strength and permeability were mainly affected by capillary pores. Furthermore, X. Hu et al. (2019) claimed that the chloride transport in AAFS seems to be more related to capillary pores rather than gel pores or air voids, which is consistent with the results

of OPC (Glass & Buenfeld, 2000; P. Mehta & Monteiro, 2014). P. Mehta and Monteiro (2014) believed that gel pores were too small to have adverse effects on chloride resistance. Glass and Buenfeld (2000) reported that air voids were not connected with each other. As shown in Fig.5-6, higher GGBFS content, lower w/b, higher Na₂O content and lower SiO₂ content result in the decrease of the volume of capillary pores. Compared with other parameters, the effect of Na₂O content on the volume of capillary pores is relatively limited. The change trend of the volume of capillary pores seems to be consistent with that of the free chloride diffusion coefficient (D_f) of AAFS concrete after 180 days of immersion in Chapter 4 (Fig.4-5). Fig.5-8 correlates the volume of capillary pores and D_f after 180 days of immersion. Compared with the poor correlation between total porosity and D_f in Fig.5-7 ($R^2 = 0.4437$), a good correlation can be obtained between the volume of capillary pores and D_f in Fig.5-8 ($R^2 = 0.8060$). Therefore, the increase of D_f , which means the decrease of chloride resistance, seems to be more related to the increase of the volume of capillary pores rather than total porosity. This finding is consistent with the previous study (X. Hu et al., 2019).

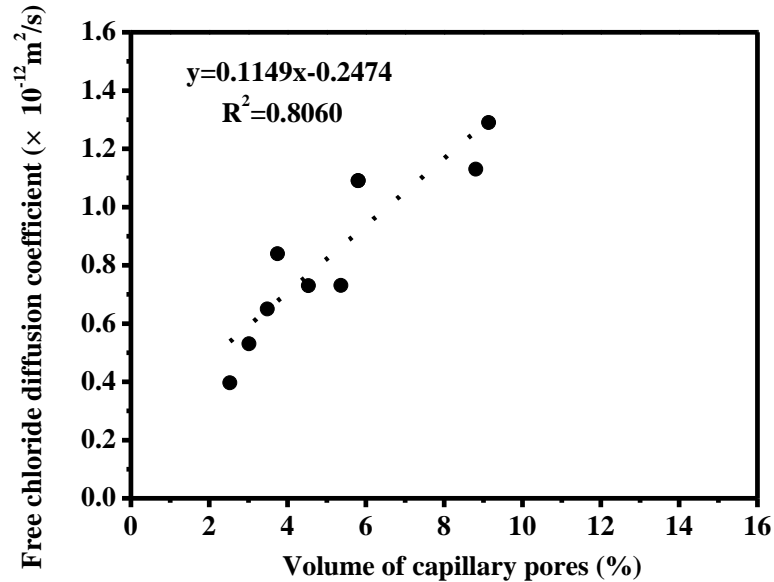


Fig.5-8 Relationship between volume of capillary pores and free chloride diffusion coefficient (D_f) after 180 days of immersion in 3.5% NaCl solution.

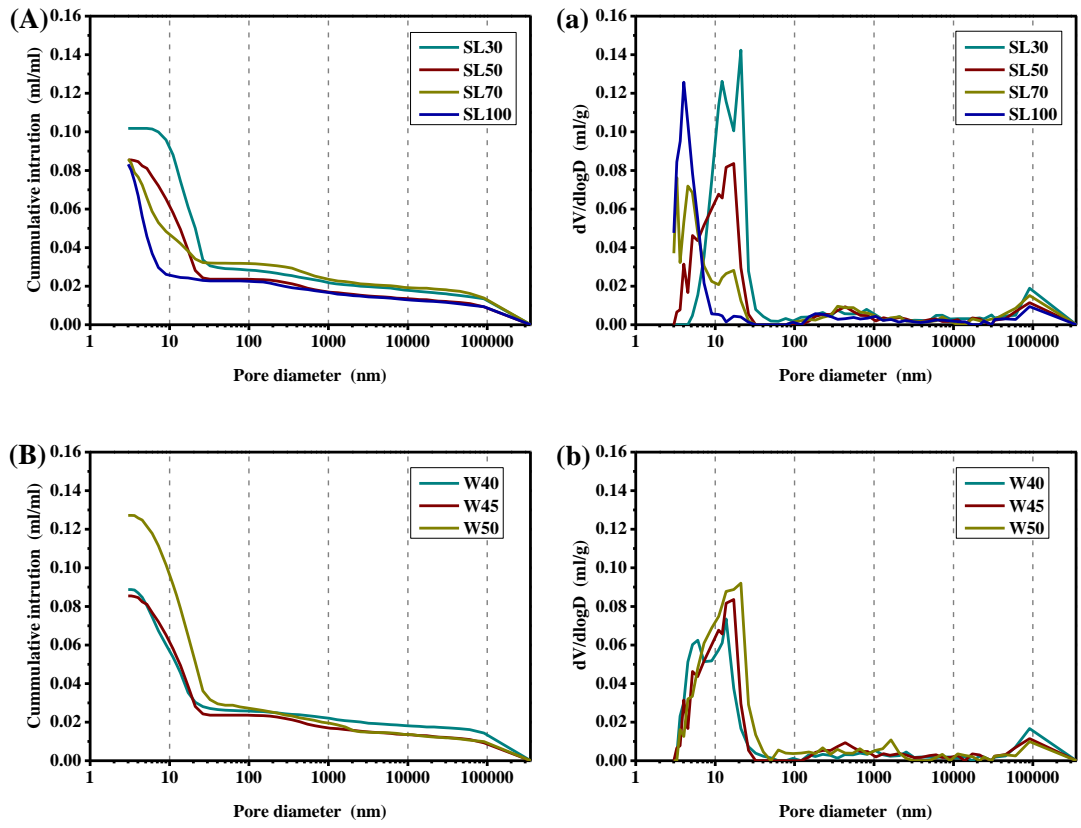
However, as described in Section 2.2.2.1, gel pores (< 10 nm) instead of capillary pores dominate the pore structure of AAFS and AAS (Fig.2-3). Although the

chloride transport in AAFS and other AAMs, as well as OPC, is mainly determined by capillary pores (Glass & Buenfeld, 2000; X. Hu et al., 2019; P. Mehta & Monteiro, 2014; Pack, Jung, Song, Kim, & Ann, 2010), Powers, Copeland, and Mann (1959) reported that capillary pores were regarded as disconnected when the capillary porosity reduced to 18%-20%. As shown in Fig.5-6, in this study, the total porosity of all AAFS mixtures is lower than 18% (7.18%-12.72%). Therefore, unlike the capillary pores with a continuous network in OPC, the capillary pores in AAFS are usually disconnected and connected through gel pores (Lloyd et al., 2009). This may mitigate the effect of capillary pores on chloride transport. In addition, this may also lead to a very significant ‘ink-bottle’ effect, which should be considered when analyzing MIP data (Lloyd et al., 2009). As the narrow channels for the movement of Cl^- , gel pores (<10 nm) may also have a certain effect on chloride transport in AAFS. Therefore, not only capillary pores but also gel pores should be analyzed.

5.3.2.1.3 THRESHOLD PORE DIAMETER

Fig.5-9 presents the effects of GGBFS content, w/b, Na_2O content and SiO_2 content on the pore size distribution (A, B, C and D) and differential pore size distribution (a, b, c and d) of AAFS mortar after 180 days of immersion in 3.5% NaCl solution, which are derived from MIP. From the differential curves (Fig.5-9a, b, c and d), different peaks corresponding to different pore diameters are observed. For example, as shown in Fig.5-9a, SL30 and SL50 display distinct peaks at around 20 nm (SL30 has bimodal curve), while the peaks of SL70 and SL100 are at around 4 nm (SL70 has bimodal curve). In Fig.5-9b, W40 presents two peaks at 5 nm and 15 nm, while the other two mixtures (W50 and W45) exhibit only one peak at around 20 nm. In Fig.5-9c, N4 presents two peaks at 5 nm and 10 nm, while N5 and N6 exhibit only one peak at around 5 nm. In Fig.5-9d, Si4 has two peaks at 5 nm and 10 nm, while Si6 exhibits only one peak at around 20 nm. The peak in differential curve corresponds to the pore system of AAFS. In view of the ion diffusion characteristic, the pore diameter corresponding to the peak (also known as threshold pore diameter) can be regarded as the minimum diameter of pores that form a continuous network throughout materials (G. Ye, 2003). With higher GGBFS content, lower w/b, higher Na_2O content and lower SiO_2 content, the threshold pore diameter moves to a lower pore diameter, indicating a denser pore system. This change trend seems to be

consistent with the change trend of the free chloride diffusion coefficient (D_f) of AAFS concrete after 180 days of immersion in Chapter 4 (Fig.4-5). Note that the threshold pore diameter is less than 10 nm in many mixtures (SL70, SL100, N4, N5, N6 and Si4), which confirms the effect of gel pores on the chloride transport in AAFS.



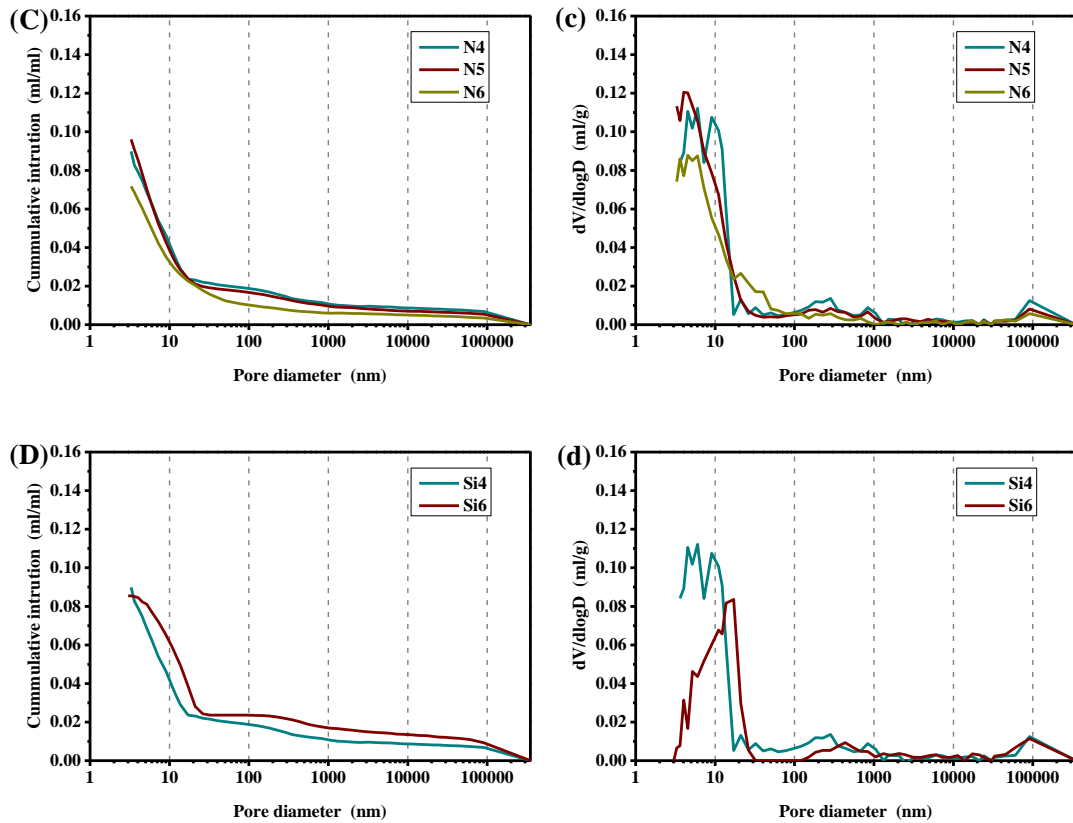


Fig.5-9 Effects of GGBFS content, w/b, Na₂O content and SiO₂ content on pore size distribution of AAFS mortar after 180 days of immersion in 3.5% NaCl solution, derived from MIP.

To compare the pore structure between AAFS and OPC, Fig.5-10 presents the pore size distribution and differential pore size distribution of OPC (42.5, w/b=0.4) at the age of 180 days (data and figure from (Z. Yu, 2015)). The corresponding OPC concrete was reported to have a chloride migration coefficient ($D_{N_{SSM}}$) of 11×10^{-12} m²/s (Z. Yu, 2015). The total porosity of OPC is higher than that of the AAFS mixtures investigated in this study. Furthermore, as observed from the differential pore size distribution curve, OPC presents a threshold pore diameter at 30 nm, which is 2-3 times larger than that of the AAFS mixtures investigated in this study. As mentioned above, the threshold pore diameter reflects the pore diameter that completes the connected pore pathway in materials. In view of the higher threshold pore diameter of OPC, the chloride penetration in OPC concrete is expected considerably faster than that in AAFS concrete. The $D_{N_{SSM}}$ of OPC concrete (11×10^{-12} m²/s) is around 10 times larger than the D_f of AAFS concrete investigated in this study, which confirms the above view.

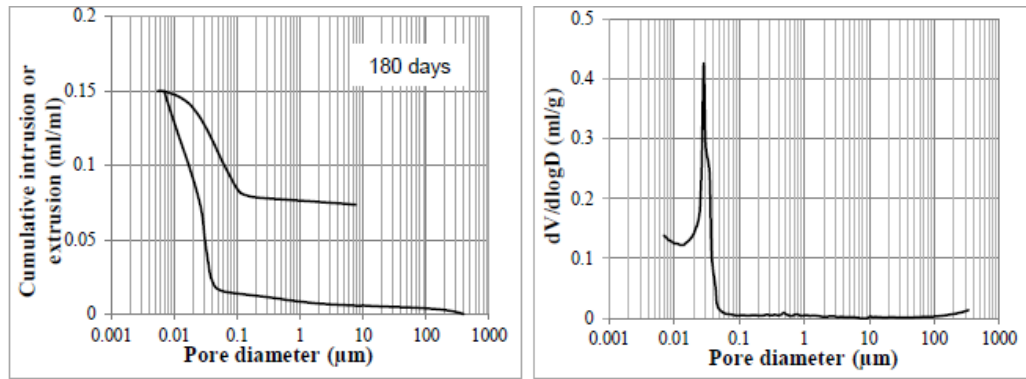


Fig.5-10 Pore size distribution of OPC (42.5, w/b=0.4) at 180 days, derived from MIP (Z. Yu, 2015).

As mentioned above, the total porosity of all AAFS mixtures investigated in this study is low (7.18%-12.72%), thus the capillary pores in AAFS are considered to be disconnected and connected through gel pores (Lloyd et al., 2009). As the narrow channels in the connected pore pathway, gel pores (<10 nm) also have a certain effect on chloride transport in AAFS. Therefore, the threshold pore diameter becomes vital to the ion transportation, although it is less than 10 nm in many mixtures (SL70, SL100, N4, N5, N6 and Si4). This explains the mismatch between the volume of capillary pores and D_f in some mixtures. As shown in Fig.5-6, there is little difference in the volume of capillary pores between W40 and W45, but the difference of 180-d D_f between W40 and W45 ($0.36 \times 10^{-12} \text{ m}^2/\text{s}$) is obvious in Fig.4-5, even greater than that between W45 and W50 ($0.20 \times 10^{-12} \text{ m}^2/\text{s}$). The lower threshold pore diameter of W40 (15 nm) than W45 (20 nm) can well explain this problem (Fig.5-9b). This view can also be used to explain the mismatch between the volume of capillary pores and D_f in N4 and N5. In addition to lower volume of capillary pores and smaller threshold pore diameter, higher tortuosity may also be beneficial. In general, tortuosity varies inversely with porosity. Using X-ray microtomography, John L Provis et al. (2012) found that in AAFS, with the increase of GGBFS content, the diffusion tortuosity increased, especially when GGBFS content was higher than 50% (Fig.5-11). Besides, the diffusion tortuosity in Fig.5-11 also increased with extended curing time, which is the result of continuous reaction. These findings are consistent with the decrease of D_f in this study (Fig.4-5).

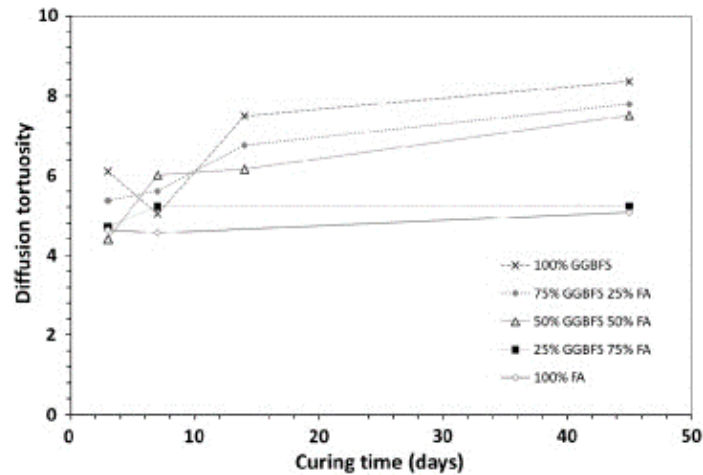


Fig.5-11 Relationship between diffusion tortuosity and curing time for AAFS, derived from X-ray microtomography (John L Provis et al., 2012).

5.3.2.2 NITROGEN ADSORPTION

Compared with MIP, nitrogen adsorption can provide more detailed information about the gel pores in AAFS mixtures (Y. Ma, 2013a; Y. Ma et al., 2018). Fig.5-12, Fig.5-13, Fig.5-14 and Fig.5-15 show the pore size distribution curves (a) and differential pore size distribution curves (b) of AAFS pastes with different GGBFS contents, water/binder ratios (w/b), Na₂O contents and SiO₂ contents after 365 days of immersion in 3.5% NaCl solution, which are obtained by nitrogen adsorption. The differential curves of AAFS (Fig.5-12b, Fig.5-13b, Fig.5-14b and Fig.5-15b) generally exhibit unimodal profiles, which is consistent with previous studies (T. Liu et al., 2020; Nedeljkovic et al., 2016; T. Yang et al., 2018; S. Zhang et al., 2021). However, Y. Ma (2013a) and Y. Ma et al. (2018) reported that the differential curves of AAFA (pure FA system) generally showed two peaks. Notably, nitrogen adsorption cannot provide detailed information about capillary pores, thus it needs to be analyzed together with the results of MIP or other measurement methods, e.g. scanning electron microscopy (SEM).

In AAFS, the pore volume in pore size distribution curves (Fig.5-12a, Fig.5-13a, Fig.5-14a and Fig.5-15a) and pore diameter corresponding to the peak in differential pore size distribution curves (Fig.5-12b, Fig.5-13b, Fig.5-14b and Fig.5-15b) change with different parameters. Because the result of nitrogen adsorption is primarily related to gel pores, the increase of pore volume in pore size distribution curves does not necessarily mean a worse pore structure (Y. Ma, 2013a; Y. Ma et al., 2018; T.

Yang et al., 2018). The formation of more gels, which may lead to the increase of the volume of gel pores, can fill capillary pores (Fig.2-2) and result in the higher chloride resistance of AAFS. In differential curves, the shift of the peak to a lower pore diameter may mean more gel pores, probably due to the formation of more reaction products. Therefore, it can be inferred that capillary pores can be well filled and chloride resistance of AAFS can be improved. This can be confirmed by MIP (Section 5.3.2.1) or other measurement methods, e.g. scanning electron microscopy (SEM). However, the lower pore volume in pore size distribution curves and lower threshold pore diameter in differential pore size distribution curves may also be attributed to the smaller diameter of gel pores.

5.3.2.2.1 EFFECT OF GGBFS CONTENT

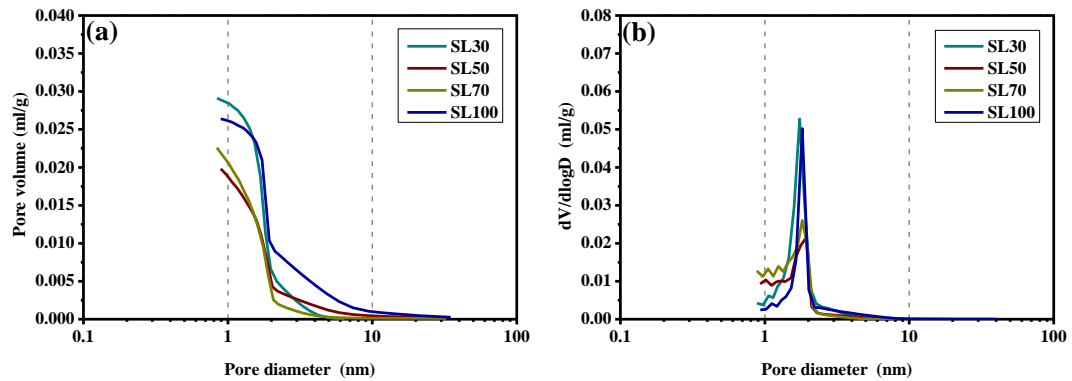


Fig.5-12 Pore size distribution of AAFS pastes with different GGBFS contents after 365 days of immersion in 3.5% NaCl solution, derived from nitrogen adsorption.

As shown in Fig.5-12a, with the increase of GGBFS content from 50% to 100%, the pore volume increases from 0.020 ml/g to 0.026 ml/g. It means that SL100 has more gel pores than SL70 and SL50, resulting from the formation of more gels. This view is consistent with the result of MIP (Fig.5-6 and Fig.5-9), in which the volume of gel pores increases with the increase of GGBFS content, while the volume of capillary pores decreases with the increase of GGBFS content. It can also be confirmed by the compressive strength development (Fig.3-9 and Fig.3-12), with is primarily determined by capillary pores (S. Zhang et al., 2021). The refinement of pore structure with increasing GGBFS content from 50% to 100% can also be observed in the differential pore size distribution curve (Fig.5-12b), which can be reflected by the movement of the threshold pore diameter to a smaller value (from 1.9 nm to 1.8 nm). Besides, due to the excessive shrinkage of SL100 (pure GGBFS system), the

microcracks caused by shrinkage may also lead to the increase of pore volume (Collins & Sanjayan, 2001; Kutti et al., 1992). This may be the reason why SL100 has many gel pores larger than 2 nm (Fig.5-12a). However, SL30 shows a higher pore volume than SL50, SL70 and SL100, which is consistent with the previous study (S. Zhang et al., 2021). The possible reason is that the measurement result is disturbed by a large number of capillary pores. The result of MIP (Fig.5-6 and Fig.5-9) and the lower compressive strength determined by capillary pores (Fig.3-9 and Fig.3-12) can confirm this view. S. Zhang et al. (2021) also reported that the pore structure of AAFS paste with 30% GGBFS content had a large number of capillary pores.

5.3.2.2.2 EFFECT OF WATER/BINDER RATIO (W/B)

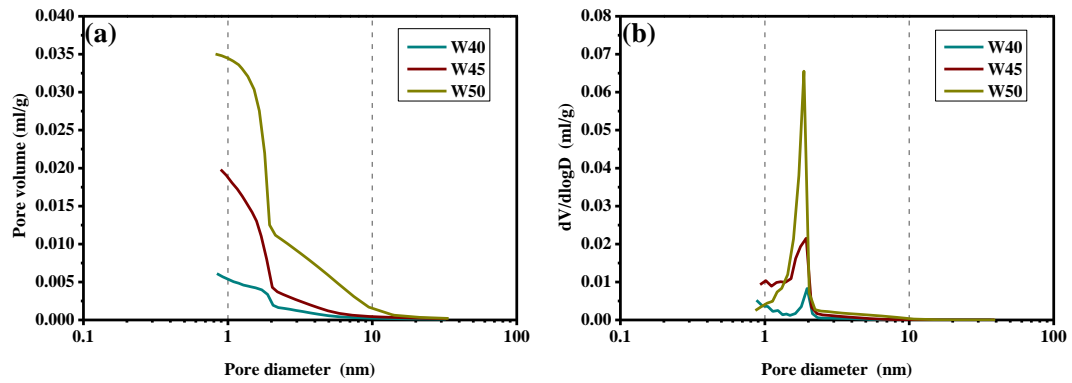


Fig.5-13 Pore size distribution of AAFS pastes with different water/binder ratios (w/b) after 365 days of immersion in 3.5% NaCl solution, derived from nitrogen adsorption.

As shown in Fig.5-13a, with the increase of w/b, not only the volume of capillary pores increases, but also the volume of gel pores increases, which is not found by MIP (after 180 days of immersion). The most likely explanation is that more space is provided and more products are generated over time. M. C. G. Juenger and Jennings (2001) assessed the microstructure of OPC by nitrogen adsorption, and found that when the water/cement ratio (w/c) was low, there was smaller space in which C-S-H could grow. In AAFS, the formation of N-A-S-H gels and C-A-S-H gels may also be affected by space limitation. More capillary pores mean more space for the growth of N-A-S-H gels and C-A-S-H gels. Therefore, high w/b may not only lead to more capillary pores at the early stage, but also increase the volume of gel pores at the later stage. The above view is consistent with the result of FTIR (Fig.5-3). In

W40, the continuous reaction of FA has relatively little effect on phase evolution in the later stage. In the differential pore size distribution curve (Fig.5-13b), with higher w/b, the peak shifts toward a lower pore diameter (from 2.0 nm to 1.9 nm). This may also be because more products lead to more gel pores. It is worth noting that although higher volume and lower threshold pore diameter caused by higher w/b mean the formation of more gels, the corresponding pore structure is still worse because there are more capillary pores at the beginning. The result of MIP (Fig.5-6 and Fig.5-9) and the lower compressive strength determined by capillary pores (Fig.3-9 and Fig.3-13) can confirm the above view.

5.3.2.2.3 EFFECT OF ALKALI CONTENT

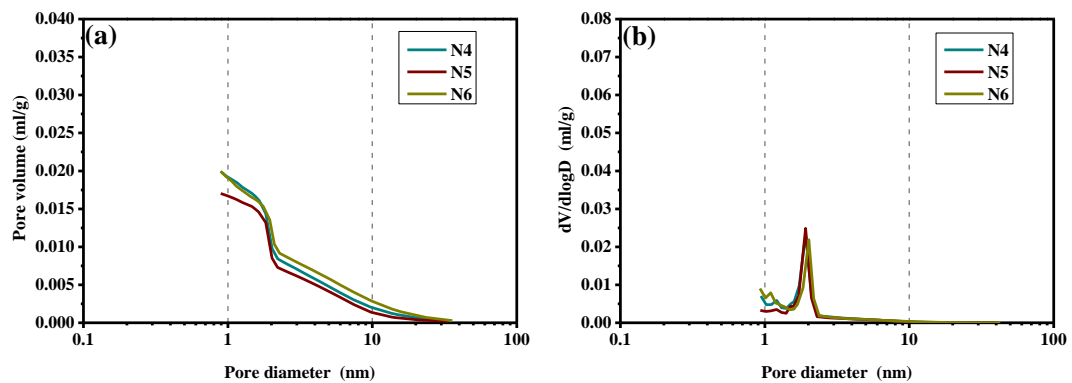


Fig.5-14 Pore size distribution of AAFA pastes with different Na_2O contents after 365 days of immersion in 3.5% NaCl solution, derived from nitrogen adsorption.

In Fig.5-14a and b, specimens with different Na_2O content exhibit similar pore size distribution curves and differential pore size distribution curves. This finding is consistent with the result of AAFA (pure FA system) reported in the previous studies (Y. Ma, 2013a; Y. Ma et al., 2018). As shown in Fig.5-14a, the pore volume of N5 is the smallest (0.017 ml/g), indicating fewer reaction products or finer gel pores. The results of FTIR (Fig.5-4) show that higher Na_2O content leads to a higher degree of reaction and hence more reaction products. Therefore, the latter explanation seems more likely. The lowest threshold pore diameter (Fig.5-14b) and highest compressive strength (Fig.3-9) of N5 confirm the above inference. Y. Ma (2013a) and Y. Ma et al. (2018) also held the same view when studying the effect of Na_2O content on AAFA. Babae and Castel (2018) claimed that higher alkalinity hindered the diffusion of Ca^{2+} from GGBFS to form C-A-S-H gels. This may be the reason for the worse result

of N6. However, this explanation contradicts the decrease of the wavenumber of the main band (Fig.5-4). A more reasonable explanation seems to be that too high alkalinity promotes the efflorescence (Z. Zhang et al., 2014) and drying shrinkage (Y. Ma & Ye, 2015) of AAFS.

5.3.2.2.4 EFFECT OF SILICATE CONTENT

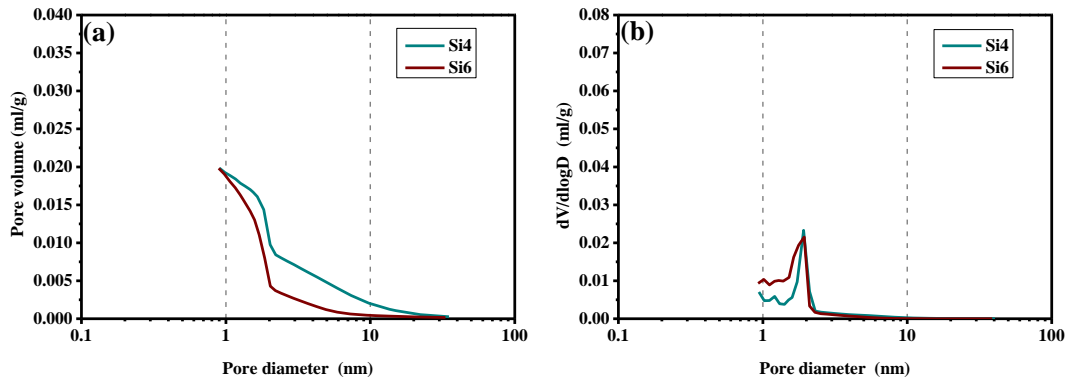


Fig.5-15 Pore size distribution of AAFS pastes with different SiO₂ contents after 365 days of immersion in 3.5% NaCl solution, derived from nitrogen adsorption.

As shown in Fig.5-15a and b, Si4 and Si6 exhibit almost the same pore volume (around 0.020 ml/g) and pore diameter corresponding to the peak (around 1.9 nm). However, in Si4, the proportion of pores larger than 2 nm is larger. This finding is consistent with the larger volume of gel pores measured by MIP (Fig.5-6 and Fig.5-9), which can only measure pores larger than 3 nm. In addition to capillary pores, large gel pores may also be harmful to the compressive strength of AAFS. This explains why Si4 has smaller volume of capillary pores (Fig.5-6) but lower compressive strength (Fig.3-9 and Fig.3-15). However, S. Zhang et al. (2021) claimed that with the increase of Ms from 1.0 to 1.5, the pore volume increased and the compressive strength decreased. The reason for the different results may be that the w/b used in the previous study (0.32) is significantly lower than that in this study (0.45), which leads to the excessive SiO₂ concentration in the activator. S. Zhang et al. (2021) reported that before Ms reached 1.0, with the increase of Ms, the pore volume decreased and the compressive strength increased, which confirmed the above view. Therefore, the optimum SiO₂ content in AAFS is not constant and may be affected by w/b and other parameters.

5.3.3 RELATIONSHIPS BETWEEN PHASE EVOLUTION, PORE STRUCTURE

AND CHLORIDE RESISTANCE

According to the literature review in Chapter 2 (Fig.2-1), different parameters (e.g. GGBFS content, w/b, Na₂O content and SiO₂ content) can seriously affect the pore structure, chloride binding capacity, pore solution and phase evolution of AAFS and other AAMs, resulting in different chloride resistance. Among these influencing factors, pore structure plays the most decisive role. Besides, the type and quantity of different phases also affect the pore structure and chloride binding capacity, which consequently determine chloride resistance. Therefore, pore structure and phase evolution are used to establish the linkages between different parameters and chloride resistance of AAFS concrete in this study, as shown in Fig.5-16. According to the phase composition and chemical bond environment measured by XRD and FTIR, as well as the pore structure measured by MIP and nitrogen adsorption, the relationship between the microstructure and chloride resistance of AAFS can be established, and the main influence mechanism of different parameters can be explained.

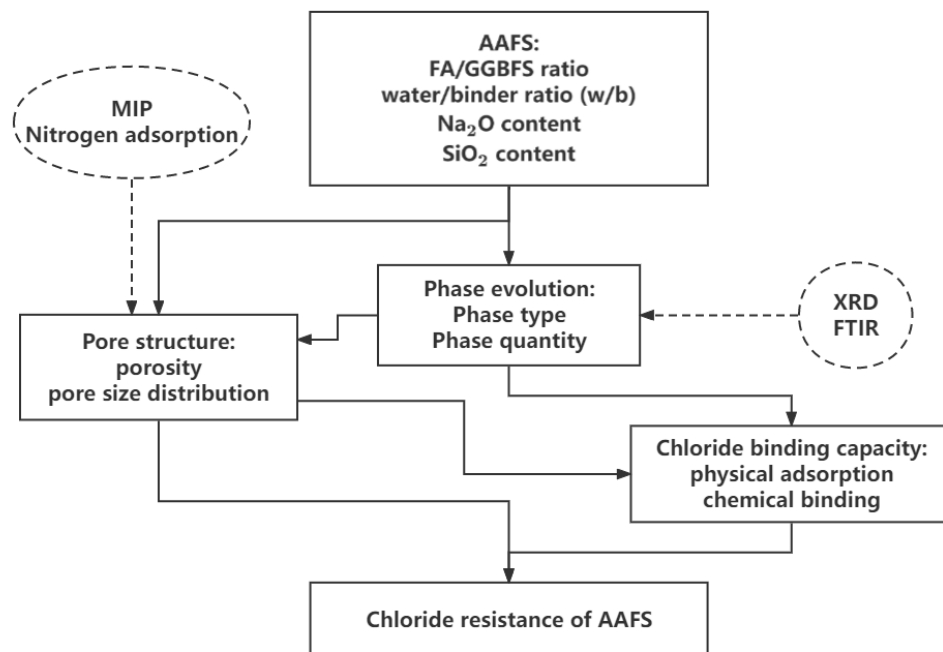


Fig.5-16 Effects of phase evolution and pore structure on chloride resistance of AAFS.

5.3.3.1 INFLUENCE MECHANISM OF GGBFS CONTENT

Based on XRD patterns (Fig.5-1a), N-A-S-H and C-A-S-H gels can coexist in AAFS.

Besides, Friedel's salt is not observed in all AAFS mixtures, which seems to indicate a lack of chemical binding capacity. This finding is consistent with the previous studies (Babaee & Castel, 2018; Ismail, Bernal, Provis, San Nicolas, et al., 2013) and the remarkably good match between the measured total and free chloride profiles described in Chapter 4. Therefore, the chloride binding of AAFS may be mainly determined by physical adsorption. The result of FTIR (Fig.5-2) shows that higher GGBFS content is conducive to the formation of C–A–S–H gels, which is consistent with most previous studies (Babaee & Castel, 2018; Bondar et al., 2019; X. Hu et al., 2019; Ismail, Bernal, Provis, San Nicolas, et al., 2013; Lee & Lee, 2016; Tennakoon et al., 2017; T. Yang et al., 2014; Zhu et al., 2014). Because the formation of C–A–S–H gels has a faster reaction rate, more reaction products are formed, which can be confirmed by the increase of the volume of gel pores measured by nitrogen adsorption (Fig.5-12). As a result, capillary pores (remnants of initial water-filled space as shown in Fig.2-2) can be rapidly filled, resulting in the reduction of volume of capillary pores (Fig.5-6) and threshold pore diameter (Fig.5-9) measured by MIP. C Shi et al. (1989) and X. Hu et al. (2019) claimed that the compressive strength, permeability and chloride resistance of AAMs were mainly controlled by capillary pores. As shown in Fig.3-9, Fig.3-12 and Fig.4-5, the compressive strength and chloride resistance increase with the increase of GGBFS content, which is consistent with the above view. Besides, a good correlation between the volume of capillary pores and D_f ($R^2 = 0.8060$) is found in Fig.5-8. However, unlike the capillary pores with a continuous network in OPC, the capillary pores in AAFS may be disconnected and connected through gel pores (Lloyd et al., 2009; Powers et al., 1959). As the narrow channels for the movement of Cl^- , large gel pores may also have a certain effect on the chloride transport in AAFS, especially for the mixtures with a threshold pore diameter less than 10 nm (SL70, SL100, N4, N5, N6 and Si4).

The result of FTIR (Fig.5-2) indicates that the continuous reaction of FA seems to lead to the formation of N–A–S–H gels in the later stage. Although the results of MIP (Fig.5-6 and Fig.5-9) and nitrogen adsorption (Fig.5-12) show that this compensation is insufficient compared with the initial gap in pore structure, this compensation leads to the reduction of the gap in the compressive strength (Fig.3-12) and chloride resistance (Fig.4-5) of mixtures with different FA/ GGBFS in the later

stage. As shown in Fig.5-12, SL100 has more gel pores larger than 2 nm, which may be the microcracks caused by the excessive shrinkage of pure GGBFS system (Collins & Sanjayan, 2001; Kutti et al., 1992). It seems to be the reason for the decline of the compressive strength of SL100 in the later stage (Fig.3-12).

5.3.3.2 INFLUENCE MECHANISM OF WATER/BINDER RATIO (W/B)

XRD patterns (Fig.5-1b) show that the positions and intensities of the peaks in AAFS mixtures with different w/b are not significantly different. However, FTIR spectra (Fig.5-3) show that the continuous reaction of FA in the later stage seems to have a greater impact in the mixture with higher w/b. The possible explanation is that higher w/b results in more capillary pores (remnants of initial water-filled space as shown in Fig.2-2) at the beginning, which provides more space for the growth of gels in the later stage. The larger volume of gel pores measured by nitrogen adsorption (Fig.5-13) confirms the above view. The same result was also obtained in OPC (M. C. G. Juenger & Jennings, 2001). Note that the formation of more gels is just to make up for the huge initial gap. The larger volume of capillary pores (Fig.5-6) and threshold pore diameter (Fig.5-9) measured by MIP show that the capillary pores caused by higher w/b are still not well filled after 180 days of immersion. However, Fig.4-5 shows that the D_f of W50 decreases significantly from 90 days to 180 days.

However, the lower compressive strength caused by higher w/b is maintained all the time (Fig.3-13). In addition to more and larger capillary pores measured by MIP (Fig.5-6 and Fig.5-9), more and larger gel pores measured by nitrogen adsorption (Fig.5-13) may also be harmful to the compressive strength of AAFS. Based on the above results, compared with the pores acting on compressive strength, the pores acting on chloride resistance seem to need a larger diameter. Therefore, although both compressive strength and chloride resistance depend on pore structure, there is no simple linear relationship between them. Compared with compressive strength, chloride resistance is easier to be improved by the filling of capillary pores in the later stage.

5.3.3.3 INFLUENCE MECHANISM OF ALKALI CONTENT

As shown in the result of XRD (Fig.5-1c), the positions and intensities of the peaks in AAFS pastes with Na_2O contents are not significantly different. However, higher

Na₂O content may accelerate the reaction kinetics (Gebregziabihier et al., 2016) and lead to the formation of more reaction products (Y. Ma et al., 2012). The reduction of the wavenumber of the main absorption band caused by higher Al substitution (Fernández-Jiménez & Palomo, 2005) in FTIR spectra (Fig.5-4) confirms the above view. According to the pore size distribution derived from MIP (Fig.5-9), higher Na₂O content leads to lower total porosity and threshold pore diameter. Higher compressive strength in Fig.3-14 and lower D_f in Fig.4-5 also confirm this, especially at the early stage.

However, the result of nitrogen adsorption (Fig.5-14) shows that N6 has a worse gel pore structure than N5. The most likely reason is that too high alkalinity promotes the efflorescence (Z. Zhang et al., 2014) and drying shrinkage (Y. Ma & Ye, 2015). This also explains the smaller gap between the compressive strength of N5 and N6 in the later stage (Fig.3-14). As described in Section 5.3.3.2, pores acting on chloride resistance appear to require a larger diameter than pores acting on compressive strength. Because these cracks grow larger over time, compared with the compressive strength (Fig.3-14), the chloride resistance of N5 cannot catch up with that of N6 at 180 days (Fig.4-5).

5.3.3.4 INFLUENCE MECHANISM OF SILICATE CONTENT

As shown in XRD patterns (Fig.5-1c), there is no significant difference in the position and intensity of the peaks in Si4 and Si6. From the result of FTIR (Fig.5-5), the increase of SiO₂ content from 4% to 6% seems to result in the conversion of main reaction products from C-A-S-H gels to N-A-S-H gels. This may result in slower formation of reaction products to fill capillary pores. The larger volume of capillary pores (Fig.5-6) and threshold pore diameter (Fig.5-9) of Si6 measured by MIP confirm the above view. However, the above findings seem to be inconsistent with the change trend of compressive strength (Fig.3-9 and Fig.3-15). The result of nitrogen adsorption (Fig.5-15) shows that Si4 has more gel pores larger than 2 nm, which may be the reason for the lower compressive strength.

As described in Section 5.3.3.2 and Section 5.3.3.3, the pores acting on chloride resistance seem to need a larger diameter than the pores acting on compressive strength. Therefore, the effect of large gel pores on compressive strength seems to be

greater than that on chloride resistance. This leads to lower compressive strength but higher chloride resistance of Si4. Although the volume of capillary pores of Si4 is lower (Fig.5-6), Si4 has more large gel pores, which result in the reduction of compressive strength. However, compared to capillary pores, these large gel pores have relatively little effect on chloride resistance. Note that the continuous reaction of FA may have a greater impact on Si6 in the later stage, leading to the smaller gap between the chloride resistance of Si4 and Si6 (Fig.4-5). The obvious shift of the peak of the main absorption band in the result of FTIR (Fig.5-5b) confirms the above view. In a longer time scale, the chloride resistance of Si6 may exceed that of Si4.

5.4 CONCLUDING REMARKS

In this chapter, the microstructure (including phase evolution and pore structure) of AAFS is studied to explore the influence mechanism of different parameters (including GGBFS content, w/b, Na₂O content and SiO₂ content) on chloride resistance. Based on the results and analyses, the main outcomes are summarised as follow:

- 1) XRD patterns show that N-A-S-H and C-A-S-H gels can coexist in AAFS. Higher GGBFS content promotes the formation of C-A-S-H gels. The effects of w/b, Na₂O content and SiO₂ content on the type of reaction products are relatively limited. Unlike the result in OPC, Friedel's salt is not observed in AAFS, which may mean that the chloride binding of AAFS is mainly determined by physical adsorption.
- 2) FTIR spectra show that the formation of C-A-S-H gels appears earlier than that of N-A-S-H gels. But the formation of N-A-S-H gels plays a leading role in the later stage. Higher GGBFS content, higher Na₂O content and lower SiO₂ content promote the formation of C-A-S-H gels in the early stage and lead to higher Al substitution. However, in the later stage, the continuous reaction of FA has a greater impact on mixtures with higher FA content, higher w/b and higher SiO₂ content.
- 3) The result of MIP shows that AAFS mixtures generally present lower total porosity and finer threshold pore than OPC. There is a good correlation between

D_f and volume of capillary pores rather than total porosity. Besides, the D_f of AAFS is also closely related to the threshold pore diameter and tortuosity.

- 4) Based on the results of MIP and nitrogen adsorption, the diameter of the pores acting on chloride resistance is larger than those acting on compressive strength. Compared with the difference of gel pores caused by different type of reaction products, the difference of capillary pores caused by different quantity of reaction products is more important for chloride resistance. Normally, higher GGBFS content, lower w/b, higher Na_2O content and lower SiO_2 content result in lower volume of capillary pores and smaller threshold pore diameter, which consequently improve chloride resistance. However, the continuous reaction of FA can reduce the initial gap and may lead to reverse results in the later stage.

CHAPTER 6: PREDICTION OF CHLORIDE TRANSPORT IN ALKALI-ACTIVATED FLY ASH-SLAG CONCRETES

6.1 INTRODUCTION

As described in Section 1.1.3, reinforcement corrosion is the main cause of the premature failure of most reinforced concrete structures, which leads to the shortening of the service life of buildings and huge economic losses (Babae & Castel, 2018; El-Reedy, 2017). In chloride-containing environments (e.g. de-icing salt and marine environment), chloride-induced corrosion usually occurs due to the chloride transport in concrete. In spite of chloride ions (Cl^-) usually do not directly damage the concrete matrix, the accumulation of Cl^- at the steel-concrete interface (SCI) leads to reinforcement corrosion, thus reducing the bearing capacity of reinforced concrete structures (J. Zhang et al., 2017a). In the classic model proposed by Tuutti (1982), the service life of reinforced concrete structures is divided into initiation phase and propagation phase (Fig.1-10). During the initiation phase, the chloride transport in concrete leads to the accumulation of Cl^- at the SCI until the passive film around the steel bar is broken down, which is otherwise stable in concrete pore solution ($\text{pH} > 12.5$) (Montemor et al., 2003). During the propagation phase, chloride-induced corrosion starts, and corrosion products (Fig.1-9) accumulate around the steel bar, resulting in internal expansive pressure and hence structural destruction. Although the reinforced concrete structure can still bear the applied load in the propagation phase (R. Zhang, Castel, & François, 2009), it is more conservative to limit the service life to the end of initiation phase, when the SCI reaches the critical chloride content (threshold value) (Babae & Castel, 2018). Therefore, as an indispensable step before attempting to apply AAFS in reinforced concrete structures under chloride-containing environments, the prediction of chloride transport in AAFS concrete is particularly important.

Compared with the binder matrix, the aggregates in concrete have negligible permeability (Pack et al., 2010). Therefore, the chloride transport in concrete mainly depends on the characteristics of binder, e.g. OPC, AAFS and other AAMs. To investigate and predict the chloride transport in OPC concrete, a large number of studies have been carried out in the past (Boddy, Bentz, Thomas, & Hooton, 1999; M. U. Khan, Ahmad, & Al-Gahtani, 2017; X. Shi, Xie, Fortune, & Gong, 2012). Based

on Fick's second law (Equation 9 or 10) and considering the time dependency of chloride diffusion coefficient (D) and surface chloride content (C_s), comparatively perfect prediction models have been established (Pack et al., 2010; H.-W. Song, Lee, & Ann, 2008). For AAFS and other AAMs, there are few data available for modelling, because they have only recently gained momentum as promising alternatives to OPC.

As described in the literature review in Chapter 2, previous studies have provided some valuable information on the chloride diffusion in AAFS and other AAMs. In Chapter 4, the effects of different parameters, including GGBFS content, w/b, Na₂O content, SiO₂ content and s/a, are further discussed. In Chapter 5, the microstructure (including phase evolution and pore structure) of AAFS is analysed to explore the influence mechanism of different parameters. However, studies concerning the chloride transport in AAFS and other AAMs mainly centred on early measurement results. Due to the limited field data spanning decades or more, there is still a great need to improve the understanding of the long-term chloride transport in AAFS to estimate the service life of reinforced AAFS concrete structures under chloride-containing environments, especially the time to the end of initiation phase. Based on a 5-weeks bulk diffusion test, Tennakoon et al. (2017) predicted the chloride transport and corresponding corrosion initiation time in AAFS concrete (40%-60% GGBFS content), and reported that the corrosion initiation time of all mixtures was longer than OPC, particularly the mixtures containing 50% or more GGBFS. Despite that, rapid chloride permeability test (RCPT) was used to establish the time dependent model of D . Although the change of RCPT results can reflect the change of D in OPC (Buenfeld & Newman, 1987; Concrete & Australia, 2009), RCPT may be inadaptable in AAFS and other AAMs due to the more complex pore solution chemistry, as described in the literature review in Chapter 2. Moreover, the possible changes of C_s in different mixtures were not studied, which may also determine the prediction model to a certain extent (Pack et al., 2010; H.-W. Song et al., 2008). Besides, the effects of a wider range of FA/GGBFS and other mixing parameters (e.g. w/b, Na₂O content, SiO₂ content and s/a) still need to be further studied.

This chapter aims to predict the long-term chloride diffusion in AAFS concretes with different GGBFS contents, water/binder ratios (w/b), Na₂O contents, SiO₂ contents

and sand/aggregate ratios (s/a) based on the measurement results (up to 2 years). The time dependent models of D in different mixtures were established. The values of C_s in different mixtures at different exposure times were compared. The subsequent chloride diffusion and chloride profile were predicted according to the time dependent D . The corrosion time was calculated in combination with the designated critical chloride content. The effects of different mixing parameters were discussed. The feasibility of replacing OPC concrete with AAFS concrete in chloride-containing environment was demonstrated.

6.2 MODELLING OF CHLORIDE DIFFUSION

6.2.1 CONVENTIONAL CHLORIDE DIFFUSION MODEL

As described in Section 2.2.1, the chloride transport in concrete involves many processes, e.g. ionic diffusion, capillary suction, permeation and migration (Table.2-1). Ionic diffusion is a process without any flow of water in saturated concrete, which is driven by concentration gradient. With water as the medium, Cl^- can move from high concentration to low concentration (J. Li et al., 2020). Although multiple processes are involved, ionic diffusion usually plays an absolutely dominant role in concrete in direct contact with seawater (such as submerged zone and tidal/splash zone), which can roughly describe the actual engineering situation (Böhni, 2005; Pack et al., 2010). To describe the chloride diffusion in concrete, many models have been built. Most models are based on Fick's second law (Equation 9 or 10), which can simulate the diffusion of unreactive species (such as Cl^-) into a semi-infinite medium.

$$c(x, t) = c_s \left[1 - \operatorname{erf} \left(\frac{x}{2\sqrt{D \cdot t}} \right) \right] \quad (9)$$

or

$$c(x, t) = c_0 + (c_s - c_0) \left[1 - \operatorname{erf} \left(\frac{x}{2\sqrt{D \cdot t}} \right) \right] \quad (10)$$

where $C(x, t)$ = chloride content (mass %) at depth x (m) and time t (s); C_s = exposure surface chloride content (mass %); C_0 = initial chloride content (mass %); D = chloride diffusion coefficient (m^2/s); and erf denotes error function.

As shown in Fig.6-1, based on Fick's second law (Equation 9 or 10), the chloride diffusion and corrosion initiation in AAFS concrete can be predicted by using MATLAB according to the early measurement results. First, the chloride profiles of different AAFS concretes are obtained by chloride diffusion test. By fitting Equation 9 or 10 to the measured chloride profiles, the D and C_s of different AAFS concretes can be determined. Because the bound chloride ions are completely removed from the pore solution and cannot induce or enhance the corrosion of reinforcement steel, the use of free chloride content is more recommended. However, total chloride content is still used in some studies and standards to ensure the safety of design. After that, the D and C_s can be substituted into Equation 9 or 10 to predict the subsequent chloride diffusion in different AAFS concretes. When the depth is specified, the variation model of chloride content with exposure time can be obtained. Besides, chloride profiles at specific times in the future can be predicted. Furthermore, the corrosion time at the SCI can also be predicted by substituting the designated critical chloride content (Angst, Elsener, Larsen, & Vennesland, 2009; Babae & Castel, 2018; Gjrv, 2014; Tennakoon et al., 2017).

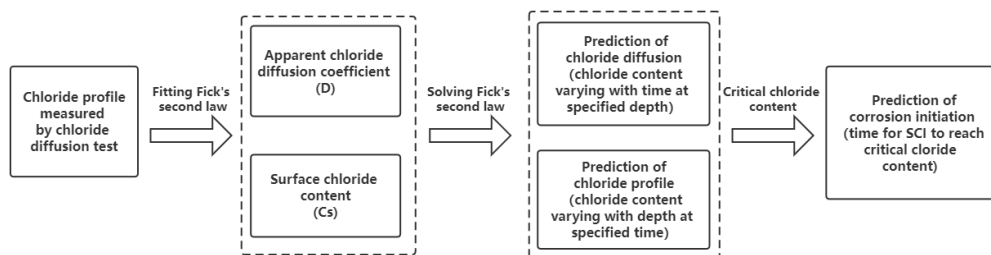


Fig.6-1 Prediction of chloride diffusion and corrosion initiation in concrete.

Based on AS 3600 and AS 5100.5, the design life, minimum characteristic compressive strength (f_c) and required cover for corrosion protection of general concrete structures and bridges under different exposure environments (submerged zone, spray zone and tidal/splash zone) are shown in Table 6-1. According to Table 6-1, the chloride diffusion in AAFS concrete at 45 and 60 mm (concrete cover depths required for general concrete structures and bridges in submerged zone, where the moisture condition of concrete is stable) and the chloride profiles of AAFS concrete at 50 and 100 years (design life of general concrete structures and bridges) can be predicted. Based on previous studies (Gjrv, 2014; Tennakoon et al., 2017), 0.077%

by weight of concrete is used as the critical chloride content of AAFS concrete to calculate the time to corrosion initiation.

Table 6-1 Design life, minimum characteristic compressive strength (f_c) and required cover for corrosion protection of general concrete structures and bridges under different exposure environments (AS 3600 and AS 5100.5).

Structure	Standard	Design life	Exposure environment	Minimum f_c^a (Mpa)	Required cover for corrosion protection under minimum f_c (mm)
General Concrete Structures	AS 3600 Concrete Structures	50 years \pm 20%	Permanently submerged (B2)	40	45
			In spray zone (C1)	50	50
			In tidal/splash zone (C2)	50	65
Bridges	AS 5100.5 Bridge design Part 5: Concrete	\geq 100 years	Permanently submerged (B2)	40	60
			In spray zone (C1)	50	70
			In tidal/splash zone (C2)	50	80 ^b

^a f_c = characteristic compressive strength of concrete at 28 days

^b when 55 MPa is used as minimum f_c

6.2.2 MODELLING OF CHLORIDE DIFFUSION COEFFICIENT

It is not accurate to establish a time independent model only based on the D obtained at a single exposure time. In fact, the D is not constant, but time-varying. With the passage of time, the continuous reaction can improve the pore structure and chloride resistance of concrete. As a result, the corresponding D decreases. As described in Section 4.3.2, the D of AAFS concrete decreases significantly from 90 day to 180 days (Fig.4-5), which is consistent with the change trend of OPC concrete (Yuanzhan Wang & Fu, 2019). Obviously, when solving Fick's second law, the time dependence of D cannot be ignored.

In general, the decline of D is more obvious in the early stage. With the extension of exposure time, the pore-filling effect decreases gradually, and the D tends to be stable. Takewaka and Mastumoto (1988) may be the first to propose the dependency

of D on t . They used a purely empiric equation, where D is proportional to $t^{-0.1}$. After that, most studies (Audenaert, Yuan, & De Schutter, 2010; Pack et al., 2010; Yuanzhan Wang & Fu, 2019) showed that the time dependency of diffusion coefficient is an exponential function, as shown in Equation 18 as follows:

$$D(t') = D_{ref}' \left(\frac{t_{ref}'}{t'} \right)^m \quad (18)$$

where $D(t')$ is the chloride diffusion coefficient (m^2/s) at the concrete age, t' ; D_{ref}' is the chloride diffusion coefficient (m^2/s) at the reference concrete age, t_{ref}' ; and m is the age factor.

Note that t' in Equation 18 denotes the concrete age (the sum of curing and exposure time) instead of the exposure time (t). In order to directly show the relationship between D and exposure time (t), Equation 19 is used in this study.

$$D(t) = D_{ref} \left(\frac{t_c + t_{ref}}{t_c + t} \right)^m \quad (19)$$

where $D(t)$ is the chloride diffusion coefficient (m^2/s) at the exposure time, t ; D_{ref} is the chloride diffusion coefficient (m^2/s) at the reference exposure time, t_{ref} , t_c is the curing time (28 days); and m is the age factor.

6.2.3 DETERMINATION OF SURFACE CHLORIDE CONTENT

Because of the contact with moulds, the segregation of aggregates, and the dielectric reaction between concrete surface and chloride environment, the composition of concrete skin is different from that of internal concrete (Andrade, Díez, & Alonso, 1997). As a result, the chloride content within a few millimetres of the concrete surface is decreased. In addition, Cl^- at the concrete surface may be washed out during the experiment (H.-W. Song et al., 2008). Therefore, the direct measurement of C_s is unreliable, and the correct way to obtain C_s is to fit Fick's second law to the measured chloride profile with D and C_s as independent variables.

Based on the hypothesis that Cl^- and surface concrete can make a chemical equilibrium in the electrical double layer (Fig.2-4), when the reinforced concrete structures are in direct contact with seawater, the time dependency of C_s in OPC can be ignored. Therefore, a constant C_s is usually used in the conventional chloride

diffusion model (Bamforth, 1999; Mangat & Molloy, 1994). The build-up of C_s is considered only under marine atmospheric conditions (Amey, Johnson, Miltenberger, & Farzam, 1998; Kassir & Ghosn, 2002). However, Uji, Matsuoka, and Maruya (1990) claimed that the build-up of C_s may also occur in tidal zone and splash zone, though the reinforced concrete structures are in direct contact with seawater. This is not surprising because wet/dry cycles of seawater are provided to the reinforced concrete structures in tidal zone and splash zone. Pack et al. (2010) proposed a logarithmic relation between C_s and t in tidal zone, as shown in Equation 20 as follows:

$$C_s(t) = \alpha \ln(\beta t + 1) + k \quad (20)$$

where $C(t)$ is the surface chloride content (mass %) at exposure time t ; α , β and k are constants.

6.3 RESULTS AND DISCUSSION

6.3.1 CHLORIDE DIFFUSION COEFFICIENT

In order to establish the prediction model, in addition to the D at 90 and 180 days obtained in Chapter 4, the D at 365 and 730 days are also measured. Overall, the D decreases with exposure time in all mixtures, which means the improvement of chloride resistance. By fitting Equation 10 to the measured D at different testing ages, the time dependent model of D can be established. Fig.6-2 shows the fitted curves of the D of AAFS concretes with different GGBFS contents, water/binder ratios (w/b), Na_2O contents, SiO_2 contents and sand/aggregate ratios (s/a). Taking the average value of D at the youngest testing age ($t_{ref} = 90$ days) as D_{ref} (Pack et al., 2010), the corresponding age factor (m) and coefficient of determination (R^2) are also given. Except SL100, W40 and N6, all mixtures have high R^2 values, which further confirms the reliability of the prediction model. The low R^2 of SL100, W40 and N6 is because the D of these mixtures remains unchanged or even increases slightly in some periods after 180 days. As discussed in Chapter 4 and Chapter 5, the possible reason is the microcracking caused by shrinkage (Collins & Sanjayan, 2001; Kutti et al., 1992; G. Wang & Ma, 2018) or efflorescence (Z. Zhang et al., 2014). Moreover, the m of W50 is obviously too large (1.1260). One possible explanation is that AAFS concrete with high w/b needs more time to fill capillary pores (remnants of initial

water-filled space as shown in Fig.2-2). Therefore, the reduction rate of D cannot slow down within 2 years, leading to an overwhelming rapid decrease in the prediction model.

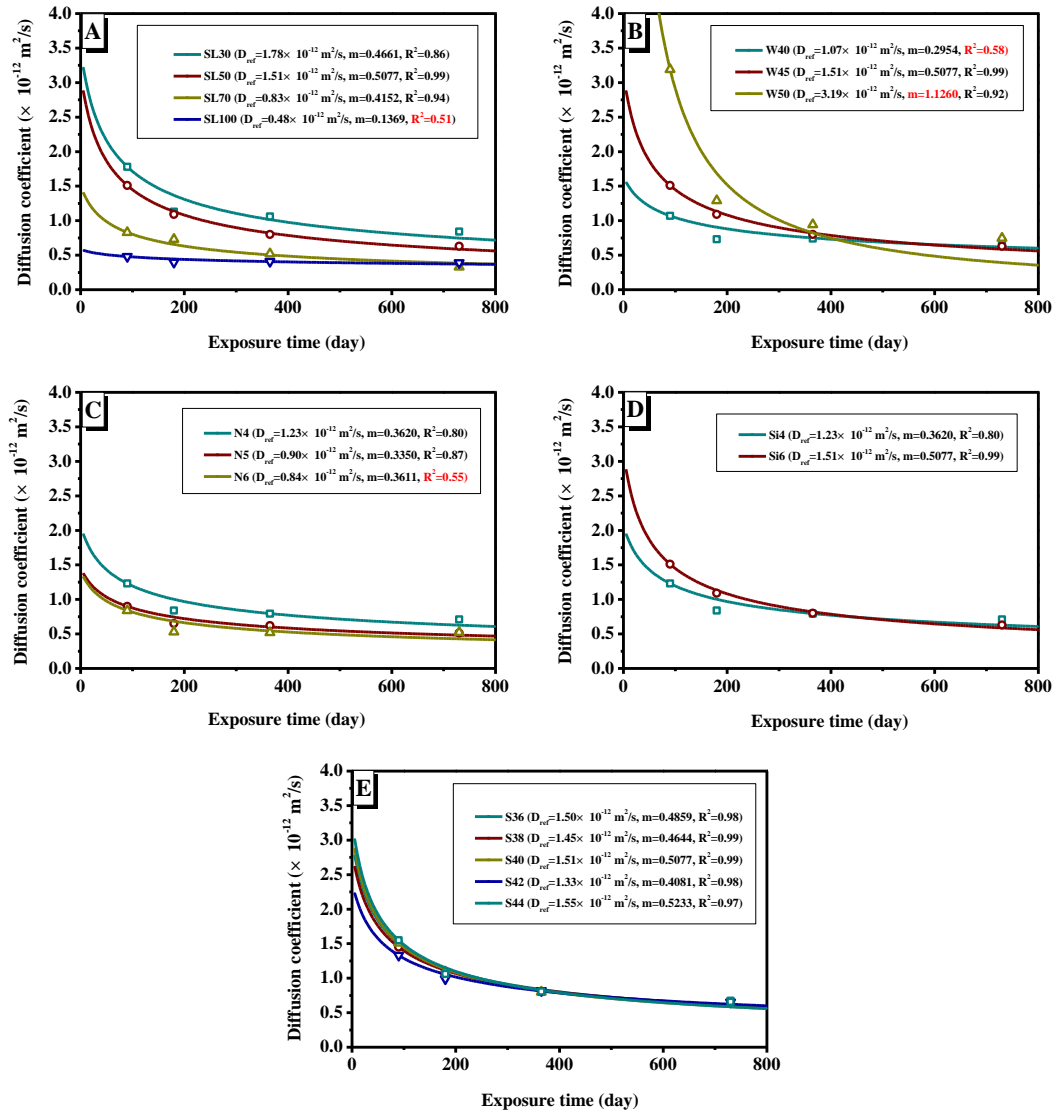


Fig.6-2 Fitted curves of apparent chloride diffusion coefficient (D) of AAFS concretes with different (A) GGBFS contents, (B) water/binder ratios (w/b), (C) Na₂O contents, (D) SiO₂ contents and (E) sand/aggregate ratios (s/a).

The fitted curves fully meet the expectation and are consistent with that of OPC concrete (Pack et al., 2010; Yuanzhan Wang & Fu, 2019). The D decreases rapidly in the early stage after exposure to NaCl solution, which means that the corresponding chloride resistance is significantly improved. This may be due to the modified microstructure, as discussed in Chapter 5. It is reported that the pore size of OPC was in the range of 8 to 700 nm at 1 day, but in the range of 16 to 64 nm after 365 days

(Roy & Idorn, 1993). Although the OPC binder matrix usually completes 85%–90% of cement hydration within 28–56 days, the rest of cement hydration can last for a very long time (Pack et al., 2010). Like cement hydration, geopolymerization is also a continual reaction process (Tennakoon et al., 2017), which is confirmed by the results of FTIR in Chapter 5 (Section 5.3.1.2). The continuous reaction of FA and GGBFS, especially the former, forms more reaction products to fill pores, resulting in narrower paths of Cl⁻. John L Provis et al. (2012) found that the longer curing of AAFS decreased the porosity and increased the tortuosity. In addition, the interconnected network may be blocked over time. With the extension of exposure time, the D still decreases but at a lower rate, which means that the chloride resistance is gradually stable. The reduction of D with time is beneficial in delaying the chloride-induced corrosion and thus prolonging the service life of structures.

In order to verify the applicability of this time dependent model, the fitted curve of SL50 is compared with the fitted curves of SL50' and OPC (Fig.6-3), which are drawn based on the parameters reported in the previous study (Tennakoon et al., 2017). The GGBFS content in SL50' is the same as that in SL50 (50%). The D_{ref} of SL50' and OPC was determined by bulk diffusion test (NT BUILD 443, $t_{ref} = 35$ days), while the m was determined by RCPT (ASTM 1202). Although the test methods are different, the fitted curves of SL50 and SL50' are very consistent, especially after 180 days. One possible explanation is that although the pore solution chemistry is different in different mixtures, it is not change significantly over time in the same mixture. As a result, when determining the change ratio of D in each mixture (quantifying m), the effect of pore solution chemistry is not significant. Therefore, it is feasible to quantify m by RCPT on the basis of determining D_{ref} by chloride diffusion test. Compared with SL50 and SL50' (0.5077 and 0.6040), the m of OPC is only 0.1920, which is similar to previous studies (Y. J. Hu & Du, 2013; Xu & Shayan, 2015). It means that aging improves the chloride resistance of AAFS concrete more significantly than that of OPC concrete. Therefore, the D of AAFS concrete is not only significantly lower than that of OPC concrete at the early stage, but also expected to remain lower in the subsequent time. When the fitted curves are extrapolated from 800 days to 100 years, the D of SL50 and SL50' are still very similar, much smaller than that of OPC. This can justify the reliability of the fitted

curves in this chapter to some extent. It also means the fitted curves obtained in this chapter can help predict the service life of a typical structure prepared with AAFS concrete, which can greatly fill the research gap. After 10 years, the change of D of SL50 and SL50' is very small, which means that the pore-filling effect is very limited.

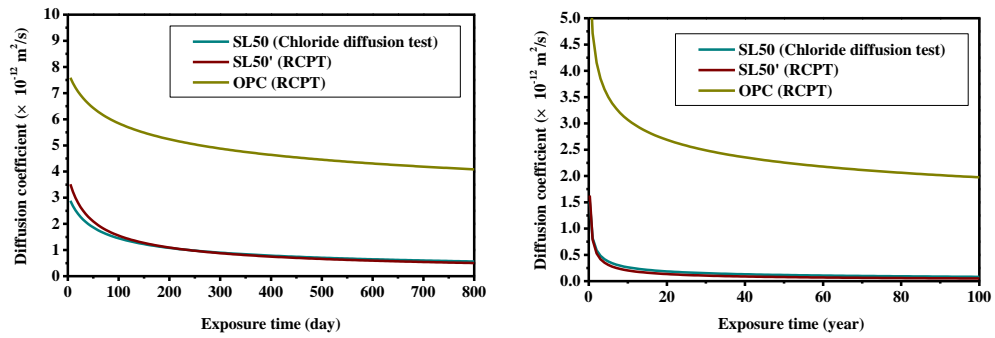
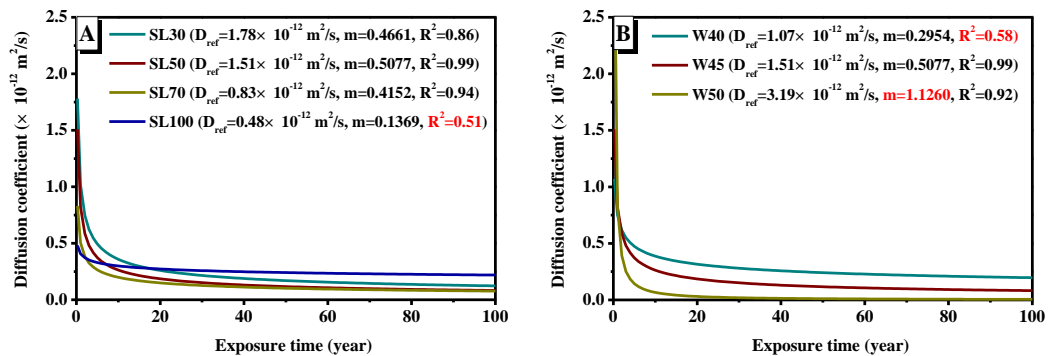


Fig.6-3 Fitted curves of apparent chloride diffusion coefficient (D) of SL50 (quantified by natural chloride diffusion test), SL50' (quantified by RCPT (Tennakoon et al., 2017)) and OPC (quantified by RCPT (Tennakoon et al., 2017)).

In Fig.6-4, the time dependent models of the D of AAFS concretes with different GGBFS contents, water/binder ratios (w/b), Na_2O contents, SiO_2 contents and sand/aggregate ratios (s/a) are extrapolated to 100 years. For W50, the measurement time of 2 years is too short, and the D needs to be measured for a longer time. To ensure the safety of the design, the measured D at 2 years ($0.75 \times 10^{-12} \text{ m}^2/\text{s}$) instead of time dependent D is used in the subsequent prediction of W50.



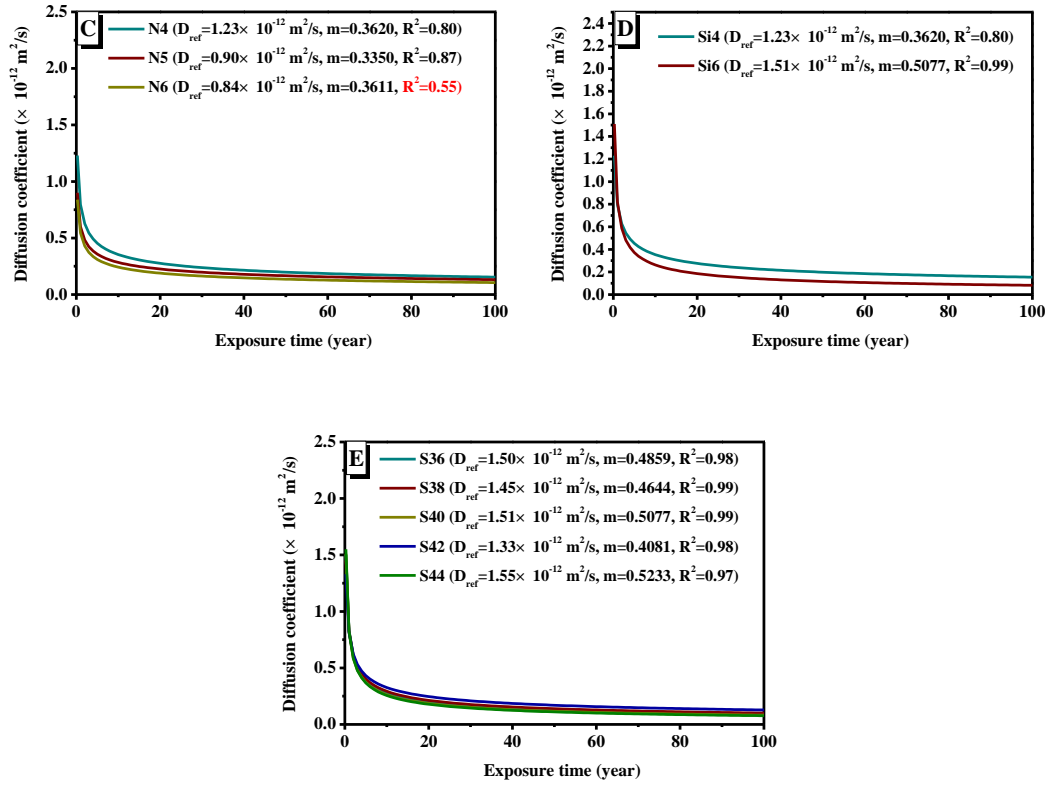


Fig.6-4 Time dependent models of apparent chloride diffusion coefficient (D) of AAFS concretes with different (A) GGBFS contents, (B) water/binder ratios (w/b), (C) Na_2O contents, (D) SiO_2 contents and (E) sand/aggregate ratios (s/a).

6.3.1.1 EFFECT OF GGBFS CONTENT

As shown in Fig.6-4A, in the early stage, the predicted D gradually decreases with the increase of GGBFS content from 30% to 100%, which is consistent with the measurement results in Chapter 4 (Fig.4-5) and previous studies (Babae & Castel, 2018; X. Hu et al., 2019; Ismail, Bernal, Provis, San Nicolas, et al., 2013; Tennakoon et al., 2017). Most previous studies considered that compared with N-A-S-H gels, C-A-S-H gels have finer pore structure and higher tortuosity, resulting in higher chloride resistance (Babae & Castel, 2018; Ismail, Bernal, Provis, San Nicolas, et al., 2013; John L Provis et al., 2012). However, according to the findings in Chapter 5, the decrease of D is mainly due to the better filling of capillary pores (remnants of initial water-filled space as shown in Fig.2-2). In AAFS, the formation of C-A-S-H gels is faster than that of N-A-S-H gels. Therefore, higher GGBFS content results in the formation of more reaction products to fill capillary pores, which consequently improve the chloride resistance of AAFS concrete at the early stage. Despite that, the findings in Chapter 5 also show that the continuous reaction of FA plays a dominant

role in the later stage, which can reduce the initial gap. This is consistent with the prediction results in Fig.6-4A. It should also be noted that the predicted D of SL100 is significantly larger in the later stage. This may be due to the excessive shrinkage of the pure GGBFS system (Collins & Sanjayan, 2001). Shrinkage cracks in SL100 can provide more channels for Cl^- , thereby reducing chloride resistance.

6.3.1.2 EFFECT OF WATER/BINDER RATIO (W/B)

In Fig.6-4B, with increasing w/b from 0.40 to 0.50, the predicted D of AAFS concrete decreases, which is contrary to the measurement results in Chapter 4 (Fig.4-5). As mentioned before, the predicted D of W50 is lower than the actual value because the measurement result of 2 years is relatively insufficient. However, without considering W50, the predicted D of W40 is still higher than that of W45 after 2 years. The possible reason is the combination of continuous reaction of FA and drying shrinkage. In the first two years, higher w/b leads to more capillary pores (remnants of initial water-filled space as shown in Fig.2-2), which provide fast channels for Cl^- . This view is confirmed by the results of MIP in Chapter 5 (Fig.5-6 and Fig.5-9). With the extension of exposure time, the continuous reaction of FA, which is confirmed by the results of FTIR in Chapter 5 (Fig.5-3), can reduce or even completely fill the initial gap. Moreover, the low w/b in W40 may lead to the microcracking caused by drying shrinkage due to the loss of capillary water (G. Wang & Ma, 2018). As a result, more channels are provided for Cl^- .

6.3.1.3 EFFECT OF ALKALI CONTENT

Compared with FA/GGBFS and w/b, Na_2O content has no significant effect on the predicted D of AAFS concrete (Fig.6-4C). In the early stage, with the increase of Na_2O content from 4% to 6%, the predicted D decreases slightly, which is consistent with the measurement results in Chapter 4 (Fig.4-5) and previous studies (Bondar et al., 2018; P Chindaprasirt & Chalee, 2014; X. Hu et al., 2019). The most possible reason is that higher alkali environment leads to more dissolved Si, Al and Ca components to form gels, resulting in finer pore structure and higher chloride resistance (X. Hu et al., 2019). With the extension of exposure time, the difference of predicted D decreases. One possible reason is that the continuous reaction of FA in the later stage leads to the filling of initial capillary pores. Moreover, high alkalinity

may promote the efflorescence (Z. Zhang et al., 2014) and drying shrinkage (Y. Ma & Ye, 2015). As a result, more cracks are provided for chloride diffusion.

6.3.1.4 EFFECT OF SILICATE CONTENT

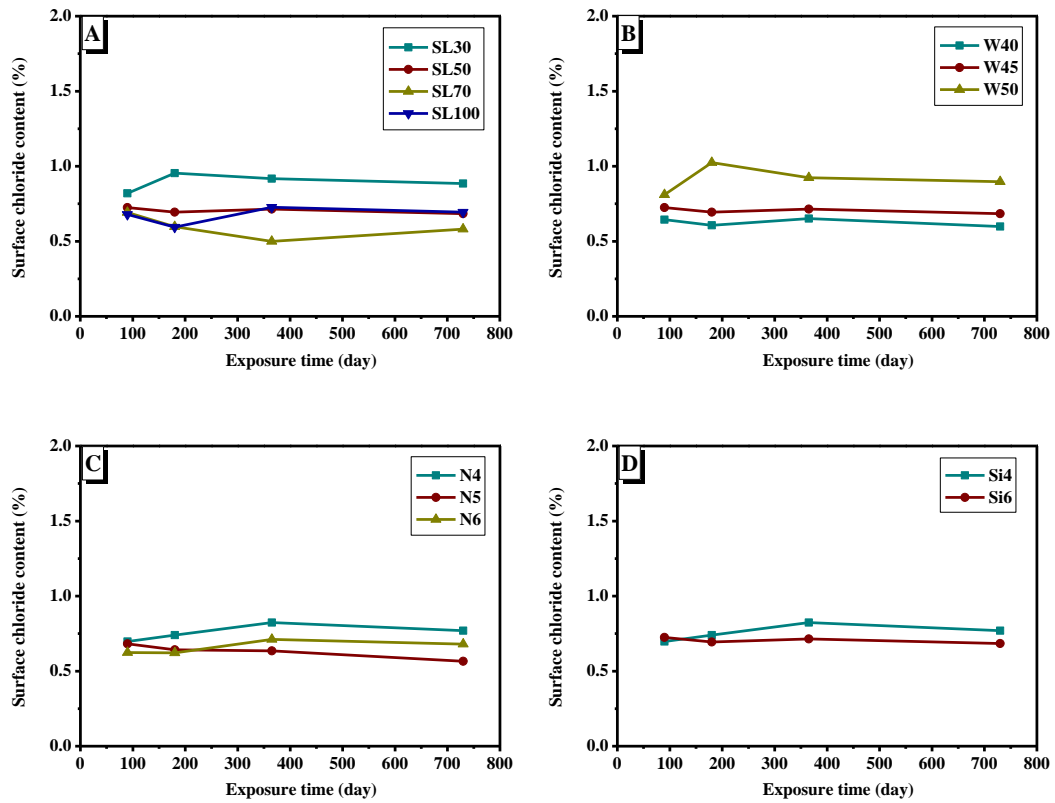
As shown in Fig.6-4D, the predicted D of Si6 is higher than that of Si4 in the first year. Thereafter, the predicted D of Si6 is lower than that of Si4 due to the faster decline rate. This prediction result is consistent with the early measurement result in Chapter 4 (Fig.4-5). According to the result of FTIR in Chapter 5 (Fig.5-5), higher SiO_2 content seems to lead to the conversion of main reaction products from C-A-S-H gels to N-A-S-H gels, resulting in the slower formation of reaction products at the early stage. The larger volume of capillary pores (Fig.5-6) and larger threshold pore diameter (Fig.5-9) of Si6 measured by MIP at 180 days can confirm this view. However, as the reaction continues, more Si components lead to the formation of more reaction products to fill capillary pores, resulting in the lower D of Si6 in the later stage (Fig.6-2D). The obvious shift of the peak of the main absorption band in Fig.5-5b confirms this view. The opposite measurement and prediction results in the first year and later period show that it is not advisable to predict the long-term chloride transport in AAFS concrete only based on the short-term measurement results.

6.3.1.5 EFFECT OF SAND/AGGREGATE RATIO (S/A)

As shown in Fig.6-4E, the influence of s/a on the predicted D of AAFS concrete is limited and has no obvious regularity. In the first five years, there is little difference among AAFS mixtures with different s/a . Thereafter, the gap of the predicted D of AAFS mixtures with different s/a gradually increases. However, the measurement result in Fig.6-2E shows that the D of different mixtures tends to be consistent. Therefore, the prediction result of D may not be accurate because the test time of two years is too short to determine the correct m . If the test time of natural chloride diffusion test (NCD) can be further extended, the measured D of different mixtures may be consistent in the subsequent time. As a result, the corresponding prediction results also tend to be consistent.

6.3.2 SURFACE CHLORIDE CONTENT

Fig.6-5 compares the surface chloride content (C_s) of AAFS concretes with different GGBFS contents, water/binder ratios (w/b), Na_2O contents, SiO_2 contents and sand/aggregate ratios (s/a) at 90, 180, 365 and 730 days. Although the values of C_s in different mixtures are different, the C_s of each mixture does not change significantly with time. This result is in line with the expectations in Section 6.2.3. As in OPC concrete (Bamforth, 1999; Mangat & Molloy, 1994), Cl^- and surface concrete may also achieve a chemical equilibrium in AAFS concrete, so a constant C_s can be used in the subsequent prediction. However, this is because the simulated environment of natural chloride diffusion test (NCD) is submerged zone. In tidal zone and splash zone (Uji et al., 1990), or marine atmospheric conditions (Amey et al., 1998; Kassir & Ghosn, 2002), the build-up of C_s may occur. To ensure the safety of the design, the maximum measured value of C_s of each mixture is used in the subsequent prediction.



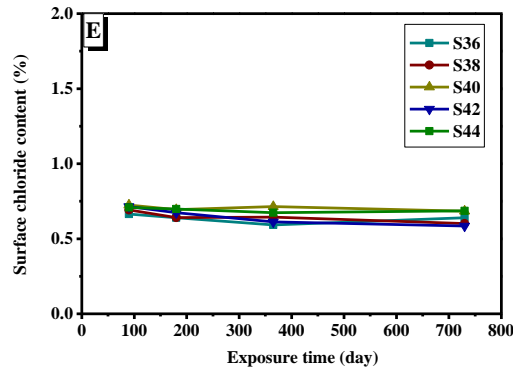


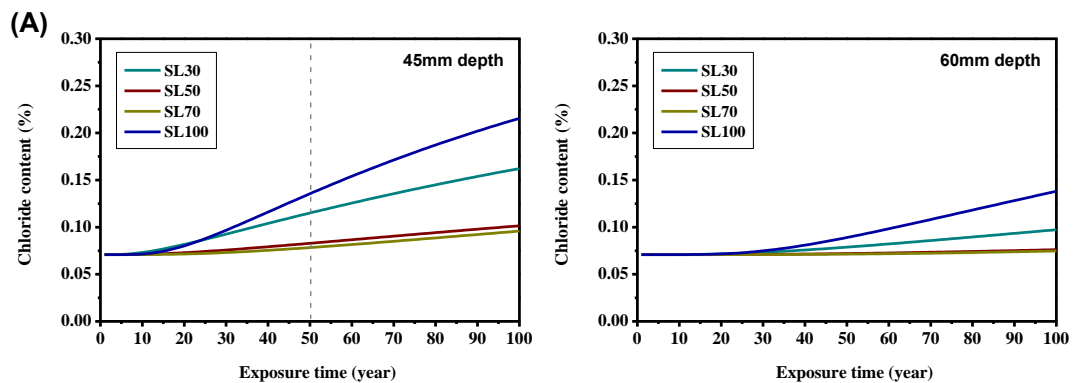
Fig.6-5 Surface chloride content (C_s) of AAFS concretes with different (A) GGBFS contents, (B) water/binder ratios (w/b), (C) Na_2O contents, (D) SiO_2 contents and (E) sand/aggregate ratios (s/a) at 90, 180, 365 and 730 days.

As shown in Fig.6-5A and B, the values of C_s in SL30 and W50 are significantly higher than those in other mixtures. The possible reason is their higher porosity, which was measured by mercury intrusion porosimetry (MIP) in Chapter 5. Higher porosity means more pore solution to contain Cl^- . Moreover, as described in Chapter 2, higher porosity also leads to a larger total surface area to adsorb Cl^- . As a result, the corresponding chloride content increases. The above view can explain the influence of different parameters. Because of the lower porosity of C-A-S-H gels, the C_s decreases with the increase of GGBFS content (Fig.6-5A). The higher C_s of SL100 in the later stage may be due to the microcracking caused by shrinkage (Collins & Sanjayan, 2001). Higher w/b leads to more capillary pores and hence higher C_s (Fig.6-5B). Higher Na_2O content leads to the formation of more gels and better pore-filling effect, resulting in lower C_s at the early stage (Fig.6-5C). The higher C_s of N6 at the later stage may be due to the interference of efflorescence (Z. Zhang et al., 2014) and drying shrinkage (Y. Ma & Ye, 2015). As shown in Fig.6-5D, the C_s of Si6 is higher than that of Si4 at 90 days. Thereafter, the C_s of Si6 is lower than that of Si4. The most likely explanation is the better pore-filling effect of Si6 in the later stage. By comparison, the influence of s/a on C_s is limited and has no obvious regularity (Fig.6-5E).

6.3.3 PREDICTION OF CHLORIDE DIFFUSION

Fig.6-6 depicts the chloride diffusion in AAFS concretes with different GGBFS contents, water/binder ratios (w/b), Na_2O contents, SiO_2 contents and sand/aggregate ratios (s/a) at 45 mm and 60 mm, which are the depths of concrete cover required for

general concrete structures and bridges in submerged zone (Table 6-1). The corresponding design life of general concrete structures and bridges is 50 years and 100 years respectively. Note that W50 adopts a constant D ($0.75 \times 10^{-12} \text{ m}^2/\text{s}$). With the increase of cover depth from 45 mm to 60 mm, the chloride content of all mixtures decreases significantly at each age, especially for mixtures with low chloride resistance. For example, the 100-year chloride content of SL30 decreases from 0.162% to 0.097%. When 0.077% is considered as the critical chloride content for corrosion initiation (Gjørsv, 2014; Tennakoon et al., 2017), for general concrete structures, all mixtures cannot prevent the chloride-induced corrosion of the reinforcement at 45 mm within 50 years. Among them, S70 has the best performance and can protect the reinforcement at 45 mm until 45 years (Fig.6-6A). For bridges, only SL50 (also named as W45, Si6 and S40), SL70, S44 can prevent the chloride-induced corrosion of the reinforcement at 60 mm within 100 years. However, compared with the very short protection time of OPC concrete (only a few years) (Pack et al., 2010; Tennakoon et al., 2017), AAFS concrete has made a great breakthrough. In theory, when applying the required cover in existing standards (AS 3600 and AS 5100.5), correctly formulated AAFS concrete (e.g. SL50 and SL70) can successfully extend the initiation phase and hence the total service life for decades or even more than 100 years. These exciting prediction results further confirm previous research results (Tennakoon et al., 2017). Nevertheless, it is worth noting that different parameters seriously affect the final prediction results of chloride diffusion in AAFS concrete. Therefore, the correct mix design of AAFS concrete is particularly critical to ensure the service life of reinforced AAFS concrete structures under chloride-containing environments.



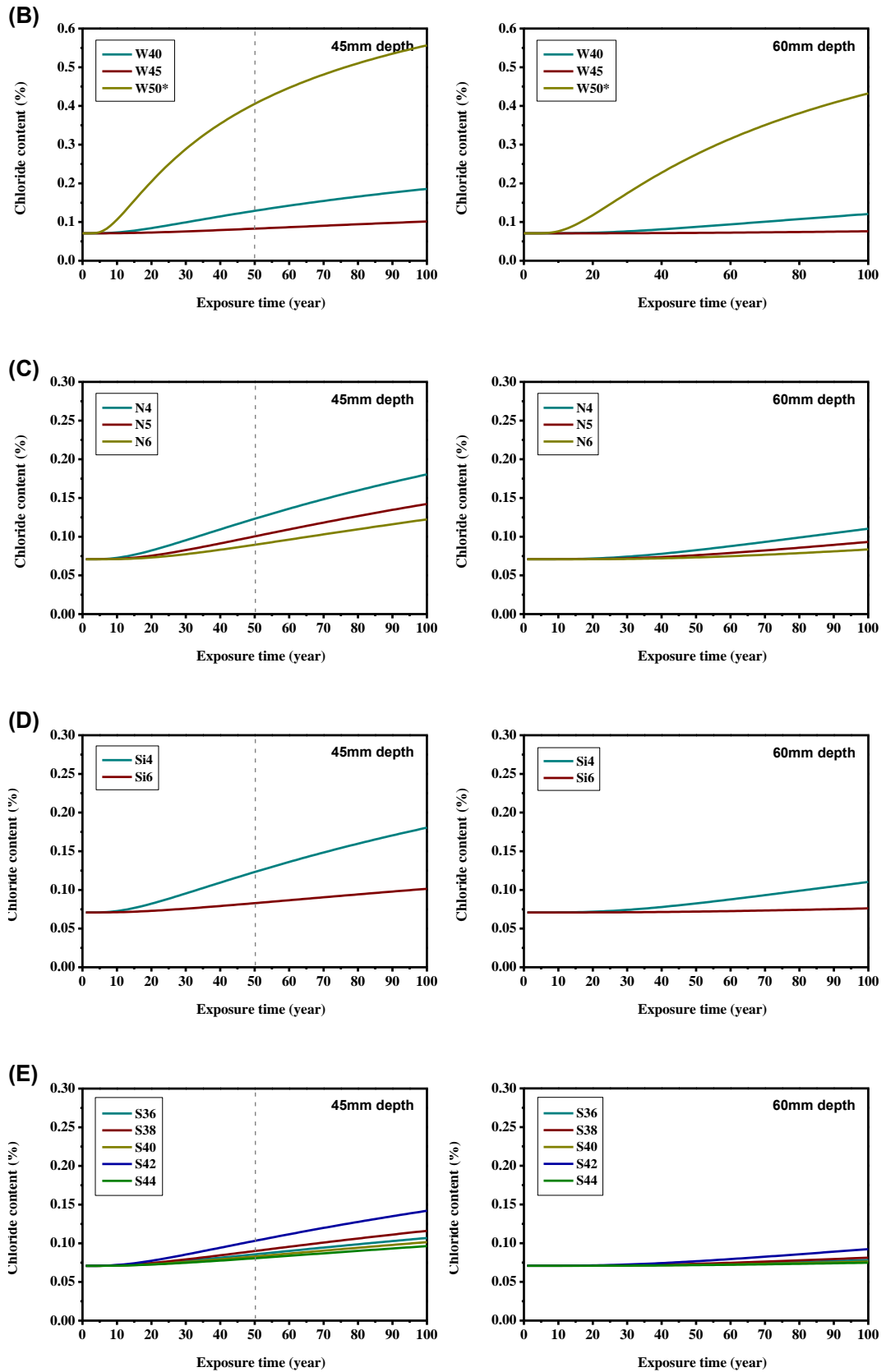


Fig.6-6 Chloride diffusion in AAFC concretes with different (A) GGBFS contents, (B) water/binder ratios (w/b), (C) Na_2O contents, (D) SiO_2 contents and (E) sand/aggregate ratios (s/a) at 45 mm and 60 mm depths. *W50 adopts a constant D ($0.75 \times 10^{-12} \text{ m}^2/\text{s}$).

As shown in Fig.6-6, the effects of different parameters (including GGBFS content, w/b, Na₂O content, SiO₂ content and s/a) on the prediction results of chloride diffusion in AAFS concrete are consistent with their effects on the predicted D (Fig.6-4). Compared with other parameters, FA/GGBFS, w/b and SiO₂ content have a more prominent effect on the prediction result of chloride diffusion. Fortunately, with increasing cover depth from 45 mm to 60 mm, the difference of chloride diffusion among different mixtures decreases significantly.

6.3.3.1 EFFECT OF GGBFS CONTENT

As shown in Fig.6-6A, due to the finer pore structure and higher tortuosity of C-A-S-H gels described in previous studies (Babae & Castel, 2018; Ismail, Bernal, Provis, San Nicolas, et al., 2013; John L Provis et al., 2012), as well as the faster filling of capillary pores described in Chapter 5, higher GGBFS content leads to lower D and hence slower chloride diffusion in AAFS concrete. Compared with SL50 and SL70, the chloride diffusion in SL30 is much faster. The 50-year chloride content of SL30 at 45 mm depth is as high as 0.115%, while the 50-year chloride content of SL50 (0.083%) and SL70 (0.078%) is close to the initial chloride content (C₀, around 0.071%). The 100-year chloride content of SL30 at 60 mm depth is 0.097%, while the 100-year chloride content of SL50 (0.076%) and SL70 (0.075%) is lower than the critical chloride content (0.077%). As described in Chapter 5, the Ca in SL30 is quickly consumed, thus the formation of N-A-S-H gels plays a dominant role at a fairly early time, resulting in a very slow overall reaction rate at ambient temperature. Besides, Babae and Castel (2018) claimed that when GGBFS content was lower than 50%, Ca²⁺ tended to adhere to N-A-S-H gels through charge balance instead of forming C-A-S-H gels. It should also be noted that due to the interference of excessive shrinkage (reported in pure GGBFS system (Collins & Sanjayan, 2001)) on the time dependent model of D (Fig.6-4A), the prediction result of the chloride diffusion in SL100 is also the worst (Fig.6-6A).

6.3.3.2 EFFECT OF WATER/BINDER RATIO (W/B)

In Fig.6-6B, the chloride content of W50 is several times higher than that of W45 in the late stage. If the correct time dependent model of D can be established and used in W50, the gap may be reduced. It can be confirmed that higher w/b leads to the

larger initial water-filled space and hence more capillary pores (Fig.2-2) at the early age. As shown in Fig.6-2B, there is little difference in the measured D between W45 and W50 at 730 days. However, whether the initial gap can finally be completely filled has not been determined. To find out, the test time of natural chloride diffusion test (NCD) needs to be extended. Besides, too small w/b in W40 leads to the microcracking caused by drying shrinkage (G. Wang & Ma, 2018), which adversely affects the modelling of D (Fig.6-4B) and the prediction of chloride diffusion. In order to prepare durable AAFS concrete, the w/b should be strictly controlled (around 0.45).

6.3.3.3 EFFECT OF ALKALI CONTENT

As shown in Fig.6-6C, compared with FA/GGBFS and w/b, Na_2O content has relatively little effect on the chloride diffusion in AAFS concrete. This prediction result is consistent with the predicted D in Fig.6-4C. Higher Na_2O content leads to better pore-filling effect, lower D and hence slower chloride diffusion (X. Hu et al., 2019). As can be seen, the gap between N5 and N6 is smaller than that between N4 and N5, which is consistent with the measurement results in Chapter 4 (Fig.4-5). As described in Section 4.3.2.3, excessive Na_2O content may hinder the diffusion of Ca^{2+} from GGBFS and limit the formation of less porous C-A-S-H gels (Babae & Castel, 2018). Moreover, excessive Na_2O content may also promote the efflorescence (Z. Zhang et al., 2014) and drying shrinkage (Y. Ma & Ye, 2015).

6.3.3.4 EFFECT OF SILICATE CONTENT

As shown in Fig.6-6D, with the increasing SiO_2 content from 4% to 6%, the predicted chloride diffusion rate increases significantly. This prediction result is consistent with the predicted D in Fig.6-4D. As discussed in Section 6.3.1.4, in the first year, higher SiO_2 content seems to lead to the conversion of main reaction products from C-A-S-H gels to N-A-S-H gels, resulting in the slower capillary pore filling. However, as the reaction continues, higher SiO_2 content leads to the formation of more reaction products to fill capillary pores in the later stage. As a result, higher SiO_2 content is conducive to the long-term chloride resistance of AAFS concrete. This real impact may be misled by short-term measurements. Therefore, because previous research results are mainly based on short-term tests, the

conclusions may be inaccurate.

6.3.3.5 EFFECT OF SAND/AGGREGATE RATIO (S/A)

As shown in Fig.6-6E, the influence of s/a on the predicted chloride diffusion rate of AAFS concrete is limited and has no obvious regularity. In the early stage, there is little difference among AAFS mixtures with different s/a. However, with the extension of prediction time, the gap of AAFS mixtures with different s/a gradually increases. The measurement result in Fig.6-2E shows that the D of different mixtures tends to be consistent. Therefore, this prediction result may not be accurate. Because the test time of two years is too short, the established time dependent model of the D of each mixture may be inaccurate, as discussed in Section 6.3.1.5. If the test time of natural chloride diffusion test (NCD) can be extended, the measured D of each mixture may be consistent in the subsequent time, which may result in the similar prediction results of chloride diffusion.

6.3.4 PREDICTION OF CHLORIDE PROFILE

Fig.6-7 compares the chloride profiles of AAFS concretes with different GGBFS contents, water/binder ratios (w/b), Na₂O contents, SiO₂ contents and sand/aggregate ratios (s/a) at 5, 20, 50 and 100 years. The chloride profiles encompass a concrete cover depth of 100 mm with increments of 1 mm from the exposed surface. Overall, with the increase of concrete cover depth, the chloride content gradually decreases from different C_s to initial chloride content (C₀, around 0.071%). At shallow depths, the C_s has a decisive effect. As shown in Fig.6-7A, B, C and D, the higher C_s of SL30, W50, N4 and Si4 results in significantly higher chloride content near the exposed surface. Therefore, in addition to the study of D, it is also necessary to consider the differences of C_s in different AAFS concrete mixtures to achieve more accurate prediction. Fortunately, when the D is similar, the difference of chloride content decreases with the increase of depth. The downward trend of chloride content changes with exposure time. At 5 and 20 years, the chloride content decreases rapidly with the increase of depth. In most mixtures, the 5-year chloride content decreases to a very low level at 30 mm depth. At 50 and 100 years, the downward trend slows down, which is consistent with the prediction results of OPC concrete (Pack et al., 2010). It means the higher chloride content at all depths. In most

mixtures, the 100-year chloride content does not stabilize until at 70 mm depth.

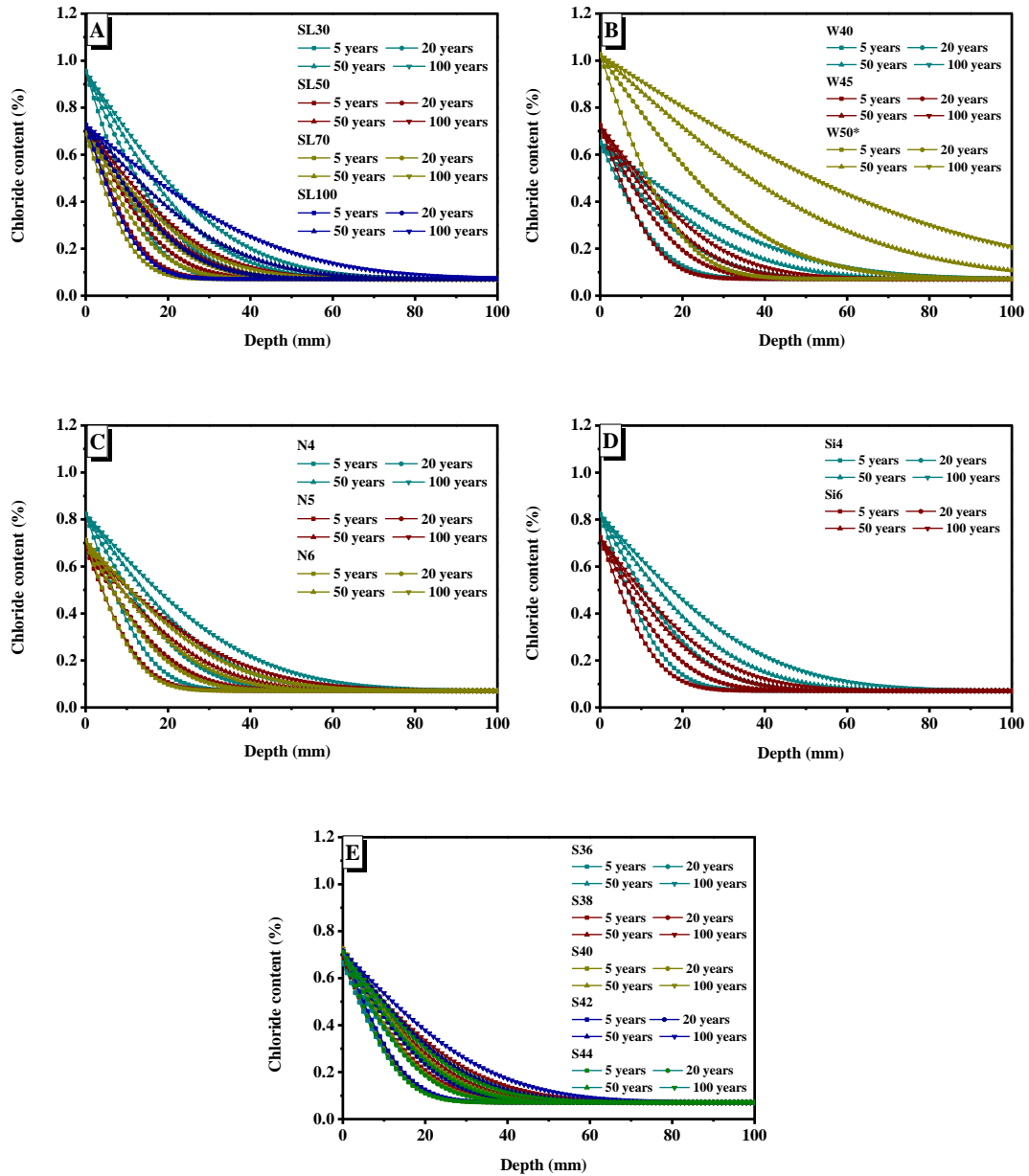


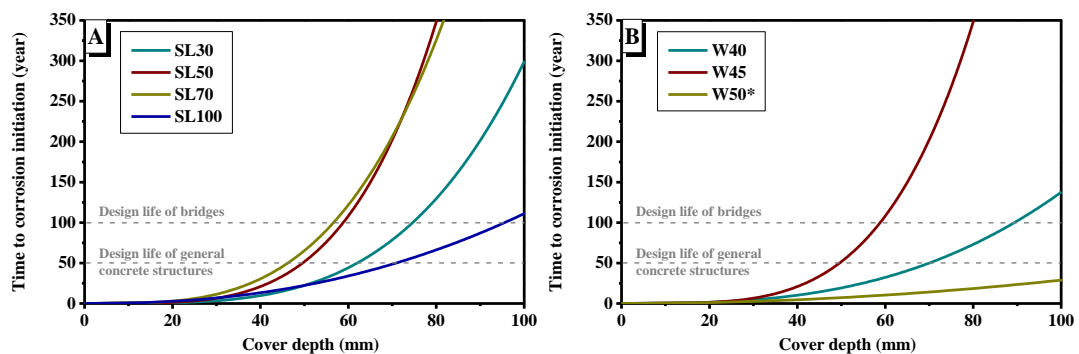
Fig.6-7 Chloride profiles of AAFCs with different (A) GGBFS contents, (B) water/binder ratios (w/b), (C) Na₂O contents, (D) SiO₂ contents and (E) sand/aggregate ratios (s/a) at 5, 20, 50 and 100 years. *W50 adopts a constant D ($0.75 \times 10^{-12} \text{ m}^2/\text{s}$).

Different parameters can affect the chloride profile through D and C_s. Excluding mixtures disturbed by shrinkage (SL100 and W40) (Collins & Sanjayan, 2001; Kutti et al., 1992; G. Wang & Ma, 2018), higher GGBFS content, lower w/b, higher Na₂O content and higher SiO₂ content usually lead to lower C_s and D. The lower C_s means the lower starting point of the descent curve. The lower D means the worse diffusivity and hence the faster downward trend of the curve. Therefore, the

corresponding AAFS concrete mixtures have a lower chloride content at each depth, as shown in Fig.6-7A, B, C and D. The s/a has limited impact on D and C_s . In Fig.6-7E, there is little difference in the chloride profiles of mixtures with different s/a at 5 years. However, the chloride profiles of mixtures with different s/a are obviously different at 100 years. It means that for a very long time, the subtle difference of D may lead to a great difference in the final prediction result. Therefore, the prediction of D should be as conservative as possible.

6.3.5 PREDICTION OF CORROSION INITIATION

Assuming the critical chloride content for corrosion initiation equates to 0.077% by weight of concrete (Tennakoon et al., 2017), the calculated time to corrosion initiation of AAFS concretes with different GGBFS contents, water/binder ratios (w/b), Na_2O contents, SiO_2 contents and sand/aggregate ratios (s/a) is depicted in Fig.6-8. However, the critical chloride content of different AAFS concrete mixtures still needs to be further determined. Babae and Castel (2018) found that the critical chloride content of AAFS (25%-75% GGBFS content) is in the range of 0.19% to 0.69% by weight of binder, while the critical chloride content suggested in OPC is 0.2% (CEB (Guide, 1992)) or 0.4% (RILEM (Recommendation, 1994)). This difference may be caused by the different alkalinity and chemical composition of pore solution. Mundra, Bernal Lopez, et al. (2017) claimed that depassivation would not occur until $[Cl^-]/[OH^-]^3 = 1.25$, thus the critical chloride content may increase with OH^- concentration. Besides, the oxidation of HS^- in the pore solution of the mixture dominated by GGBFS may lead to misleading electrochemical test results (Mundra, Bernal Lopez, et al., 2017).



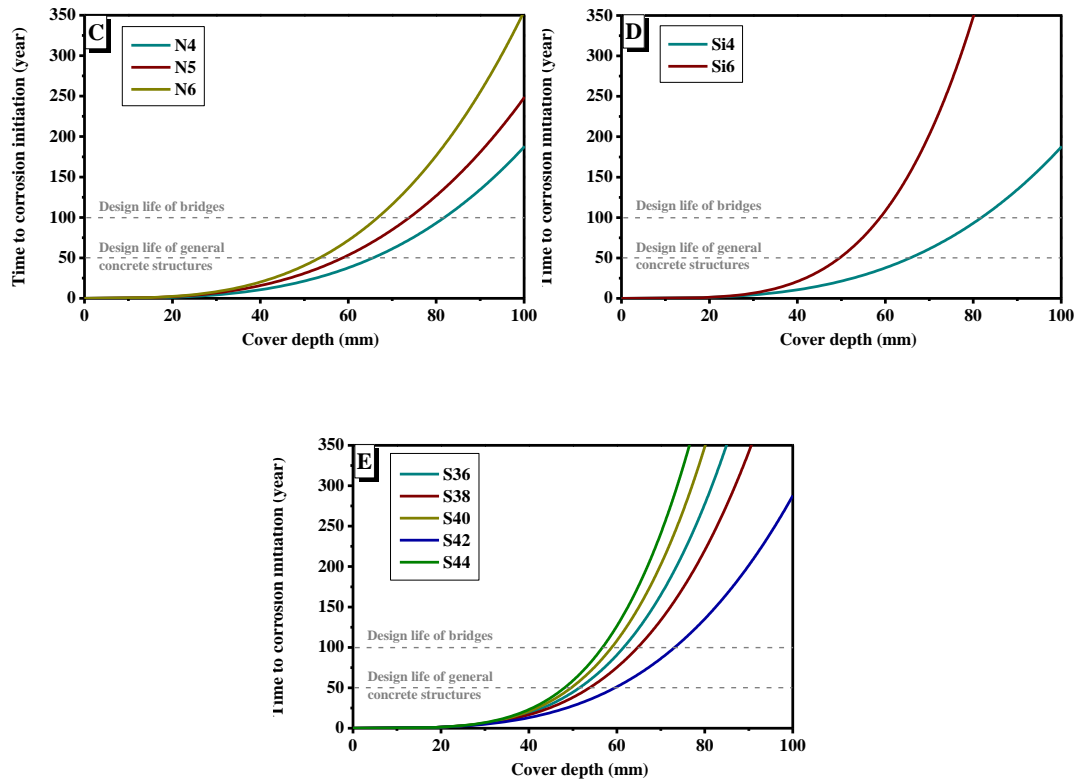


Fig.6-8 Time to corrosion initiation of AAFS concretes with different (A) GGBFS contents, (B) water/binder ratios (w/b), (C) Na₂O contents, (D) SiO₂ contents and (E) sand/aggregate ratios (s/a). *W50 adopts a constant D ($0.75 \times 10^{-12} \text{ m}^2/\text{s}$).

As shown in Fig.6-8, excluding mixtures disturbed by shrinkage (SL100 and W40) (Collins & Sanjayan, 2001; Kutti et al., 1992; G. Wang & Ma, 2018), higher GGBFS content, lower w/b, higher Na₂O content and higher SiO₂ content usually lead to the longer time to corrosion initiation at all depths, which is consistent with the lower chloride content at the same time (Fig.6-7). In order to make the initiation phase exceed the design life of general concrete structures (50 years), the required concrete covers of SL30, SL50 and SL70 are 62 mm, 49 mm and 46 mm (Fig.6-8A). For bridges (100 years), the corresponding required concrete covers are 75 mm, 59 mm and 57 mm. When SL50 and SL70 are applied, the corresponding protective layers (46-59 mm) can be realized in practical engineering to avoid corrosion initiation within the service life, which is almost impossible to achieve by using OPC concrete with a thickness of less than 100mm (Pack et al., 2010). For bridges, even the existing standards of OPC (60 mm, AS 5100.5) can be implemented. However, excessive w/b (W50 in Fig.6-8B), low Na₂O content (N4 and N5 in Fig.6-8C) and low SiO₂ content (Si4 in Fig.6-8D) may lead to the worse prediction results, which is

consistent with the predicted D in Fig.6-4. Therefore, the range of these parameters also needs to be limited to a certain range. Based on the existing prediction results, it is recommended to use 50%-70% GGBFS content, 0.45 w/b, 6% Na_2O content and 6% SiO_2 content in the design of AAFS concrete to achieve a long initiation phase. The values of these parameters are also within the optimal range summarized in Chapter 2. Besides, the change of s/a also seriously affects the predicted corrosion time of the protective layer over 40 mm (Fig.6-8E), which cannot be ignored. However, the measurement result in Fig.6-2E shows that the D of different mixtures tends to be consistent. As discussed in Section 6.3.1.5 and Section 6.3.3.5, the test time of two years is too short to establish the accurate time dependent model of D . If the test time of natural chloride diffusion test (NCD) can be extended, the measured D of each mixture may be consistent in the subsequent time, which may result in the similar predicted D and corrosion time.

6.4 CONCLUDING REMARKS

In this chapter, the time dependent models of D in different mixtures are established and the values of C_s in different mixtures are compared. The obtained results are used to predict the subsequent chloride diffusion and chloride profile, as well as the time to corrosion initiation. The following concluding remarks can be drawn:

- 1) In each mixture, the D obtained by natural chloride diffusion test exponentially decreases with time, while the corresponding C_s does not change significantly with time. Excluding the interference of shrinkage and efflorescence, higher GGBFS content, lower w/b, higher Na_2O content and higher SiO_2 content usually lead to the reduction of D and C_s , which is beneficial to the subsequent prediction results. For W50 with too high w/b (0.50), the modelling of D requires a longer measurement time. By comparison, the influence of s/a is limited and has no obvious regularity at the early age. With the extension of prediction time, the gap of mixtures with different s/a gradually increases. However, it may be the deviation caused by insufficient test time.
- 2) According to the chloride diffusion at 45 mm and 60 mm depths (required for general concrete structures and bridges), correctly formulated AAFS concrete can successfully extend the initiation phase for decades or even more than 100 years

compared with OPC concrete. The effects of different parameters on the prediction results of chloride diffusion are consistent with their effects on the predicted D . With the increase of cover depth, the difference of chloride diffusion among different mixtures decreases.

- 3) As the exposure time increases from 5 to 100 years, the downward trend of chloride profile slows down, which means the higher chloride content at each depth. The C_s has a decisive effect at shallow depths. With the increase of depth, the D gradually plays an important role. Excluding the interference of shrinkage, higher GGBFS content, lower w/b, higher Na_2O content and higher SiO_2 content usually lead to the lower chloride content at each depth. For a very long time (100 years), s/a also has a significant impact on the predicted chloride profile, but this may be due to the inaccurate prediction of D .
- 4) When correctly formulated AAFS (e.g. SL50 and SL70) is used, the required depth of protective layer (46-59 mm) can be realized in practical engineering to avoid corrosion initiation within the service life of general concrete structures and bridges (50 and 100 years). 50%-70% GGBFS content, 0.45 w/b, 6% Na_2O content and 6% SiO_2 content are suggested to delay corrosion initiation. Besides, s/a also affects the predicted corrosion time of deep protective layer (> 40 mm), which may be due to the inaccurate prediction of D . The critical chloride content is assumed to be 0.077% in this study, but it may vary with different parameters (e.g. GGBFS content), which needs to be studied in the future.

CHAPTER 7: EFFECTS OF MG-BASED ADMIXTURES ON CHLORIDE RESISTANCE OF ALKALI-ACTIVATED FLY ASH-SLAG SYSTEMS

7.1 INTRODUCTION

As described in Section 2.6.2, different Mg-based admixtures, including MgO, Mg-Al LDH and calcined Mg-Al LDH (CLDH), have been used to modify OPC and other cementitious materials. For OPC, Choi et al. (2014) reported that adding 5 wt.% MgO reduced the capillary pores between 30 and 300 nm, thus affecting the compressive strength and chloride diffusion. Z. H. Shui et al. (2012) found that although the addition of Mg-Al-NO₃ LDH coarsened the pore structure of OPC concrete and led to an increase in the total electrical charge passed, the higher chloride binding capacity had a greater positive impact on chloride resistance. Zhengxian Yang, Fischer, and Polder (2015) compared the improvement effect of adding 5 wt.% Mg-Al-pAB LDH and Mg-Al-NO₂ LDH on the chloride resistance of OPC mortar, and found that the former was better. S. Yoon et al. (2014) confirmed the recrystallisation of CLDH in OPC matrix, which led to stronger chloride binding capacity. P. Duan, Chen, Ma, and Shui (2013) concluded that the addition of 2 wt.% CLDH improved the chloride resistance of OPC and sulphoaluminate cement, which was attributed to the exchange and immobilization of chloride ions.

With regards to the effect of Mg-based admixtures on the chloride resistance of AAFS and other AAMs, only a limited number of publications can be found. Through rapid chloride permeability test (RCPT) and ponding test, H. Yoon et al. (2018) found that adding 5 wt.% MgO increased total electrical charge, but decreased the chloride penetration depth of AAFS binder (50 wt.% GGBFS). When NaOH solution replaced Na₂O·nSiO₂ solution as activator, both test methods showed that the added MgO improved the chloride resistance of AAFS binder (H. Yoon et al., 2018). Based on non-steady-state migration (NSSM) test, T. Liu et al. (2020) reported that AAFS mortars (70 wt.% GGBFS) modified by 4 wt.% MgO, Mg-Al-NO₃ LDH and CLDH had the smaller chloride migration coefficient (D_{NSSM}), and considered that CLDH had the best improvement effect. Ke, Bernal, Hussein, et al. (2017) found the addition of 5 wt.% CLDH also led to the smaller D_{NSSM} in carbonate-activated GGBFS, which was attributed to more compact microstructure

and increased chloride binding capacity. However, in order to shorten the test time, the above studies mainly evaluated chloride resistance by RCPT and NSSM test, which only focused on pore structure and could not consider chloride binding (Yuanzhan Wang & Fu, 2019). Previous studies on modified OPC (Z. H. Shui et al., 2012; Zhengxian Yang et al., 2015) showed that the results of RCPT and NSSM test were not completely consistent with the results of chloride diffusion test, which could consider chloride binding and reflect the real situation. Therefore, previous studies on the chloride resistance of modified AAFS may not be completely accurate. Consequently, it is necessary to conduct chloride diffusion test in AAFS modified by different Mg-based admixtures, and analyse the measurement result in combination with pore structure and chloride binding.

This chapter aims to investigate the effects of different Mg-based admixtures on the chloride resistance of AAFS mortars by chloride diffusion test. AAFS mixes with 0 and 5 wt.% MgO, Mg-Al-CO₃ LDH and CLDH addition are studied, and OPC is used as a reference sample. Compressive strengths at different ages are determined. A slightly modified bulk diffusion test is performed, and the chloride diffusion in different mortar specimens is assessed according to chloride diffusion coefficient (D). To better understand the influence mechanism of different Mg-based admixtures, additional information is discussed, including pore structure determined by nitrogen adsorption test and phase composition identified by X-ray diffractometry (XRD). These results are expected to provide a more scientific basis for the application of Mg-based admixtures in reinforced AAFS concrete structures under marine environment.

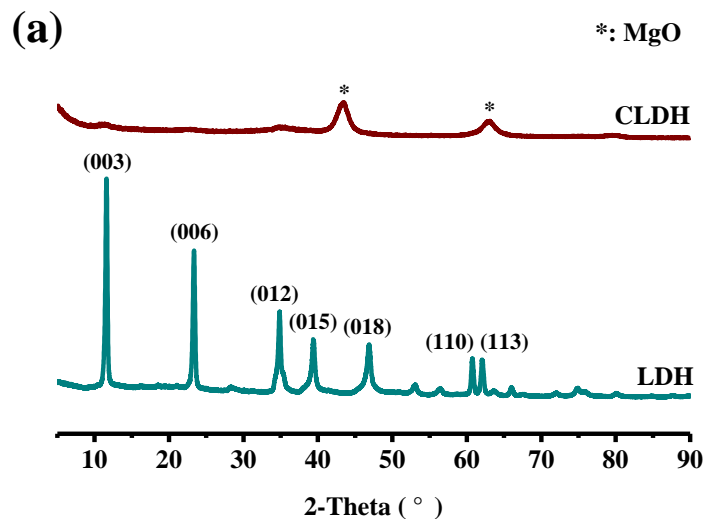
7.2 MATERIALS AND EXPERIMENTAL METHODS

7.2.1 MATERIALS

The precursors and activators used in this chapter to manufacture AAFS mortars and pastes are the same as those in Chapter 3. The chemical and physical properties (including chemical composition, particle size distribution, morphology and phase composition) of FA and GGBFS were given in Section 3.2.1. According to Section 3.2.2, sodium silicate (Na₂O·nSiO₂) solution was prepared by mixing analytical grade sodium hydroxide (NaOH, > 98% purity), industrial grade waterglass

($\text{Na}_2\text{O} = 12.19 \text{ wt.}\%$, $\text{SiO}_2 = 28.18 \text{ wt.}\%$, $\text{H}_2\text{O} = 58.92 \text{ wt.}\%$) and distilled water. To prepare OPC reference samples, PO 42.5 cement produced by Yangchun Cement Pty Ltd (Shandong Province, China) was used. In the preparation of AAFS and OPC mortars, ISO standard sand from Xiamen ISO Standard Sand Company Limited, Fujian, China, was used as fine aggregate.

Mg-based admixtures including MgO, Mg-Al- CO_3 LDH and calcined Mg-Al- CO_3 LDH were used in this chapter. Analytical grade MgO ($> 98\%$ purity) was provided by Zhiyuan Chemistry Reagent Company Limited, Tianjin, China. Commercial Mg-Al- CO_3 LDH was supplied by Shaoyang Heaven Assistant Chemical Industry Company Limited, Hunan, China. Calcined Mg-Al- CO_3 LDH (abbreviated as CLDH) was prepared by thermally treating Mg-Al- CO_3 LDH at $550 \text{ }^\circ\text{C}$ for 4 hours with a heating rate of $5 \text{ }^\circ\text{C}/\text{min}$ (Ke et al., 2016; T. Liu et al., 2020). Then, the CLDH was cooled naturally to $105 \text{ }^\circ\text{C}$ in the furnace, moved to a sealed centrifuge tube and stored in a desiccator under vacuum (Ke et al., 2016; T. Liu et al., 2020). The X-ray diffractometry (XRD) patterns and Fourier transform infrared spectroscopy (FTIR) spectra of Mg-Al- CO_3 LDH and CLDH are presented in Fig.7-1.



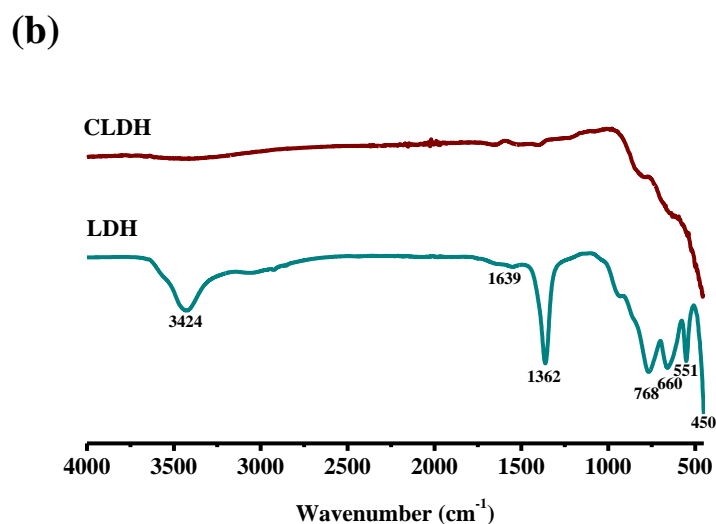


Fig.7-1 XRD patterns (a) and FTIR spectra (b) of Mg-Al-CO₃ LDH and CLDH.

As shown in Fig.7-1(a), the main diffraction peaks of Mg-Al LDH are very sharp, especially d(003) at 11.6° and d(006) at 23.4° (Cai et al., 2022; Cao et al., 2019; P. Duan et al., 2013; Guo, Wu, Duan, & Zhang, 2020). This corresponds to high purity and complete crystal structure. In CLDH, the well-defined diffraction peaks of the original sample are replaced by MgO peaks at 43.4° and 62.9°, which is consistent with previous studies (Cao et al., 2019; P. Duan et al., 2013; Guo et al., 2020). In Fig.7-1(b), the broad band at around 3424 cm⁻¹ is attributed to physically adsorbed water molecules and hydroxyl groups on brucite-like layers (Cao et al., 2019; Hang, Truc, Duong, Pébère, & Olivier, 2012), which becomes less intense in CLDH. The weak band at 1639 cm⁻¹ is related to the bending vibration of interlayer water molecules (Cao et al., 2019; Hang et al., 2012). The strong band observed at 1362 cm⁻¹ is due to the v₃ asymmetric stretching of carbonate anions (Cao et al., 2019; Guo et al., 2020). This band becomes very weaker in CLDH, indicating that most carbonate anions were removed by calcination. The bands at 768 cm⁻¹, 660 cm⁻¹ and 551 cm⁻¹ should be related with the vibrations of M-O (M = Mg, Al) in brucite-like layers (Cao et al., 2019; Hang et al., 2012; D. Li et al., 2011).

7.2.2 SAMPLE PREPARATION

AAFS and OPC mortars (M) and pastes (P) were prepared according to the mix proportions shown in Table 7-1. Five sets of mortars were prepared: AAFS mortars without admixture (M-A), AAFS mortars with 5 wt.% MgO (M-M), AAFS mortars with 5 wt.% Mg-Al-CO₃ LDH (M-L), AAFS mortars with 5 wt.% CLDH (M-C) and

OPC mortars (M-OPC). The mix proportion of M-A was derived from that of SL50 designed in Chapter 3, which exhibits a good combination of workability, compressive strength and chloride resistance. In this mix proportion, FA/GGBFS mass ratio was kept at 1:1. Na₂O and SiO₂ contents provided by alkali activator were kept at 4% and 6% of the total mass of precursors (FA+GGBFS), respectively. The water/binder mass ratio (w/b) was maintained at 0.45. The binder/sand mass ratio was kept at 1:2. For microstructural analysis, five sets of pastes with the same binder constituents were prepared: P-A, P-M, P-L, P-C and P-OPC.

Table 7-1 Mix proportions of AAFS and OPC mortars (M) and pastes (P).

Sample ID	Binder			Activator			Admixture			Sand (wt.%)
	FA (wt.%)	GGBFS (wt.%)	Cement (wt.%)	Na ₂ O (wt.%)	SiO ₂ (wt.%)	w/b	MgO (wt.%)	Mg-Al-CO ₃ LDH (wt.%)	CLDH (wt.%)	
M-A	50	50		4%	6%	0.45				200
M-M	50	50		4%	6%	0.45	5%			200
M-L	50	50		4%	6%	0.45		5%		200
M-C	50	50		4%	6%	0.45			5%	200
M-OPC			100			0.45				200
P-A	50	50		4%	6%	0.45				
P-M	50	50		4%	6%	0.45	5%			
P-L	50	50		4%	6%	0.45		5%		
P-C	50	50		4%	6%	0.45			5%	
P-OPC			100			0.45				

AAFS mortars and pastes were prepared by a JJ-5 rotary mixer. To achieve a uniform dispersion, the precursors (FA+GGBFS), admixture and sand (for mortars only) were first dry mixed for 2 mins at medium speed. Subsequently, the alkali activator was slowly added. The mortar and paste were immediately mixed for 2 mins at low speed. After scraping down the blade and bowl, mixing continued for another 2 mins at medium speed. Then, the mortar was poured into cubic moulds (40 mm × 40 mm × 40 mm and 70 mm × 70 mm × 70 mm), and the paste was poured

into plastic bottles (\varnothing 36 mm \times 68 mm). The cubic moulds and bottles were then put on a vibrating table for 2 mins to remove air bubbles and sealed to prevent moisture loss (Y. Ma, 2013a; Z. Yu, 2015). After curing at room temperature (20 °C) for 24 hours, the mortar and paste samples were demolded and placed in a curing chamber (relative humidity of 95% and temperature of $20 \pm 2^\circ\text{C}$) until the testing day. OPC reference samples were also prepared according to the same steps.

7.2.3 EXPERIMENTAL METHODS

7.2.3.1 COMPRESSIVE STRENGTH

According to NEN-EN-196-1, the compressive strength of AAFS and OPC mortar cubes (40 mm \times 40 mm \times 40 mm) at 3, 7, 28 and 63 days was measured. The compression load was applied by an Instron-5984 universal testing machine (Instron, UK) at a rate of 2.4 kN/s. For each mix proportion at each testing age, the average result of at least three replicates was calculated.

7.2.3.2 CHLORIDE DIFFUSION TEST

Bulk diffusion tests were carried out on AAFS and OPC mortar cubes (70 mm \times 70 mm \times 70 mm) according to a slightly modified form of ASTM C1556. After 28 days of curing, the surfaces of each mortar cube were sealed with paraffin wax, and only one surface was not sealed to achieve one-dimensional diffusion (Hall, 1977). Subsequently, sealed mortar cubes were immersed in 165 g/L NaCl solution for 35 days. A DRB-H1 concrete grinding machine was used to obtain powder samples. After removing paraffin wax, 10 layers were ground from the exposed surface of each mortar cube and each layer was kept at 2 mm. The powder samples were then sieved with a 0.6 mm sieve, dried in an oven (55 °C) for 2 hours, and cooled to 20 °C in a desiccator (Yanru Wang et al., 2019). Afterwards, the powder samples were sealed and stored until the testing day. According to JTJ270-98 described in 4.2.3 Section, the free (water-soluble) chloride content of each powder sample was determined by AgNO_3 titration to obtain the chloride profile.

After finishing the bulk diffusion test and titration, the apparent chloride diffusion coefficient (D) was determined by fitting Fick's second law expressed in Equation 10 to the measured chloride profile through a non-linear regression analysis (MATLAB).

7.2.3.3 NITROGEN ADSORPTION TEST

In this chapter, the pore structure analysis was conducted by nitrogen adsorption test using an ASAP 2460 surface area and porosimetry analyser (Micromeritics, USA). After 28 days of curing, AAFS and OPC pastes were crushed. Subsequently, fragments from the centre of specimens were chosen and crushed into small pieces (1-2 mm³). The reaction was stopped by solvent exchange with isopropanol (S. Zhang et al., 2021). After 24 hours of immersion in isopropanol, small pieces were dried in an oven (60 °C) until the mass was constant (X. Hu et al., 2019). Before the test, the investigated samples were degassed at 60 °C. After obtaining the test results, Barrett-Joyner-Halenda (BJH) model was used to calculate the pore size distribution (Barrett et al., 1951).

7.2.3.4 X-RAY DIFFRACTOMETRY (XRD)

To determine the products of potential chemical binding, powder samples obtained from AAFS and OPC pastes before and after immersion in simulated chloride-rich pore solution were analysed by X-ray diffractometry (XRD). Based on previous studies (Ke, Bernal, Hussein, et al., 2017; Ke, Bernal, et al., 2017b), simulated chloride-rich pore solution was prepared (Table 7-2). The chloride concentration was kept at 0.75 mol/L, slightly higher than that in seawater (0.6-0.7 mol/L) (Neville, 1995; J. Zhang et al., 2019b). After 28 days of curing, AAFS and OPC pastes were crushed into pieces. Afterward, the fragments in the centre were further crushed in sealed plastic bags with a hammer (Ke, Bernal, Hussein, et al., 2017) and sieved to obtain particles of 0.25-0.90 mm. 2g sieved paste particles were immediately added to 12 mL simulated chloride-rich pore solutions in 15 mL centrifuge tubes. The centrifuge tubes were then sealed to minimise water evaporation and sample carbonation. The total immersion time was 60 days, in which the centrifuge tubes were periodically shaken (2 minutes every 3 days) to reach reaction equilibrium (J. Zhang et al., 2019b). The storage temperature was controlled at 20 ± 2 °C (Geng, Pan, Wang, Chen, & Zhu, 2021; J. Zhang et al., 2019b). After immersion, the particles separated from simulated chloride-rich pore solutions were washed with distilled water.

Table 7-2 Stoichiometric compositions of simulated chloride-rich pore solution.

NaCl (mol/L)	NaOH (mol/L)	Total Na ⁺ (mol/L)	[Cl ⁻]/[OH ⁻]
0.75	0.25	1.00	3.0

Both the non-immersed and immersed samples were ground into fine powders and sieved using a 0.045 mm mesh. After that, the powders were dried in an oven (60 °C) for 2 hours. For XRD analysis, a PW 3040/60 X'Pert Pro powder diffractometer (PANalytical, Netherland) with Cu-K α radiation ($\lambda = 1.5418 \text{ \AA}$) was used. The powder samples were step-scanned from 10 to 35° 2 θ . The step size was 0.02° and the count time was 2 s/step.

7.3 RESULTS AND DISCUSSION

7.3.1 COMPRESSIVE STRENGTH

Fig.7-2 shows the compressive strength of AAFS and OPC mortars at 3, 7, 28 and 63 days. As expected, the compressive strength of all mortars increases with the increase of curing age. The reasonable explanation is the continuous reaction and the enhancement of pore structure. Although the performance at 3 days is worse, after 7 days, the compressive strength of all AAFS mortars except M-L is higher than that of OPC reference sample (M-OPC). At 28 days, the compressive strength of M-A is 60.43 MPa, which is ~131% of M-OPC (46.08 MPa).

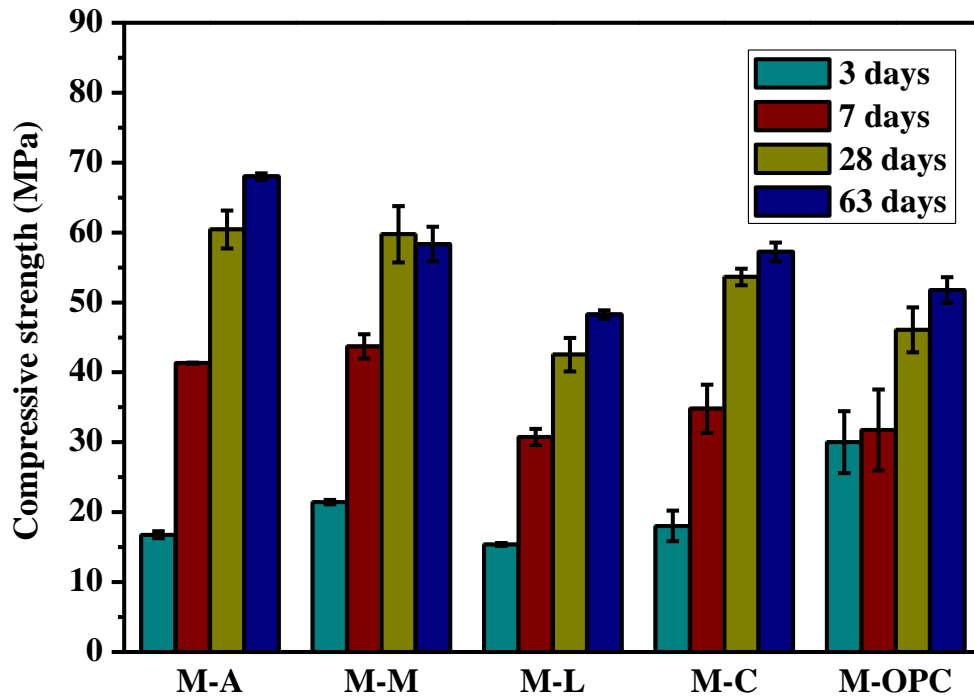


Fig.7-2 Compressive strength of AAFS and OPC mortars at 3, 7, 28 and 63 days.

As shown in Fig.7-2, the addition of 5 wt.% MgO to AAFS mortar significantly improves the compressive strength in the short term (~28% at 3 days and ~6% at 7 days). At 7 days, the compressive strength of M-M is up to 43.71 MPa. This observation is consistent with previous studies (Hwang, Vo, Tran, & Yehualaw, 2018; Jin, Gu, & Al-Tabbaa, 2014, 2015; T. Liu et al., 2020). One possible reason is that MgO can promote the formation of more reaction products to fill capillary pores (Jin et al., 2014, 2015). However, the results show that the addition of MgO is not effectiveness on the compressive strength at 28 days. At 63 days, the compressive strength of M-M even decreases slightly (from 59.75 MPa to 58.35 MPa), which is only ~86% of its counterpart without MgO (M-A). Hwang et al. (2018) obtained similar results and claimed that the reasons were the reduction of aluminosilicate content and the expansion of hydrotalcite-like phases (Mg-Al-OH LDH).

The addition of 5 wt.% Mg-Al-CO₃ LDH results in a significant reduction in compressive strength at all testing ages (Fig.7-2), which is consistent with the observation in sulphoaluminate cement concrete (P. Duan et al., 2013). At 28 days, the compressive strength of M-L is only 42.54 MPa, about 70% of M-A (60.43 MPa), and even lower than M-OPC (46.08 MPa). Similar results were obtained in other

types of Mg-Al LDH (T. Liu et al., 2020; Zhengxian Yang et al., 2015). T. Liu et al. (2020) found that adding 2-4 wt.% Mg-Al-NO₃ LDH resulted in a slight decrease in the compressive strength of AAFS mortar dominated by GGBFS (70 wt.%). In addition, Zhengxian Yang et al. (2015) reported that the addition of 5-10 wt.% Mg-Al-pAB LDH and Mg-Al-NO₂ LDH significantly reduced the compressive strength and flexural strength of OPC mortar.

As with MgO, adding CLDH is beneficial at 3 days. Ke et al. (2016) claimed that Mg-Al-OH LDH formed via recrystallisation could act as a nucleation seed to promote gel precipitation. However, Fig.7-2 shows that the subsequent compressive strength development of M-C exhibits the same trend with M-L. Compared with Mg-Al-CO₃ LDH, the negative impact of CLDH on compressive strength is relatively small. At 63 days, M-C (57.23 MPa) shows the same compressive strength level as M-M (58.35 MPa), about 84-86 % of M-A (68.03 MPa). This observed trend is consistent with the decrease in the compressive strength of AAFS containing 70 wt.% GGBFS (T. Liu et al., 2020), but completely opposite to the increase in the compressive strength of carbonate-activated GGBFS (Ke, Bernal, Hussein, et al., 2017).

7.3.2 CHLORIDE DIFFUSIVITY

7.3.2.1 CHLORIDE PROFILES

Fig.7-3 compares the chloride profiles of four AAFS mortar samples and one OPC reference mortar sample. As expected, a similar trend can be found in different mixes. The chloride content near the exposure surface decreases sharply along the diffusion depth. As the diffusion depth increases, the downward trend slows down until a relatively stable value is reached, which is considered as the initial chloride content (C₀). As observed, although it is not obvious near the exposed surface, the chloride content of M-OPC is generally higher than that of AAFS mixes, which is consistent with previous studies (Tennakoon et al., 2017; T. Yang et al., 2014). The addition of 5 wt.% MgO and CLDH results in a slight decrease in chloride content near the exposed surface. When the diffusion depth is greater than 8 mm, the improvement effect of CLDH is better. Compared with other mixes, the chloride content of M-L is significantly higher in the first 6 mm depth. This may be due to the coarser pore

structure, which corresponds to the lower compressive strength (Fig.7-2). However, the chloride content in the deeper layer decreases sharply, resulting in a small final stability value. This trend is similar to the OPC mortar with 5 wt.% Mg-Al-pAB LDH, indicating stronger chloride resistance (Zhengxian Yang et al., 2015). Compared with other mortar samples, the initial chloride content (C_0) of M-L and M-C is lower and reaches earlier. This may be because more chloride ions are bound in the added or recrystallised Mg-Al LDH.

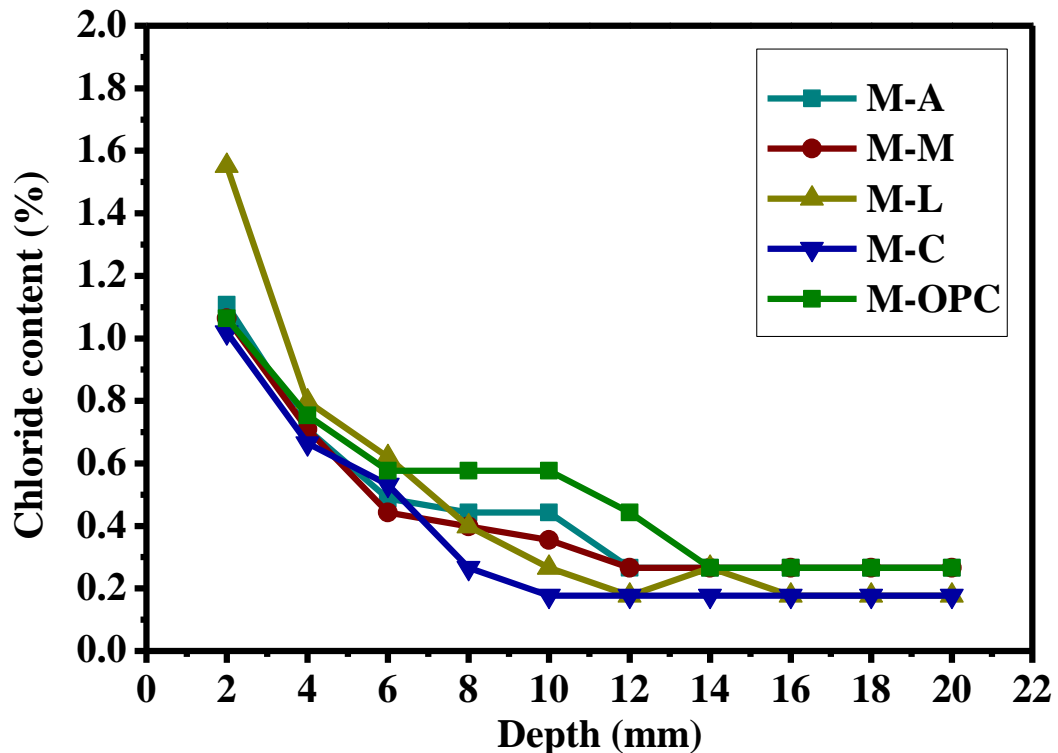


Fig.7-3 Comparison of chloride profiles of AAFS and OPC mortars after 35 days of immersion in 165 g/L NaCl solution.

7.3.2.2 CHLORIDE DIFFUSION COEFFICIENTS (D)

By fitting Fick's second law expressed in Equation 10 to the measured chloride profiles (Fig.7-3), the corresponding apparent chloride diffusion coefficients (D) are determined. Fig.7-4 shows the fitting curves of AAFS and OPC mortars. As observed, the determined coefficient (R^2) is greater than 0.93 in all mixes. Compared with M-OPC, AAFS mixes have higher exposure surface chloride content (C_s) and lower D, which is consistent with the previous calculation (Tennakoon et al., 2017). In addition, the calculated C_s of M-L (2.16%) is significantly higher than that of other AAFS mixes (around 1.43%), which corresponds to the higher chloride content near

the exposure surface (Fig.7-3). Fortunately, due to the rapid decline of chloride content with depth, the D of M-L is not large. It should be noted that since D is coupled with Cs in the curve-fitting, only the value of D may not reflect the actual chloride resistance (Zhengxian Yang et al., 2015). Besides, during the curve-fitting using Equation 10, D is assumed to be constant. But actually, it is time-dependent (Yuanzhan Wang & Fu, 2019). In more complex environments, e.g. tidal zone and splash zone (Uji et al., 1990) and marine atmospheric conditions (Kassir & Ghosn, 2002), the build-up of Cs may also occur.

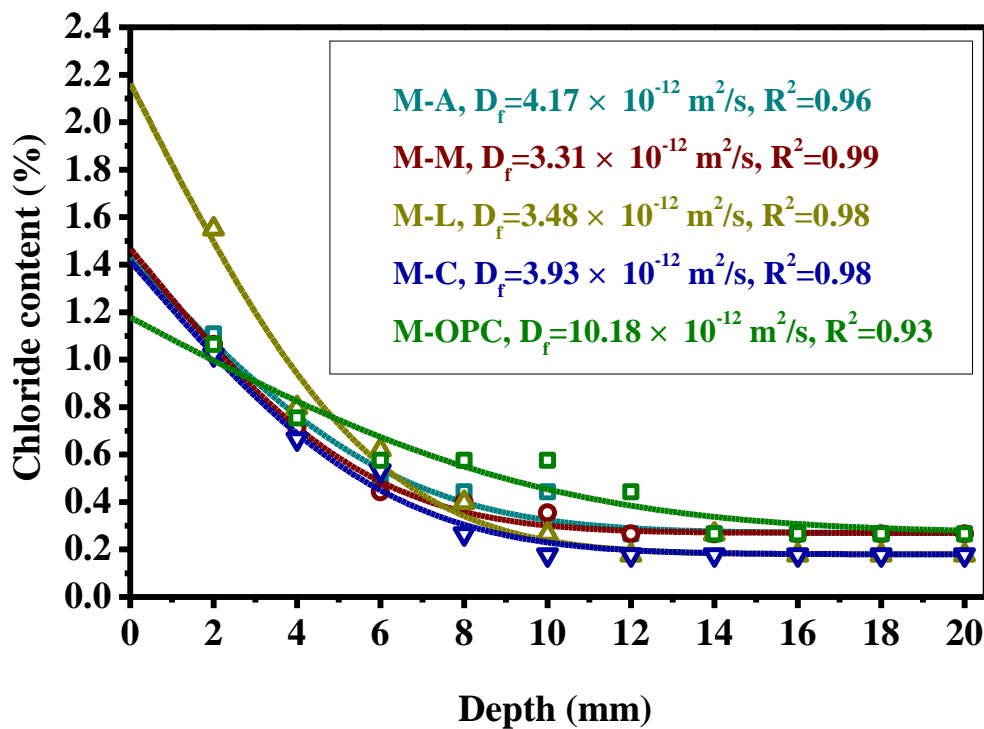


Fig.7-4 Fitting curves of AAFS and OPC mortars after 35 days of immersion in 165 g/L NaCl solution.

The calculated apparent chloride diffusion coefficients (D) of AAFS and OPC mortars are compared in Fig.7-5. The D of M-A ($4.17 \times 10^{-12} \text{ m}^2/\text{s}$) is about 41% of that of M-OPC ($10.18 \times 10^{-12} \text{ m}^2/\text{s}$), which means the higher chloride resistance of AAFS mixes. This finding agrees with the results of previous chloride diffusion tests, including bulk diffusion test (Babae & Castel, 2018; Tennakoon et al., 2017) and ponding test (Ismail, Bernal, Provis, San Nicolas, et al., 2013). Moreover, the addition of all Mg-based admixtures leads the decrease in the D of AAFS mortar, which is consistent with the results of NSSM test (T. Liu et al., 2020). It means that

all Mg-based admixtures used in this study can effectively improve the chloride resistance of AAFS mortar, and the addition amount (5 wt.%) is reasonable.

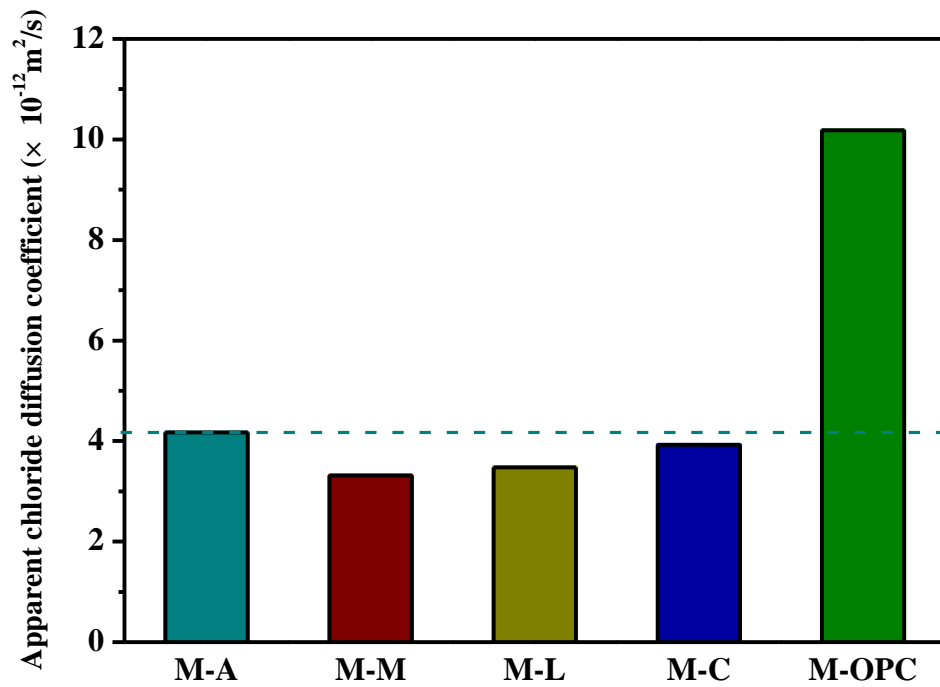


Fig.7-5 Apparent chloride diffusion coefficients (D) of AAFS and OPC mortars after 35 days of immersion in 165 g/L NaCl solution.

As shown in Fig.7-5, the addition of 5 wt.% MgO has the highest contribution to improving the chloride resistance of AAFS mortar. The D of M-M ($3.31 \times 10^{-12} \text{ m}^2/\text{s}$) is ~21% lower than that of M-A ($4.17 \times 10^{-12} \text{ m}^2/\text{s}$). Similar results were obtained in ponding test (H. Yoon et al., 2018) and NSSM test (T. Liu et al., 2020). Through ponding test, H. Yoon et al. (2018) found that the addition of 5 wt.% MgO led to the chloride penetration depth of AAFS binder decreased from 3.9 mm to 3.5 mm. When NaOH solution replaced $\text{Na}_2\text{O} \cdot n\text{SiO}_2$ solution as activator, the reduction of chloride penetration depth was more obvious (from 4.4 mm to 3.6 mm). T. Liu et al. (2020) reported that the addition of 2 wt.% and 4 wt.% MgO reduced the D_{NSSM} of AAFS mortar by 14% and 16%, respectively. Combined with the result of this study, it can be concluded that the chloride resistance of AAFS tends to increase with higher MgO content. However, the added MgO should not be excessive. Based on the increased chloride penetration depth, H. Yoon et al. (2018) considered that adding 10 wt.% MgO was harmful.

In Fig.7-5, the D of M-L ($3.48 \times 10^{-12} \text{ m}^2/\text{s}$) is ~83% of M-A ($4.17 \times 10^{-12} \text{ m}^2/\text{s}$). It

means that the addition of 5 wt.% Mg-Al-CO₃ LDH helps to enhance the chloride resistance of AAFS mortar, although it has a negative impact on the compressive strength development during this period (Fig.7-2). This finding coincided with previous studies on other types of Mg-Al LDH (T. Liu et al., 2020; Z. H. Shui et al., 2012; Zhengxian Yang et al., 2015). In NSSM test, T. Liu et al. (2020) found that the incorporation of 4 wt.% Mg-Al-NO₃ LDH reduced the D_{NSSM} of AAFS mortar by 17%, which is coincident with the result of bulk diffusion test in OPC concrete (Z. H. Shui et al., 2012). Zhengxian Yang et al. (2015) investigated the influence of 5 wt.% Mg-Al-pAB LDH and Mg-Al-NO₂ LDH on the chloride ingress in OPC mortar by NSSM test, and found that the D_{NSSM} decreased by 12% and 7%, respectively. Noted that if the total (acid-soluble) chloride content instead of free (water-soluble) chloride content is used in bulk diffusion test, higher chloride binding capacity may make the measurement result worse (Zhengxian Yang et al., 2015). But in fact, under the same pore structure, higher chloride binding capacity is conducive to the chloride resistance of AAFS and OPC.

Fig.7-5 shows that the addition of 5 wt.% CLDH also prevents the chloride diffusion in AAFS mortar, which corresponds to the result of NSSM test (T. Liu et al., 2020). Similar results were obtained in carbonate-activated GGBFS, OPC and sulphoaluminate cement (P. Duan et al., 2013; Ke, Bernal, Hussein, et al., 2017; S. Yoon et al., 2014). Nevertheless, the D of M-C (3.93×10^{-12} m²/s) is larger than that of M-M (3.31×10^{-12} m²/s) and M-L (3.48×10^{-12} m²/s), indicating that the enhancement effect of CLDH is relatively poor. This finding is contrary to the smaller D_{NSSM} measured by NSSM test (T. Liu et al., 2020). The most reasonable explanation is that, unlike NSSM test, bulk diffusion test can consider chloride binding (Yuanzhan Wang & Fu, 2019). In addition, the order of chloride resistance (M-M > M-L > M-C > M-A > M-OPC) is also different from that of compressive strength (M-A > M-M > M-C > M-OPC > M-L), which needs to be explained from the perspective of microstructure. Therefore, it is necessary to discuss the influence mechanism of each Mg-based admixture in combination with pore structure and phase composition.

7.3.3 PORE STRUCTURE

Like other cementitious materials, AAFS binder is not completely impenetrable and

contains several types of pores that influence compressive strength and ionic transport. As described in Section 2.2.2.1, these pores can be classified into three classes: gel pores (<10 nm), capillary pores (10–10,000 nm) and air voids (>10,000 nm). Gel pores are the smallest pores, which exist in reaction products and mainly affect shrinkage and creep rather than strength and permeability (X. Hu et al., 2019; C Shi et al., 1989). Entrapped/entrained air voids have the largest size and are harmful to mechanical properties. However, their volume fraction is not high and they are not connected with each other (Glass & Buenfeld, 2000; Pack et al., 2010). Therefore, they normally do not influence transport properties. When considering strength and ionic transport, capillary pores are the most important because they are usually interconnected and filled with pore solution (X. Hu et al., 2019; Pack et al., 2010). In addition to the volume fraction, the connectivity of capillary pores can also determine the rate of chloride transport (Pack et al., 2010; G. Ye, 2005). From the preliminary studies using mercury intrusion porosimetry (MIP) and other methods (Nedeljković, Šavija, Zuo, Luković, & Ye, 2018), pores larger than 100 nm are hardly observed in AAFS, especially in silicate-activated mixes. Therefore, the pore structure of AAFS is well matched with the measurement range of nitrogen adsorption test (S. Zhang et al., 2021).

The pore volume and pore size distribution of AAFS and OPC pastes derived from nitrogen adsorption test are shown in Fig.7-6(a) and (b), respectively. Fig.7-6(a) shows that the cumulative pore volume of P-OPC (0.0905 ml/g) is much higher than that of AAFS mixes (0.0378-0.0571 ml/g), indicating a coarser pore structure. Moreover, the higher total pore volume of OPC is mainly attributed to the higher volume of capillary pores, while most of pores in AAFS belong to gel pores. These findings are consistent with the MIP results obtained in previous studies (T. Liu et al., 2020; H. Yoon et al., 2018), which can explain why the compressive strength (Fig.7-2) and chloride resistance (Fig.7-5) of OPC are generally weaker than AAFS. In pore size distribution curves (Fig.7-6(b)), the pore diameter corresponding to the peak can be regarded as the threshold pore diameter, which is the most widely distributed pore diameter (H. Yoon et al., 2018). As the previous results (T. Liu et al., 2020; H. Yoon et al., 2018), the influence of different Mg-based admixtures on the threshold pore diameter of AAFS is less apparent.

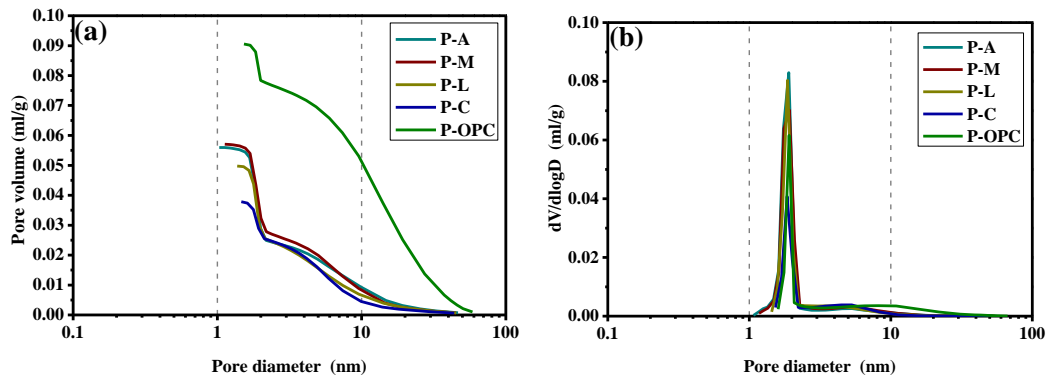


Fig.7-6 Cumulative pore volume (a) and pore size distribution (b) of AAFS and OPC pastes, derived from nitrogen adsorption test.

In MgO-modified AAFS sample (P-M), although the total pore volume is slightly higher, the volume of capillary pores is lower (Fig.7-6(a)), which is consistent with the result of MgO-modified OPC (Choi et al., 2014). It means that gels are rapidly formed to fill capillary pores, which corresponds to higher compressive strength (Fig.7-2) and chloride resistance (Fig.7-5). Similar results were obtained in the scanning electron microscope (SEM) images of MgO-modified AAS samples (Hwang et al., 2018; Jin et al., 2014, 2015). The mechanism of adding MgO to accelerate the alkali-activation may be that the dissolution of MgO can lead to fast heat release and increase of pH (Jin et al., 2014; Park et al., 2020). In addition, hydrotalcite-like phases (Mg-Al-OH LDH) were detected in AAS (Hwang et al., 2018; Jin et al., 2014, 2015). Due to the greater volume, these phases can increase expansion and refine pore structure (Hwang et al., 2018). In AAFS, the same phases may also be generated, but this needs to be identified by XRD.

Compared with unmodified AAFS sample (P-A), P-L and P-C exhibit lower total pore volume as well as lower volume of capillary pores (Fig.7-6(a)). These results seem to indicate a more compact pore structure, but are clearly not consistent with lower compressive strength (Fig.7-2). For these contradictory results, the most reasonable explanation is that the addition of Mg-Al-CO₃ LDH and CLDH leads to more air voids, which cannot be measured by nitrogen adsorption test. The higher total porosity measured by MIP (T. Liu et al., 2020; Zhengxian Yang et al., 2015) can confirm the above viewpoint. The reason may be the reduced workability and the uneven distribution of Mg-Al LDH (Zhengxian Yang et al., 2015). Because these air voids are not connected with each other, their influence on chloride diffusion is

limited (Glass & Buenfeld, 2000; Pack et al., 2010). This explains why the D of M-L and M-C does not increase (Fig.7-5). Compared with P-L, the volume of capillary pores and gel pores in P-C is smaller, which can explain the smaller reduction of compressive strength (Fig.7-2). The reason may be that recrystallised Mg-Al LDH can act as a nucleation seed to promote gel precipitation (Ke et al., 2016), which is consistent with the increase of compressive strength of M-C at 3 days (Fig.7-2). However, the better effect of Mg-Al-CO₃ LDH on enhancing chloride resistance needs to be discussed in combination with phase composition.

7.3.4 PHASE COMPOSITION

The XRD patterns of AAFS and OPC pastes before and after 60 days of immersion in simulated chloride-rich pore solution are shown in Fig.7-7. As the remnant crystalline phase of raw materials, quartz (SiO₂, PDF# 01-079-1910) is identified in both AAFS and OPC. Calcite (CaCO₃, PDF# 01-071-3699) and gaylussite (Na₂Ca(CO₃)₂·5H₂O, PDF# 00-021-0343) are also detected as major carbonates (Ke et al., 2016). Low intensity peaks at around 29.3° 2θ are found in all mixes, indicating that poorly crystalline C-S-H (PDF# 00-034-0002) and C-(A)-S-H (PDF# 00-033-0306) are the primary reaction products of OPC and AAFS, respectively (Ismail, Bernal, Provis, San Nicolas, et al., 2013; Z. Shi, Shi, Wan, Li, et al., 2018). Peaks related to N-A-S-H phases (PDF# 00-039-0217) are also observed in all AAFS mixes, confirming the co-existence of N-A-S-H gels and C-A-S-H gels (J. Zhang et al., 2019a, 2019b). In Fig.7-7 (b), the peaks of N-A-S-H phases are more remarkable after 60 days of immersion. It means that the formation of N-A-S-H gels plays a dominant role in the later stage, which is consistent with the more significant improvement of compressive strength (Chapter 3) and chloride resistance (Chapter 4). Due to Van der Waals force and/or electrostatic force, chloride ions can be physically adsorbed on these primary reaction products (Ismail, Bernal, Provis, San Nicolas, et al., 2013). N-A-S-H gels are generally considered to have stronger physical chloride binding capacity due to their higher specific surface area, although their more porous structure is actually detrimental to chloride resistance (Cai et al., 2022). However, the chloride binding capacity of these primary reaction products is much lower than Mg-Al LDH and Ca-Al LDH (Cai et al., 2022; Ke, Bernal, et al., 2017a, 2017b).

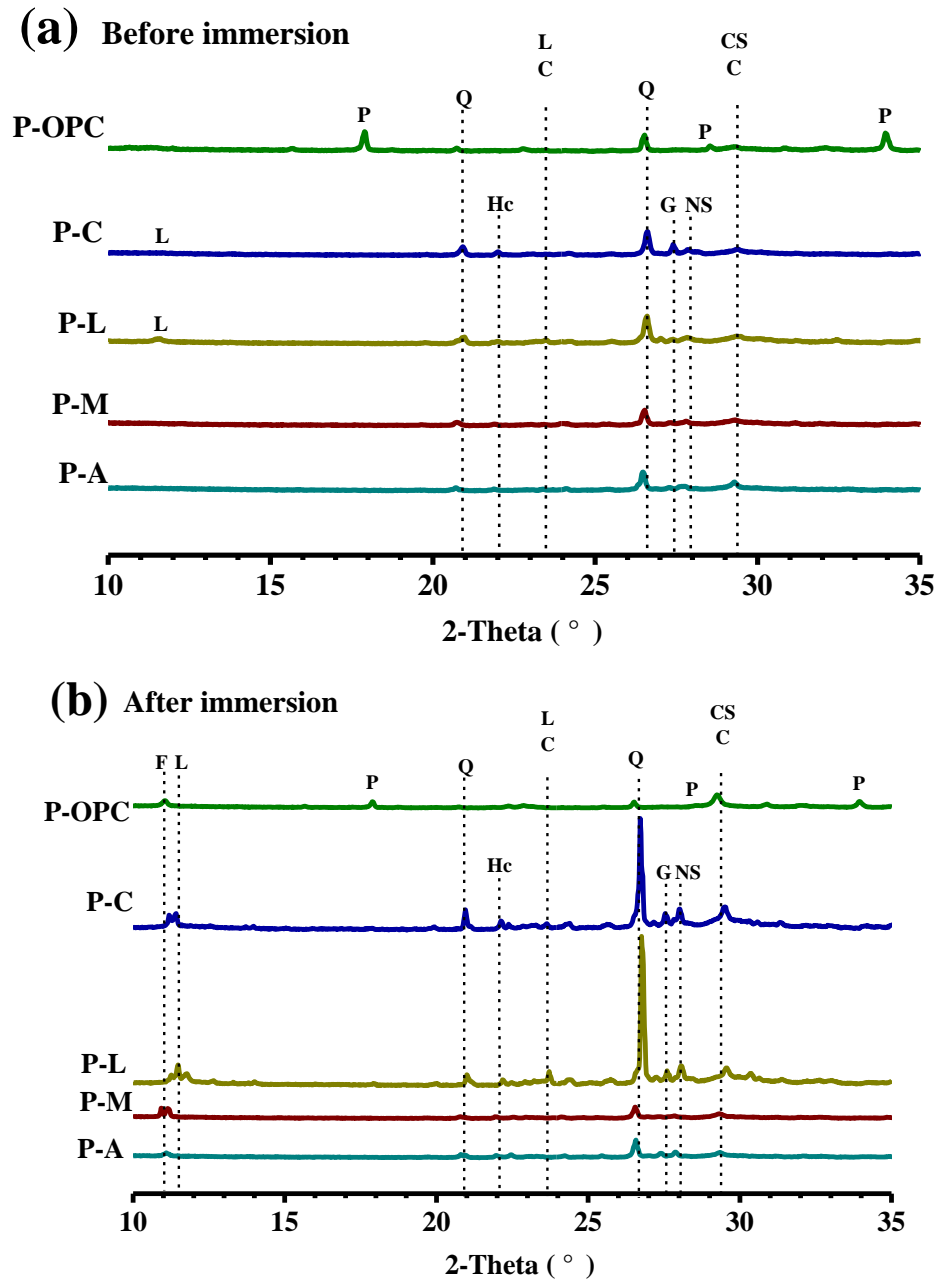


Fig.7-7 XRD patterns of AAFS and OPC pastes before (a) and after (b) 60 days of immersion in simulated chloride-rich pore solution. L: Mg-Al-CO₃ LDH (Mg₆Al₂(OH)₁₆CO₃·4H₂O, PDF# 00-014-0191); P: portlandite (Ca(OH)₂, PDF# 00-044-1481); Q: quartz (SiO₂, PDF# 01-079-1910); Hc: hemicarboaluminate (C₄Ac_{0.5}H₁₂, PDF# 00-036-0129); C: calcite (CaCO₃, PDF# 01-071-3699); G: gaylussite (Na₂Ca(CO₃)₂·5H₂O, PDF# 00-021-0343); NS: N-A-S-H (PDF# 00-039-0217); CS: C-S-H (PDF# 00-034-0002)/C-(A)-S-H (PDF# 00-033-0306); F: Friedel's salt (Ca₂Al(OH)₆Cl·2H₂O, PDF# 00-042-0558).

Fig.7-7(b) shows the formation of Friedel's salt (Ca₂Al(OH)₆Cl·2H₂O, PDF# 00-042-0558) in P-OPC after adsorption equilibrium, which can be regarded as Ca-Al LDH, indicating that chemical binding is another mechanism of interaction between

Portland cement and chloride ions (Ismail, Bernal, Provis, San Nicolas, et al., 2013). Although Friedel's salt is also observed in unmodified AAFS (P-A) after adsorption equilibrium, the intensity of the peak is lower. This finding is consistent with previous studies (Babae & Castel, 2018; Ismail, Bernal, Provis, San Nicolas, et al., 2013), which concluded that due to the absence of Mg-Al LDH and Ca-Al LDH (AFm phase), the chloride binding of unmodified AAFS was mainly determined by physical adsorption rather than chemical binding. Therefore, in previous studies (Ismail, Bernal, Provis, San Nicolas, et al., 2013; Lee & Lee, 2016; J. Zhang et al., 2019b), the bound chloride content of AAFS containing 50 wt.% GGBFS was generally lower than that of OPC at low chloride concentrations. As shown in Fig.7-7(b), the addition of Mg-based admixtures leads to the appearance of Friedel's salt and/or Mg-Al LDH ($\text{Mg}_6\text{Al}_2(\text{OH})_{16}\text{CO}_3 \cdot 4\text{H}_2\text{O}$, PDF# 00-014-0191) in AAFS. Because of their similar structures, Friedel's salt and Mg-Al LDH are often confused, but their XRD patterns are slightly different (J. Zhang et al., 2019b).

Surprisingly, the formation of Mg-Al LDH is not observed in P-M before and after adsorption equilibrium (Fig.7-7(a) and (b)). The possible reasons are the use of $\text{Na}_2\text{O} \cdot n\text{SiO}_2$ solution as activator and the incorporation of FA. J. Zhang et al. (2019a) found that the amount of Mg-Al LDH was lower in silicate-activated GGBFS. Morandau and White (2015) claimed that the addition of 13 wt.% MgO could not change this result. On the one hand, the lower initial pH of $\text{Na}_2\text{O} \cdot n\text{SiO}_2$ solution may be unfavourable to the formation of Mg-Al LDH (Morandau & White, 2015; S. Song & Jennings, 1999). On the other hand, more Si in $\text{Na}_2\text{O} \cdot n\text{SiO}_2$ solution may enhance the incorporation of Al in primary reaction products, thus reducing the Al to form Mg-Al LDH (Morandau & White, 2015). In addition, more Si can lead to lower Ca/Si ratio. Therefore, magnesium ions are more likely to participate in the formation of primary reaction products than Mg-Al LDH (M. Khan & Castel, 2018). In AAFS, the more Si dissolved from FA may have similar effects. Moreover, J. Zhang et al. (2019b) claimed that the Al tended to form N-A-S-H and zeolite phases in AAFS, which might inhibit the formation of Mg-Al LDH. However, as shown in Fig.7-7(b), the addition of 5 wt.% MgO leads to a significant increase in the intensity of the peak assigned to Friedel's salt, which is even more than that in P-OPC. In AAMs, Friedel's salt is considered to be transformed from the poorly crystalline

AFm phase (Ca-Al LDH) (Ke, Bernal, Hussein, et al., 2017), which is not always identifiable by XRD (Ke, Bernal, et al., 2017b; John L Provis & Bernal, 2014). Park et al. (2020) reported that the addition of MgO in AAS accelerated the reaction and increased the content of Mg-Al LDH and AFm phase. Therefore, although the addition of 5 wt.% MgO is not enough to form Mg-Al LDH, more AFm phase may be formed, thus forming more Friedel's salt after ion-exchange.

As shown in Fig.7-7(a) and (b), there is no obvious difference between the XRD patterns of P-L and P-C before and after adsorption equilibrium. Mg-Al LDH is identified in both P-L and P-C before immersion, which is obvious in the former (Fig.7-7(a)). After adsorption equilibrium, more Mg-Al LDH forms alongside with Friedel's salt (Fig.7-7(b)). These observations are consistent with previous studies (Ke, Bernal, Hussein, et al., 2017; Ke et al., 2016; T. Liu et al., 2020), which can confirm the recrystallisation of CLDH in AAFS. Although the replacement order of anions in Mg-Al LDH is $\text{CO}_3^{2-} > \text{OH}^- > \text{Cl}^-$, the main binding mechanism of Mg-Al LDH is surface adsorption (90%) instead of ion-exchange (10%) (Ke, Bernal, et al., 2017b). Therefore, the chloride binding capacity of added Mg-Al- CO_3 LDH and recrystallised Mg-Al-OH LDH is not much different. Unlike P-A and P-M, the intensity of the peak assigned to Friedel's salt in P-L and P-C is very weak (Fig.7-7(b)). Ke, Bernal, Hussein, et al. (2017) also obtained similar results in carbonate-activated GGBFS with 5 wt.% CLDH addition. Although the content of Ca-Al LDH decreases, the overall content of LDHs (Mg-Al LDH + Ca-Al LDH) in P-L and P-C is still higher than that in unmodified AAFS sample (P-A). Ke, Bernal, et al. (2017b) found that when the chloride concentration was higher than 0.25 mol/L, the chloride binding capacity of Mg-Al LDH was better than Ca-Al LDH. Therefore, the addition of LDH and CLDH can improve the total chloride binding capacity of AAFS. Besides, the intensity of the peak related to Mg-Al LDH in P-L before and after immersion is higher than that in P-C (Fig.7-7(a) and (b)), indicating that more Mg-Al LDH can be used to bind chloride ions. One possible explanation is that recrystallised Mg-Al LDH can act as a nucleation seed to promote gel precipitation at the initial stage (Ke et al., 2016), which hinders the subsequent recrystallisation of CLDH. Moreover, because most of the recrystallised Mg-Al LDH may be wrapped by gels, chloride ions mainly distributed in capillary pores may not be well adsorbed.

The above findings seem to explain why M-L has stronger chloride resistance than M-C (Fig.7-5).

In Fig.7-7(a), hemicarboaluminate ($C_4Ac_{0.5}H_{12}$, PDF# 00-036-0129) is also identified in all AAFS mixes (Ke et al., 2016; Ke, Bernal, et al., 2017b; John L Provis & Bernal, 2014). As a member of Ca-Al LDH, hemicarboaluminate can bind chloride ions through ion-exchange [2]. Note that only part of hemicarboaluminate can be converted to Friedel's salt [2], so the corresponding peaks in Fig.7-7(b) cannot be regarded as pure Friedel's salt.

7.3.5 EFFECTS OF MG-BASED ADMIXTURES

Based on experimental results, the compressive strength and chloride resistance of AAFS mortars are significantly higher than OPC reference samples due to the finer pore structure. All Mg-based admixtures used in this chapter can further improve the chloride resistance of AAFS mortars, although they seem to be detrimental to the compressive strength development. Through microstructural analysis, the influence mechanism of different Mg-based admixtures can be discussed.

7.3.5.1 EFFECT OF MAGNESIUM OXIDE

Compared with Mg-Al- CO_3 LDH and CLDH, adding MgO has better effect on improving the chloride resistance of AAFS mortars (Fig.7-5). This can be explained by the improvement of both pore structure and chloride binding capacity. On the one hand, the added MgO can accelerate the alkali-activation and lead to the formation of more reaction products to fill capillary pores (Jin et al., 2014; Park et al., 2020). The higher compressive strength before 28 days in Fig.7-2 and the lower volume of capillary pores in Fig.7-6 confirm the above view. As described in Section 2.2.2, compared with other influencing factors, pore structure plays a more important role in chloride diffusion in AAFS and other cementitious materials. In addition, the volume fraction and connectivity of capillary pores are critical (Pack et al., 2010; G. Ye, 2005). Therefore, the better filling of capillary pores leads to the best effect of MgO. On the other hand, although the addition of 5 wt.% MgO is insufficient to form Mg-Al LDH in AAFS due to the use of $Na_2O \cdot nSiO_2$ solution and the incorporation of FA, more Friedel's salt (Ca-Al LDH) is formed after immersion in simulated chloride-rich pore solution (Fig.7-7(b)). The chloride binding capacity of

Friedel's salt is significantly higher than that of primary reaction products (Ke, Bernal, et al., 2017a, 2017b), resulting in higher chloride binding capacity of MgO-modified AAFS.

7.3.5.2 EFFECTS OF LDH AND CLDH

Judging from the lower compressive strength in Fig.7-2, the addition of 5 wt.% Mg-Al-CO₃ LDH and CLDH can seriously affect the pore structure of AAFS. However, the result of nitrogen adsorption test (Fig.7-6) shows that air voids (>10,000 nm) are mainly affected. Compared with capillary pores, air voids have particularly small volume fraction and are not connected with each other, resulting in limited influence on chloride diffusion (Glass & Buenfeld, 2000; Pack et al., 2010). The added Mg-Al-CO₃ LDH seems to have no or minor influence on alkali-activation. By comparison, Mg-Al LDH formed via recrystallisation may act as a nucleation seed to promote gel precipitation [2]. The smaller volume of capillary pores in CLDH-modified AAFS can support this view (Fig.7-6). Therefore, compared with LDH-modified AAFS mortars, CLDH-modified AAFS mortars have higher compressive strength (Fig.7-2) and smaller D_{NSSM} measured by NSSM test (T. Liu et al., 2020), which cannot consider chloride binding (Yuanzhan Wang & Fu, 2019). The XRD patterns in Fig.7-7(b) show that the overall content of LDHs (Mg-Al LDH + Ca-Al LDH) in LDH-modified AAFS and CLDH-modified AAFS is higher, which can improve the total chloride binding capacity. Because the unfavourable pore structure caused by Mg-Al-CO₃ LDH and CLDH has little impact on chloride diffusion, the significantly improved chloride binding capacity leads to the stronger chloride resistance of LDH-modified AAFS mortars and CLDH-modified AAFS mortars. This is consistent with similar results obtained in OPC (Z. H. Shui et al., 2012) and can be confirmed by the lower and earlier initial chloride content (C_0) in chloride profiles (Fig.7-3).

Fig.7-7(a) and (b) show that the intensity of the peak related to Mg-Al LDH in LDH-modified AAFS is higher than that in CLDH-modified AAFS, which means that more Mg-Al LDH can be used to adsorb chloride ions. It may be due to that recrystallised Mg-Al LDH can act as a nucleation seed to promote gel precipitation (Ke et al., 2016), thereby hindering the subsequent recrystallisation of CLDH. Because the main binding mechanism of Mg-Al LDH is surface adsorption (90%) rather than ion-exchange (10%) (Ke, Bernal, et al., 2017b), there is little difference in

the chloride binding capacity of added Mg-Al-CO₃ LDH and recrystallised Mg-Al-OH LDH. As a result, the total chloride binding capacity of LDH-modified AAFS is stronger than that of CLDH-modified AAFS. In addition, act as a nucleation seed, the recrystallised Mg-Al LDH may be wrapped by gels (primary reaction products), so it cannot adsorb chloride ions mainly existing capillary pores. These views seem to explain why LDH-modified AAFS has lower D than CLDH-modified AAFS (Fig.7-5).

7.4 CONCLUDING REMARKS

In this chapter, the effects of different Mg-based admixtures (MgO, Mg-Al-CO₃ LDH and CLDH) on the compressive strength and chloride diffusivity of AAFS mortars are investigated. Strong correlations among chloride resistance, pore structure and phase composition are identified. Based on the experimental results and analysis, the main outcomes are summarised as follow:

- 1) The addition of 5 wt.% MgO, Mg-Al-CO₃ LDH and CLDH is not conducive to the compressive strength development of AAFS mortars. Although MgO and CLDH lead to stronger early compressive strength, they have a negative impact on subsequent compressive strength development. Mg-Al-CO₃ LDH results in a significant reduction in the compressive strength of AAFS mortars at all ages, even worse than OPC reference sample.
- 2) Chloride diffusion test shows that the chloride resistance of AAFS mortars is significantly higher than that of OPC reference sample. All Mg-based admixtures investigated in this chapter further improve the chloride resistance of AAFS mortars when the addition amount is 5 wt.%. Compared with Mg-Al-CO₃ LDH and CLDH, MgO has better improvement effect.
- 3) Compared with OPC, AAFS has lower total pore volume and lower volume of capillary pores. Adding 5 wt.% MgO in AAFS promotes the formation of more reaction products to fill capillary pores. The addition of 5 wt.% Mg-Al-CO₃ LDH and CLDH seems to cause more air voids in AAFS, which mainly affect compressive strength rather than chloride diffusion.
- 4) Friedel's salt (Ca-Al LDH) is observed in OPC and unmodified AAFS after

immersion in simulated chloride-rich pore solution. Adding 5 wt.% MgO in AAFS results in more Friedel's salt rather than Mg-Al LDH. 5 wt.% Mg-Al-CO₃ LDH and CLDH can increase the overall content of Mg-Al LDH and Ca-Al LDH in AAFS, especially the former.

- 5) Through microstructural analysis, 5 wt.% MgO results in finer pore structure and higher chloride binding capacity, both of which can improve the chloride resistance of AAFS mortars. Although 5 wt.% Mg-Al-CO₃ LDH and CLDH lead to more air voids and lower compressive strength, the enhanced chloride binding capacity has a greater positive impact on the results of chloride diffusion test. This phenomenon is more obvious in LDH-modified AAFS than in CLDH-modified AAFS.

CHAPTER 8: CONCLUSIONS AND RECOMMENDATIONS

8.1 CONCLUSIONS

Through this research, AAFA concretes with different FA/GGBFS ratios, water/binder ratios (w/b), Na₂O contents, SiO₂ contents and sand/aggregate ratios (s/a) are prepared. The engineering properties (including workability and compressive strength) of different AAFA concretes are investigated. The evolution of the chloride resistance of different AAFA concretes is comprehensively studied. The corresponding microstructure (including phase evolution and pore structure) is also analysed to explain the influence mechanism of different parameters at different ages. The long-term (up to 100 years) chloride diffusion in different AAFA concretes is predicted. The effects of different Mg-based admixtures are discussed. The general conclusions of this research are as follows:

- 1) Compared with OPC concrete, AAFA concrete can achieve similar or even better engineering properties. Most AAFA concretes designed in this study are regarded as flow/high flow concretes (slump > 100 mm). But low w/b and unreasonable s/a lead to the decline of slump. Except for SL30 and N4 (also named as Si4), the compressive strength of all AAFA concretes is higher than 50 MPa at 28 days. With the passage of time, the compressive strength of AAFA concrete continues to increase slowly. However, the compressive strength of SL100 and W40 declines in some periods. The most likely explanation is shrinkage and efflorescence.
- 2) The chloride resistance of AAFA concrete is generally better than that of OPC concrete. FA/GGBFS and w/b have a more prominent effect on the chloride resistance and water absorption of AAFA concrete compared with other parameters (Na₂O content, SiO₂ content and s/a). Higher GGBFS content ($\geq 50\%$) and lower w/b (≤ 0.45) are obviously beneficial. The D_f also gradually decreases with increasing Na₂O content and decreasing SiO₂ content, while s/a ratio has no obvious effect.
- 3) The microstructure of different AAFA mixtures (including phase evolution and pore structure) is used to establish the linkages between different parameters and

chloride resistance. Compared with the type of reaction products, the quantity of reaction products to fill capillary pores seems to be more important for the chloride resistance of AAFS concrete. Higher GGBFS content, higher Na₂O content and lower SiO₂ content promote the rapid formation of C-A-S-H gels at the beginning, leading to higher chloride resistance. However, the continuous reaction of FA can reduce the initial gap. Unlike the result in OPC, no Friedel's salt or a small amount of Friedel's salt is observed in AAFS, indicating a lack of chemical binding capacity.

- 4) There is a good correlation between D_f and volume of capillary pores rather than total porosity. Besides, the D_f of AAFS is also closely related to the threshold pore diameter and tortuosity. Because capillary pores in AAFS are considered to be disconnected, large gel pores may also have a certain effect on the chloride transport in AAFS concrete. Normally, higher GGBFS content, lower w/b, higher Na₂O content and lower SiO₂ content result in lower volume of capillary pores and smaller threshold pore diameter, which consequently improve chloride resistance.
- 5) In general, higher GGBFS content, lower w/b, higher Na₂O content and higher SiO₂ content lead to the reduction of D and C_s , resulting in the better long-term prediction results. For a very long time, s/a also has a certain impact. Based on exciting prediction results, correctly formulated AAFS concrete (50%-70% GGBFS content, 0.45 w/b, 6% Na₂O content and 6% SiO₂ content) can successfully extend the initiation phase, so as to prolong the total service life of the reinforced AAFS concrete structures under chloride-containing environments for decades or even more than 100 years. However, the interference of shrinkage and efflorescence, insufficient measurement time and inaccurate critical chloride content may still lead to unsatisfactory prediction results.
- 6) Mg-based admixtures (MgO, Mg-Al-CO₃ LDH and CLDH) can improve the chloride resistance of AAFS, although they are not conducive to the compressive strength development. Adding 5 wt.% MgO helps to fill capillary pores and leads to the formation of more Friedel's salt, thereby improving chloride resistance. The addition of 5 wt.% Mg-Al-CO₃ LDH and CLDH seems to result in more air

voids, which primarily affect compressive strength rather than chloride diffusion. However, both Mg-Al-CO₃ LDH and CLDH can increase the overall content of Mg-Al LDH and Friedel's salt, especially the former. Therefore, the enhanced chloride binding has a greater positive impact on chloride resistance.

8.2 RECOMMENDATIONS FOR THE FUTURE RESEARCH

Based on the outcomes of the work undertaken in this research, at least six areas need further research:

- 1) As described in Section 2.2.2, not only phase evolution and pore structure, but also chloride binding capacity and pore solution can affect the chloride resistance of AAFS concrete. It is suggested to study the chloride binding capacity and pore solution of different AAFS concretes to explore their effects on chloride resistance. Note that no Friedel's salt or a small amount of Friedel's salt is observed in AAFS. Therefore, the chloride binding of AAFS may be mainly determined by physical adsorption. As a result, chemical chloride binding capacity obtained according to the difference between total chloride content and free chloride content is insignificant and cannot show the actual bound chloride content.
- 2) This research shows that the formation of reaction products acts on the capillary pores, and then affects the chloride transport in AAFS concrete. However, there are more capillary pores around interfacial transition zone (ITZ). There is no targeted research on the ITZ of AAFS concrete, which is very important for further studying the influence mechanism of different parameters on the chloride resistance of AAFS concrete. To investigate the ITZ of AAFS concrete, scanning electron microscopy (SEM) and nanoindentation can be used.
- 3) The measurement results of 2 years are relatively insufficient for the prediction of 100 years, especially for the AAFS concrete with high w/b (e.g. W50). Due to larger initial water-filled space, W50 needs more time to fill capillary pores. Therefore, the reduction rate of D cannot slow down within 2 years, leading to an overwhelming rapid decrease in the time dependent model of D. To ensure the safety of the design, the measured D at 2 years instead of time dependent D has

to be used in the subsequent prediction. In the prediction of OPC concrete, the measurement data of several years or even decades have been used. In order to obtain more accurate prediction results of different AAFS concretes, longer term natural chloride diffusion tests should be carried out.

- 4) In this study, the critical chloride content for corrosion initiation is assumed to be 0.077% by weight of concrete. Due the different alkalinity and chemical composition of pore solution, the corresponding critical chloride content of different AAFS concretes may be different, resulting in the deviation of the predicted corrosion time. Although some studies have been devoted to the critical chloride content of different AAFS concretes. The findings have not been applied to the long-term prediction of the chloride transport in AAFS concrete. Because of the long initiation period of AAFS concrete, it is unrealistic to measure reinforced concrete directly. Inductively coupled plasma/atomic emission spectroscopy (ICP-OES) can used to measure the alkalinity and chemical composition of the pore solution obtained by high pressure device. Accordingly, the simulated pore solutions can be prepared for the determination of critical chloride content.
- 5) As shown in Fig.2-1, not only material characteristics, but also external conditions (e.g. external chloride concentration, temperature, wet-dry cycling action, freeze-thaw and other aggressive substances) can affect the chloride transport in AAFS concrete. Compared with the simulated marine environment in this study, the actual marine environment is more complex. The effects of different external conditions on the chloride resistance of AAFS concrete should also be studied. It is important to note that due to the wet/dry cycles of seawater, the build-up of C_s may occur in tidal zone and splash zone. This seriously affects the prediction result, which cannot be ignored. For tidal zone and splash zone, a prediction model considering not only the time dependency of D but also the time dependency of C_s should be established.
- 6) As described in Section 2.6, not only Mg-based admixtures, but also other admixtures (such as SF and nanoparticles (nano-SiO₂ and nano-TiO₂)) can change the pore structure and/or chloride binding capacity, thus affecting the

chloride resistance of AAFS and other AAMs. However, previous studies on the effects of other admixtures were also limited to short-term tests (e.g. RCPT and NSSM test), which could not consider chloride binding and reflect the real situation. An in-depth understanding of the influence mechanism is also lacking. It is recommended to perform chloride diffusion tests to explore the effects of other admixtures.

REFERENCE

- Abdalqader, A., Jin, F., & Al-Tabbaa, A. (2019). Performance of magnesia-modified sodium carbonate-activated slag/fly ash concrete. *Cement and Concrete Composites*, 103, 160-174.
- Abdalqader, A. F., Jin, F., & Al-Tabbaa, A. (2015). Characterisation of reactive magnesia and sodium carbonate-activated fly ash/slag paste blends. *Construction and Building Materials*, 93, 506-513.
- Adak, D., Sarkar, M., & Mandal, S. (2014). Effect of nano-silica on strength and durability of fly ash based geopolymer mortar. *Construction and Building Materials*, 70, 453-459.
- Adam, A. (2009). Strength and durability properties of alkali activated slag and fly ash-based geopolymer concrete.
- Ahmaruzzaman, M. (2010). A review on the utilization of fly ash. *Progress in energy and combustion science*, 36(3), 327-363.
- Ajay, V., Rajeev, C., & Yadav, R. (2012). Effect of micro silica on the strength of concrete with ordinary Portland cement. *Res J Eng Sci ISSN*, 2278, 9472.
- Akturk, B., & Kizilkanat, A. B. (2020). Improvement of durability and drying shrinkage of sodium carbonate activated slag through the incorporation of calcium hydroxide and sodium hydroxide. *Construction and Building Materials*, 243, 118260.
- Akturk, B., Nayak, S., Das, S., & Kizilkanat, A. B. (2019). Microstructure and Strength Development of Sodium Carbonate-Activated Blast Furnace Slags. *Journal of Materials in Civil Engineering*, 31(11), 04019283.
- Al-Otaibi, S. (2008). Durability of concrete incorporating GGBS activated by water-glass. *Construction and Building Materials*, 22(10), 2059-2067.
- Alanazi, H., Hu, J., & Kim, Y.-R. (2019). Effect of slag, silica fume, and metakaolin on properties and performance of alkali-activated fly ash cured at ambient temperature. *Construction and Building Materials*, 197, 747-756.
- Alexander, M. (2016). *Marine Concrete Structures: Design, Durability and Performance*: Woodhead Publishing.
- Aligizaki, K. K. (2005). *Pore structure of cement-based materials: testing, interpretation and requirements*: Crc Press.
- Allen, A. J., Thomas, J. J., & Jennings, H. M. (2007). Composition and density of nanoscale calcium-silicate-hydrate in cement. *Nature materials*, 6(4), 311-316.
- Amer, I., Kohail, M., El-Feky, M., Rashad, A., & Khalaf, M. A. (2021). A review on alkali-activated slag concrete. *Ain Shams Engineering Journal*, 12(2), 1475-1499.
- Amey, S. L., Johnson, D. A., Miltenberger, M. A., & Farzam, H. (1998). Predicting the service life of concrete marine structures: an environmental methodology. *Structural Journal*, 95(2), 205-214.
- Andrade, C., Díez, J. M., & Alonso, C. (1997). Mathematical modeling of a concrete surface "skin effect" on diffusion in chloride contaminated media. *Advanced Cement Based Materials*, 6(2), 39-44.
- Angst, U., Elsener, B., Larsen, C. K., & Vennesland, Ø. (2009). Critical chloride content in reinforced concrete—a review. *Cement and Concrete Research*, 39(12), 1122-1138.
- Arbi, K., Nedeljković, M., Zuo, Y., & Ye, G. (2016). A review on the durability of alkali-activated fly ash/slag systems: advances, issues, and perspectives.

- Industrial & Engineering Chemistry Research*, 55(19), 5439-5453.
- Ašperger, S. (2004). *Chemical kinetics and inorganic reaction mechanisms*: Springer.
- Asprogerakas, A., Koutelia, A., Kakali, G., & Tsivilis, S. (2014). *Durability of fly ash geopolymer mortars in corrosive environments, compared to that of cement mortars*. Paper presented at the Advances in Science and Technology.
- ASTM, C. (2012). Standard test method for electrical indication of concrete's ability to resist chloride ion penetration. *C1202-18*.
- Audenaert, K., Yuan, Q., & De Schutter, G. (2010). On the time dependency of the chloride migration coefficient in concrete. *Construction and Building Materials*, 24(3), 396-402.
- Babae, M., & Castel, A. (2016). Chloride-induced corrosion of reinforcement in low-calcium fly ash-based geopolymer concrete. *Cement and Concrete Research*, 88, 96-107.
- Babae, M., & Castel, A. (2018). Chloride diffusivity, chloride threshold, and corrosion initiation in reinforced alkali-activated mortars: Role of calcium, alkali, and silicate content. *Cement and Concrete Research*, 111, 56-71.
- Bahafid, S., Ghabezloo, S., Faure, P., Duc, M., & Sulem, J. (2018). Effect of the hydration temperature on the pore structure of cement paste: Experimental investigation and micromechanical modelling. *Cement and Concrete Research*, 111, 1-14.
- Balcikanli, M., & Ozbay, E. (2016). Optimum design of alkali activated slag concretes for the low oxygen/chloride ion permeability and thermal conductivity. *Composites Part B: Engineering*, 91, 243-256.
- Bamforth, P. (1999). The derivation of input data for modelling chloride ingress from eight-year UK coastal exposure trials. *Magazine of Concrete Research*, 51(2), 87-96.
- Barrett, E. P., Joyner, L. G., & Halenda, P. P. (1951). The determination of pore volume and area distributions in porous substances. I. Computations from nitrogen isotherms. *Journal of the American Chemical Society*, 73(1), 373-380.
- Behfarnia, K., & Rostami, M. (2017). Effects of micro and nanoparticles of SiO₂ on the permeability of alkali activated slag concrete. *Construction and Building Materials*, 131, 205-213.
- Beran, A., Voll, D., & Schneider, H. (2001). Dehydration and structural development of mullite precursors: an FTIR spectroscopic study. *Journal of the European Ceramic Society*, 21(14), 2479-2485.
- Berke, N., Bentur, A., & Diamond, S. (2014). *Steel corrosion in concrete: fundamentals and civil engineering practice*: CRC Press.
- Bernal, S. A., de Gutiérrez, R. M., & Provis, J. L. (2012). Engineering and durability properties of concretes based on alkali-activated granulated blast furnace slag/metakaolin blends. *Construction and Building Materials*, 33, 99-108.
- Bernal, S. A., Provis, J. L., Walkley, B., San Nicolas, R., Gehman, J. D., Brice, D. G., . . . van Deventer, J. S. (2013). Gel nanostructure in alkali-activated binders based on slag and fly ash, and effects of accelerated carbonation. *Cement and Concrete Research*, 53, 127-144.
- Bernal, S. A., San Nicolas, R., Myers, R. J., de Gutiérrez, R. M., Puertas, F., van Deventer, J. S., & Provis, J. L. (2014). MgO content of slag controls phase evolution and structural changes induced by accelerated carbonation in alkali-activated binders. *Cement and Concrete Research*, 57, 33-43.

- Berrocal, C. G. (2017). *Corrosion of steel bars in fibre reinforced concrete: Corrosion mechanisms and structural performance*: Chalmers University of Technology.
- Bi, X., Zhang, H., & Dou, L. (2014). Layered double hydroxide-based nanocarriers for drug delivery. *Pharmaceutics*, 6(2), 298-332.
- Boddy, A., Bentz, E., Thomas, M., & Hooton, R. (1999). An overview and sensitivity study of a multimechanistic chloride transport model. *Cement and Concrete Research*, 29(6), 827-837.
- Böhni, H. (2005). *Corrosion in reinforced concrete structures*: Elsevier.
- Bondar, D., Basheer, M., & Nanukuttan, S. (2019). Suitability of alkali activated slag/fly ash (AA-GGBS/FA) concretes for chloride environments: Characterisation based on mix design and compliance testing. *Construction and Building Materials*, 216, 612-621.
- Bondar, D., Lynsdale, C. J., Milestone, N. B., & Hassani, N. (2012). Oxygen and chloride permeability of alkali-activated natural pozzolan concrete. *ACI Materials Journal*, 109(1), 53-61.
- Bondar, D., Ma, Q., Soutsos, M., Basheer, M., Provis, J. L., & Nanukuttan, S. (2018). Alkali activated slag concretes designed for a desired slump, strength and chloride diffusivity. *Construction and Building Materials*, 190, 191-199.
- Booher, H. B., Martello, D. V., Tamilia, J. P., & Irdi, G. A. (1994). Microscopic study of spheres and microspheres in fly ash. *Fuel*, 73(2), 205-213.
- Bragg, W. H., & Bragg, W. L. (1913). The reflection of X-rays by crystals. *Proceedings of the Royal Society of London A: Mathematical, Physical and Engineering Sciences*, 88(605), 428-438.
- Brough, A., & Atkinson, A. (2002). Sodium silicate-based, alkali-activated slag mortars: Part I. Strength, hydration and microstructure. *Cement and Concrete Research*, 32(6), 865-879.
- Brough, A., Holloway, M., Sykes, J., & Atkinson, A. (2000). Sodium silicate-based alkali-activated slag mortars: Part II. The retarding effect of additions of sodium chloride or malic acid. *Cement and Concrete Research*, 30(9), 1375-1379.
- Buenfeld, N., & Newman, J. (1987). Examination of three methods for studying ion diffusion in cement pastes, mortars and concrete. *Materials and Structures*, 20(1), 3-10.
- Build, N. (1999). 492. Concrete, mortar and cement-based repair materials: Chloride migration coefficient from non-steady-state migration experiments. *Nordtest method*, 492(10).
- Bye, G. C. (1999). *Portland cement: composition, production and properties*: Thomas Telford.
- Cai, W., Xu, Z., Zhang, Z., Hu, J., Huang, H., Ma, Y., . . . Wei, J. (2022). Chloride binding behavior of synthesized reaction products in alkali-activated slag. *Composites Part B: Engineering*, 238, 109919.
- Cao, Y., Zheng, D., Dong, S., Zhang, F., Lin, J., Wang, C., & Lin, C. (2019). A composite corrosion inhibitor of MgAl layered double hydroxides co-intercalated with hydroxide and organic anions for carbon steel in simulated carbonated concrete pore solutions. *Journal of the Electrochemical Society*, 166(11), C3106.
- Cardoso, L. P., Tronto, J., Crepaldi, E. L., & Barros Valim, J. (2003). Removal of benzoate anions from aqueous solution using Mg-Al layered double

- hydroxides. *Molecular Crystals and Liquid Crystals*, 390(1), 49-56.
- Chao, Y.-F., Chen, P.-C., & Wang, S.-L. (2008). Adsorption of 2, 4-D on Mg/Al-NO₃ layered double hydroxides with varying layer charge density. *Applied Clay Science*, 40(1-4), 193-200.
- Cheah, C. B., Tan, L. E., & Ramli, M. (2019). The engineering properties and microstructure of sodium carbonate activated fly ash/slag blended mortars with silica fume. *Composites Part B: Engineering*, 160, 558-572.
- Chen, H., Wang, J., Pan, T., Zhao, Y., Zhang, J., & Cao, C. (2003). Physicochemical Properties and Electrochemical Performance of Al-substituted α Ni(OH)₂ with Additives for Ni-Metal Hydride Batteries. *Journal of the Electrochemical Society*, 150(11), A1399-A1404.
- Chen, Y., Shui, Z., Chen, W., & Chen, G. (2015). Chloride binding of synthetic Ca-Al-NO₃ LDHs in hardened cement paste. *Construction and Building Materials*, 93, 1051-1058.
- Cheng, Y., Hongqiang, M., Hongyu, C., Jiabin, W., Jing, S., Zonghui, L., & Mingkai, Y. (2018). Preparation and characterization of coal gangue geopolymers. *Construction and Building Materials*, 187, 318-326.
- Chi, L., Wang, Z., Zhou, Y., Lu, S., & Yao, Y. (2018). Layered Double Hydroxides Precursor as Chloride Inhibitor: Synthesis, Characterization, Assessment of Chloride Adsorption Performance. *Materials*, 11(12), 2537.
- Chi, M. (2012). Effects of dosage of alkali-activated solution and curing conditions on the properties and durability of alkali-activated slag concrete. *Construction and Building Materials*, 35, 240-245.
- Chi, M., & Huang, R. (2013). Binding mechanism and properties of alkali-activated fly ash/slag mortars. *Construction and Building Materials*, 40, 291-298.
- Chindaprasirt, P., & Chalee, W. (2014). Effect of sodium hydroxide concentration on chloride penetration and steel corrosion of fly ash-based geopolymer concrete under marine site. *Construction and Building Materials*, 63, 303-310.
- Chindaprasirt, P., Jaturapitakkul, C., Chalee, W., & Rattanasak, U. (2009). Comparative study on the characteristics of fly ash and bottom ash geopolymers. *Waste management*, 29(2), 539-543.
- Choi, S.-w., Jang, B.-s., Kim, J.-h., & Lee, K.-m. (2014). Durability characteristics of fly ash concrete containing lightly-burnt MgO. *Construction and Building Materials*, 58, 77-84.
- Claisse, P. (2005). Transport properties of concrete. *Concrete International*, 27(1), 43-48.
- Clayden, N., Esposito, S., Aronne, A., & Pernice, P. (1999). Solid state ²⁷Al NMR and FTIR study of lanthanum aluminosilicate glasses. *Journal of non-crystalline solids*, 258(1-3), 11-19.
- Colleparidi, M., Marcialis, A., & Turriziani, R. (1970). The kinetics of penetration of chloride ions into the concrete. *Il cemento*, 67(4), 157-164.
- Collins, F., & Sanjayan, J. (2001). Microcracking and strength development of alkali activated slag concrete. *Cement and Concrete Composites*, 23(4-5), 345-352.
- Concrete, C., & Australia, A. (2009). Chloride resistance of concrete. *Report, June*.
- Costa, D. G., Rocha, A. B., Souza, W. F., Chiaro, S. S. X., & Leitão, A. A. (2012). Comparative Structural, thermodynamic and electronic analyses of ZnAlAn-hydroxalite-like compounds (An⁻ Cl⁻, F⁻, Br⁻, OH⁻, CO₃²⁻ or NO₃⁻): An ab initio study. *Applied Clay Science*, 56, 16-22.
- Costa, F., & Ribeiro, D. (2020). Reduction in CO₂ emissions during production of

- cement, with partial replacement of traditional raw materials by civil construction waste (CCW). *Journal of Cleaner Production*, 276, 123302.
- Criado, M. (2015). The corrosion behaviour of reinforced steel embedded in alkali-activated mortar. In *Handbook of Alkali-Activated Cements, Mortars and Concretes* (pp. 333-372): Elsevier.
- Criado, M., Aperador, W., & Sobrados, I. (2016). Microstructural and mechanical properties of alkali activated Colombian raw materials. *Materials*, 9(3), 158.
- Criado, M., Bastidas, D., Fajardo, S., Fernández-Jiménez, A., & Bastidas, J. (2011). Corrosion behaviour of a new low-nickel stainless steel embedded in activated fly ash mortars. *Cement and Concrete Composites*, 33(6), 644-652.
- Dakhane, A., Madavarapu, S. B., Marzke, R., & Neithalath, N. (2017). Time, temperature, and cationic dependence of alkali activation of slag: Insights from Fourier transform infrared spectroscopy and spectral deconvolution. *Applied spectroscopy*, 71(8), 1795-1807.
- Darmayanti, L., Notodarmojo, S., Damanhuri, E., Kadja, G. T., & Mukti, R. R. (2019). *Preparation of alkali-activated fly ash-based geopolymer and their application in the adsorption of copper (II) and zinc (II) ions*. Paper presented at the MATEC Web of Conferences.
- Davidovits, J. (1989). Geopolymers and geopolymeric materials. *Journal of thermal analysis*, 35(2), 429-441.
- Davidovits, J. (1991). Geopolymers: inorganic polymeric new materials. *Journal of Thermal Analysis and calorimetry*, 37(8), 1633-1656.
- Davidovits, J. (1999). *Chemistry of geopolymeric systems, terminology*. Paper presented at the Geopolymer.
- De Vargas, A. S., Dal Molin, D. C., Vilela, A. C., Da Silva, F. J., Pavao, B., & Veit, H. (2011). The effects of Na₂O/SiO₂ molar ratio, curing temperature and age on compressive strength, morphology and microstructure of alkali-activated fly ash-based geopolymers. *Cement and Concrete Composites*, 33(6), 653-660.
- Deb, P. S., Nath, P., & Sarker, P. K. (2014). The effects of ground granulated blast-furnace slag blending with fly ash and activator content on the workability and strength properties of geopolymer concrete cured at ambient temperature. *Materials & Design (1980-2015)*, 62, 32-39.
- Deb, P. S., Nath, P., & Sarker, P. K. (2015). Drying shrinkage of slag blended fly ash geopolymer concrete cured at room temperature. *Procedia Engineering*, 125, 594-600.
- Deb, P. S., Sarker, P. K., & Barbhuiya, S. (2015). Effects of nano-silica on the strength development of geopolymer cured at room temperature. *Construction and Building Materials*, 101, 675-683.
- Deb, P. S., Sarker, P. K., & Barbhuiya, S. (2016). Sorptivity and acid resistance of ambient-cured geopolymer mortars containing nano-silica. *Cement and Concrete Composites*, 72, 235-245.
- Duan, P., Chen, W., Ma, J., & Shui, Z. (2013). Influence of layered double hydroxides on microstructure and carbonation resistance of sulphoaluminate cement concrete. *Construction and Building Materials*, 48, 601-609.
- Duan, P., Yan, C., Luo, W., & Zhou, W. (2016). Effects of adding nano-TiO₂ on compressive strength, drying shrinkage, carbonation and microstructure of fluidized bed fly ash based geopolymer paste. *Construction and Building Materials*, 106, 115-125.

- Duan, X., & Evans, D. G. (2006). *Layered double hydroxides* (Vol. 119): Springer Science & Business Media.
- Duxson, P., Provis, J. L., Lukey, G. C., & Van Deventer, J. S. (2007). The role of inorganic polymer technology in the development of 'green concrete'. *Cement and Concrete Research*, 37(12), 1590-1597.
- El-Reedy, M. A. (2017). *Steel-reinforced concrete structures: Assessment and repair of corrosion*: CRC press.
- Elakneswaran, Y., Nawa, T., & Kurumisawa, K. (2009). Electrokinetic potential of hydrated cement in relation to adsorption of chlorides. *Cement and Concrete Research*, 39(4), 340-344.
- Elsharief, A., Cohen, M. D., & Olek, J. (2003). Influence of aggregate size, water cement ratio and age on the microstructure of the interfacial transition zone. *Cement and Concrete Research*, 33(11), 1837-1849.
- Fan, Y., Yin, S., Wen, Z., & Zhong, J. (1999). Activation of fly ash and its effects on cement properties. *Cement and Concrete Research*, 29(4), 467-472.
- Fang, G., Ho, W. K., Tu, W., & Zhang, M. (2018). Workability and mechanical properties of alkali-activated fly ash-slag concrete cured at ambient temperature. *Construction and Building Materials*, 172, 476-487.
- Fang, S., Lam, E. S. S., Li, B., & Wu, B. (2020). Effect of alkali contents, moduli and curing time on engineering properties of alkali activated slag. *Construction and Building Materials*, 249, 118799.
- Faucon, P., Petit, J. C., Charpentier, T., Jacquinet, J. F., & Adenot, F. (1999). Silicon substitution for aluminum in calcium silicate hydrates. *Journal of the American Ceramic Society*, 82(5), 1307-1312.
- Fernández-Jiménez, A., García-Lodeiro, I., & Palomo, A. (2007). Durability of alkali-activated fly ash cementitious materials. *Journal of materials science*, 42(9), 3055-3065.
- Fernández-Jiménez, A., & Palomo, A. (2003). Characterisation of fly ashes. Potential reactivity as alkaline cements☆. *Fuel*, 82(18), 2259-2265.
- Fernández-Jiménez, A., & Palomo, A. (2005). Mid-infrared spectroscopic studies of alkali-activated fly ash structure. *Microporous and Mesoporous Materials*, 86(1-3), 207-214.
- Fernández-Jiménez, A., Palomo, A., Sobrados, I., & Sanz, J. (2006). The role played by the reactive alumina content in the alkaline activation of fly ashes. *Microporous and Mesoporous Materials*, 91(1-3), 111-119.
- Fetter, G., Ramos, E., Olguin, M., Bosch, P., Lopez, T., & Bulbulian, S. (1997). Sorption of $^{131}\text{I}^-$ by hydrotalcites. *Journal of Radioanalytical and Nuclear Chemistry*, 221(1-2), 63-66.
- Ganesan, N., Abraham, R., & Raj, S. D. (2015). Durability characteristics of steel fibre reinforced geopolymer concrete. *Construction and Building Materials*, 93, 471-476.
- Gao, X., Yu, Q., & Brouwers, H. (2015). Reaction kinetics, gel character and strength of ambient temperature cured alkali activated slag-fly ash blends. *Construction and Building Materials*, 80, 105-115.
- Gao, X., Yu, Q., & Brouwers, H. (2016). Assessing the porosity and shrinkage of alkali activated slag-fly ash composites designed applying a packing model. *Construction and Building Materials*, 119, 175-184.
- García-Lodeiro, I., Fernández-Jiménez, A., Blanco, M. T., & Palomo, A. (2008). FTIR study of the sol-gel synthesis of cementitious gels: C-S-H and N-A-

- S–H. *Journal of Sol-Gel Science and Technology*, 45(1), 63-72.
- Garcia-Lodeiro, I., Palomo, A., & Fernández-Jiménez, A. (2015). Crucial insights on the mix design of alkali-activated cement-based binders. In *Handbook of alkali-activated cements, mortars and concretes* (pp. 49-73): Elsevier.
- Gardner, C. R. (1985). Potential and limitations of drug targeting: an overview. *Biomaterials*, 6(3), 153-160.
- Gebregziabihier, B. S., Thomas, R. J., & Peethamparan, S. (2016). Temperature and activator effect on early-age reaction kinetics of alkali-activated slag binders. *Construction and Building Materials*, 113, 783-793.
- Geng, J., Pan, C., Wang, Y., Chen, W., & Zhu, Y. (2021). Chloride binding in cement paste with calcined Mg-Al-CO₃ LDH (CLDH) under different conditions. *Construction and Building Materials*, 273, 121678.
- Gerhardt, R. (1988). As review of conventional and non-conventional pore characterization techniques. *MRS Online Proceedings Library (OPL)*, 137.
- Gjørsv, O. E. (2014). Durability analysis. In *Durability Design of Concrete Structures in Severe Environments* (pp. 116-147): CRC Press.
- Glass, G., & Buenfeld, N. (2000). Chloride - induced corrosion of steel in concrete. *Progress in Structural Engineering and Materials*, 2(4), 448-458.
- Glavind, M. (2009). Sustainability of cement, concrete and cement replacement materials in construction. In *Sustainability of construction materials* (pp. 120-147): Elsevier.
- Gluth, G. J., Arbi, K., Bernal, S. A., Bondar, D., Castel, A., Chithiraputhiran, S., . . . Ducman, V. (2020). RILEM TC 247-DTA round robin test: carbonation and chloride penetration testing of alkali-activated concretes. *Materials and Structures*, 53(1), 1-17.
- Goh, K.-H., Lim, T.-T., & Dong, Z. (2008). Application of layered double hydroxides for removal of oxyanions: a review. *Water research*, 42(6-7), 1343-1368.
- Golewski, G. L. (2020). Energy savings associated with the use of fly ash and nanoadditives in the cement composition. *Energies*, 13(9), 2184.
- Gonen, T., & Yazicioglu, S. (2007). The influence of mineral admixtures on the short and long-term performance of concrete. *Building and Environment*, 42(8), 3080-3085.
- Goto, S., & Roy, D. M. (1981). The effect of w/c ratio and curing temperature on the permeability of hardened cement paste. *Cement and Concrete Research*, 11(4), 575-579.
- Goudie, A. S. (2006). Global warming and fluvial geomorphology. *Geomorphology*, 79(3-4), 384-394.
- Grice, J. D. (2005). The structure of spurrite, tilleyite and scawtite, and relationships to other silicate-carbonate minerals. *The Canadian Mineralogist*, 43(5), 1489-1500.
- Gruskovnjak, A., Lothenbach, B., Holzer, L., Figi, R., & Winnefeld, F. (2006). Hydration of alkali-activated slag: comparison with ordinary Portland cement. *Advances in cement research*, 18(3), 119-128.
- Guang, Y. (2003). The microstructure and permeability of cementitious materials. *DUP Science*.
- Guide, C. D. (1992). Durable concrete structures, Comité Euro-International du Béton. In: Thomas Telford, UK.
- Gunasekara, C. (2016). Influence of properties of fly ash from different sources on

- the mix design and performance of geopolymer concrete.
- Gunasekara, C., Bhuiyan, S., Law, D., Setunge, S., & Ward, L. (2017). Corrosion resistance in different fly ash based geopolymer concretes. *HPC/CIC Tromsø; Norway*.
- Gunasekara, C., Law, D. W., & Setunge, S. (2016). Long term permeation properties of different fly ash geopolymer concretes. *Construction and Building Materials, 124*, 352-362.
- Guo, L., Wu, Y., Duan, P., & Zhang, Z. (2020). Improving sulfate attack resistance of concrete by using calcined Mg-Al-CO₃ LDHs: Adsorption behavior and mechanism. *Construction and Building Materials, 232*, 117256.
- Haha, M. B., Le Saout, G., Winnefeld, F., & Lothenbach, B. (2011). Influence of activator type on hydration kinetics, hydrate assemblage and microstructural development of alkali activated blast-furnace slags. *Cement and Concrete Research, 41*(3), 301-310.
- Haha, M. B., Lothenbach, B., Le Saout, G., & Winnefeld, F. (2011). Influence of slag chemistry on the hydration of alkali-activated blast-furnace slag—Part I: Effect of MgO. *Cement and Concrete Research, 41*(9), 955-963.
- Hall, C. (1977). Water movement in porous building materials—I. Unsaturated flow theory and its applications. *Building and Environment, 12*(2), 117-125.
- Hang, T. T. X., Truc, T. A., Duong, N. T., Pébère, N., & Olivier, M.-G. (2012). Layered double hydroxides as containers of inhibitors in organic coatings for corrosion protection of carbon steel. *Progress in organic coatings, 74*(2), 343-348.
- Hasholt, M. T., & Jensen, O. M. (2015). Chloride migration in concrete with superabsorbent polymers. *Cement and Concrete Composites, 55*, 290-297.
- Hendriks, C., Worrell, E., DeJager, D., Block, K., & Riemer, P. (2000). Emission reduction of greenhouse gases from the cement industry, IEA Greenhouse gas R&D Programme. In.
- Hochstetter, C. (1842). Untersuchung über die Zusammensetzung einiger Mineralien. *Journal für praktische Chemie, 27*(1), 375-378.
- Hornain, H., Marchand, J., Duhot, V., & Moranville-Regourd, M. (1995). Diffusion of chloride ions in limestone filler blended cement pastes and mortars. *Cement and Concrete Research, 25*(8), 1667-1678.
- Hu, X., Shi, C., Shi, Z., & Zhang, L. (2019). Compressive strength, pore structure and chloride transport properties of alkali-activated slag/fly ash mortars. *Cement and Concrete Composites, 104*, 103392.
- Hu, Y. J., & Du, Y. L. (2013). *The time-dependence of chloride penetration resistance of concrete by the rapid chloride permeability test*. Paper presented at the Applied Mechanics and Materials.
- HUKELER, P. (1994). Grundlagen der Korrosion und der Potentialmessung bei Stahlbetonbauten.
- Huntzinger, D. N., & Eatmon, T. D. (2009). A life-cycle assessment of Portland cement manufacturing: comparing the traditional process with alternative technologies. *Journal of Cleaner Production, 17*(7), 668-675.
- Hwang, C.-L., Vo, D.-H., Tran, V.-A., & Yehualaw, M. D. (2018). Effect of high MgO content on the performance of alkali-activated fine slag under water and air curing conditions. *Construction and Building Materials, 186*, 503-513.
- Ishwarya, G., Singh, B., Deshwal, S., & Bhattacharyya, S. (2019). Effect of sodium carbonate/sodium silicate activator on the rheology, geopolymerization and

- strength of fly ash/slag geopolymer pastes. *Cement and Concrete Composites*, 97, 226-238.
- Ismail, I., Bernal, S. A., Provis, J. L., Hamdan, S., & van Deventer, J. S. (2013a). Drying-induced changes in the structure of alkali-activated pastes. *Journal of materials science*, 48(9), 3566-3577.
- Ismail, I., Bernal, S. A., Provis, J. L., Hamdan, S., & van Deventer, J. S. (2013b). Microstructural changes in alkali activated fly ash/slag geopolymers with sulfate exposure. *Materials and Structures*, 46(3), 361-373.
- Ismail, I., Bernal, S. A., Provis, J. L., San Nicolas, R., Brice, D. G., Kilcullen, A. R., . . . van Deventer, J. S. (2013). Influence of fly ash on the water and chloride permeability of alkali-activated slag mortars and concretes. *Construction and Building Materials*, 48, 1187-1201.
- Ismail, I., Bernal, S. A., Provis, J. L., San Nicolas, R., Hamdan, S., & van Deventer, J. S. (2014). Modification of phase evolution in alkali-activated blast furnace slag by the incorporation of fly ash. *Cement and Concrete Composites*, 45, 125-135.
- Jena, S., Panigrahi, R., & Sahu, P. (2019). Mechanical and Durability Properties of Fly Ash Geopolymer Concrete with Silica Fume. *Journal of The Institution of Engineers (India): Series A*, 100(4), 697-705.
- Jeon, D., Jun, Y., Jeong, Y., & Oh, J. E. (2015). Microstructural and strength improvements through the use of Na₂CO₃ in a cementless Ca (OH) 2-activated Class F fly ash system. *Cement and Concrete Research*, 67, 215-225.
- Jiang, J.-y., Sun, G.-w., & Wang, C.-h. (2013). Numerical calculation on the porosity distribution and diffusion coefficient of interfacial transition zone in cement-based composite materials. *Construction and Building Materials*, 39, 134-138.
- Jin, F., Gu, K., & Al-Tabbaa, A. (2014). Strength and drying shrinkage of reactive MgO modified alkali-activated slag paste. *Construction and Building Materials*, 51, 395-404.
- Jin, F., Gu, K., & Al-Tabbaa, A. (2015). Strength and hydration properties of reactive MgO-activated ground granulated blastfurnace slag paste. *Cement and Concrete Composites*, 57, 8-16.
- Jindal, B. B., & Sharma, R. (2020). The effect of nanomaterials on properties of geopolymers derived from industrial by-products: A state-of-the-art review. *Construction and Building Materials*, 252, 119028.
- Jithendra, C., & Elavenil, S. (2020). Effects of silica fume on workability and compressive strength properties of aluminosilicate based flowable geopolymer mortar under ambient curing. *Silicon*, 12(8), 1965-1974.
- Juenger, M., Winnefeld, F., Provis, J. L., & Ideker, J. (2011). Advances in alternative cementitious binders. *Cement and Concrete Research*, 41(12), 1232-1243.
- Juenger, M. C. G., & Jennings, H. M. (2001). The use of nitrogen adsorption to assess the microstructure of cement paste. *Cement and Concrete Research*, 31(6), 883-892.
- Júnior, N. S. A., Neto, J. S. A., Santana, H. A., Cilla, M. S., & Ribeiro, D. V. (2021). Durability and service life analysis of metakaolin-based geopolymer concretes with respect to chloride penetration using chloride migration test and corrosion potential. *Construction and Building Materials*, 287, 122970.
- Kassir, M. K., & Ghosn, M. (2002). Chloride-induced corrosion of reinforced concrete bridge decks. *Cement and Concrete Research*, 32(1), 139-143.

- Ke, X., Bernal, S. A., Hussein, O. H., & Provis, J. L. (2017). Chloride binding and mobility in sodium carbonate-activated slag pastes and mortars. *Materials and Structures*, 50(6), 252.
- Ke, X., Bernal, S. A., & Provis, J. L. (2016). Controlling the reaction kinetics of sodium carbonate-activated slag cements using calcined layered double hydroxides. *Cement and Concrete Research*, 81, 24-37.
- Ke, X., Bernal, S. A., & Provis, J. L. (2017a). *Chloride binding capacity of synthetic C-(A)-S-H type gels in alkali-activated slag simulated pore solutions*. Paper presented at the Proceedings of the 1st international conference on construction materials for sustainable future, Zadar, Croatia.
- Ke, X., Bernal, S. A., & Provis, J. L. (2017b). Uptake of chloride and carbonate by Mg-Al and Ca-Al layered double hydroxides in simulated pore solutions of alkali-activated slag cement. *Cement and Concrete Research*, 100, 1-13.
- Ke, X., Bernal, S. A., & Provis, J. L. (2018). Layered double hydroxides modify the reaction of sodium silicate-activated slag cements. *Green Materials*(2049-1220).
- Khan, M., & Castel, A. (2018). Effect of MgO and Na₂SiO₃ on the carbonation resistance of alkali activated slag concrete. *Magazine of Concrete Research*, 70(13), 685-692.
- Khan, M., Kayali, O., & Troitzsch, U. (2016). Chloride binding capacity of hydrotalcite and the competition with carbonates in ground granulated blast furnace slag concrete. *Materials and Structures*, 49(11), 4609-4619.
- Khan, M. I., & Siddique, R. (2011). Utilization of silica fume in concrete: Review of durability properties. *Resources, Conservation and Recycling*, 57, 30-35.
- Khan, M. U., Ahmad, S., & Al-Gahtani, H. J. (2017). Chloride-induced corrosion of steel in concrete: an overview on chloride diffusion and prediction of corrosion initiation time. *International Journal of Corrosion*, 2017.
- Khatib, J. M., Baalbaki, O., & ElKordi, A. A. (2018). Metakaolin. In *Waste and Supplementary Cementitious Materials in Concrete* (pp. 493-511): Elsevier.
- Kim, Y. Y., Lee, B.-J., Saraswathy, V., & Kwon, S.-J. (2014). Strength and durability performance of alkali-activated rice husk ash geopolymer mortar. *The Scientific World Journal*, 2014.
- Koch, G., Varney, J., Thompson, N., Moghissi, O., Gould, M., & Payer, J. (2016). International measures of prevention, application, and economics of corrosion technologies study. *NACE International IMPACT Report*.
- Komljenović, M., Bašćarević, Z., & Bradić, V. (2010). Mechanical and microstructural properties of alkali-activated fly ash geopolymers. *Journal of hazardous materials*, 181(1-3), 35-42.
- Kunther, W., Ferreiro, S., & Skibsted, J. (2017). Influence of the Ca/Si ratio on the compressive strength of cementitious calcium-silicate-hydrate binders. *Journal of Materials Chemistry A*, 5(33), 17401-17412.
- Kupwade-Patil, K., & Allouche, E. N. (2013). Examination of chloride-induced corrosion in reinforced geopolymer concretes. *Journal of Materials in Civil Engineering*, 25(10), 1465-1476.
- Kutti, T., Berntsson, L., & Chandra, S. (1992). Shrinkage of cements with high content of blast-furnace slag. *Proceedings of Fly ash, silica fume, slag and natural pozzolans in concrete. Istanbul*, 615-625.
- L'Hôpital, E., Lothenbach, B., Le Saout, G., Kulik, D., & Scrivener, K. (2015). Incorporation of aluminium in calcium-silicate-hydrates. *Cement and*

- Concrete Research*, 75, 91-103.
- Law, D. W., Adam, A. A., Molyneaux, T. K., & Patnaikuni, I. (2012). Durability assessment of alkali activated slag (AAS) concrete. *Materials and Structures*, 45(9), 1425-1437.
- Law, D. W., Adam, A. A., Molyneaux, T. K., Patnaikuni, I., & Wardhono, A. (2015). Long term durability properties of class F fly ash geopolymer concrete. *Materials and Structures*, 48(3), 721-731.
- Lecomte, I., Henrist, C., Liégeois, M., Maseri, F., Rulmont, A., & Cloots, R. (2006). (Micro)-structural comparison between geopolymers, alkali-activated slag cement and Portland cement. *Journal of the European Ceramic Society*, 26(16), 3789-3797.
- Lee, N., Jang, J. G., & Lee, H.-K. (2014). Shrinkage characteristics of alkali-activated fly ash/slag paste and mortar at early ages. *Cement and Concrete Composites*, 53, 239-248.
- Lee, N., & Lee, H.-K. (2015). Reactivity and reaction products of alkali-activated, fly ash/slag paste. *Construction and Building Materials*, 81, 303-312.
- Lee, N., & Lee, H.-K. (2016). Influence of the slag content on the chloride and sulfuric acid resistances of alkali-activated fly ash/slag paste. *Cement and Concrete Composites*, 72, 168-179.
- Li, D., Wang, F., Yu, X., Wang, J., Liu, Q., Yang, P., . . . Zhang, M. (2011). Anticorrosion organic coating with layered double hydroxide loaded with corrosion inhibitor of tungstate. *Progress in organic coatings*, 71(3), 302-309.
- Li, J., Gao, L., Hou, D., Wang, P., Zhou, Y., Ding, Q., & Xiong, C. (2020). Insights on the ion migration throughout the nano-channel of ettringite under an external electric field: Structure, dynamics, and mechanisms. *Construction and Building Materials*, 262, 120074.
- Li, N., Shi, C., Wang, Q., Zhang, Z., & Ou, Z. (2017). Composition design and performance of alkali-activated cements. *Materials and Structures*, 50(3), 178.
- Liu, T., Chen, Y., Yu, Q., Fan, J., & Brouwers, H. (2020). Effect of MgO, Mg-Al-NO₃ LDH and calcined LDH-CO₃ on chloride resistance of alkali activated fly ash and slag blends. *Construction and Building Materials*, 250, 118865.
- Liu, Y., Shi, C., Zhang, Z., & Li, N. (2019). An overview on the reuse of waste glasses in alkali-activated materials. *Resources, Conservation and Recycling*, 144, 297-309.
- Liu, Z., Zhang, D.-w., Li, L., Wang, J.-x., Shao, N.-n., & Wang, D.-m. (2019). Microstructure and phase evolution of alkali-activated steel slag during early age. *Construction and Building Materials*, 204, 158-165.
- Lloyd, R. R., Provis, J. L., Smeaton, K. J., & van Deventer, J. S. (2009). Spatial distribution of pores in fly ash-based inorganic polymer gels visualised by Wood's metal intrusion. *Microporous and Mesoporous Materials*, 126(1-2), 32-39.
- Lodeiro, I. G., Macphee, D. E., Palomo, A., & Fernández-Jiménez, A. (2009). Effect of alkalis on fresh C-S-H gels. FTIR analysis. *Cement and Concrete Research*, 39(3), 147-153.
- Longhi, M. A., Rodríguez, E. D., Walkley, B., Zhang, Z., & Kirchheim, A. P. (2020). Metakaolin-based geopolymers: Relation between formulation, physicochemical properties and efflorescence formation. *Composites Part B: Engineering*, 182, 107671.
- Lv, L., Sun, P., Gu, Z., Du, H., Pang, X., Tao, X., . . . Xu, L. (2009). Removal of

- chloride ion from aqueous solution by ZnAl-NO₃ layered double hydroxides as anion-exchanger. *Journal of hazardous materials*, 161(2-3), 1444-1449.
- Lv, L., Wang, Y., Wei, M., & Cheng, J. (2008). Bromide ion removal from contaminated water by calcined and uncalcined MgAl-CO₃ layered double hydroxides. *Journal of hazardous materials*, 152(3), 1130-1137.
- Ma, Q., Nanukuttan, S. V., Basheer, P. M., Bai, Y., & Yang, C. (2016). Chloride transport and the resulting corrosion of steel bars in alkali activated slag concretes. *Materials and Structures*, 49(9), 3663-3677.
- Ma, R., Liu, Z., Li, L., Iyi, N., & Sasaki, T. (2006). Exfoliating layered double hydroxides in formamide: a method to obtain positively charged nanosheets. *Journal of Materials Chemistry*, 16(39), 3809-3813.
- Ma, Y. (2013a). Microstructure and Engineering Properties of Alkali Activated Fly Ash-as an environment friendly alternative to Portland cement. *Delft Technical University of Technology*.
- Ma, Y. (2013b). Microstructure and Engineering Properties of Alkali Activated Fly Ash-as an environment friendly alternative to Portland cement.
- Ma, Y., Hu, J., & Ye, G. (2012). The effect of activating solution on the mechanical strength, reaction rate, mineralogy, and microstructure of alkali-activated fly ash. *Journal of materials science*, 47(11), 4568-4578.
- Ma, Y., Wang, G., Ye, G., & Hu, J. (2018). A comparative study on the pore structure of alkali-activated fly ash evaluated by mercury intrusion porosimetry, N₂ adsorption and image analysis. *Journal of materials science*, 53(8), 5958-5972.
- Ma, Y., Yang, X., Hu, J., Zhang, Z., & Wang, H. J. C. P. B. E. (2019). Accurate determination of the “time-zero” of autogenous shrinkage in alkali-activated fly ash/slag system. 177, 107367.
- Ma, Y., & Ye, G. (2015). The shrinkage of alkali activated fly ash. *Cement and Concrete Research*, 68, 75-82.
- Maiti, M., Sarkar, M., Maiti, S., Malik, M. A., & Xu, S. (2020). Modification of geopolymer with size controlled TiO₂ nanoparticle for enhanced durability and catalytic dye degradation under UV light. *Journal of Cleaner Production*, 255, 120183.
- Mangat, P., & Molloy, B. (1994). Prediction of long term chloride concentration in concrete. *Materials and Structures*, 27(6), 338-346.
- Mangat, P., & Ojedokun, O. O. (2019). Bound chloride ingress in alkali activated concrete. *Construction and Building Materials*, 212, 375-387.
- Mangat, P., & Ojedokun, O. O. (2020). Free and bound chloride relationships affecting reinforcement cover in alkali activated concrete. *Cement and Concrete Composites*, 103692.
- Manzano, H., Dolado, J. S., & Ayuela, A. (2009). Aluminum incorporation to dreierketten silicate chains. *The Journal of Physical Chemistry B*, 113(9), 2832-2839.
- McLellan, B. C., Williams, R. P., Lay, J., Van Riessen, A., & Corder, G. D. (2011). Costs and carbon emissions for geopolymer pastes in comparison to ordinary portland cement. *Journal of Cleaner Production*, 19(9-10), 1080-1090.
- Mehta, A., Siddique, R., Ozbakkaloglu, T., Shaikh, F. U. A., & Belarbi, R. (2020). Fly ash and ground granulated blast furnace slag-based alkali-activated concrete: Mechanical, transport and microstructural properties. *Construction and Building Materials*, 257, 119548.

- Mehta, P., & Monteiro, P. (2014). *Concrete: microstructure, properties, and materials*: McGraw-Hill Education.
- Memon, F. A., Nuruddin, M. F., & Shafiq, N. (2013). Effect of silica fume on the fresh and hardened properties of fly ash-based self-compacting geopolymer concrete. *International Journal of Minerals, Metallurgy, and Materials*, 20(2), 205-213.
- Mineral commodity summaries 2021*. (2021). Retrieved from Reston, VA: <http://pubs.er.usgs.gov/publication/mcs2021>
- Mithun, B., & Narasimhan, M. (2016). Performance of alkali activated slag concrete mixes incorporating copper slag as fine aggregate. *Journal of Cleaner Production*, 112, 837-844.
- Miyata, S. (1975). The Syntheses of Hydrotalcite-Like Compounds and Their Structures and Physico-Chemical Properties—I: the Systems Mg²⁺-Al³⁺-NO³⁻, Mg²⁺-Al³⁺-Cl⁻, Mg²⁺-Al³⁺-ClO⁴⁻, Ni²⁺-Al³⁺-Cl⁻ and Zn²⁺-Al³⁺-Cl⁻. *Clays and Clay Minerals*, 23(5), 369-375.
- Miyata, S., & Kumura, T. (1973). Synthesis of new hydrotalcite-like compounds and their physico-chemical properties. *Chemistry Letters*, 2(8), 843-848.
- Mobili, A., Belli, A., Giosuè, C., Bellezze, T., & Tittarelli, F. (2016). Metakaolin and fly ash alkali-activated mortars compared with cementitious mortars at the same strength class. *Cement and Concrete Research*, 88, 198-210.
- Mohseni, E., Miyandehi, B. M., Yang, J., & Yazdi, M. A. (2015). Single and combined effects of nano-SiO₂, nano-Al₂O₃ and nano-TiO₂ on the mechanical, rheological and durability properties of self-compacting mortar containing fly ash. *Construction and Building Materials*, 84, 331-340.
- Montemor, M., Simoes, A., & Ferreira, M. (2003). Chloride-induced corrosion on reinforcing steel: from the fundamentals to the monitoring techniques. *Cement and Concrete Composites*, 25(4-5), 491-502.
- Monticelli, C., Natali, M., Balbo, A., Chiavari, C., Zanotto, F., Manzi, S., & Bignozzi, M. (2016). Corrosion behavior of steel in alkali-activated fly ash mortars in the light of their microstructural, mechanical and chemical characterization. *Cement and Concrete Research*, 80, 60-68.
- Monticelli, C., Natali, M., Balbo, A., Chiavari, C., Zanotto, F., Manzi, S., & Bignozzi, M. (2016). A study on the corrosion of reinforcing bars in alkali-activated fly ash mortars under wet and dry exposures to chloride solutions. *Cement and Concrete Research*, 87, 53-63.
- Morandau, A. E., & White, C. E. (2015). Role of magnesium-stabilized amorphous calcium carbonate in mitigating the extent of carbonation in alkali-activated slag. *Chemistry of Materials*, 27(19), 6625-6634.
- Moukwa, M. (1989). Penetration of chloride ions from sea water into mortars under different exposure conditions. *Cement and Concrete Research*, 19(6), 894-904.
- Mucsi, G., Kumar, S., Csőke, B., Kumar, R., Molnár, Z., Rácz, Á., . . . Debreczeni, Á. (2015). Control of geopolymer properties by grinding of land filled fly ash. *International Journal of Mineral Processing*, 143, 50-58.
- Mundra, S., Bernal Lopez, S., Criado, M., Hlaváček, P., Ebell, G., Reinemann, S., . . . Provis, J. (2017). Steel corrosion in reinforced alkali-activated materials. *RILEM Technical Letters*, 2, 33-39.
- Mundra, S., Bernal, S. A., & Provis, J. L. (2017). *Corrosion initiation of steel reinforcement in simulated alkali-activated slag pore solution*. Paper

- presented at the 1st international conference of construction materials for sustainable future, CoMS2017, Zadar, Croatia.
- Myers, R. J., Bernal, S. A., & Provis, J. L. (2014). A thermodynamic model for C-(N-) ASH gel: CNASH_{ss}. Derivation and validation. *Cement and concrete research*, 66, 27-47.
- Myers, R. J., Bernal, S. A., & Provis, J. L. (2017). Phase diagrams for alkali-activated slag binders. *Cement and Concrete Research*, 95, 30-38.
- Nath, P., & Sarker, P. K. (2014). Effect of GGBFS on setting, workability and early strength properties of fly ash geopolymer concrete cured in ambient condition. *Construction and Building Materials*, 66, 163-171.
- Nath, S., & Kumar, S. (2020). Role of particle fineness on engineering properties and microstructure of fly ash derived geopolymer. *Construction and Building Materials*, 233, 117294.
- Nawab, L., & Ghani, U. (2017). Synthesis and characterization of chloride resistant cement from industrial waste through geopolymerization. *Journal of Cleaner Production*, 156, 577-580.
- Nedeljkovic, M., Arbi, K., Zuo, Y., & Ye, G. (2016). *Physical properties and pore solution analysis of alkali activated fly ash-slag pastes*. Paper presented at the Proceedings of the International RILEM Conference on Materials, Systems and Structures in Civil Engineering, Conference segment on Concrete with Supplementary Cementitious materials, Lyngby, Denmark.
- Nedeljković, M., Ghiassi, B., van der Laan, S., Li, Z., & Ye, G. (2019). Effect of curing conditions on the pore solution and carbonation resistance of alkali-activated fly ash and slag pastes. *Cement and Concrete Research*, 116, 146-158.
- Nedeljković, M., Šavija, B., Zuo, Y., Luković, M., & Ye, G. (2018). Effect of natural carbonation on the pore structure and elastic modulus of the alkali-activated fly ash and slag pastes. *Construction and Building Materials*, 161, 687-704.
- Neithalath, N., & Jain, J. (2010). Relating rapid chloride transport parameters of concretes to microstructural features extracted from electrical impedance. *Cement and Concrete Research*, 40(7), 1041-1051.
- Nematollahi, B., Sanjayan, J., & Shaikh, F. U. A. (2015). Synthesis of heat and ambient cured one-part geopolymer mixes with different grades of sodium silicate. *Ceramics International*, 41(4), 5696-5704.
- Neville, A. M. (1995). *Properties of concrete* (Vol. 4): Longman London.
- Nishimura, T., Kakiuchi, N., Inoue, M., & Uemura, S. (2000). Palladium (II)-supported hydrotalcite as a catalyst for selective oxidation of alcohols using molecular oxygen. *Chemical Communications*(14), 1245-1246.
- Nodehi, M., & Taghvaei, V. M. (2021). Alkali-activated materials and geopolymer: a review of common precursors and activators addressing circular economy. *Circular Economy and Sustainability*, 1-32.
- Noushini, A., Castel, A., Aldred, J., & Rawal, A. (2020). Chloride diffusion resistance and chloride binding capacity of fly ash-based geopolymer concrete. *Cement and Concrete Composites*, 105, 103290.
- Nuaklong, P., Sata, V., & Chindaprasirt, P. (2016). Influence of recycled aggregate on fly ash geopolymer concrete properties. *Journal of Cleaner Production*, 112, 2300-2307.
- Okoye, F. N., Prakash, S., & Singh, N. B. (2017). Durability of fly ash based geopolymer concrete in the presence of silica fume. *Journal of Cleaner*

- Production*, 149, 1062-1067.
- Osio-Norgaard, J., Gevaudan, J. P., & Srubar III, W. V. (2018). A review of chloride transport in alkali-activated cement paste, mortar, and concrete. *Construction and Building Materials*, 186, 191-206.
- Ouyang, X., Ma, Y., Liu, Z., Liang, J., & Ye, G. (2020). Effect of the sodium silicate modulus and slag content on fresh and hardened properties of alkali-activated fly ash/slag. *Minerals*, 10(1), 15.
- Pacheco-Torgal, F., Castro-Gomes, J., & Jalali, S. (2008). Alkali-activated binders: A review. Part 2. About materials and binders manufacture. *Construction and Building Materials*, 22(7), 1315-1322.
- Pacheco-Torgal, F., Labrincha, J., Leonelli, C., Palomo, A., & Chindaprasit, P. (2014). *Handbook of alkali-activated cements, mortars and concretes*: Elsevier.
- Pack, S.-W., Jung, M.-S., Song, H.-W., Kim, S.-H., & Ann, K. Y. (2010). Prediction of time dependent chloride transport in concrete structures exposed to a marine environment. *Cement and Concrete Research*, 40(2), 302-312.
- Page, C., Short, N., & El Tarras, A. (1981). Diffusion of chloride ions in hardened cement pastes. *Cement and Concrete Research*, 11(3), 395-406.
- Pal, S., Mukherjee, A., & Pathak, S. (2003). Investigation of hydraulic activity of ground granulated blast furnace slag in concrete. *Cement and Concrete Research*, 33(9), 1481-1486.
- Palomo, A., Grutzeck, M., & Blanco, M. (1999). Alkali-activated fly ashes: a cement for the future. *Cement and Concrete Research*, 29(8), 1323-1329.
- Pan, Z., Tao, Z., Cao, Y., Wuhner, R., & Murphy, T. (2018). Compressive strength and microstructure of alkali-activated fly ash/slag binders at high temperature. *Cement and Concrete Composites*, 86, 9-18.
- Panesar, D. K. (2019). Supplementary cementing materials. In *Developments in the Formulation and Reinforcement of Concrete* (pp. 55-85): Elsevier.
- Papadakis, V. G. (1999). Effect of fly ash on Portland cement systems: Part I. Low-calcium fly ash. *Cement and Concrete Research*, 29(11), 1727-1736.
- Papadakis, V. G. (2000). Effect of fly ash on Portland cement systems: Part II. High-calcium fly ash. *Cement and Concrete Research*, 30(10), 1647-1654.
- Pargar, F., Koleva, D., & van Breugel, K. (2017). Determination of chloride content in cementitious materials: from fundamental aspects to application of Ag/AgCl chloride sensors. *Sensors*, 17(11), 2482.
- Park, S., Park, H. M., Yoon, H., Seo, J., Yang, C.-M., Provis, J. L., & Yang, B. (2020). Hydration kinetics and products of MgO-activated blast furnace slag. *Construction and Building Materials*, 249, 118700.
- Parthiban, K., & Mohan, K. S. R. (2017). Influence of recycled concrete aggregates on the engineering and durability properties of alkali activated slag concrete. *Construction and Building Materials*, 133, 65-72.
- Paschmann, H., Grube, H., & Thielen, G. (1995). Prüfverfahren und Untersuchungen zum Eindringen von Flüssigkeiten und Gasen in Beton sowie zum chemischen Widerstand von Beton. *Deutscher Ausschuss für Stahlbeton*(450), 3-54.
- Pegado, L., Labbez, C., & Churakov, S. V. (2014). Mechanism of aluminium incorporation into C-S-H from ab initio calculations. *Journal of Materials Chemistry A*, 2(10), 3477-3483.
- Perraton, D., Aitcin, P., & Vezina, D. (1988). Permeabilities of silica fume concrete.

Special Publication, 108, 63-84.

- Phoo-ngernkham, T., Chindaprasirt, P., Sata, V., Hanjitsuwan, S., & Hatanaka, S. (2014). The effect of adding nano-SiO₂ and nano-Al₂O₃ on properties of high calcium fly ash geopolymer cured at ambient temperature. *Materials & Design, 55*, 58-65.
- Potgieter-Vermaak, S., Potgieter, J., Belleil, M., DeWeerd, F., & Van Grieken, R. (2006). The application of Raman spectrometry to the investigation of cement: Part II: A micro-Raman study of OPC, slag and fly ash. *Cement and Concrete Research, 36*(4), 663-670.
- Poursae, A. (2016). Corrosion of steel in concrete structures. In *Corrosion of Steel in Concrete Structures* (pp. 19-33): Elsevier.
- Powers, T. C., Copeland, L. E., & Mann, H. (1959). *Capillary continuity or discontinuity in cement pastes*. Retrieved from
- Prakasam, G., Murthy, A. R., & Saffiq Rehemam, M. (2020). Mechanical, durability and fracture properties of nano-modified FA/GGBS geopolymer mortar. *Magazine of Concrete Research, 72*(4), 207-216.
- Praveenkumar, T., Vijayalakshmi, M., & Meddah, M. (2019). Strengths and durability performances of blended cement concrete with TiO₂ nanoparticles and rice husk ash. *Construction and Building Materials, 217*, 343-351.
- Provis, J. L. (2009). Activating solution chemistry for geopolymers. In *Geopolymers* (pp. 50-71): Elsevier.
- Provis, J. L. (2014). Geopolymers and other alkali activated materials: why, how, and what? *Materials and Structures, 47*(1-2), 11-25.
- Provis, J. L., & Bernal, S. A. (2014). Geopolymers and related alkali-activated materials. *Annual Review of Materials Research, 44*, 299-327.
- Provis, J. L., Myers, R. J., White, C. E., Rose, V., & van Deventer, J. S. (2012). X-ray microtomography shows pore structure and tortuosity in alkali-activated binders. *Cement and Concrete Research, 42*(6), 855-864.
- Provis, J. L., Palomo, A., & Shi, C. (2015). Advances in understanding alkali-activated materials. *Cement and Concrete Research, 78*, 110-125. doi:<https://doi.org/10.1016/j.cemconres.2015.04.013>
- Provis, J. L., & Van Deventer, J. S. (2013). *Alkali activated materials: state-of-the-art report, RILEM TC 224-AAM* (Vol. 13): Springer Science & Business Media.
- Provis, J. L., & Van Deventer, J. S. J. (2009). *Geopolymers: structures, processing, properties and industrial applications*: Elsevier.
- Puertas, F., Martínez-Ramírez, S., Alonso, S., & Vazquez, T. (2000). Alkali-activated fly ash/slag cements: strength behaviour and hydration products. *Cement and Concrete Research, 30*(10), 1625-1632.
- Qu, Z., Yu, Q., & Brouwers, H. (2018). Relationship between the particle size and dosage of LDHs and concrete resistance against chloride ingress. *Cement and Concrete Research, 105*, 81-90.
- Ramezani-pour, A. A., & Moeini, M. A. (2018). Mechanical and durability properties of alkali activated slag coating mortars containing nanosilica and silica fume. *Construction and Building Materials, 163*, 611-621.
- Rashad, A., Bai, Y., Basheer, P., Milestone, N., & Collier, N. (2013). Hydration and properties of sodium sulfate activated slag. *Cement and Concrete Composites, 37*, 20-29.
- Rashad, A. M. (2013). Alkali-activated metakaolin: A short guide for civil Engineer–

- An overview. *Construction and Building Materials*, 41, 751-765.
- Rashad, A. M., Khafaga, S. A., & Ghariieb, M. (2021). Valorization of fly ash as an additive for electric arc furnace slag geopolymer cement. *Construction and Building Materials*, 294, 123570.
- Ravikumar, D., & Neithalath, N. (2013a). An electrical impedance investigation into the chloride ion transport resistance of alkali silicate powder activated slag concretes. *Cement and Concrete Composites*, 44, 58-68.
- Ravikumar, D., & Neithalath, N. (2013b). Electrically induced chloride ion transport in alkali activated slag concretes and the influence of microstructure. *Cement and Concrete Research*, 47, 31-42.
- Recommendation, R. D. (1994). Draft recommendation for repair strategies for concrete structures damaged by reinforcement corrosion. *Materials and Structures*, 27(171), 415-436.
- Ren, D., Yan, C., Duan, P., Zhang, Z., Li, L., & Yan, Z. (2017). Durability performances of wollastonite, tremolite and basalt fiber-reinforced metakaolin geopolymer composites under sulfate and chloride attack. *Construction and Building Materials*, 134, 56-66.
- Richardson, I. G. (2008). The calcium silicate hydrates. *Cement and Concrete Research*, 38(2), 137-158.
- Rickard, W. D., Temuujin, J., & van Riessen, A. (2012). Thermal analysis of geopolymer pastes synthesised from five fly ashes of variable composition. *Journal of non-crystalline solids*, 358(15), 1830-1839.
- Rodríguez, E., Bernal, S., de Gutiérrez, R. M., & Puertas, F. (2008). Alternative concrete based on alkali-activated slag. *Materiales de Construcción*, 58(291), 53-67.
- Roelofs, J., Lensveld, D., Van Dillen, A., & De Jong, K. (2001). On the structure of activated hydrotalcites as solid base catalysts for liquid-phase aldol condensation. *Journal of Catalysis*, 203(1), 184-191.
- Rostami, M., & Behfarnia, K. (2017). The effect of silica fume on durability of alkali activated slag concrete. *Construction and Building Materials*, 134, 262-268.
- Rowles, M. R., Hanna, J. V., Pike, K. J., Smith, M. E., & O'Connor, B. H. (2007). ²⁹Si, ²⁷Al, ¹H and ²³Na MAS NMR Study of the Bonding Character in Aluminosilicate Inorganic Polymers. *Applied Magnetic Resonance*, 32(4), 663-689. doi:10.1007/s00723-007-0043-y
- Roy, D. M., & Idorn, G. (1993). *Concrete microstructure*.
- Sabir, B., Wild, S., & Bai, J. (2001). Metakaolin and calcined clays as pozzolans for concrete: a review. *Cement and Concrete Composites*, 23(6), 441-454.
- Saha, S., & Rajasekaran, C. (2017). Enhancement of the properties of fly ash based geopolymer paste by incorporating ground granulated blast furnace slag. *Construction and Building Materials*, 146, 615-620.
- San Nicolas, R., & Provis, J. L. (2015). The interfacial transition zone in alkali-activated slag mortars. *Frontiers in Materials*, 2, 70.
- Sanchez, F., & Sobolev, K. (2010). Nanotechnology in concrete—a review. *Construction and Building Materials*, 24(11), 2060-2071.
- Sastry, K. G. K., Sahitya, P., & Ravitheja, A. (2020). Influence of nano TiO₂ on strength and durability properties of geopolymer concrete. *Materials Today: Proceedings*.
- Scott, A., & Alexander, M. (2016). Effect of supplementary cementitious materials (binder type) on the pore solution chemistry and the corrosion of steel in

- alkaline environments. *Cement and Concrete Research*, 89, 45-55.
- Shi, C. (1996). Strength, pore structure and permeability of alkali-activated slag mortars. *Cement and Concrete Research*, 26(12), 1789-1799.
- Shi, C., Jiménez, A. F., & Palomo, A. (2011). New cements for the 21st century: The pursuit of an alternative to Portland cement. *Cement and Concrete Research*, 41(7), 750-763. doi:<https://doi.org/10.1016/j.cemconres.2011.03.016>
- Shi, C., Roy, D., & Krivenko, P. (2003). *Alkali-activated cements and concretes*: CRC press.
- Shi, C., Tang, X., & Li, Y. (1989). *Studies on the activation of phosphorus slag*. Paper presented at the Proceedings of the Third International Conference on the Use of Fly Ash, Silica Fume, Slag and Natural Pozzolans in Concrete.
- Shi, X., Xie, N., Fortune, K., & Gong, J. (2012). Durability of steel reinforced concrete in chloride environments: An overview. *Construction and Building Materials*, 30, 125-138.
- Shi, Z., Shi, C., Wan, S., Li, N., & Zhang, Z. (2018). Effect of alkali dosage and silicate modulus on carbonation of alkali-activated slag mortars. *Cement and Concrete Research*, 113, 55-64.
- Shi, Z., Shi, C., Wan, S., & Zhang, Z. (2018). Effects of alkali dosage and silicate modulus on alkali-silica reaction in alkali-activated slag mortars. *Cement and Concrete Research*, 111, 104-115.
- Shimizu, H., Okubo, M., Nakamoto, A., Enomoto, M., & Kojima, N. (2006). Enhancement of the Curie Temperature by Isomerization of Diarylethene (DAE) for an Organic– Inorganic Hybrid System: $\text{Co}_4(\text{OH})_7(\text{DAE})_0.5 \cdot 3\text{H}_2\text{O}$. *Inorganic chemistry*, 45(25), 10240-10247.
- Shui, Z., Yu, R., Chen, Y., Duan, P., Ma, J., & Wang, X. (2018). Improvement of concrete carbonation resistance based on a structure modified Layered Double Hydroxides (LDHs): Experiments and mechanism analysis. *Construction and Building Materials*, 176, 228-240.
- Shui, Z. H., Ma, J. T., Chen, W., & Gao, X. (2012). *The effect of layered double hydroxides on the concrete resistance of chloride-ion penetration*. Paper presented at the Key Engineering Materials.
- Siddique, R. (2011). Utilization of silica fume in concrete: Review of hardened properties. *Resources, Conservation and Recycling*, 55(11), 923-932.
- Siddique, R., & Khan, M. I. (2011). *Supplementary cementing materials*: Springer Science & Business Media.
- Singh, S., Munjal, P., & Thammishetti, N. (2015). Role of water/cement ratio on strength development of cement mortar. *Journal of Building Engineering*, 4, 94-100.
- Škvára, F., Jílek, T., & Kopecký, L. (2005). Geopolymer materials based on fly ash. *Ceram.-Silik*, 49(3), 195-204.
- Škvára, F., Kopecký, L., Šmilauer, V., & Bittnar, Z. (2009). Material and structural characterization of alkali activated low-calcium brown coal fly ash. *Journal of hazardous materials*, 168(2-3), 711-720.
- Somna, K., Jaturapitakkul, C., Kajitvichyanukul, P., & Chindapasirt, P. (2011). NaOH-activated ground fly ash geopolymer cured at ambient temperature. *Fuel*, 90(6), 2118-2124.
- Song, H.-W., Lee, C.-H., & Ann, K. Y. (2008). Factors influencing chloride transport in concrete structures exposed to marine environments. *Cement and Concrete Composites*, 30(2), 113-121.

- Song, S., & Jennings, H. M. (1999). Pore solution chemistry of alkali-activated ground granulated blast-furnace slag. *Cement and Concrete Research*, 29(2), 159-170.
- Standard, C. (2002). GB/T, 50081-2002 Method for testing mechanical properties of normal concrete. *Beijing, China*.
- Standard, C. (2003). Standard of Test Method of Performance on Ordinary Fresh Concrete (GB/T 50080-2002). *China Building Industry Press, Beijing, China*.
- Stanish, K., Hooton, R. D., & Thomas, M. D. (2001). *Testing the Chloride Penetration Resistance of Concrete: A Literature Review*. Retrieved from
- Sun, G., Young, J. F., & Kirkpatrick, R. J. (2006). The role of Al in C–S–H: NMR, XRD, and compositional results for precipitated samples. *Cement and Concrete Research*, 36(1), 18-29.
- Tahri, W., Hu, X., Shi, C., & Zhang, Z. (2021). Review on corrosion of steel reinforcement in alkali-activated concretes in chloride-containing environments. *Construction and Building Materials*, 293, 123484.
- Takewaka, K., & Mastumoto, S. (1988). Quality and cover thickness of concrete based on the estimation of chloride penetration in marine environments. *Special Publication*, 109, 381-400.
- Talling, B., & Brandstetr, J. (1989). Present state and future of alkali-activated slag concretes. *Special Publication*, 114, 1519-1546.
- Taylor, H. (1973). Crystal structures of some double hydroxide minerals. *Mineralogical Magazine*, 39(304), 377-389.
- Taylor, H. F. (1997). *Cement chemistry* (Vol. 2): Thomas Telford London.
- Tennakoon, C., Shayan, A., Sanjayan, J. G., & Xu, A. (2017). Chloride ingress and steel corrosion in geopolymer concrete based on long term tests. *Materials & Design*, 116, 287-299.
- Thomas, R., Ariyachandra, E., Lezama, D., & Peethamparan, S. (2018). Comparison of chloride permeability methods for Alkali-Activated concrete. *Construction and Building Materials*, 165, 104-111.
- Thomas, R. J., Ye, H., Radlinska, A., & Peethamparan, S. (2016). Alkali-activated slag cement concrete. *Concr. Int*, 38(1), 33-38.
- Thorne, D., & Watt, J. (1965). Composition and pozzolanic properties of pulverised fuel ashes. II. Pozzolanic properties of fly ashes, as determined by crushing strength tests on lime mortars. *Journal of applied chemistry*, 15(12), 595-604.
- Tran, V. M., Nawa, T., & Stitmannathum, B. (2014). Chloride binding isotherms of various cements basing on binding capacity of hydrates. *Computers and Concrete*, 13(6), 695-707.
- Tsyganok, A. I., Tsunoda, T., Hamakawa, S., Suzuki, K., Takehira, K., & Hayakawa, T. (2003). Dry reforming of methane over catalysts derived from nickel-containing Mg–Al layered double hydroxides. *Journal of Catalysis*, 213(2), 191-203.
- Turner, L. K., & Collins, F. G. (2013). Carbon dioxide equivalent (CO₂-e) emissions: A comparison between geopolymer and OPC cement concrete. *Construction and Building Materials*, 43, 125-130.
- Tuutti, K. (1982). Corrosion of steel in concrete.
- Uji, K., Matsuoka, Y., & Maruya, T. (1990). Formulation of an equation for surface chloride content of concrete due to permeation of chloride. *Elsevier Applied Science*, 258-267.
- Vu, T. H., Gowripalan, N., De Silva, P., Kidd, P., & Sirivivatnanon, V. (2018).

CARBONATION AND CHLORIDE INDUCED STEEL CORROSION RELATED ASPECTS IN FLY ASH/SLAG BASED GEOPOLYMERS-A CRITICAL REVIEW. Paper presented at the 5th International fib Congress.

- Wang, A., Zheng, Y., Zhang, Z., Liu, K., Li, Y., Shi, L., & Sun, D. (2020). The durability of alkali-activated materials in comparison with ordinary portland cements and concretes: A review. *Engineering*.
- Wang, D., Zhang, W., Ruan, Y., Yu, X., & Han, B. (2018). Enhancements and mechanisms of nanoparticles on wear resistance and chloride penetration resistance of reactive powder concrete. *Construction and Building Materials*, 189, 487-497.
- Wang, G., & Ma, Y. (2018). Drying shrinkage of alkali-activated fly ash/slag blended system. *Journal of Sustainable Cement-Based Materials*, 7(4), 203-213.
- Wang, H., Chen, J., Cai, Y., Ji, J., Liu, L., & Teng, H. H. (2007). Defluoridation of drinking water by Mg/Al hydrotalcite-like compounds and their calcined products. *Applied Clay Science*, 35(1-2), 59-66.
- Wang, Q., & O'Hare, D. (2012). Recent advances in the synthesis and application of layered double hydroxide (LDH) nanosheets. *Chemical reviews*, 112(7), 4124-4155.
- Wang, S.-D., & Scrivener, K. L. (1995). Hydration products of alkali activated slag cement. *Cement and Concrete Research*, 25(3), 561-571.
- Wang, S.-D., Scrivener, K. L., & Pratt, P. (1994). Factors affecting the strength of alkali-activated slag. *Cement and Concrete Research*, 24(6), 1033-1043.
- Wang, S.-L., Cheng, C.-Y., Tzou, Y.-M., Liaw, R.-B., Chang, T.-W., & Chen, J.-H. (2007). Phosphate removal from water using lithium intercalated gibbsite. *Journal of hazardous materials*, 147(1-2), 205-212.
- Wang, S., Hseu, R., Chang, R., Chiang, P., Chen, J., & Tzou, Y. (2006). Adsorption and thermal desorption of Cr (VI) on Li/Al layered double hydroxide. *Colloids and Surfaces A: Physicochemical and Engineering Aspects*, 277(1-3), 8-14.
- Wang, Y., Cao, Y., Ma, Y., Xiao, S., Hu, J., & Wang, H. (2021). Fresh and hardened properties of alkali-activated fly ash/slag binders: effect of fly ash source, surface area, and additives. *Journal of Sustainable Cement-Based Materials*, 1-24.
- Wang, Y., Cao, Y., Zhang, P., Ma, Y., Zhao, T., Wang, H., & Zhang, Z. (2019). Water absorption and chloride diffusivity of concrete under the coupling effect of uniaxial compressive load and freeze–thaw cycles. *Construction and Building Materials*, 209, 566-576.
- Wang, Y., Cao, Y., Zhang, Z., Huang, J., Zhang, P., Ma, Y., & Wang, H. (2022). Study of acidic degradation of alkali-activated materials using synthetic C-(N)-ASH and NASH gels. *Composites Part B: Engineering*, 230, 109510.
- Wang, Y., & Fu, K. (2019). Comparisons of instantaneous chloride diffusion coefficients determined by RCM method and chloride natural diffusion test. *Construction and Building Materials*, 223, 595-604.
- Wardhono, A., Gunasekara, C., Law, D. W., & Setunge, S. (2017). Comparison of long term performance between alkali activated slag and fly ash geopolymer concretes. *Construction and Building Materials*, 143, 272-279.
- Washburn, E. W. (1921). The dynamics of capillary flow. *Physical review*, 17(3), 273.

- Watt, J., & Thorne, D. (1965). Composition and pozzolanic properties of pulverised fuel ashes. I. Composition of fly ashes from some British power stations and properties of their component particles. *Journal of applied chemistry*, 15(12), 585-594.
- Wei, X., Li, D., Ming, F., Yang, C., Chen, L., & Liu, Y. (2021). Influence of low-temperature curing on the mechanical strength, hydration process, and microstructure of alkali-activated fly ash and ground granulated blast furnace slag mortar. *Construction and Building Materials*, 269, 121811.
- Wei, Z. S., & Zongjin, L. (2009). Preparation and microstructure of na-psds geopolymeric matrix. *Ceramics-silikaty*, 53(2), 88-97.
- Weng, L., Sagoe-Crentsil, K., Brown, T., & Song, S. (2005). Effects of aluminates on the formation of geopolymers. *Materials Science and Engineering: B*, 117(2), 163-168.
- Whitesides, G. M. (2005). Nanoscience, nanotechnology, and chemistry. *Small*, 1(2), 172-179.
- Whiting, D. (1981). Rapid determination of the chloride permeability of concrete. *pca*.
- Xu, A., & Shayan, A. (2015). *Determination of chloride diffusion coefficient of concrete: comparison of bulk diffusion and electrical field method*. Paper presented at the Concrete Institute of Australia Conference, 27th, 2015, Melbourne, Victoria, Australia.
- Xue, S., Zhang, P., Bao, J., He, L., Hu, Y., & Yang, S. (2020). Comparison of mercury intrusion porosimetry and multi-scale X-ray CT on characterizing the microstructure of heat-treated cement mortar. *Materials Characterization*, 160, 110085.
- Yan, Y., Yang, S.-Y., Miron, G. D., Collings, I. E., L'Hôpital, E., Skibsted, J., . . . Lothenbach, B. (2022). Effect of alkali hydroxide on calcium silicate hydrate (CSH). *Cement and Concrete Research*, 151, 106636.
- Yang, K., Yang, C., Magee, B., Nanukuttan, S., & Ye, J. (2016). Establishment of a preconditioning regime for air permeability and sorptivity of alkali-activated slag concrete. *Cement and Concrete Composites*, 73, 19-28.
- Yang, L., Dadwhal, M., Shahrivari, Z., Ostwal, M., Liu, P. K., Sahimi, M., & Tsotsis, T. T. (2006). Adsorption of arsenic on layered double hydroxides: effect of the particle size. *Industrial & Engineering Chemistry Research*, 45(13), 4742-4751.
- Yang, T., Yao, X., & Zhang, Z. (2014). Quantification of chloride diffusion in fly ash-slag-based geopolymers by X-ray fluorescence (XRF). *Construction and Building Materials*, 69, 109-115.
- Yang, T., Zhu, H., Zhang, Z., Gao, X., Zhang, C., & Wu, Q. (2018). Effect of fly ash microsphere on the rheology and microstructure of alkali-activated fly ash/slag pastes. *Cement and Concrete Research*, 109, 198-207.
- Yang, Z., Fischer, H., & Polder, R. (2015). Laboratory investigation of the influence of two types of modified hydrotalcites on chloride ingress into cement mortar. *Cement and Concrete Composites*, 58, 105-113.
- Yang, Z., Ha, N., Jang, M., & Hwang, K. H. (2009). *Geopolymer concrete fabricated by waste concrete sludge with silica fume*. Paper presented at the Materials Science Forum.
- Ye, G. (2003). Experimental study and numerical simulation of the development of the microstructure and permeability of cementitious materials.

- Ye, G. (2005). Percolation of capillary pores in hardening cement pastes. *Cement and Concrete Research*, 35(1), 167-176.
- Ye, H., & Radlińska, A. (2016). Fly ash-slag interaction during alkaline activation: Influence of activators on phase assemblage and microstructure formation. *Construction and Building Materials*, 122, 594-606.
- Ye, N., Yang, J., Liang, S., Hu, Y., Hu, J., Xiao, B., & Huang, Q. (2016). Synthesis and strength optimization of one-part geopolymer based on red mud. *Construction and Building Materials*, 111, 317-325.
- Yip, C. K., Lukey, G., & Van Deventer, J. (2005). The coexistence of geopolymeric gel and calcium silicate hydrate at the early stage of alkaline activation. *Cement and Concrete Research*, 35(9), 1688-1697.
- Yoon, H., Park, S. M., & Lee, H.-K. (2018). Effect of MgO on chloride penetration resistance of alkali-activated binder. *Construction and Building Materials*, 178, 584-592.
- Yoon, S., Moon, J., Bae, S., Duan, X., Giannelis, E. P., & Monteiro, P. M. (2014). Chloride adsorption by calcined layered double hydroxides in hardened Portland cement paste. *Materials Chemistry and Physics*, 145(3), 376-386.
- Young, J. F., Mindess, S., & Darwin, D. (2002). *Concrete*: Prentice Hall.
- Yu, P., Kirkpatrick, R. J., Poe, B., McMillan, P. F., & Cong, X. (1999). Structure of calcium silicate hydrate (C - S - H): Near - , Mid - , and Far - infrared spectroscopy. *Journal of the American Ceramic Society*, 82(3), 742-748.
- Yu, Z. (2015). Microstructure development and transport properties of portland cement-fly ash binary systems: in view of service life predictions.
- Yuan, Q., Shi, C., De Schutter, G., Audenaert, K., & Deng, D. (2009). Chloride binding of cement-based materials subjected to external chloride environment—a review. *Construction and Building Materials*, 23(1), 1-13.
- Zandalinas, S. I., Fritschi, F. B., & Mittler, R. (2021). Global warming, climate change, and environmental pollution: Recipe for a multifactorial stress combination disaster. *Trends in Plant Science*.
- Zhang, B., Wang, J., Wu, B., Guo, X., Wang, Y., Chen, D., . . . Ma, X. (2018). Unmasking chloride attack on the passive film of metals. *Nature communications*, 9(1), 2559.
- Zhang, J., Shi, C., & Zhang, Z. (2019a). Carbonation induced phase evolution in alkali-activated slag/fly ash cements: The effect of silicate modulus of activators. *Construction and Building Materials*, 223, 566-582.
- Zhang, J., Shi, C., & Zhang, Z. (2019b). Chloride binding of alkali-activated slag/fly ash cements. *Construction and Building Materials*, 226, 21-31.
- Zhang, J., Shi, C., & Zhang, Z. (2020). Effect of Na₂O concentration and water/binder ratio on carbonation of alkali-activated slag/fly ash cements. *Construction and Building Materials*, 121258.
- Zhang, J., Shi, C., Zhang, Z., & Ou, Z. (2017a). Durability of alkali-activated materials in aggressive environments: A review on recent studies. *Construction and Building Materials*, 152, 598-613.
- Zhang, J., Shi, C., Zhang, Z., & Ou, Z. (2017b). Durability of alkali-activated materials in aggressive environments: A review on recent studies. *Construction & Building Materials*, 152, 598-613. doi:10.1016/j.conbuildmat.2017.07.027
- Zhang, R., Castel, A., & François, R. (2009). Serviceability limit state criteria based on steel–concrete bond loss for corroded reinforced concrete in chloride

- environment. *Materials and Structures*, 42(10), 1407-1421.
- Zhang, S., Li, Z., Ghiassi, B., Yin, S., & Ye, G. (2021). Fracture properties and microstructure formation of hardened alkali-activated slag/fly ash pastes. *Cement and Concrete Research*, 144, 106447.
- Zhang, T., & Gjrrv, O. E. (1996). Diffusion behavior of chloride ions in concrete. *Cement and Concrete Research*, 26(6), 907-917.
- Zhang, Y., Sun, W., & Li, Z. (2008). Infrared spectroscopy study of structural nature of geopolymeric products. *Journal of Wuhan University of Technology-Mater. Sci. Ed.*, 23(4), 522-527.
- Zhang, Z., Provis, J. L., Reid, A., & Wang, H. (2014). Fly ash-based geopolymers: the relationship between composition, pore structure and efflorescence. *Cement and Concrete Research*, 64, 30-41.
- Zhao, M. Q., Zhang, Q., Huang, J. Q., & Wei, F. (2012). Hierarchical nanocomposites derived from nanocarbons and layered double hydroxides - properties, synthesis, and applications. *Advanced Functional Materials*, 22(4), 675-694.
- Zhao, Y., Dong, J., Wu, Y., & Jin, W. (2016). Corrosion-induced concrete cracking model considering corrosion product-filled paste at the concrete/steel interface. *Construction and Building Materials*, 116, 273-280.
- Zhao, Y., & Jin, W. (2016). *Steel Corrosion-Induced Concrete Cracking*: Butterworth-Heinemann.
- Zhao, Y., Qiu, J., Zhang, S., Guo, Z., Ma, Z., Sun, X., & Xing, J. (2020). Effect of sodium sulfate on the hydration and mechanical properties of lime-slag based eco-friendly binders. *Construction and Building Materials*, 250, 118603.
- Zhou, Y., Genurk, B., Willam, K., & Attar, A. (2014). Carbonation-induced and chloride-induced corrosion in reinforced concrete structures. *Journal of Materials in Civil Engineering*, 27(9), 04014245.
- Zhu, H., Zhang, Z., Zhu, Y., & Tian, L. (2014). Durability of alkali-activated fly ash concrete: chloride penetration in pastes and mortars. *Construction and Building Materials*, 65, 51-59.
- Zhuang, X. Y., Chen, L., Komarneni, S., Zhou, C. H., Tong, D. S., Yang, H. M., . . . Wang, H. (2016). Fly ash-based geopolymer: clean production, properties and applications. *Journal of Cleaner Production*, 125, 253-267.
- Zuo, Y., Nedeljkovi, M., & Ye, G. (2018). Coupled thermodynamic modelling and experimental study of sodium hydroxide activated slag. *Construction and Building Materials*, 188, 262-279.
- Zuo, Y., Nedeljkovi, M., & Ye, G. (2019). Pore solution composition of alkali-activated slag/fly ash pastes. *Cement and Concrete Research*, 115, 230-250.